Stall-induced vibrations of a blade section in deep-stall

Hansen, Morten Hartvig

Published in:
Research in Aeroelasticity EFP-2007-II

Publication date:
2009

Document Version
Publisher's PDF, also known as Version of record

Citation (APA):
Hansen, M. H. (2009). Stall-induced vibrations of a blade section in deep-stall. In T. Buhl (Ed.), Research in Aeroelasticity EFP-2007-II (pp. 114-121). Roskilde: Danmarks Tekniske Universitet, Risø Nationallaboratoriet for Bæredygtig Energi. (Denmark. Forskningscenter Risoe. Risoe-R; No. 1698(EN)).

Research in Aeroelasticity EFP-2007-II

Risø-R-Report

Edited by Thomas Buhl
Risø-R-1698(EN)
June 2009

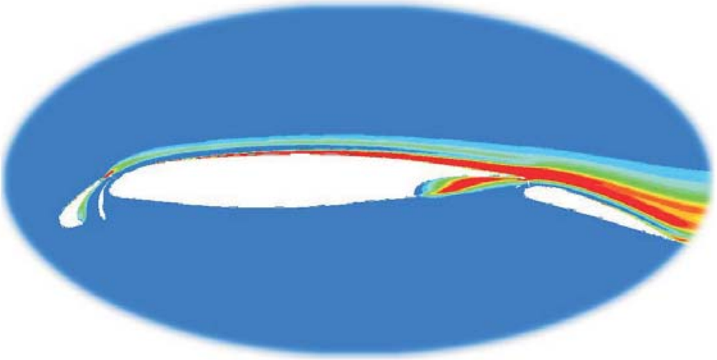

Risø DTU
National Laboratory for Sustainable Energy

Author: Thomas Buhl (ed.)
Title: Research in Aeroelasticity EFP-2007-II
Division: Wind Energy Division

Risø-R-1698(EN)
June 2009

Abstract (max. 2000 char.):

This report contains results from the EFP-2007-II project "Program for Research in Applied Aeroelasticity". The main results can be summed up into the following bullets:

- 2D CFD was used to investigate tower shadow effects on both upwind and downwind turbines, and was used to validate the tower shadow models implemented in the aeroelastic code HAWC2.
- Using a streamlined tower reduces the tower shadow by 50% compared to a cylindrical tower. Similar reductions can be achieved using a four legged lattice tower.
- The application of laminar/turbulent transition in CFD computations for airfoils is demonstrated. For attached flow over thin airfoils (18%) 2D computations provide good results while a combination of Detached Eddy Simulation and laminar/turbulent transition modeling improve the results in stalled conditions for a thick airfoil.
- The unsteady flow in the nacelle region of a wind turbine is dominated by large flow gradients caused by unsteady shedding of vortices from the root sections of the blades.
- The averaged nacelle wind speed compares well to the freestream wind speed, whereas the nacelle flow angle is highly sensitive to vertical positioning and tilt in the inflow.
- The trailing edge noise model, TNO, was implemented and validated. The results showed that the noise was not predicted accurately, but the model captured the trends and can be used in airfoil design. The model was implemented in the airfoil design tool AIRFOILOPT and existing airfoils can be adjusted to maintain the aerodynamic characteristics, but with reduced noise in the order of up to 3dB in total sound power level and up to 1dB with A-weighting.
- 2D CFD simulations are performed to verify their capability in predicting multi element airfoil configurations. The present computations show good agreement with measured performance from wind tunnel experiments.
- The stochastic fluctuations of the aerodynamic forces on blades in deep-stall have an insignificant effect on the risk of stallinduced vibrations predicted by quasi-steady aerodynamic models, but more realistic models of deep-stall aerodynamics must be developed to finally conclude on the real risk of stallinduced vibrations at standstill.
- Finite element analysis shows that local blade cross section deformations caused by global blade deflection do not have significant influence on the aerodynamic performance.

ISSN 0106-2840
ISBN 978-87-550-3759-5

Contract no.:
ENS 033001/33033-0266

Group's own reg. no.:
1110065-01 to 1110065-08

Sponsorship:
Danish Energy Authorities

Cover :
Multi element airfoil

Pages: 147
Tables: 19
References:

Information Service Department
Risø National Laboratory for Sustainable Energy
Technical University of Denmark
P.O.Box 49
DK-4000 Roskilde
Denmark
Telephone +45 46774005
bibl@risoe.dtu.dk
Fax +45 46774013
www.risoe.dtu.dk

Contents

1 Preface

The Energy Research Project "Program for Research in Applied Aeroelasticity, EFP-2007-II" was carried out in cooperation between two institutes at the Technical University of Denmark (DTU), Risø National Laboratory for Sustainable Energy (Risø DTU) and the Department of Mechanical Engineering (DTU MEK), from 1 April 2008 to 31 March 2009. From the onset of the project, six milestones were defined which represent the main part of the research activity. Apart from the work focused on the milestones, also analysis of current problems and further development of the existing models were carried out.

Several researchers at DTU MEK and Risø DTU have been involved in the project work and have contributed to the research presented in this report. To enable reference to the different parts of the report, the names of the authors are indicated for each chapter. It should, however, be emphasized that the report is not a detailed report of the complete activity within the project. Thus, not all of the contributors to the project appear as authors to the different chapters. For a detailed description of the results from the project, please see Chapter 14 in which a complete list of publications in the project can be found.

At DTU MEK, the following researchers from the Fluid Mechanics Section of the Department of Mechanical Engineering have been involved in the project:

Kurt S. Hansen
Martin O.L. Hansen
Gabriel Hernandez
Robert Mikkelsen
Wen Zhong Shen
Jens N. Sørensen
Stig Øye

At Risø DTU, primarily the researchers from the Aeroelastic Design Group have contributed to the project:

Peter B. Andersen
Christian Bak
Andreas Bechmann
Franck Bertagnolio
Thomas Buhl
Mads Døssing
Mac Gaunaa
Anders M. Hansen
Morten H. Hansen
Bjarne S. Kallesøe
Gunner C. Larsen
Torben J. Larsen
Helge A. Madsen
Helen Markou
Flemming Rasmussen
Niels N. Sørensen
Niels Troldborg
Frederik Zahle

2 Summary

2.1 Introduction

This report contains the results from the Energy Research Project "Program for Research in Applied Aeroelasticity, EFP-2007-II" covering the period from April 1^{st} 2008 to March 31^{st} 2009. The partners in the project are the two institutes at Technical University of Denmark (DTU), Risø National Laboratory for Sustainable Energy (Risø DTU) and the Department of Mechanical Engineering (DTU MEK). The overall objectives of the project are to ensure the development of an aeroelastic design complex, which can create the basis for the next generation of wind turbines and make new design concepts possible. The project forms a strategic cooperation between Risø DTU and DTU MEK and the wind turbine industry with emphasis on obtaining a suitable balance between long-term strategic research, applied research and technological development. To obtain synergy between the different subjects and to ensure an optimal, dynamic cooperation with the industry, while maintaining the continuity of the research, the project is organized as a research program within applied aeroelasticity with a combination of research activities with specific short-term targets within one year and general continuous long-term research activities. This research project has been the tenth in a row of one-year projects, which has ensured a continuous development since 1997, where the activity in this row of projects is described in [1–10].

2.2 Evaluation of Tower Shadow Effects on Various Wind Turbine Concepts

A 2D CFD study has been carried out to evaluate the effects of tower shadow on a blade section for an upwind turbine and three downwind turbine concepts; one with a traditional tubular tower, another with a streamlined tower and lastly, one with a four legged configuration. Two turbines were used as basis for the study: Firstly the NREL Phase VI turbine, which was used for validation against experimental results; secondly the UPWIND 5 MW reference turbine, since it is representative in size of modern turbines.

The 2D simulations succeeded in capturing the unsteady interaction between the blade section and the tower wake, and the results for the Phase VI turbine were in good agreement with the experimental data for low wind speed cases, whereas for higher wind speeds with flow separation, the agreement was not as favourable. For the downwind tubular tower configuration of the UPWIND turbine, the tower wake gave rise to a significant tower shadow with a 20% reduction in the blade normal force. Changing the tower clearance did not give rise to significant reduction of the tower shadow. Using a streamlined tower, however, reduced the tower shadow 50% compared to the cylindrical tower, and eliminated the unsteady blade/vortex interaction seen on the conventional tower. Simulations with a four leg configuration showed that the tower shadow could be reduced with such a configuration. The tower wake was, however, significantly more turbulent.

Comparison of the Navier-Stokes simulations and the aeroelastic code HAWC2 showed that the overall agreement was good, and that appropriate adjustment of the tower drag coefficient can be used to fit the HAWC2 results to the CFD simulations.

2.3 Characterisation of the Unsteady Flow in the Nacelle Region of a Modern Wind Turbine

A 3D Navier-Stokes solver has been used to investigate the flow in the nacelle region of a wind turbine where anemometers are typically placed to measure the flow speed and the turbine yaw angle. A 500 kW turbine was modelled with rotor and nacelle geometry in order to capture the complex separated flow in the blade root region of the rotor. A number of steady state and unsteady simulations were carried out for wind speeds ranging from 6 m/s to 16 m/s as well as two yaw and tilt angles. The flow in the nacelle region was found to be highly unsteady, dominated by unsteady vortex shedding from the cylindrical part of the blades which interacted with the root vortices from each blade, generating high tangential velocities in the nacelle region. For pure axial inflow the averaged nacelle wind speed varied approximately linearly with the free stream wind speed, whereas the nacelle flow angle changed significantly with wind speed. The nacelle anemometry showed significant dependence on both yaw and tilt angles with yaw errors of up to 10° when operating in a tilted inflow.

2.4 Correlation Based Transition Modeling of Laminar to Turbulent Transition

For thin airfoils a very good agreement is observed between measurements, Xfoil computation and predictions by the 2D EllipSys code for low angles of attack. For a thick airfoil and a cylinder the coupling of the DES methodology and the laminar/turbulent transition model is demonstrated. For the airfoil these computations show an improved agreement with the measured data in stall, compared to 2D computations. In the cylinder case the computations show that the code is capable of predicting the flow from the laminar region at a Reynolds number of 10 to the fully turbulent/transitional flow at a Reynolds number above one million. The use of the combined DES/transitional methodology improves the prediction of the drag crisis on the cylinder compared to pure DES simulation. Additionally, the DES/transitional methodology predicts the correct flow phenomena including laminar separation and turbulent reattachment followed by turbulent separation.

2.5 Aeroacoustics

The aim of this contribution is two-sided. Firstly, an existing trailing edge noise model is validated by comparison with experimental data. Measured airfoil surface pressure fluctuations are compared with the component of the model that relates the turbulent boundary layer characteristics to the surface pressure. Far field sound pressure levels are also considered for comparisons between model results and experimental data. Secondly, the model is implemented into an airfoil design code that is normally used for aerodynamic optimization. An existing wind turbine airfoil is optimized in order to reduce its noise emission, trying at the same time to preserve its aerodynamic performances and geometric characteristics. The modifications resulting from this new design are analyzed.

2.6 Design of High Lift, Low Noise Airfoils and High Aerodynamic Performance

Noise from wind turbines has several sources such as gear, generator and aerodynamics. This work focuses on the aerodynamic noise, also called aeroacoustics. The generation of this noise is commonly divided into different sources, where the noise generated from the trailing edge is one of a few dominant sources. The objective of this work is to design airfoils which are aerodynamically high performing and have reduced noise. The first of three steps in this investigation was implementation and validation of an advanced trailing edge noise model (TNO), which showed that the model does not predict the noise level accurately, but captured the correct trends. Thus, the model can be used qualitatively in a design process. The second step involved the implementation of the model in the airfoil design tool AIRFOILOPT and testing the implementation by reducing the noise on the Risø-B1-18 and the NACA63418 airfoils showed that the noise could be reduced between 1 and 2.5dB, while still maintaining its aerodynamic characteristics. The third and last step was the design of a high performance and high lift airfoil which had its basis in the Risø-C2-18. While maintaining the aerodynamic performance the trailing edge total sound power level could be reduced with up to 3dB requiring a thin trailing edge and lower stiffness compared to the Risø-C2-18 airfoil. However, introducing the A-weight into the sound power level showed somewhat less significant reduction, around 1dB.

2.7 Prediction of Multi Element Airfoils With the EllipSys Code

Based on the comparison between the computed results and the available measured data, it has been verified that the EllipSys2D Navier-Stokes solver is capable of predicting the flow around a multi element airfoil. Secondly, it has been shown that the correlation based transition method implemented in the code is robust and stable also under these conditions. The mesh used in the present computations, has a very high resolution and ongoing test has shown that the mesh is more than fine enough in the normal direction.

2.8 Stall-induced vibrations of a blade section in deep-stall

Prediction of stall-induced vibrations of wind turbines at standstill is currently based on models that do not include the stochastic behavior of the aerodynamic forces due to the complex vortex structures shed from the blades when the flow around their airfoils is fully separated. This stochastic behavior is here modeled as self-induced turbulence using stochastic inflow velocities. Numerical simulation and local bifurcation analysis of an airfoil section with a single degree of freedom subject to quasi-steady aerodynamic forces in the stochastic inflow show that the self-induced turbulence adds a small averaged damping force to the airfoil motion. The added damping effect of the stochastic aerodynamic forces is insignificant in practice; however, there may be other aerodynamic phenomena in deep-stall (e.g. time lag effects like in traditional dynamic stall models) that influence the real risk of stall-induced vibrations at standstill.

2.9 Global Blade Deflections Effect on Local Airfoil Deformation and Performance

The local effects on airfoil deformation and performance caused by global blade deflections are examined using the aeroelastic code HAWC2 as well as a detailed finite element model of a turbine blade. It is found that the local airfoils only undergo a very small deformation even at large blade tip deflections, and the aerodynamic lift, drag and moment coefficients do not change. Simulations with the new airfoil data support the conclusion that the airfoil deformations do not affect the aerodynamic performance. However the results may be blade design dependant, so a more flexible blade or a blade with another load carrying design could have another and more severe response. The finite element analysis shows an elastic blade twist of 0.6 deg at normal operation conditions. This will affect the aerodynamic performance of the blade, but this is also accounted for in e.g. the aeroelastic code HAWC2, which has a torsional degree of freedom in the blades.

References

[1] H.A. Madsen. (Ed.) Forskning i aeroelasticitet. rapport for EFP-97 (in danish). Risø-R-1066(da), Risø National Laboratory for Sustainable Energy, August 1998.

[2] H.A. Madsen. (Ed.) Forskning i aeroelasticitet - EFP-98 (in danish). Risø-R-1129(da), Risø National Laboratory for Sustainable Energy, August 1999.

[3] H.A. Madsen. (Ed.) Forskning i aeroelasticitet - EFP-99 (in danish). Risø-R-1196(da), Risø National Laboratory for Sustainable Energy, November 2000.

[4] H.A. Madsen. (Ed.) Forskning i aeroelasticitet - EFP-2000 (in danish). Risø-R-1272(da), Risø National Laboratory for Sustainable Energy, July 2001.

[5] H.A. Madsen. (Ed.) Forskning i aeroelasticitet EFP-2001 (in danish). Risø-R-1349(da), Risø National Laboratory for Sustainable Energy, December 2002.

[6] C. Bak. (Ed.) Forskning i aeroelasticitet EFP-2002 (in danish). Risø-R-1434(da), Risø National Laboratory for Sustainable Energy, Februar 2004.

[7] C. Bak. (Ed.) Forskning i aeroelasticitet EFP-2004 (in danish). Risø-R-1509(da), Risø National Laboratory for Sustainable Energy, May 2005.

[8] C. Bak. (Ed.) Research in aeroelasticity EFP-2005. Risø-R-1559(da), Risø National Laboratory for Sustainable Energy, May 2006.

[9] C. Bak. (Ed.) Research in aeroelasticity EFP-2006. Risø-R-1611(da), Risø National Laboratory for Sustainable Energy, July 2007.

[10] C. Bak. (Ed.) Research in aeroelasticity EFP-2007. Risø-R-1649(EN), Risø National Laboratory for Sustainable Energy, July 2008.

3 Evaluation of Tower Shadow Effects on Various Wind Turbine Concepts

Author: Frederik Zahle, Helge Aa. Madsen and Niels N. Sørensen

A 2D CFD study has been carried out to evaluate the effects of tower shadow on a blade section for an upwind turbine and three downwind turbine concepts; one with a traditional tubular tower, another with a streamlined tower and lastly, one with a four legged configuration. Two turbines were used as basis for the study: Firstly the NREL Phase VI turbine, which was used for validation against experimental results; secondly the UPWIND 5 MW reference turbine, since it is representative in size of modern turbines.

The 2D simulations succeeded in capturing the unsteady interaction between the blade section and the tower wake, and the results for the Phase VI turbine were in good agreement with the experimental data for low wind speed cases, whereas for higher wind speeds with flow separation, the agreement was not as favourable. For the downwind tubular tower configuration of the UPWIND turbine, the tower wake gave rise to a significant tower shadow with a 20% reduction in the blade normal force. Changing the tower clearance did not give rise to significant reduction of the tower shadow. Using a streamlined tower, however, reduced the tower shadow 50% compared to the cylindrical tower, and eliminated the unsteady blade/vortex interaction seen on the conventional tower. Simulations with a four leg configuration showed that the tower shadow could be reduced with such a configuration. The tower wake was, however, significantly more unsteady.

Comparison of the Navier-Stokes simulations and the aeroelastic code HAWC2 showed that the overall agreement was good, and that adjustment of the tower drag coefficient could improve the HAWC2 computations somewhat particularly for the four legged tower case.

3.1 Introduction

Tower shadow on a wind turbine is caused by the interaction of the passing blades with the modified flowfield around the tower. On an upwind turbine, the perturbation of the flow is caused by a reduction in velocity of the oncoming flow as a result of the presence of the tower. As such, tower shadow on upwind turbines is not very severe, and gives rise to a quasi-steady aerodynamic response on the blades. On a downwind turbine, the tower shadow is significantly more severe, because the rotor passes through the tower wake, which is highly unsteady due to the bluff body vortex shedding inherent to high Reynolds number flow over circular cylinders. The interaction of the blade with the tower wake, or in short the blade-wake interaction (BWI), is therefore dominated by two effects: firstly, the presence of the tower that in average creates a velocity deficit, which will cause the incidence on the blade to decrease rapidly when it travels through the wake, and secondly, the blade will occasionally encounter the vortices which are shed from the tower. Figure 1 shows a schematic of the flow situation for the two types of turbines.

The primary concern with the downwind concept of a wind turbine is the noise that is generated as the blades pass through the unsteady wake behind the tower. From the early development of downwind turbines low frequency noise has been reported as an issue with this concept [2, 3, 10]. Madsen et al. [4] showed that the interaction of the blades with the unsteady tower wake can give rise to an increase of the low frequency noise of a downwind turbine. Zahle and Sørensen [16] used 3D CFD to investigate the aerodynamic interaction between the rotor and the tower on a downwind turbine and showed that direct encounters of the blades with wake vortices gives rise to large impulses on the blade forces.

In this work the interaction between the blade and the tower for a number of different turbine concepts is investigated using a two-dimensional flow solver. The aim is firstly to quantify and

(a) upwind configuration

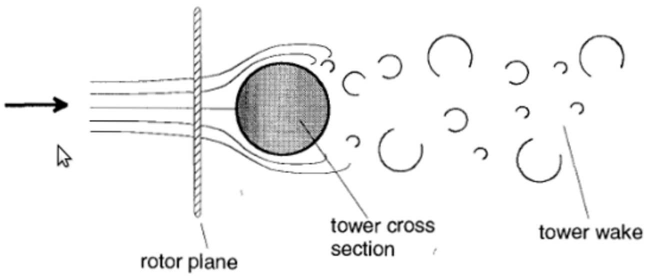

(b) downwind configuration

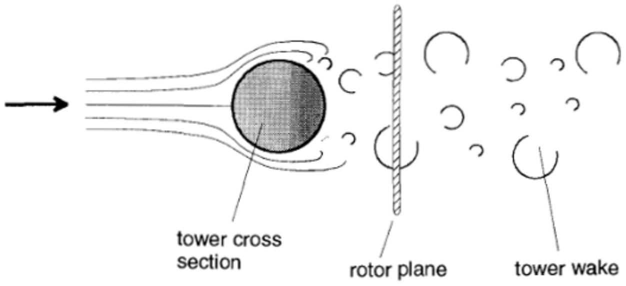

Figure 1. Schematic of the flow in the vicinity of the tower on an upwind and downwind wind turbine. From [14].

compare the tower shadow for the different concepts, and secondly, to make a comparison of the CFD results with the aeroelastic code HAWC2, that is capable of modelling both upwind and downwind tower shadow effects. Two turbines were used as basis for the study from which 2D equivalent blade/tower configurations were created: Firstly the NREL Phase VI turbine, which was used for validation against experimental results; secondly the UPWIND 5 MW reference turbine, since it is representative in size of modern turbines.

3.2 Computational Solver

3.2.1 Base Solver

For all computations the EllipSys2D pressure based incompressible Reynolds averaged Navier-Stokes flow solver written by Michelsen [6, 7] and Sørensen [11] is used. The code uses the finite volume method, solving for the primitive variables $u, v, w,$ and p, in general curvilinear coordinates. The variables are stored in a collocated grid arrangement, and odd/even pressure decoupling is avoided using the Rhie-Chow interpolation [8]. The iterative SIMPLE or PISO algorithm is used to advance the solution in time using a second-order accurate scheme. The convective terms are discretised using the Quadratic Upstream Interpolation for Convective Kinematics Scheme, QUICK, and the viscous terms are discretised using the central difference scheme. The momentum equations are solved decoupled from each other using a red/black Gauss-Seidel point solver. To accelerate the convergence of the pressure-correction equation a multigrid solution strategy is implemented combined with the additive Schwarz method, where each sub-domain is solved for simultaneously. The code is fully parallelised using the MPI library with a multiblock decomposition of the solution domain. The block-block communication is done through one layer of ghost cells around each block. The cell vertices are required to coincide on interfaces such that conservation can be maintained. For computations of flow over aerofoils and wind turbine blades the EllipSys2D code uses the $k-\omega$ SST model by Menter [5], because of its good performance in wall bounded adverse pressure gradient flows.

3.2.2 The Overset Grid Method

The overset grid method, also known as chimera or composite grid method, addresses many of the limitations of traditional structured grid methods, while at the same time maintaining their advantages such as solution strategies and parallelisation. The method allows for the decomposition of the problem into a number of simpler grids, which overlap each other arbitrarily. If dealing with a multibody problem, appropriate body-fitted grids can be generated around each component, making it possible to model virtually any configuration. Since each body grid is independent of the other grids, problems involving relative movement of bodies are naturally handled.

Important flow features can be resolved by refined meshes, which together with the body fitted meshes can be embedded in background meshes that are successively coarsened towards the farfield where there is no need for high resolution of flow features. To accommodate the solid bodies and refined grids, cells are removed from the background grids where necessary.

In the present implementation by Zahle [15] each group of simply connected blocks is solved using boundary conditions on the overlapping interfaces based on interpolated values of velocity from neighbouring grids using trilinear interpolation. Since this interpolation is non-conservative, the lack of mass conservation must be addressed. An explicit correction of the conservation error is implemented, since a divergence free field is required to solve the pressure-correction equation. The correction is placed in internal cells along the overset boundaries and is distributed proportionally to the local mass flux. As stated above, only velocities are interpolated, since interpolation of velocities and pressure would lead to an ill-posed problem. The solution of the pressure is thus obtained on the basis of the mass fluxes calculated from the momentum equations.

The additional cost associated with the overset grid method is caused by the need for determining the connectivity between each block group and communication of boundary conditions between these groups. In EllipSys2D the connectivity routines are fully parallelised and apply a stencil jumping technique to locate cells. Likewise, the communication of flow field data must be carried out in a parallel manner. To minimize communication latency, non-blocking MPI calls are used to transfer information between individual processors.

3.3 Computational Setup

3.3.1 The Cyclic Boundary Method

The method used to simulate the flow over a 2D blade section of a wind turbine is shown schematically in Figure 2. The blade section traveled through the domain at a velocity given by the angular speed, Ω, and the local blade radius, r. The domain width was given by the circumferential distance covered by the given blade section over one revolution. To account for the rotor induction, the nominal inflow velocity V_0 was reduced according to the induction factor, a, at the given blade section, which can be extracted either from 3D CFD simulations or BEM simulations. To simulate the cyclic passages of the blade section through the domain, the overset grid connectivity routines were modified slightly. In the solver the actual position of the moving blade section is not shifted as it crosses the lateral domain boundary. Instead, an integral count of the domain width is subtracted from the coordinates supplied to the hole cutting and search requests made in each time step.

3.3.2 NREL Phase VI Layout

The NREL Phase VI turbine is a two-bladed 10 m diameter stall regulated wind turbine. The turbine can be operated in both an upwind and downwind configuration at various teeter and cone angles. In both configurations the rotor was mounted with a 1.4 m clearance to the tower,

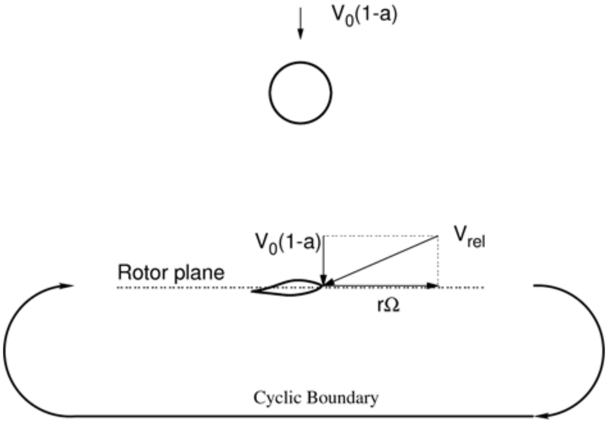

Figure 2. Schematic of the 2D domain used to simualate the flow over a blade section of a wind turbine.

corresponding to 3.5 tower diameters. The blades were twisted and tapered and fitted with the S809 profile. In the present work, Sequence B of the experimental dataset is used. Here, the rotor is operated at a pitch setting of 3 degrees towards feather and a cone angle of 3.4 degrees. The turbine was run at a rotational speed of 72 rpm. Tables 1 and 2 summarise the dimensions of the turbine and the computational domain.

Rotor diameter	10.05 m
Rotor cone angle	3.40 deg
Rotor tilt angle	0.00 deg
Rotor pitch angle	3.00 deg
Nacelle height	12.20 m
Shaft length	1.40 m
Tower diameter	0.40 m

Table 1. Summary of the dimensions of the NREL Phase VI turbine.

Blade section chord	0.46 m
Blade section twist	1.39 deg.
Tower Diameter	0.40 m
Tower Distance	1.63 m
Domain width	25.26 m
Blade velocity	30.31 m/s
Inflow velocity	5.63 m/s

Table 2. 2D CFD domain layout at the 80% spanwise section on the NREL Phase VI turbine.

Figure 3 shows the 2D layout of the turbine for the 80% blade section. As stated above, the shaft length is 1.4 m, however, including the rotor cone angle the tower distance increases to 1.64 m.

The computational grid used for the NREL configuration consisted of four individual block groups: one for the blade section, one for the tower, and two Cartesian grids to resolve the tower wake and one to cover the rest of the domain. The aerofoil grid contained 256 cells in the chordwise direction and 64 cells in the normal direction with a first cell height of 1×10^{-5}. The tower grid had the same dimensions. The two curvilinear grids were generated using HypGrid2D [12]. The refined Cartesian grid around the tower consisted of 192×192 cells, which were distributed evenly. The farfield grid contained 768×192 cells, which were stretched locally in the flow direction to capture the wake of the blade section. The grid was stretched in the lateral direction to resolve the tower wake, but was otherwise uniformly distributed. With 768 cells in the lateral direction, this resulted in approoximately 12 cells resolving the blade chord. Figure 4 shows a detailed view of the grid.

To ensure that the relative movement between the aerofoil grid and background grid was less than one cell width per time step, a rather small time step was required. A time step of 4.167×10^{-4} s was thus used, which corresponded to 2000 time steps per revolution. Table 3 summarises the solver settings used for the NREL Phase VI turbine.

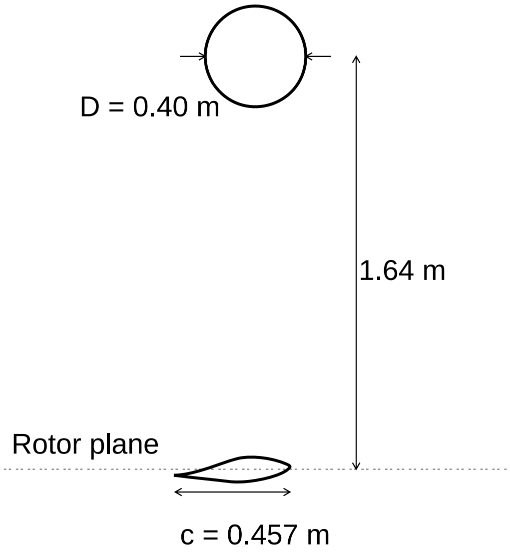

Figure 3. Downwind configuration for the 80% radius blade section on the NREL Phase VI turbine.

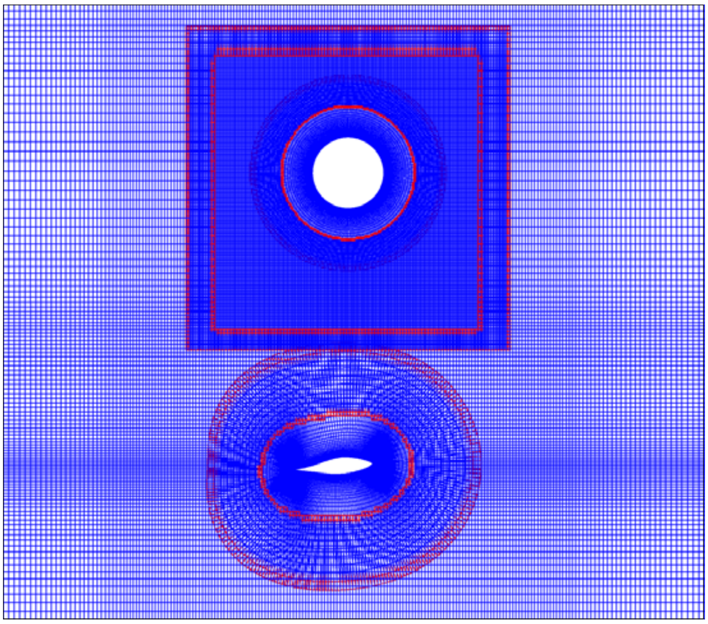

Figure 4. Computational grid for the 80% radius blade section on the downwind NREL Phase VI turbine.

3.3.3 UPWIND 5 MW Layout

The UPWIND 5 MW reference turbine has the overall dimensions summarised in Table 4. The basic dimensions were kept equal for the upwind and downwind configurations. To simplify the comparison between the aeroelastic and CFD simulations, the blade was assumed rigid. To obtain an approximately correct tower clearance, the blade deflection was included assuming a linear deflection along the span. Based on aeroelastic simulations on the rotor, the deflection was approximated with a deflection angle of 2.2 degrees. When in the upwind configuration this resulted in a reduced tower clearance, and oppositely an increased tower clearance when in the downwind configuration. Since it was not possible to include the effect of tilt in the CFD

Time integration	PISO
Convective terms	QUICK
Subiterations	6
Time step Phase VI	4.167×10^{-4} s
Time steps per rev	2000
Turbulence model	$k-\omega$ SST

Table 3. Summary of the solver settings used in the NREL Phase VI turbine simulations.

simulations the cone angle was increased accordingly to obtain the correct tower clearance.

Rotor diameter	63.0 m
Rotor cone angle	2.5 deg
Rotor tilt angle	5.0 deg
Blade deflection angle	2.2 deg
Nacelle height	90.0 m
Shaft length	4.95 m
Tubular tower diameter bottom	6.0 m
Tubular tower diameter top	4.0 m
Lattice tower side length bottom	12.0 m
Lattice tower side length top	4.0 m

Table 4. Summary of the dimensions of the UPWIND 5 MW turbine.

Two alternatives to the traditional tubular tower were also investigated, namely a streamlined tower, which was shaped as a NACA 0050 aerofoil and a four legged lattice tower. The streamlined tower was made such that it had the same frontal area as the tubular tower, which resulted in a length of 10.24 m. The four legged configuration also maintained the same distance to the tower center, and also had a reduced clearance due to the larger leg side length at the bottom of the tower.

Based on the above dimensions, four equivalent 2D layouts were generated for the CFD study at r/R=0.4, 0.6 and 0.8. Figure 5 and 6 show the rotor/tower configurations for the three blade sections for the upwind and downwind turbines, as well as the streamlined and four leg tower configurations. Table 5 summarises overall dimensions of the layouts as well as the blade and inlet velocities.

r/R	0.40	0.60	0.80
Blade section chord [m]	4.15	3.42	2.66
Blade section twist [deg.]	9.23	5.35	2.24
Tower Diameter [m]	4.56	4.84	5.12
Upwind Tower Distance [m]	7.28	8.44	9.61
Downwind Tower Distance [m]	9.20	11.32	13.44
Domain width [m]	158.34	237.50	316.67
Blade velocity [m/s]	24.29	36.44	48.57
Inflow velocity [m/s]	5.95	5.52	5.29

Table 5. Summary of the 2D CFD domain layouts at the three spanwise locations for the upwind and downwind configurations.

The computational grid for the UPWIND turbine was generated in the same fashion as for the

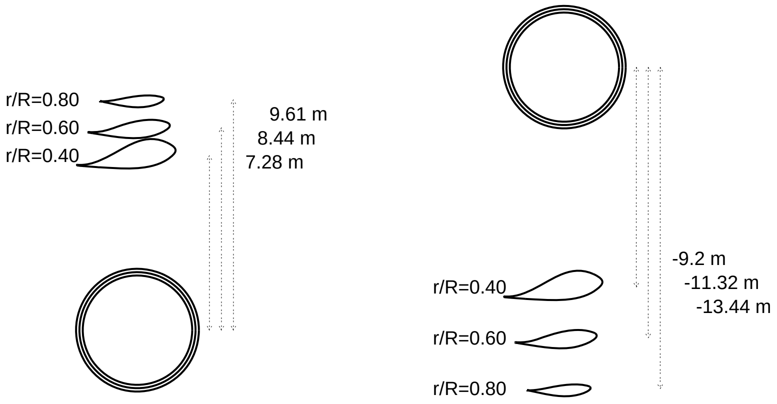

Figure 5. Upwind and downwind configurations for the 40%, 60% and 80% radius blade sections.

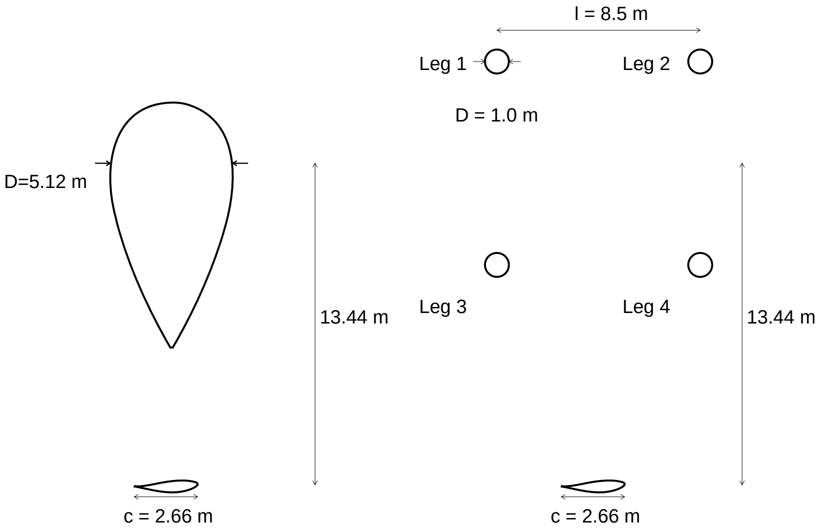

Figure 6. Downwind streamlined and four leg configurations for the 80% radius blade section.

NLEL Phase VI turbine with four block groups. The farfield grids were refined in the lateral direction with increasing domain size. The 40% blade section contained 768 cells, the 60% section contained 960 cells, and the 80% section contained 1280 cells. Figures 7 and 8 show two of the the grids used. Here, the 80% radius section on the downwind tubular and lattice tower configurations for the UPWIND turbine.

The time step used in the UPWIND simulations was 2.0×10^{-3} s, corresponding to 3258 time steps per revolution. Table 6 summarises the solver settings used in the simulations.

3.4 NREL Phase VI Results

The simulations of the NREL Phase VI turbine served primarily as validation of the 2D solver, since excellent experimental data is available from the Unsteady Aerodynamics Experiment

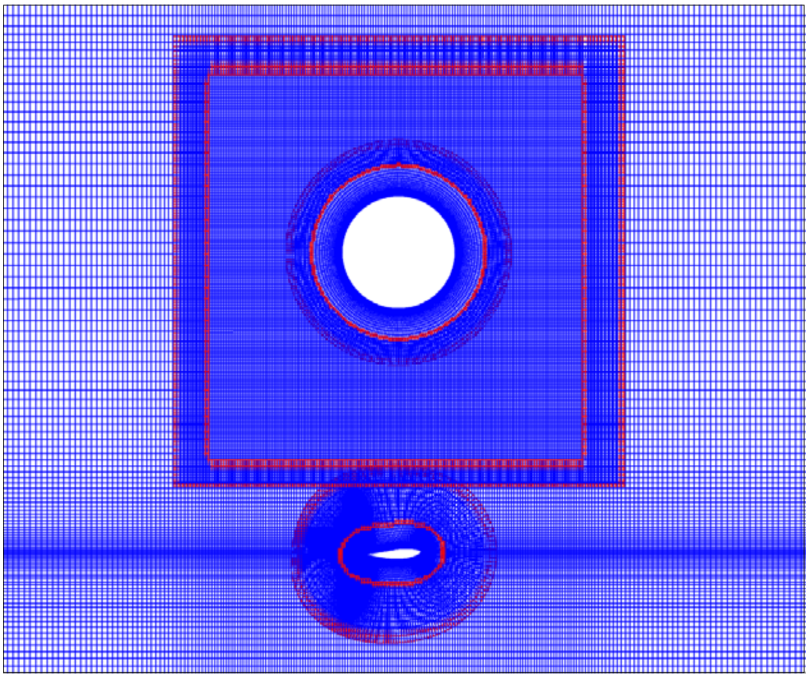

Figure 7. 2D mesh for the tubular tower configurations for the 80% radius blade section.

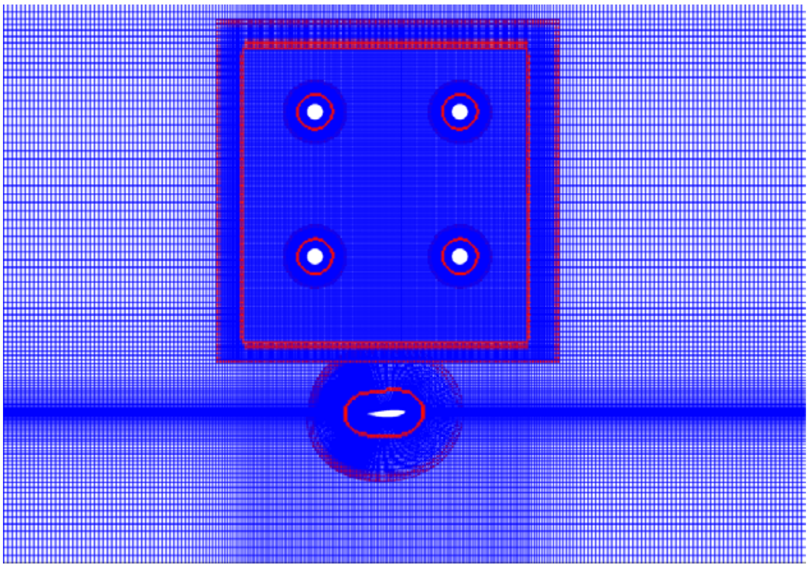

Figure 8. 2D mesh for the lattice tower configurations for the 80% radius blade section.

carried out in the NASA Ames wind tunnel [1, 9] . This dataset has previously been used to validate the 3D solver [13, 16]. Three nominal wind speeds were simulated, 7 m/s, 10 m/s, and 15 m/s. While at the low wind speed the flow is attached on the outer parts of the blade, the flow is partially or fully separated at the higer wind speeds. It was therefore expected that the 2D solver would have difficulty capturing the correct behaviour at the higher wind speeds.

All simulations were run for 40 revolutions, to achieve sufficient data for averaging of the unsteady forces. Figure 9 shows a typical time series from the simulations.

Figure 10 shows the normal force as a function of azimuth angle at the 80% radius blade section

Time integration	PISO
Convective terms	QUICK
Subiterations	6
Time step UPWIND	2.0×10^{-3} s
Time steps per rev	3258
Turbulence model	$k-\omega$ SST

Table 6. Summary of the solver settings used in the UPWIND turbine simulations.

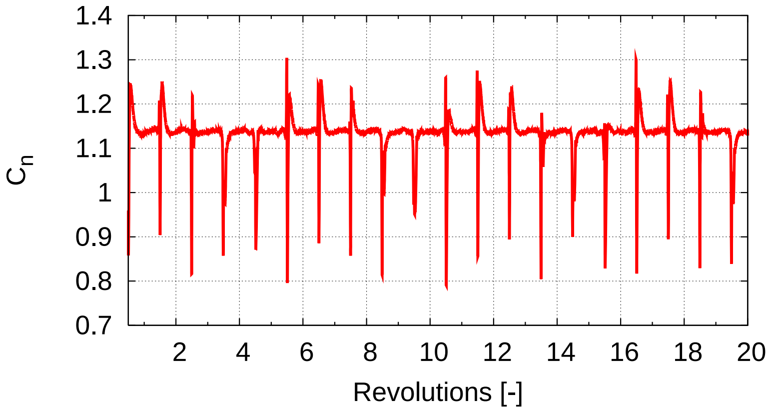

Figure 9. Time series of the normal force for the 80% radius blade section for the NREL Phase VI turbine at a wind speed of 10 m/s.

for the three wind speeds. Although the inflow velocity was reduced according to the induction factors extracted from 3D CFD simulations, it seems that the normal force is consistently overestimated in 2D, compared to the experimental results. That aside, the 2D solver successfully captures the unsteady interaction of the blade section with the tower wake, predicting a tower shadow in good correspondance with the experimental results for the low wind speed case. At the higher wind speeds, the fact that the stall characteristics are not captured correctly in 2D, results in a less favourable correspondance.

3.5 UPWIND Turbine Results

The second turbine that was investigated was the UPWIND 5 MW turbine, which as opposed to the NREL Phase VI turbine is pitch regulated. In the following sections the results for the different configurations will be presented. Firstly, the upwind configuration; secondly, the downwind tubular tower configuration, where also the influence of tower clearance was investigated; thirdly, the streamlined downwind configuration; and finally the four legged lattice configuration, where three different relative rotor/tower orientations were investigated. For all configurations the normal force on the blade section is used as basis of comparison.

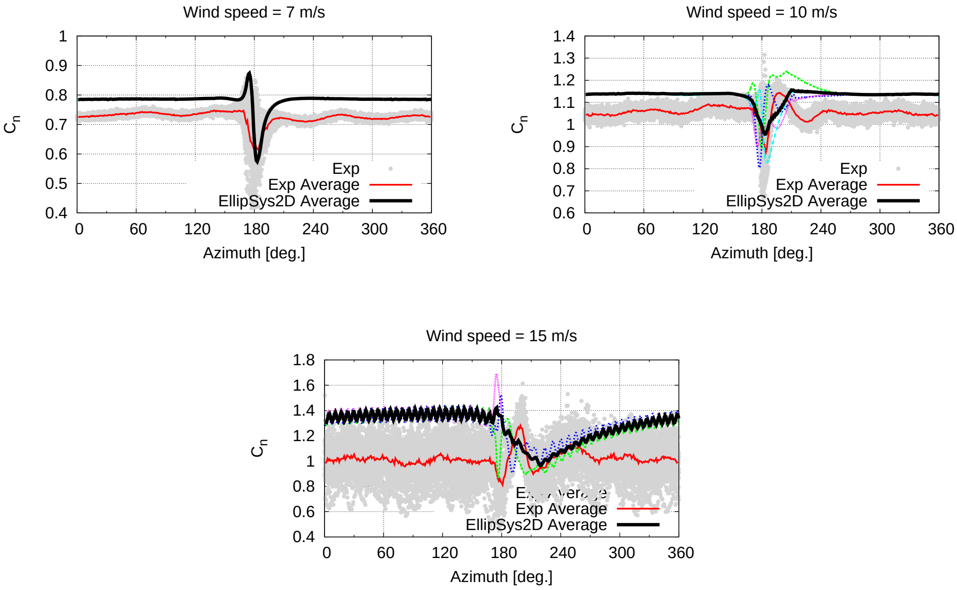

Figure 10. Normal force coefficient as function of blade azimuth for the 80% radius blade section for the NREL Phase VI turbine at three wind speeds. The black lines are the azimuthally averaged forces.

3.5.1 Upwind Configuration

Figure 11 shows the normal force for the three radial positions r/R=0.4, 0.6, and 0.8. The tower shadow gives rise to a reduction in the normal force of 156 N at r/R=0.8, corresponding to 4.2% relative to the undisturbed level. The tower shadow is slightly bigger towards the root of the blade due to the smaller tower clearance. In Figure 11 five consecutive revolutions are plotted and shows that there is very little variability between each tower passage.

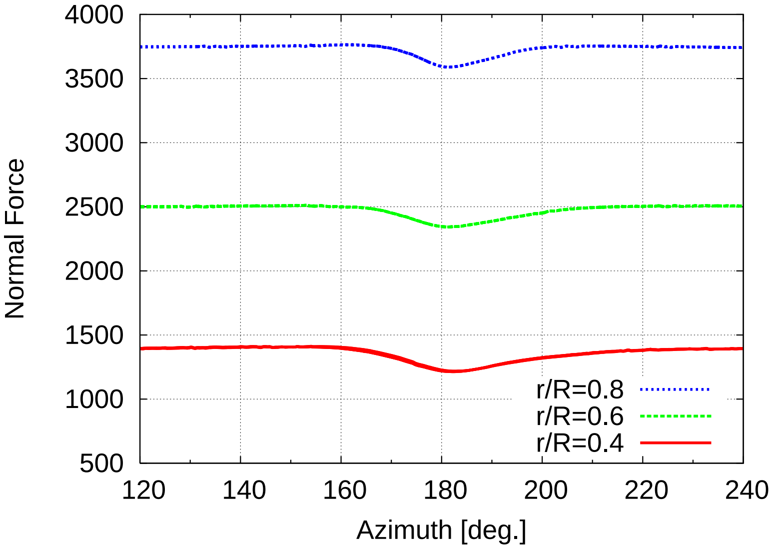

Figure 11. Normal force as function of blade azimuth angle for the three blade sections.

3.5.2 Downwind Configuration – Tubular Tower

Turning to the downwind configuration using the same tower configuration, the tower shadow changes character, since the blade now passes through the unsteady wake of the tower. Figure 12 shows the normal force on the three blade sections as function of azimuth angle for five consecutive revolutions. On the outermost section the tower shadow gives rise to a reduction in the normal force of 740 N, corresponding to a 19.8% reduction, thus considerably more severe than for the upwind configuration. There is surprisingly little variation between each tower passage for this specific blade section, which is due to the fact that the blade passage frequency is very close to twice the tower vortex shedding frequency. In contrast to this behaviour there is considerably more variation between passages on the two other sections further inboard, which is seen both at the entry to the tower wake as well as the exit, where the recovery to the undisturbed level varies significantly. Despite the fact that the tower clearance reduces significantly for the inner sections the tower shadow reduces from 740 N to 585 N and 480 N for the 60% and 40% sections, respectively.

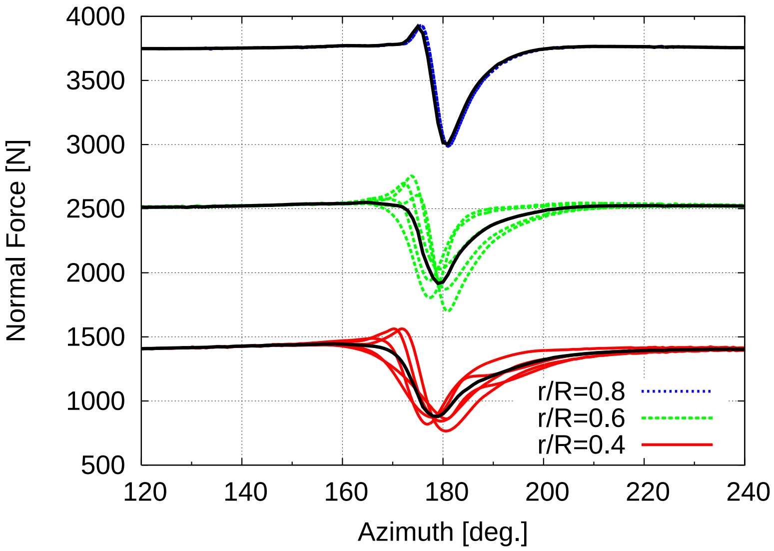

Figure 12. Normal force as function of blade azimuth angle for the three downwind blade sections. The black lines are the azimuthally averaged forces.

Figure 13 shows the instantaneous flow field for a tower passage. As can be seen the reduction in axial velocity is considerable in the wake of the tower. In this snapshot the blade passes upstream of a vortex cast from the left side of the tower, which gives rise to an increase in normal force as the blade enters the tower wake region.

For the standard downwind configuration, the influence of tower clearance was also investigated. Figure 14 shows the blade normal force as function of azimuth angle for four different tower clearances. An increase in tower distance from 10 m to 13.44 m results in a 4% decrease in the tower shadow, indicating that it is not feasible to reduce tower shadow effects by increasing the tower distance.

3.5.3 Downwind Configuration – Streamlined Tower

There are two effects that should be dealt with to reduce tower shadow on a downwind turbine: one being the velocity deficit behind the tower, and the other being the unsteady vortex shedding. The large deficit on a circular cylinder is caused by the bluff body separation of the shear layer. The depth of the deficit is reflected in the drag coefficient of the body, which in the

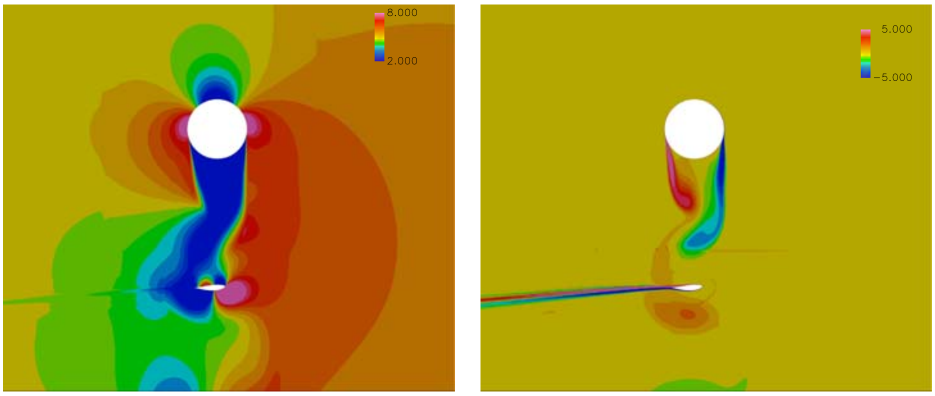

Figure 13. Snapshot of axial velocity and vorticity for the tubular configuration for the 80% radius blade section.

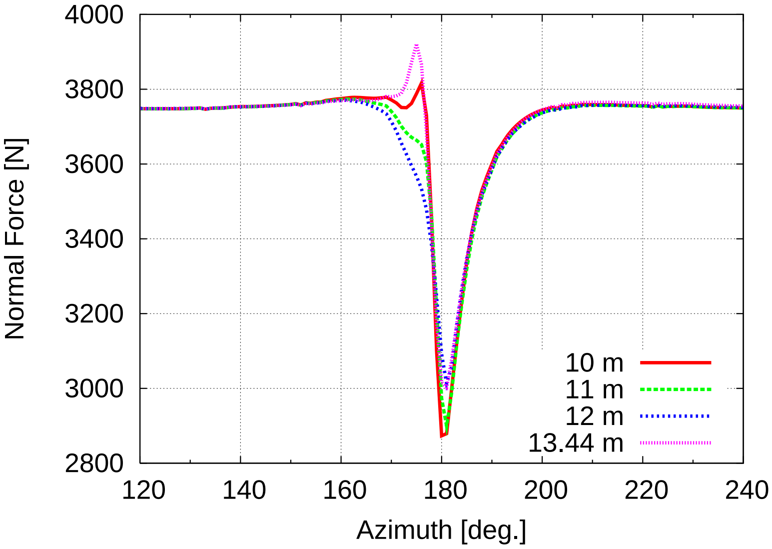

Figure 14. Influence of variation of tower clearance. Azimuthally averaged normal force as function of blade azimuth angle for the 80% span blade sections.

present case is approximately 0.5. Thus, reducing the drag coefficient of the body will reduce the tower shadow. Eliminating, or at least reducing the unsteady vortex shedding is also crucial to making a downwind concept viable. This can most easily be achieved by streamlining the body into an aerofoil shape.

As such, the tower shadow effects were investigated for a tower shaped like a NACA 0050 profile. Figure 15 shows the normal force acting on the 80% span blade section as a function of azimuth angle. Clearly, the tower shadow is reduced significantly compared to the conventional tubular tower. Also, the unsteady vortex shedding has been eliminated, since the flow separates at a much later stage on the profile than on the cylinder.

The concern with such a configuration, however, is that the tower clearance is reduced significantly, and that the size of the tower is likely to be prohibitive for it to be viable.

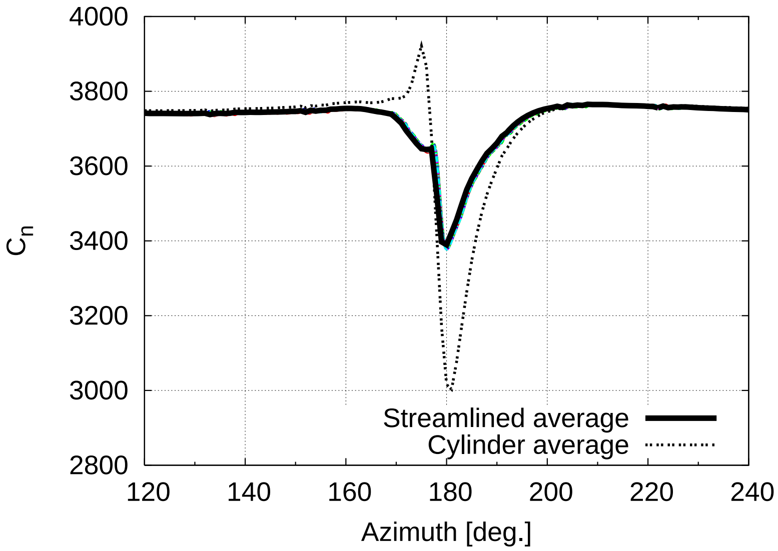

Figure 15. Time history of the normal force for the streamlined tower configuration for the 80% radius blade section.

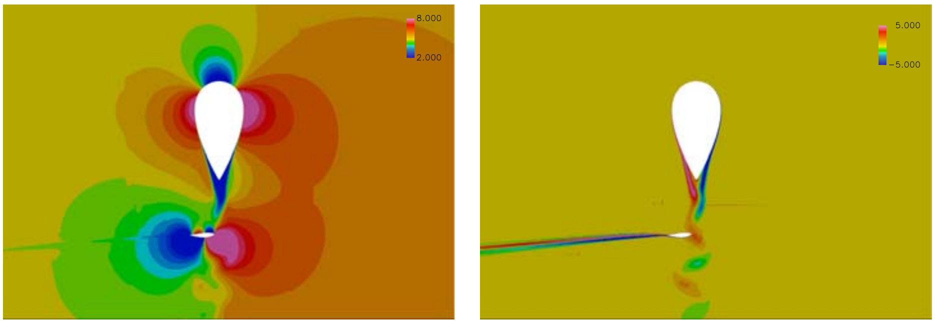

Figure 16. Snapshot of axial velocity and vorticity for the streamlined configuration for the 80% radius blade section.

3.5.4 Downwind Configuration – Four Leg Tower

An alternative to the tubular tower is a tower consisting of four legs connected by diagonal beams. In 2D only the four main legs can be modelled, although the diagonal beams are likely to contribute to the deficit and unsteadiness of the flow in the wake of the tower.

Figures 17 to 19 show the normal force as function of azimuth for the 80% span blade section for a 0°, 22.5°, and 45° orientation of the tower to the rotor plane. As is evident the average tower shadow is reduced also for this configuration compared to the conventional tubular tower. However, the unsteadiness of the flow is quite significant, since the blade interacts with the distinct wakes from each tower leg.

The flow fields for the three cases are shown in Figures 20 to 22. When two tower legs are aligned with each other in the flow direction, the wake deficit behind them increases, and the vortex shedding behind the second tower is strongly affected due to the interaction with the wake from the upstream tower leg. This is reflected in the blade normal force response as a larger reduction, but with less variation between consecutive passages.

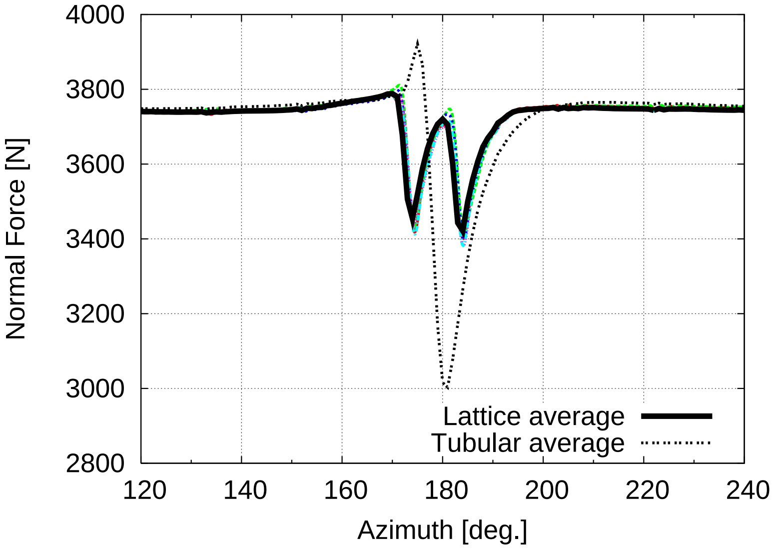

Figure 17. Time history of the normal force for the four leg configuration for the 80% radius blade section at 0 degrees orientation to the tower.

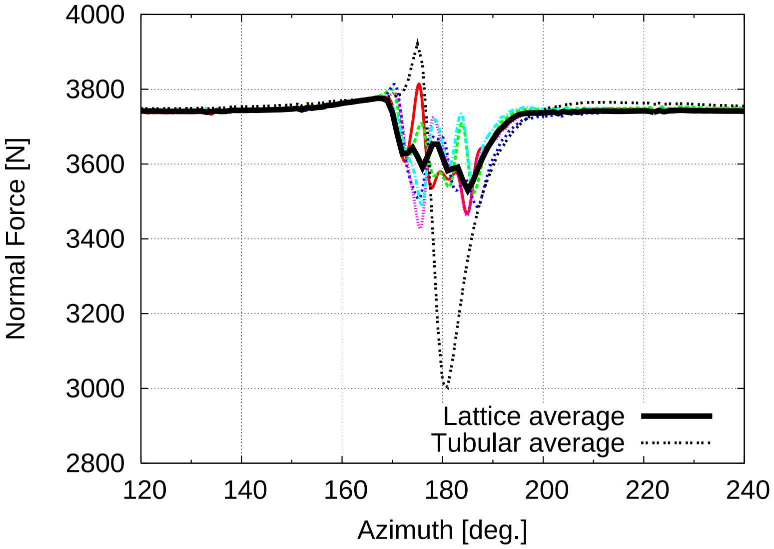

Figure 18. Time history of the normal force for the four leg configuration for the 80% radius blade section at 22.5 degrees orientation to the tower.

3.5.5 Comparison of EllipSys2D and HAWC2

Another important aspect of the present work has been to use the CFD results to validate the tower shadow models implemented in HAWC2. The HAWC2 model of the turbine was set up to resemble the setup used in the CFD simulations as closely as possible. As such the elasticity of the blades was not included, and the blade deflection was assumed to be linear using a constant deflection angle of 2.2 degrees. The upwind tower shadow model is based on the potential flow solution of flow around a circular cylinder and is described in [17]. The downwind tower shadow model, the so-called JET wake model, is based on the boundary layer solution for a jet flowing into a fluid at rest and is described in detail in a paper by Madsen et al. [4]. For the computation of wakes behind multiple tower legs, the JET model is also used, where the wake from the upwind tower is superimposed on the downwind tower wake.

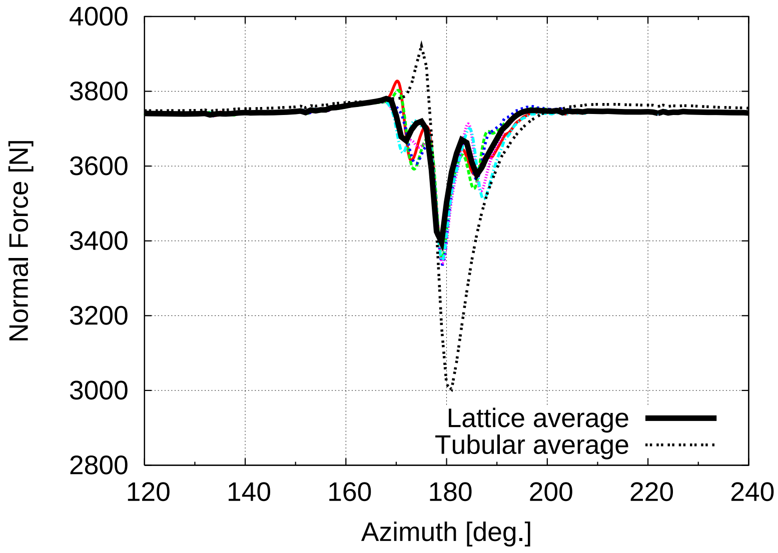

Figure 19. Time history of the normal force for the four leg configuration for the 80% radius blade section at 45 degrees orientation to the tower.

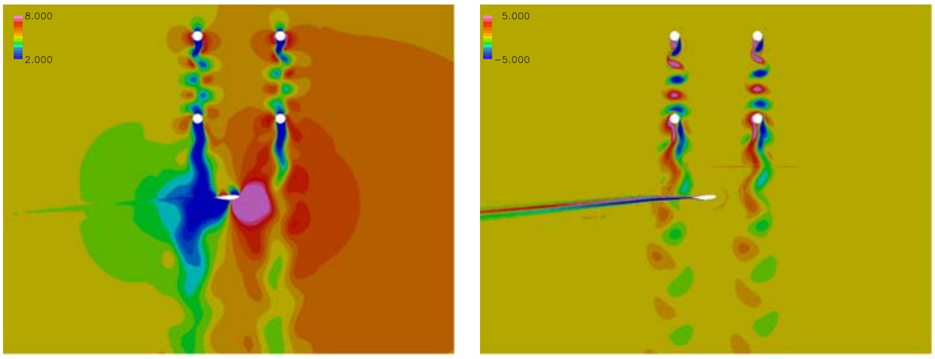

Figure 20. Snapshot of axial velocity and vorticity for the four leg configuration for the 80% radius blade section at 0 degrees orientation to the tower.

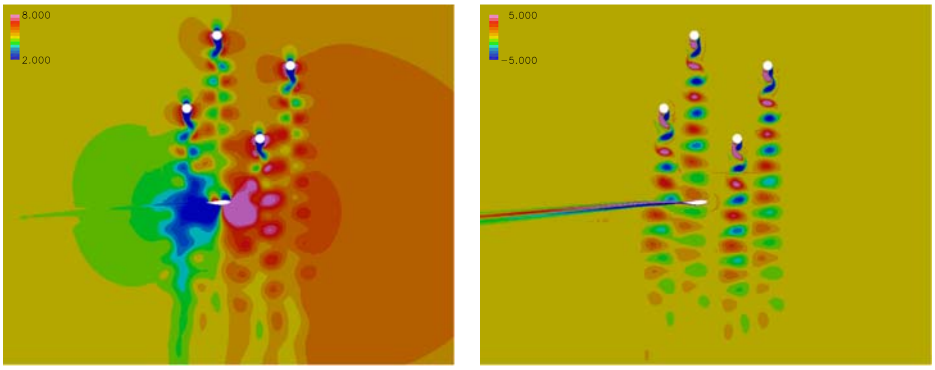

Figure 21. Snapshot of axial velocity and vorticity for the four leg configuration for the 80% radius blade section at 22.5 degrees orientation to the tower.

3.5.6 Upwind Configuration

Figure 23 shows the comparison of EllipSys2D and HAWC2 for the upwind configuration of the UPWIND turbine for the three blade sections modelled in this work. For the sake of com-

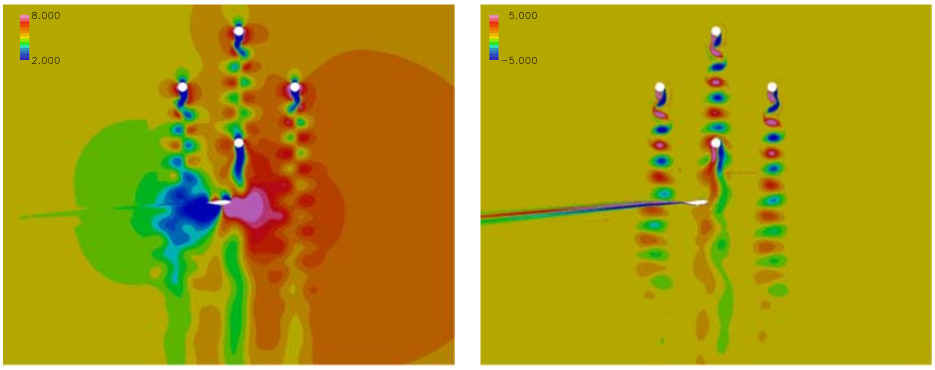

Figure 22. Snapshot of axial velocity and vorticity for the four leg configuration for the 80% radius blade section at 45 degrees orientation to the tower.

parison the freestream level of the normal force of the two computations have been shifted to match each other. The tower shadow predicted by HAWC2 is consistently larger than that predicted by EllipSys2D. Also, the recoverery to the freestream level differs slightly with HAWC2 predicting a faster recovery.

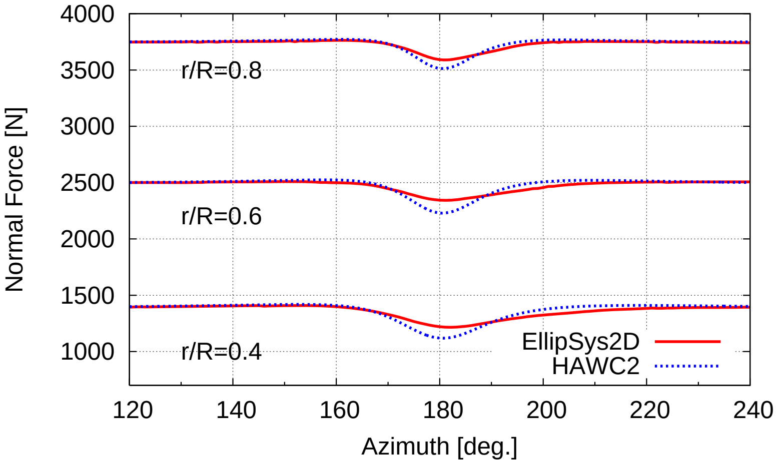

Figure 23. Comparison of HAWC2 and EllipSys2D normal force coefficients as function of blade azimuth for the upwind configuration of the UPWIND turbine at the three radial sections.

3.5.7 Downwind Configuration

Figure 24 shows the same comparison of EllipSys2D and HAWC2 codes for the downwind configuration of the UPWIND turbine. Here, two different drag coefficients have been used in HAWC2; as is evident a C_d=0.4 results in a good agreement between the two codes at the 80% blade section, whereas HAWC2 predicts a larger tower shadow on the two inner sections. Similar to the upwind configuration, the recovery from the tower shadow is faster in the HAWC2 simulation than in EllipSys2D.

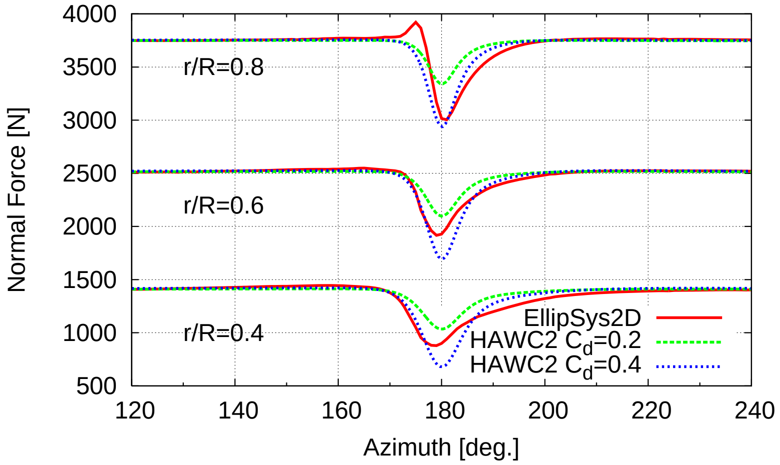

Figure 24. Comparison of HAWC2 and EllipSys2D normal force coefficients as function of blade azimuth for the downwind configuration of the UPWIND turbine at the three radial sections.

3.5.8 Four Leg Tower Configuration

Figure 23 shows the comparison of EllipSys2D and HAWC2 codes for the downwind four leg tower configuration of the UPWIND turbine. The HAWC2 code clearly captures the qualitative behaviour very well for all three tower orientations. The tower shadow is overpredicted significantly for a drag coefficient of 0.4, which for the cylindrical tower gave the best comparison. This indicates that the parameters used to superimpose the two wakes need to be tuned slightly.

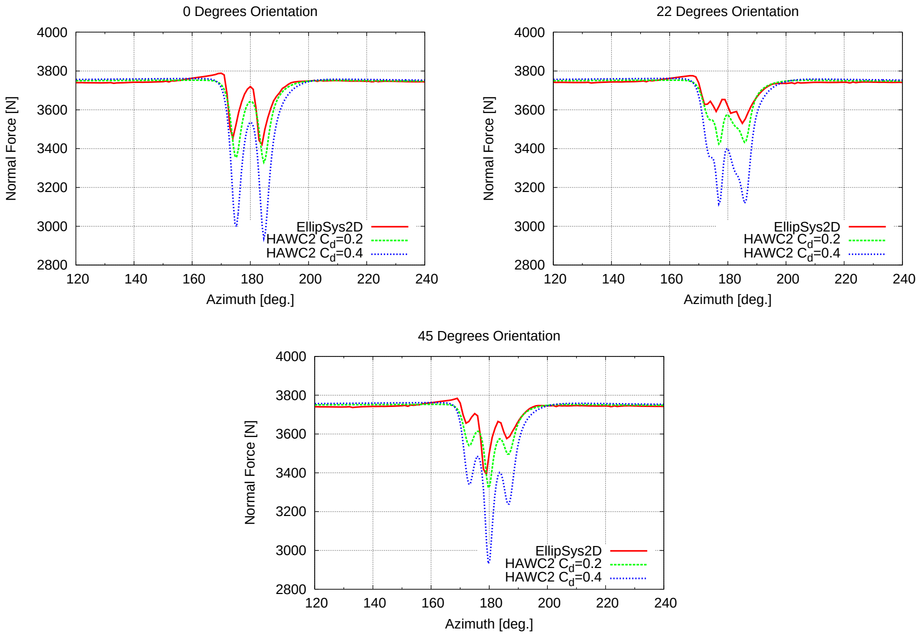

Figure 25. Comparison of HAWC2 and EllipSys2D normal force coefficients as function of blade azimuth for the four leg tower configuration for the three tower orientations.

3.6 Conclusions

A 2D CFD study has been carried out to investigate the tower shadow for two different turbines, both in upwind and downwind configurations. The NREL Phase VI turbine was used to validate the 2D solver against the experimental data from the Unsteady Aerodynamics Experiment carried out by NREL in the NASA Ames 120×80 ft wind tunnel. At the lowest wind speed of 7 m/s good correspondence was achieved between the simulations and experimental data. For the higher wind speeds the average behaviour was not captured as well.

The results for the UPWIND turbine showed that the tower shadow on a downwind turbine is approximately five times greater than on an upwind turbine. Using a streamlined tower was shown to reduce the tower shadow by 50% compared to the conventional tower. Using a four legged construction for the tower also reduced the tower shadow compared to the circular tower. However, the blade response was found to be very unsteady due to the interaction with the individual wakes behind each tower leg.

Finally, the 2D CFD results were compared to HAWC2 simulations on the UPWIND turbine. For the upwind configuration the aeroelastic code overestimated the tower shadow slightly compared to EllipSys2D, and the recovery from the tower shadow was also found to be faster than for the CFD results. For the tubular downwind configuration, the best correspondence between the two codes was obtained when a drag coefficient of 0.4 was used in the aeroelastic code. However, on the inner sections of the blade, the tower shadow was overestimated by HAWC2. Again, the recovery was faster in HAWC2. For the four legged configuration, the qualitative behaviour was caputed very well by the aeroelastic code, whereas the magnitude of the tower shadow was overestimated significantly.

References

[1] D. Fingersh, D. Simms, M. Hand, D. Jager, J. Cortrell, M. Robinson, S. Schreck, and S. Larwood. Wind tunnel testing of NREL's unsteady aerodynamics experiment. *AIAA paper 2001-0035*, 2001.

[2] N. D. Kelly. Acoustic noise generation by the DOE/NASA MOD-1 wind turbine. In *Proceedings of Workshop on Wind Turbine Dynamics*, Cleveland State University, Cleveland, Ohio, 24-26 February 1981.

[3] S. Ljungren. A preliminary assessment of environmental noise from large wecs, based on experiences from swedish prototypes. Technical Report FFA TN 1884-48, FFA, 1984.

[4] H. A. Madsen, J. Johansen, N. N. Sørensen, G. C. Larsen, and M. H. Hansen. Simulation of low frequency noise from a downwind wind turbine rotor. In *Proceedings of the 26th ASME Conference on Wind Energy*, number AIAA-2007-0623, Reno, NV, USA, 8-11 January 2007.

[5] F. R. Menter. Zonal two-equation $k-\omega$ models for aerodynamic flows. *AIAA paper 93-2906*, 1993.

[6] J. A. Michelsen. Basis3D—a platform for development of multiblock PDE solvers. Technical Report AFM 92-05, Technical University of Denmark, 1992.

[7] J. A. Michelsen. Block structured multigrid solution of 2D and 3D elliptic PDEs. Technical Report AFM 94-06, Technical University of Denmark, 1994.

[8] C. M. Rhie and W. L. Chow. Numerical study of the turbulent flow past an aerofoil with trailing edge separation. *AIAA journal*, 21:1525–1532, 1983.

[9] S. Schreck. The NREL full-scale wind tunnel experiment introduction to the special issue. *Wind Energy*, 5(2-3):77–84, 2002.

[10] K. P. Sheppard and H. H. Hubbard. Physical characteristics and perception of low frequency noise from wind turbines. *Journal of Noise Control Engineering*, 1991.

[11] N. N. Sørensen. General purpose flow solver applied to flow over hills. Technical Report Risø-R-827(EN), Risoe National Laboratory, 1995.

[12] N. N. Sørensen. HypGrid2D—a 2-D mesh generator. Technical report, Risø-R-1035(EN), Risoe National Laboratory, 1998.

[13] N. N. Sørensen, J. A. Michelsen, and S. Schreck. Navier-Stokes predictions of the NREL Phase VI rotor in the NASA Ames 80ft × 120 ft wind tunnel. *Wind Energy*, 5:151–169, 2002. doi: 10.1002/we.64.

[14] S. Wagner, R. Bareiss, and G. Guidatti. *Wind Turbine Noise*. European Commission (DGXII), EUR 16823. Springer-Verlag, Berlin, Heidelberg, 1996.

[15] F. Zahle. *Wind Turbine Aerodynamics Using an Incompressible Overset Grid Method*. PhD thesis, Imperial College, London, 2006.

[16] F. Zahle and N. N. Sørensen. Wind turbine rotor-tower interaction using an incompressible overset grid method. *Journal of Wind Energy*, DOI: 10.1002/we.327, 2009.

[17] T. J. Larsen. How 2 HAWC2, the user's manual. Technical Report Risø-R-1597 (ver. 3-7)(EN), Risø National Laboratory, DTU, Roskilde, Denmark, January 2009.

4 Characterisation of the Unsteady Flow in the Nacelle Region of a Modern Wind Turbine

Author: Frederik Zahle and Niels N Sørensen

A 3D Navier-Stokes solver has been used to investigate the flow in the nacelle region of a wind turbine where anemometers are typically placed to measure the flow speed and the turbine yaw angle. A 500 kW turbine was modelled with rotor and nacelle geometry in order to capture the complex separated flow in the blade root region of the rotor. A number of steady state and unsteady simulations were carried out for wind speeds ranging from 6 m/s to 16 m/s as well as two yaw and tilt angles. The flow in the nacelle region was found to be highly unsteady, dominated by unsteady vortex shedding from the cylindrical part of the blades which interacted with the root vortices from each blade, generating high tangential velocities in the nacelle region. For pure axial inflow the averaged nacelle wind speed varied approximately linearly with the free stream wind speed, whereas the nacelle flow angle changed significantly with wind speed. The nacelle anemometry showed significant dependence on both yaw and tilt angles with yaw errors of up to 10° when operating in a tilted inflow.

4.1 Introduction

On modern wind turbines nacelle anemometry measurements are used primarily in the yaw control of the turbine, for startup and shutdown, but can also be used to establish the power curve of the turbine. The industry standard for measuring the flow speed and yaw angle is to place a sonic anemometer at the rear of the nacelle which measures the horizontal velocity components. It is, however, well-known that there is considerable uncertainty associated with this measurement technique. One factor of uncertainty is due to the highly unsteady flow in the near wake of the rotating blades. Another factor is that a measurement in hub height might not be representative of the average flow speed and yaw angle across the entire rotor disc. The variation in inflow could be caused by the upstream terrain, wakes from neighbouring turbines, atmospheric turbulence and velocity shear. Another issue is that standard practice is to establish the relationship between the freestream wind speed (FSWS) and the nacelle wind speed (NWS) as well as the freestream flow angle (FSFA) and the nacelle flow angle (NFA) based on one reference turbine, which is subsequently used on other turbines regardless of local conditions such as terrain and park effects.

An analysis by Dahlberg et al. [1] based on experimental data from a number of wind farms identified critical issues in relation to power curve measurements using the nacelle wind speed. The tilt angle of the flow over the nacelle was identified as one issue that was critical to correct measurement. Masson and Smaïli [4] used CFD to investigate the detailed flow over the nacelle establishing relationships between the FSWS and the NWS. In this work an actuator disc was used in place of the actual blade geometry.

The mechanical power of a wind turbine is approximately proportional to $cos^2(\psi)$, where ψ is the yaw angle [3]. This means that a yaw error of 10° results in a reduction of 3% in the power production. Over the life span of a wind turbine this amounts to a significant loss in production, as well as increases in fatigue loads on the turbine due to the cyclic variation in the loading. These simple considerations suggest that correct measurement of the yaw angle should be of very high priority in the design of the turbine, and it could even be argued that with the continuous increase in size of wind turbines, alternative methods for measuring the yaw angle should be investigated to overcome the difficulties outlined above.

The aim of this work is to investigate the flow properties in the nacelle region of a turbine for a number of wind speeds to assess whether characteristic flow patterns can be identified, which could lead to improvements to the guidelines for placement of the nacelle anemometer or the corrections applied to the measured flow quantities. The turbine that was used in this work is the 40 m diameter Nordtank NKT 500/41 stall regulated turbine, which is equipped with LM 19.1 blades, and has a nominal power output of 500 kW. Although this turbine is not pitch regulated, it is believed that it is still representative of a modern turbine, and can provide useful insight into the basic flow mechanisms that govern in the nacelle region of a turbine. The present turbine was also chosen because a recent measurement campaign has been carried out on this turbine by Diznabi [2]. This work will, however, focus solely on the numerical results.

4.2 Computational Setup

4.2.1 Flow Solver

For all computations the EllipSys3D pressure based incompressible Reynolds averaged Navier-Stokes flow solver written by Michelsen [6, 7] and Sørensen [10] is used. The code uses the finite volume method, solving for the primitive variables u, v, w, and p, in general curvilinear coordinates. The variables are stored in a collocated grid arrangement, and odd/even pressure decoupling is avoided using the Rhie-Chow interpolation [9]. The iterative SIMPLE or PISO algorithm is used to advance the solution in time using a second-order accurate scheme. The convective terms are discretised using either the second order upwind difference scheme, SUDS, or the Quadratic Upstream Interpolation for Convective Kinematics Scheme, QUICK, and the viscous terms are discretised using central differencing. The momentum equations are solved decoupled from each other using a red/black Gauss-Seidel point solver. To accelerate the convergence of the pressure-correction equation a multigrid solution strategy is implemented combined with the additive Schwarz method, where each sub-domain is solved for simultaneously. To further accelerate the convergence of the solution, grid and time step sequencing is used.

The code is fully parallelised using the MPI library with a multiblock decomposition of the solution domain. The block-block communication is done through one layer of ghost cells around each block. The cell vertices are required to coincide on interfaces such that conservation can be maintained.

For computations of flow over aerofoils and wind turbine blades the EllipSys3D code uses the $k-\omega$ SST model by Menter [5], because of its good performance in wall bounded adverse pressure gradient flows.

4.2.2 Computational Mesh

The stall regulated Nordtank 500 turbine is equipped with LM 19.1 blades, and has a cylindrical nacelle with a diameter of 2.0 m and a total length of 8.9 m including the spinner. The computational model of the turbine has been simplified compared to the actual geometry. The model contains the three blades, spinner and nacelle, however, the tower has been omitted since this simplifies the meshing considerably. To simplify the computational effort further, the nacelle was not stationary but rotated along with the spinner and rotor. Furthermore, the rotor was completely rigid. All simulations were carried out with uniform inflow, therefore no ground boundary was included in the simulations.

The computational surface mesh was generated using Gridgen and contained a total of 108 blocks of 32×32 cells. The blades were resolved with 256 cells in the chordwise direction and 96 cells in the spanwise direction, with a 64×64 tip cap. The nacelle was resolved with 24 blocks of 32×32. The volume mesh was generated using the hyperbolic mesh generator HypGrid [11] and grown out to form a sphere with a diameter of approximately 280 m corresponding to 7 rotor diameters with 128 cells in the normal direction. The first cell height in the boundary layer was set to 1×10^{-6} to ensure y^+ values of less than 2. The mesh thus contained a total of 432 blocks of 32×32×32, totalling 14.2 million cells. Figures 26 and 27 show sideviews of the mesh as well as the detailed surface mesh on the nacelle.

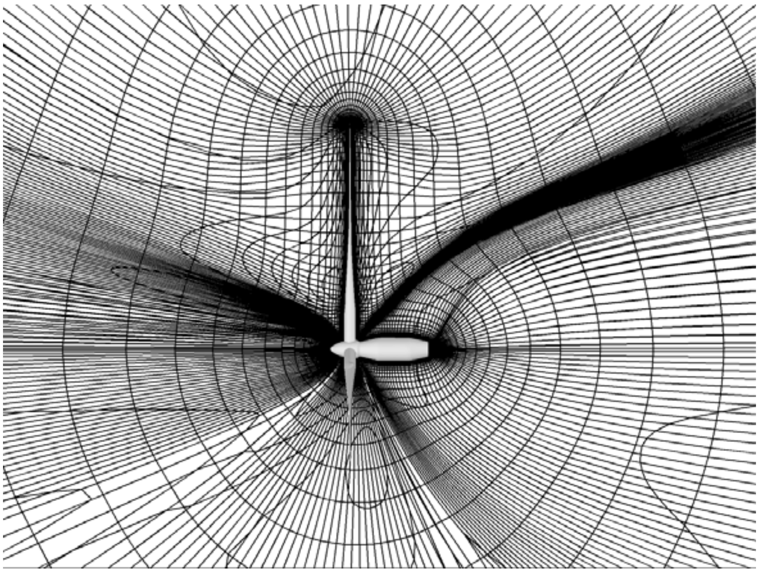

Figure 26. Sideview of the mesh showing only every second grid point.

In Figure 27 the position of the nacelle aneometer is indicated by a red sphere. The exact coordinates of the anemometer position is *x*=0 m, *y*=2.1 m, *z*=7.17 m.

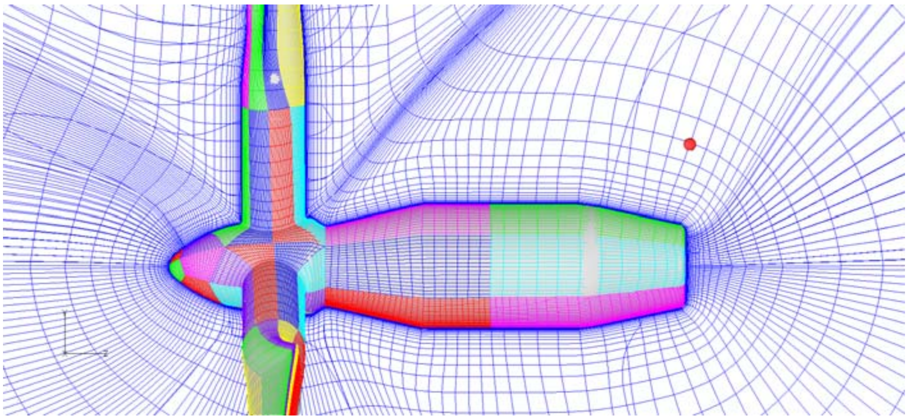

Figure 27. Detailed view of the mesh around the nacelle showing only every second grid point.

4.3 Computational Parameters

A total of nine simulations were carried out in this study: Six steady state moving mesh simulations with an inflow velocity ranging from 6 m/s to 16 m/s in steps of 2 m/s. In these simulations the turbine had zero yaw and tilt. Three unsteady moving mesh simulation were carried out at 8 m/s at 0°, 5°, and 10° yaw. Since the domain is axi-symmetric, these simulations were also used to investigate the effect of tilt.

The computations were all carried out using the QUICK scheme to discretise the convective terms while the SIMPLE algorithms was used to solve the coupled velocity/pressure equations for the steady state and unsteady simulations. All simulations were carried out assuming fully turbulent flow using the The $k-\omega$ SST model. The Nordtank turbine rotates at a speed of 27.1 RPM or 2.8379 rad/s. To obtain a reasonable temporal resolution, the time step in the unsteady simulations was set to $\Delta t = 2.012755 \times 10^{-3}$ at the finest grid level corresponding to 1100 time steps per revolution or 0.328° per time step. At the two coarser grid levels the time steps were successively increased by a factor of two yielding a time step of $\Delta t = 8.051018 \times 10^{-3}$ at grid level 3. Table 7 summarises the computational parameters.

Computational Parameters	
Time integration	SIMPLE
Convective terms	QUICK
Turbulence model	$k-\omega$ SST
Time step	2.012755×10^{-3} seconds
Subiterations	4

Table 7. Summary of the computational parameters for the simulations.

The simulations were carried out on the Risø DTU cluster *Thyra* which contains 128 nodes of two dual core 2.2Ghz AMD CPU's connected by means of an Infiniband network. On 14 nodes a steady state simulation is fully converged in approximately 4 hours using three levels of grid sequencing. The unsteady simulations were run on 27 nodes with three layers of grid and time step sequencing. On the finest grid and time step level one revolution was computed in approximately 2.4 hours.

4.4 Results

Figure 28 shows the mechanical power as a function of wind speed for the steady state computations. As can be seen there is good agreement at the lower wind speeds, whereas EllipSys3D overestimates the power at higher wind speeds. This trend has also been observed in other simulations on stall regulated turbines, and can mainly be attributed to the fact that RANS solvers generally have difficulty predicting the stall on thick aerofoils correctly. Figures 29 and 30 show the tangential and normal force distributions on the blade for the six wind speeds. Table 4.4 summarises the mechanical power and thrust force of the turbine.

Wind speed [m/s]	Mech. Power [kW]	Thrust [N]
6	65.2	24.80
8	182.3	37.80
10	330.4	49.20
12	480.0	57.50
14	610.5	63.30
16	720.0	67.80

Table 8. Mechanical power and thrust force for the steady state computations.

Three unsteady computations were also carried out at a wind speed of 8 m/s. One with axial flow corresponding to the steady state computations and two at 5° and 10° yaw, respectively. Table 9 summarises the results of these simulations on the three grid levels. As can be seen the unsteady simulations predict a slightly higher mechanical power than the steady state computations. The solution was found to be sufficiently mesh independent since the mechanical power varied with approximately 1% between grid level 2 and 1. The results also show that the yawed inflow conditions result in a reduction in power production proportional to $cos^{1.7}(\psi)$ and a reduction in thrust proportional to $cos^{0.8}(\psi)$, which is in good agreement with the findings in Madsen et al. [3].

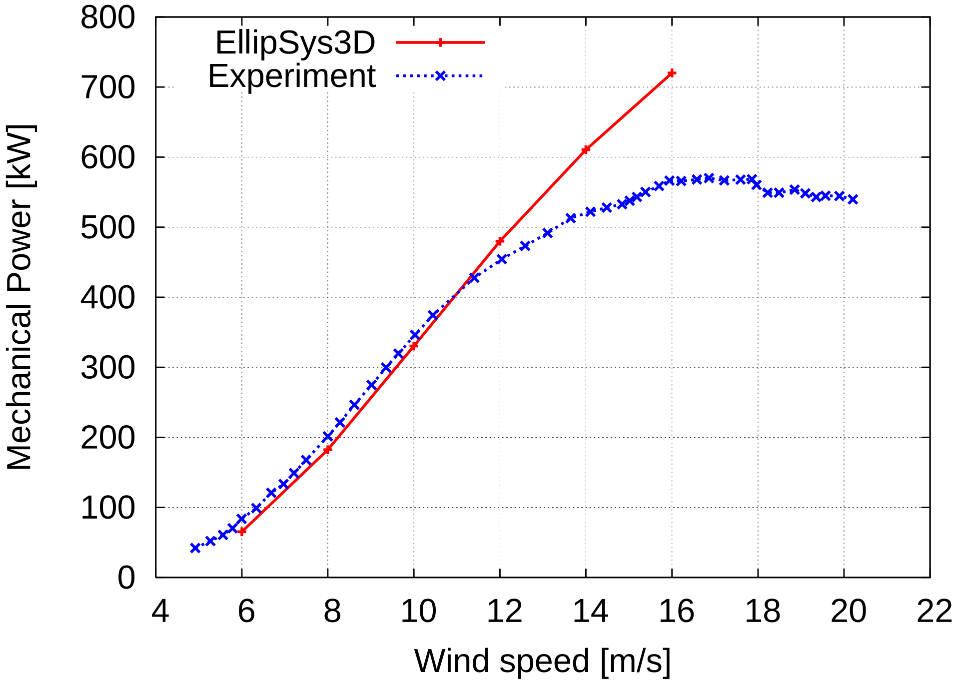

Figure 28. Power curve calculated using EllipSys3D compared to experimental results [8].

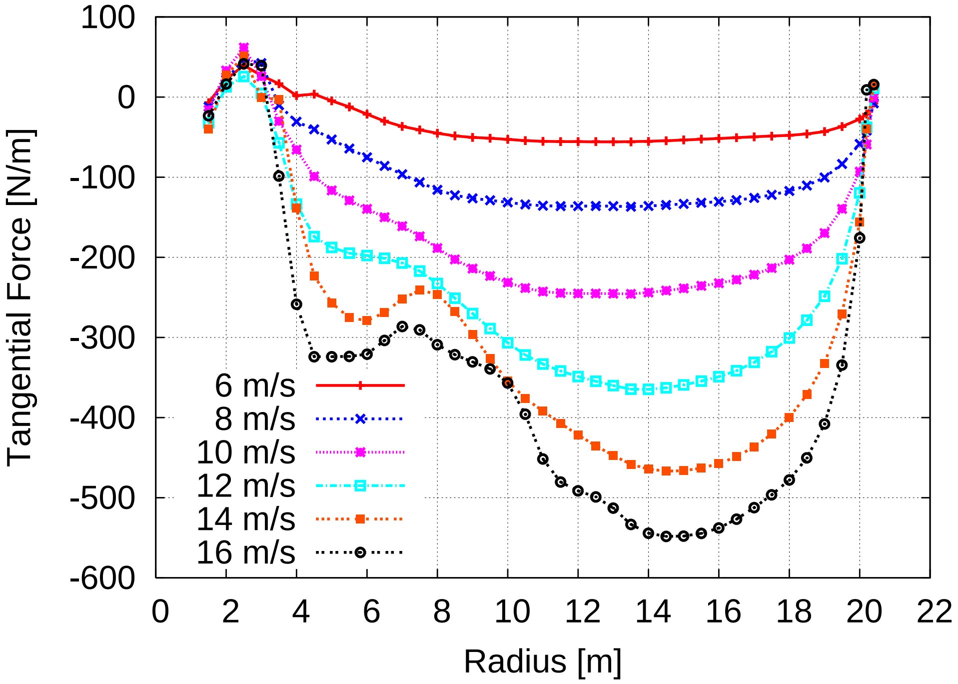

Figure 29. Normal force distribution along the blade for the six wind speeds.

Turning to the analysis of the flow characteristics in the nacelle region, firstly, the steady state computations will be analysed. These simulations were all carried out with zero yaw and tilt angles. Since the solution is steady state there is no true time variation in the solution. To obtain azimuthally varying flow quantities, the Cartesian velocity components were transformed to a polar coordinate system, and based on the tangential velocity, V_ϕ, and the axial velocity, W, the

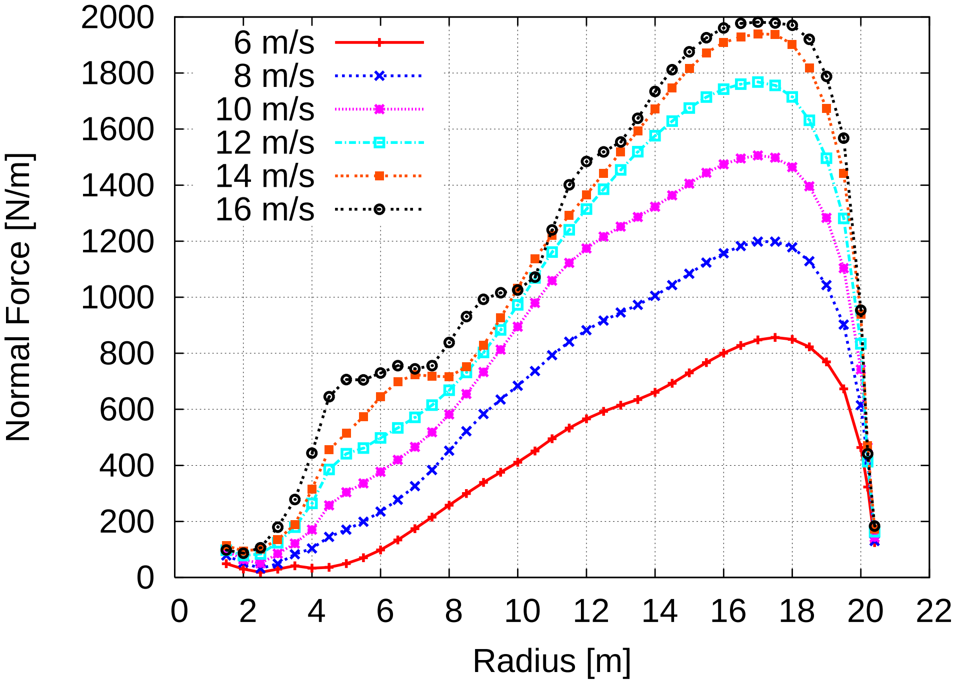

Figure 30. Normal force distribution along the blade for the six wind speeds.

Name	Mech. Power [kW]			Thrust [N]		
Grid level	L3	L2	L1	L3	L2	L1
0yaw-s	-	-	182.3	-	-	37.8
0yaw-u	88.3	186.0	188.0	39.6	38.5	39.2
5yaw-u	86.8	185.0	186.8	39.5	38.4	39.1
10yaw-u	82.5	182.0	183.3	39.0	38.1	38.8

Table 9. Mechanical power and thrust force for the unsteady computations.

nacelle wind speed (NWS_ϕ) and the nacelle flow angle (NFA_ϕ) were computed as a function of the azimuthal angle ϕ:

$$V_\phi = -U sin(\phi) + V cos(\phi) \tag{1}$$

$$NWS_\phi = \sqrt{V_\phi^2 + W^2} \tag{2}$$

$$NFA_\phi = atan(V_\phi/W) \tag{3}$$

Following a right handed coordinate system, V_ϕ is, when viewed from downstream, defined positive for a clockwise rotation around the z-axis, which is oriented in the axial direction. NFA_ϕ is defined positive for an anti-clockwise rotation around the y-axis, when viewed from above. To obtain an azimuthal average of the NWS and NFA, these quantities were integrated along a circle with a radius corresponding to the vertical position of the probe locations.

$$NWS = \int_0^{2\pi} NWS_\phi d\phi|_{z=const}^{r=const}. \tag{4}$$

$$NFA = \int_0^{2\pi} NFA_\phi d\phi|_{z=const}^{r=const}. \tag{5}$$

where r is equal to the y poisition of the probe and z is equal to the z-position of the probe. The NWS and NFA extracted from the unsteady simulations were simply constructed substituting the time averaged U and W velocities in the expressions in Equations 2 and 3.

Figures 31 to 33 show contour plots of the z-vorticity, the nacelle flow angle, and the tangential velocity in an x-y plane at z=7.17 m, corresponding to the nacelle probe position for the 8 m/s steady state simulation. Each blade appears to generate three counter-rotating vortices that induce high tangential velocities, thus locally increasing the tangential flow angles. The large negative flow angles are generated at the interfaces between the outermost vortices of negative vorticity and the neighbouring vortices of positive vorticity. The strongest inner vortex of positive vorticity generates the positive flow angles close to the nacelle surface. Notice also that the flow angle as expected is positive in the region where the blade generates a positive torque due to the wake rotation which is opposite to the blade rotation.

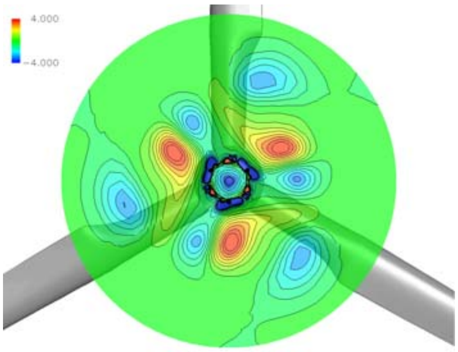

Figure 31. Contour plot of the z-vorticity at z=7.17 m.

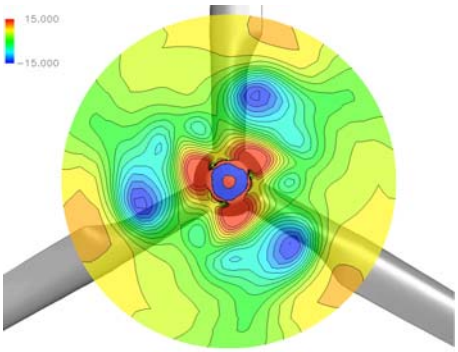

Figure 32. Contour plot of the NFA_l at z=7.17 m.

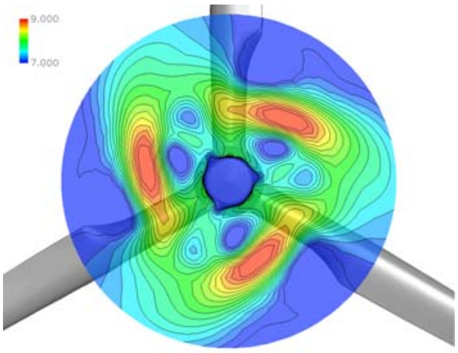

Figure 33. Contour plot of the NWS_ϕ at z=7.17 m.

Figure 34 shows the azimuthally averaged NWS versus the FSWS for the steady state simulations at the nacelle anemometer position. The extracted velocity is quite close to the FSWS at the lower wind speeds, but exceeds the FSWS slightly at higher freestream wind speeds. This result suggests that, although present, the variation of axial induction with wind speed has limited influence in the nacelle region where the blades are cylindrical and non-lifting.

In relation to positioning of nacelle anemometers, it is relevant to investigate the sensitivity of the NWS and the NFA to the vertical position of the nacelle anemometer. Figure 35 shows

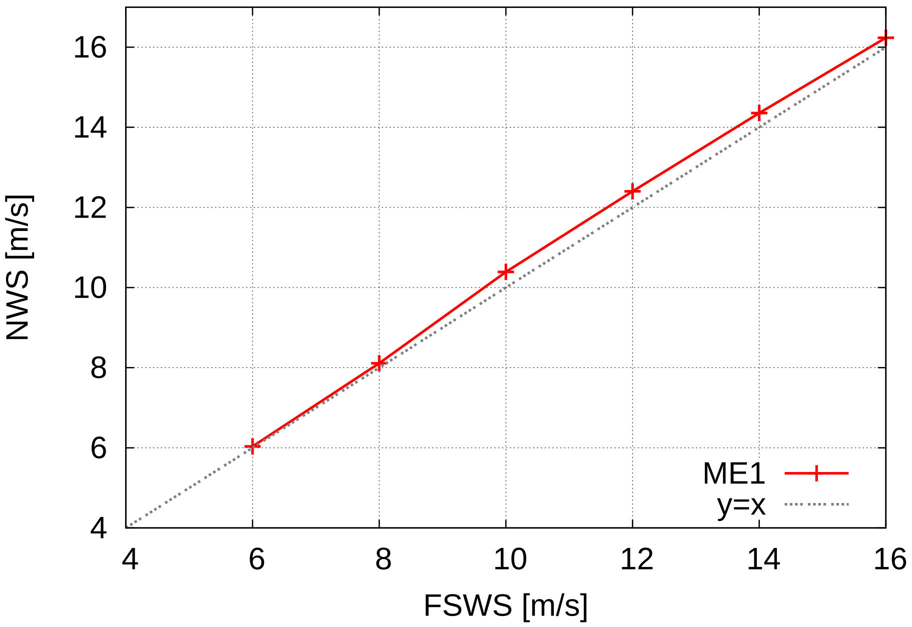

Figure 34. Nacelle wind speed (NWS) versus freestream wind speed (FSWS) extracted at the nacelle probe position.

the normalized NWS as a function of vertical distance at *z*=7.17 m, corresponding to the plane where the nacelle probe is positioned for the six wind speeds. The NWS varies significantly with vertical distance as much as 15% from *y*=1.5 m to *y*=2.5 m, where the velocity gradient is strongest. Figure 34 suggested that the normalised NWS did not vary significantly with wind speed. However, Figure 35 clearly shows that this is not the case. It so happens that at a height of *y*=2.1 m, where the nacelle anemometer is located, the normalized NWS is quite close to 1 for all wind speeds. However, as is also evident, the NWS varies significantly at other vertical positions, with as much as 8% at *y*=2.5 m.

Figure 36 shows the NFA as a function of vertical distance. As for the NWS the flow angle is also highly sensitive to the vertical position with a variation of as much as 12° from *z*=1.5 m to *z*=2.5 m. A perhaps more critical finding is that at the nacelle probe position the flow angle varies between -6.5° and 0° for the six wind speeds, which complicates the use of corrections of the measured flow angle on operating turbines.

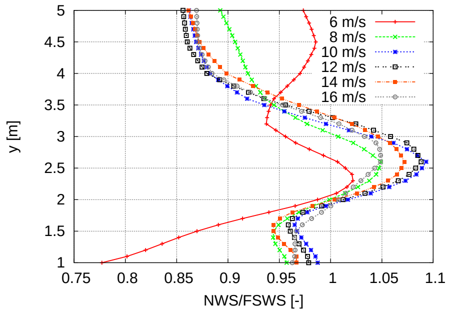

Figure 35. Azimuthally averaged nacelle wind speed (NWS/FSWS) as a function of vertical distance extracted at z=7.17 m.

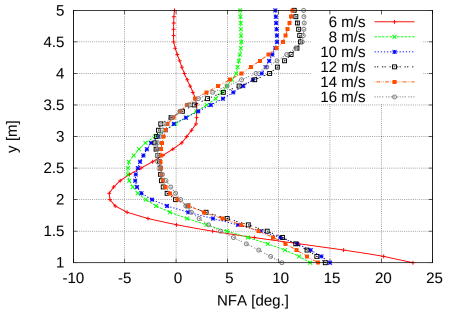

Figure 36. Azimuthally averaged nacelle flow angle (NFA) as a function of vertical distance extracted at z=7.17 m.

Steady state simulations provide fast and reliable results for flows that are physically steady state. However, for inherently unsteady flows, a steady state solution does not necessarily provide an average solution equivalent to the average of an unsteady solution. A steady state solution converges towards *one* solution that is steady, which depends on the exact initial conditions and numerical settings. As such it was necessary also to carry out an unsteady simulation to validate to what extent the steady state solutions were representative of the mean flow in the nacelle region of the turbine.

Figures 37 and 38 show the NWS and the NFA for 10 consecutive revolutions at the nacelle probe position, as well as the azimuthally binned curve. The NWS signal is highly unsteady and the blade passages are smeared considerably but still detectable in the azimuthally binned curve. There is also large variation in the flow angle, with variations of ±15 °. In the flow angle signal a 3P frequency is clearly visible. The steady state solution is also shown in the figures, which captures the 3P frequency for both the velocity and flow angle.

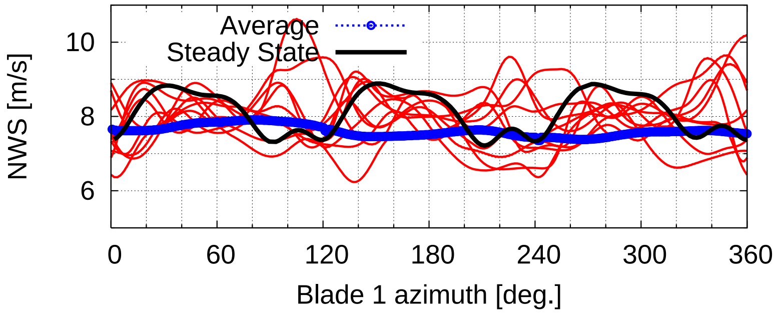

Figure 37. Nacelle wind speed (NWS) as a function of blade 1 azimuthal angle extracted at the nacelle probe.

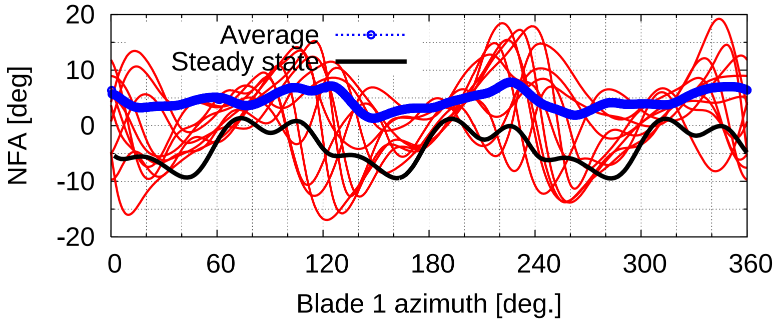

Figure 38. Nacelle flow angle (NFA) as a function of blade 1 azimuthal angle extracted at the nacelle probe.

Turning to the variation of the NWS and the NFA as a function of vertical distance above the nacelle, Figures 39 and 40 show the averaged profiles over 10 revolutions as well as the steady state solution. Looking firstly at the NWS it can be seen that the unsteady and steady state solutions qualitatively agree quite well, predicting the minimum and maximum positions of velocity at the same heights. The steady state solution does, however, overpredict the wind speed compared to the unsteady solution by approximately 4%. This is likely due to the fact that the wake vortices in the steady state solution are stationary, whereas the unsteady solution contains higher frequency shedding of the vortices, which on average will cause a smearing of gradients in the flow. The same trend is visible for the NFA in Figure 40, where the steady state flow angle is 4° lower than that extracted in the unsteady simulation. However, the location of minimum flow angle is predicted in the same vertical position in both simulations.

The last part of the present investigation concerns the effect of tilt and yaw on the measured flow quantities on the nacelle. Looking firstly at the case of tilt, Figure 41 shows the normalized

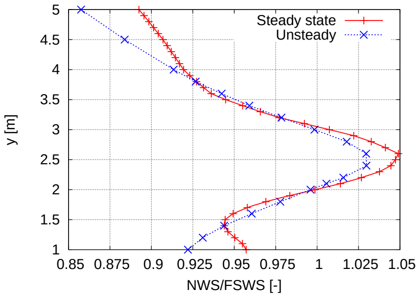

Figure 39. Comparison of the steady state and unsteady averaged normalized nacelle wind speed (NWS/FSWS).

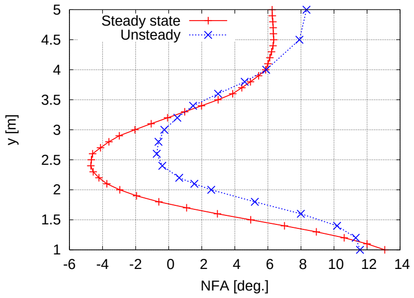

Figure 40. Comparison of the steady state and unsteady averaged nacelle flow angle (NFA).

NWS for three tilt angles, 0°, 5°, and 10°. The tilt angle clearly has a strong effect on the measured flow speed, with a 10% reduction in the NWS from 0° tilt to 10° tilt at the anemometer position. The reason for the large shift in flow speed is that the root vortex which gives rise to a speed up effect is shifted upwards due to the tilt angle. Likewise, the NFA is strongly affected by tilt, giving rise to a 10° difference in the measured flow angle when the tilt is increased from 0° tilt to 10°.

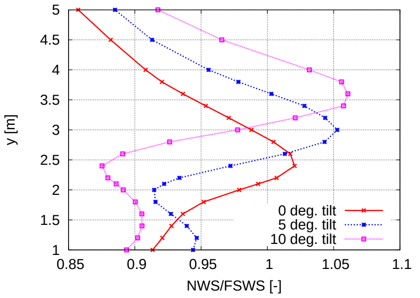

Figure 41. Effect of tilt on the nacelle wind speed (NWS/FSWS) as a function of vertical distance.

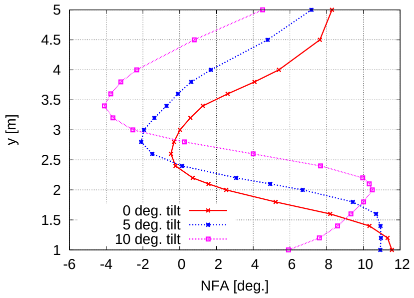

Figure 42. Effect of tilt on the nacelle flow angle (NFA) as a function of vertical distance.

When the turbine operates in yaw the NWS profile changes, however, not as drastically as for tilt. As is evident the speedup region shifts downwards with increasing yaw angle, due to the movement of the root vortices. The measured NWS at the nacelle anemometer position shifts approximately 4% when operating in yaw. The NFA is predicted quite accurately relatively to the zero yaw computation with only little error. As for the NWS, the minimum flow angle position is also shifted downwards for increasing yaw angle.

4.5 Conclusions

In this work the characteristics of the flow in the nacelle region of a stall regulated turbine has been investigated. It has been shown that a distinct flow pattern exists with a complex set of vortical structures, which induce high tangential velocities in the region where nacelle anemometers are typically placed. It was found that the flow pattern persists for a number of different wind speeds, yaw and tilt angles. From the steady state simulations it was found that the nacelle wind speed was predicted quite accurately compared to the free stream wind speed, whereas the nacelle flow angle was more sensitive. This sensitivity was shown to be related to the very high gradients in the tangential wind speed resulting in a significant variation in nacelle flow angle with height above the nacelle. When operating in tilt the flow around the nacelle influenced the nacelle wind speed and flow angle considerably. Yaw misalignment did

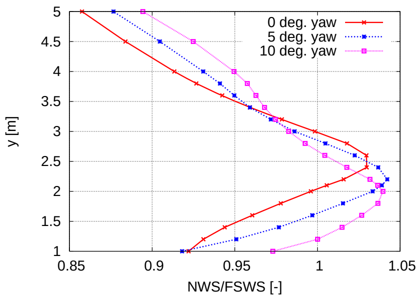

Figure 43. Effect of yaw on the nacelle wind speed (NWS/FSWS) as a function of vertical distance.

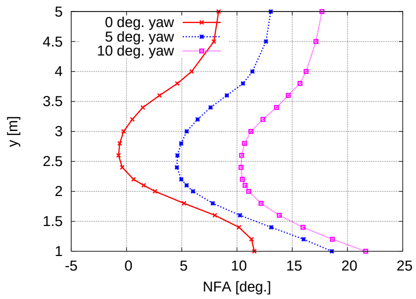

Figure 44. Effect of yaw on the nacelle flow angle (NFA) as a function of vertical distance.

not have as strong an influence on the measurement of wind speed and flow angle. In general these findings suggest that a detailed numerical analysis of the flow in the nacelle region of a turbine could be very useful for positioning the nacelle anemometer. Furthermore, the results indicate that it is very difficult to make simple corrections to the measured quantities that will be valid for all flow conditions, particularly off-design conditions.

Acknowledgements

The author wishes to thank Babak Diznabi for supplying the surface geometry of the Nordtank 500 nacelle and spinner.

References

[1] J.-A. Dahlberg, S. Frandsen, H. A. Madsen, I. Antoniou, T. Friis Pedersen, R. Hunter, H. Klug, and A. Albers. Is the nacelle mounted anemometer an acceptable option in performance testing. In *Proceedings of the European Wind Energy Conference*, pages 624–237, Nice, France, 1-5 March 1999.

[2] B. Diznabi. Investigation of the flow relation to nacelle anemometry. Master's thesis, Danish Technical University, Lyngby, Denmark, 2009.

[3] H. A. Madsen, N. N. Sørensen, and S. Schreck. Yaw aerodynaics analyzed with three codes in comparison with experiment. In *41st Aerospace Sciences Meeting and Exhibit*, number AIAA 2003-519, Reno, Nevada, USA, 6-9 January 2003.

[4] C. Masson and A. Smaïli. Numerical study of turbulent flow around a wind turbine nacelle. *Wind Energy*, 9:281–298, 2006.

[5] F. R. Menter. Zonal two-equation $k-\omega$ models for aerodynamic flows. *AIAA paper 93-2906*, 1993.

[6] J. A. Michelsen. Basis3D—a platform for development of multiblock PDE solvers. Technical Report AFM 92-05, Technical University of Denmark, 1992.

[7] J. A. Michelsen. Block structured multigrid solution of 2D and 3D elliptic PDEs. Technical Report AFM 94-06, Technical University of Denmark, 1994.

[8] U. S. Paulsen. Konceptundersøgelse Nordtank NTK 500/41 måling af effektkurve. Technical Report Risø-I-889(DA), Risø National Laboratory, Roskilde, Denmark, November 1995.

[9] C. M. Rhie and W. L. Chow. Numerical study of the turbulent flow past an aerofoil with trailing edge separation. *AIAA journal*, 21:1525–1532, 1983.

[10] N. N. Sørensen. General purpose flow solver applied to flow over hills. Technical Report Risø-R-827(EN), Risoe National Laboratory, 1995.

[11] N. N. Sørensen. HypGrid2D—a 2-D mesh generator. Technical report, Risø-R-1035(EN), Risoe National Laboratory, 1998.

5 Correlation Based Transition Modeling of Laminar to Turbulent Transition

Author: Niels N Sørensen

5.1 Introduction

The present chapter describes the ongoing work on implementation and verification of the correlation based transition model of of Menter et al. [1, 2]. The applications used here are all chosen based on relevance for wind energy aerodynamics. Firstly, the model is applied to four airfoils from the NACA 64XXX series, to illustrate the good agrement with measurement and the Xfoil code. Secondly, the model is applied to three dimensional flows along with the Detached Eddy Simulation (DES) technique for two cases of highly separated flow, namely the flow over a cylinder and the flow over a 35% thick DU-96-W-351 airfoil.

5.2 Code description

The in-house flow solver EllipSys3D is used in all computations presented here. The code is developed in co-operation between the Department of Mechanical Engineering at the Technical University of Denmark and The Department of Wind Energy at Risø National Laboratory, see [3, 4] and [5]. The EllipSys3D code is a multiblock finite volume discretization of the incompressible Reynolds Averaged Navier-Stokes (RANS) equations in general curvilinear coordinates. The code uses a collocated variable arrangement, and Rhie/Chow interpolation [6] is used to avoid odd/even pressure decoupling. As the code solves the incompressible flow equations, no equation of state exists for the pressure, and in the present work the Semi-Implicit Method for Pressure-Linked Equations (SIMPLE) algorithm of Patankar and Spalding [7, 8] or the Pressure Implicit with Splitting of Operators (PISO) algorithm of Issa [9, 10] is used to enforce the pressure/velocity coupling, for steady state and transient computations respectively. The EllipSys3D code is parallelized with the Message-Passing Interface (MPI) for executions on distributed memory machines, using a non-overlapping domain decomposition technique.

Both steady state and unsteady computations can be performed. For the unsteady computations the solution is advanced in time using a 2nd order iterative time-stepping (or dual time-stepping) method. In each global time-step the equations are solved in an iterative manner, using under relaxation. First, the momentum equations are used as a predictor to advance the solution in time. At this point in the computation the flowfield will not fulfil the continuity equation. The rewritten continuity equation (the so-called pressure correction equation) is used as a corrector making the predicted flowfield satisfy the continuity constraint. This two step procedure corresponds to a single sub-iteration, and the process is repeated until a convergent solution is obtained for the time step. When a convergent solution is obtained, the variables are updated, and we continue with the next time step. Thus, when the sub-iteration process is finished all terms are evaluated at the new time level.

For steady state computations, the global time-step is set to infinity and dual time stepping is not used, this corresponds to the use of local time stepping. In order to accelerate the overall algorithm, a multi-level grid sequence is used in the steady state computations. The convective terms are discretized using a third order Quadratic Upstream Interpolation for Convective Kinematics (QUICK) upwind scheme, implemented using the deferred correction approach first suggested by Khosla and Rubin [11]. Central differences are used for the viscous terms, in each sub-iteration only the normal terms are treated fully implicit, while the terms from non-orthogonality and the variable viscosity terms are treated explicitly.

In the present work the turbulence in the boundary layer is modeled by the k-ω Shear Stress Transport (SST) eddy viscosity model [12] using it either in its basic form or using the DES version proposed by Strelets [13], to account for the deep stall physics. The laminar to turbulent transition process is modeled by the $\gamma - \widetilde{Re}_\theta$ correlation based transition model of Menter et al. [1]. Due to problems often referred to Modeled Stress Depletion (MSD) reported for the standard DES method, when the resolved LES layer penetrates too deep into the RANS boundary layer, the DDES variation of the DES methodology proposed by Menter [14] using the f2zone as a shield function was tested. The problem of the LES region contaminating the RANS layer can happen when computing flows with high values of inflow turbulence typically used with the correlation based transition model. The equations for the turbulence model and the transition model are solved after the momentum and pressure correction equations in every sub-iteration/pseudo time step, and in agreement with the recommendations of Menter et al. [1], a second order upwind Total Variation Diminishing (TVD) scheme based on the MinMod limiter is used for the transport equations for turbulence and transition. The three momentum equations, the $k-\omega$ equations and the two transition model equations are solved decoupled using a red/black Gauss-Seidel point solver. The solution of the Poisson system arising from the pressure-correction equation is accelerated using a multigrid method.

5.3 Computational grid

All meshes used in the present study both for the two dimensional airfoil computations and the meshes for the three dimensional computations are generated with the 2D enhanced hyperbolic grid generation program HypGrid2D [15]. For the three dimensional cases the 3D nature of the meshes is obtained by first generating a 2D slice, and afterwards sweeping this grid in the span-wise direction.

5.3.1 Two Dimensional Airfoil Grids

The computational grids around the two dimensional airfoils are constructed using 384 × 384 cells, see Fig. 45. The outer boundary is placed approximately 20 chord-lengths from the airfoil surface, and the off-wall spacing of the first cell is 1×10^{-6} chord lengths. The stretching in the normal direction is very weak close to the wall, placing the first 256 cells within $\frac{1}{10}$ of the airfoil chord. The outlet is specified on the part of the downstream boundary covering from 40 to 110 degrees, zero being straight above the airfoil.

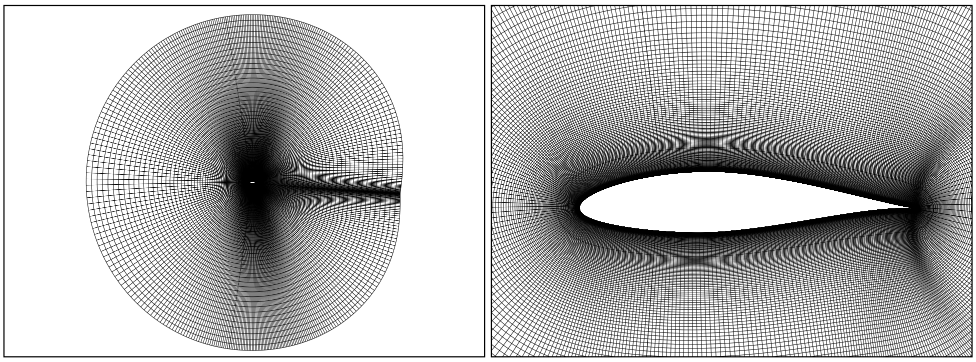

Figure 45. The O-mesh configuration used for the airfoil computations, here shown for the NACA64-418 geometry. The mesh has 384 cells in the chordwise direction and 384 cells in the normal direction.

5.3.2 Three Dimensional Grids

For the cylinder flow, the O-mesh has 256 cells around the surface of the cylinder, 256 cells in the normal direction with a first cell height ($\frac{\Delta z}{D}$) of 1×10^{-5} and the outer domain boundary placed approximately 30 diameters away from the surface. In the span-wise direction 128 cells are used along the $2 \times D$ span, giving a cell size of around 0.0156D. The grid holds in total 8.4 million cells. The surface of the cylinder is modeled as a no-slip surface, and periodic conditions are used in the spanwise direction. The outer domain boundary is specified as inlet, except for the area downstream of the cylinder covering around +/- 45 degrees in azimuth direction, where outlet condition is used specifying fully developed flow.

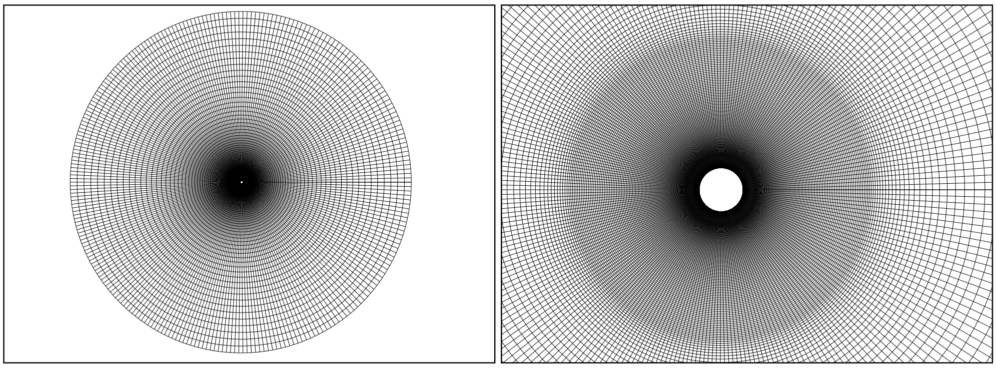

Figure 46. Mesh around the circular cylinder.

The O-mesh for the DU-96-W351 airfoil was generated using 512 cells in the chordwise direction, 256 cells in the normal direction with a first cell height ($\frac{\Delta z}{C}$) of 5×10^{-6} and the outer domain boundary placed approximately 60 chords away from the surface, see Figure 47. In the span-wise direction 128 cells are used along the $2 \times C$ span, giving a cell size of around $0.0156 \times C$. The grid holds in total 17 million grid points. The surface of the airfoil is modeled as a no-slip surface, and periodic conditions are used in the spanwise direction. The outer domain boundary is specified as inlet, except for the area downstream of the airfoil covering around +/- 45 degrees in azimuth direction, where outlet condition is used specifying fully developed flow.

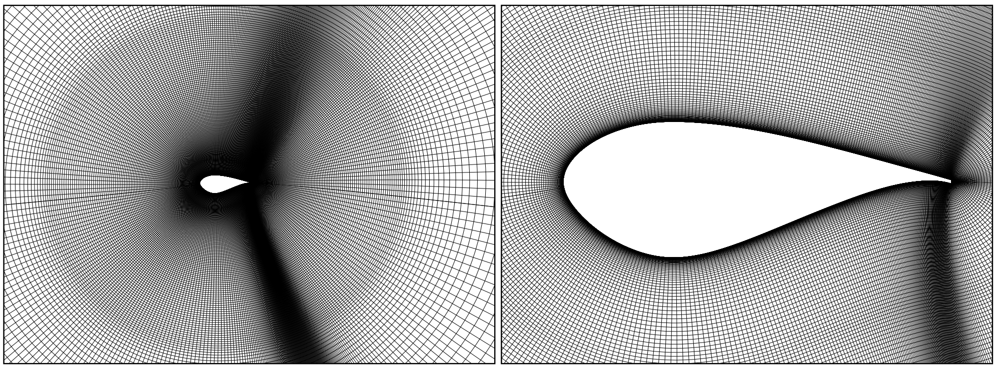

Figure 47. Mesh around the DU profile.

5.4 2D Airfoil Results

Four airfoils are studied, namely the NACA64-018, 218, 418 and 618. The results computed with the EllipSys2D code are compared with the measurements of Abbott and Doenhoff [16] and computations carried out using the Xfoil code [17]. All computations are performed at a Reynolds number of six million. In the EllipSys2D computations a very low inflow turbulence intensity of 0.01% is used to assure natural transition, similar to what was measured in the NASA LTPT [18].

All computations presented in the present work are performed using steady state computations with under relaxation factors of 0.8, 0.2, 0.7 and 0.7 for momentum, pressure, turbulence and transition equations, respectively, using the SIMPLE algorithm. The convective terms are discritized using the QUICK scheme for the momentum equations and a blend of 60% QUICK and 40% UDS for the turbulent and transitional equations. The computations are performed using a five level grid sequence.

Looking at the computed lift, Figure 48 a very good agreement is observed between measurements and the two computational codes for low angles of attack between -6 and 6 degrees for all airfoils, with the exception of the NACA64-618 airfoil. As also reported by Timmer [19], there seems to be an angle offset in the measurements for this case supported by the present study by the good agreement between the EllipSys and Xfoil results. Looking at the lift/drag curves, similar good agreement is observed, especially at the low lift values. For the lift/drag curves the good agreement with the measured values, are supporting the assumption that the offset observed for the lift as function of angle of attack for the NACA64-618 are caused by an angle offset in the measurements, see Figure 49.

Looking at the deep stall part of the curves, it can be observed that The EllipSys code generally predicts C_l max at slightly lower angles compared to the predictions of Xfoil, but that both computer codes predict higher C_l max than the observed values in the experiment. The experiment was performed for a relatively narrow airfoil section with a ratio of span divided by the chord of only 1.5. The present author has not been able to verify that any boundary layer control (suction/blowing) is applied at the side faces of the LTPT to minimize eventual effects of the developing boundary layers at the side walls in connection with the fairing of the airfoil section with the tunnel walls. The developing boundary layer at the side walls may, especially at high angles of attack, play an important role in the exact development of the stall of the airfoil, introducing highly three-dimensional flow patterns near the fairings with the walls. Another direct indication that the stalling characteristics are not necessarily very accurate can be deduced by comparing the lift at positive and negative angles of attack for a symmetric airfoil, as reported by Timmer [19]. When comparing the negative and positive lift values for the NACA64-018 symmetric airfoil, Timmer demonstrates that the max lift varies around 7%, and attributes this to inaccuracies in the airfoil geometry and angle of attack setting mechanism. For the asymmetrical airfoils, no such simple test can be performed, but similar deviations may be expected.

Comparing the pressure coefficients C_p computed with EllipSys and the Xfoil code, excellent agreement is observed between -6 and 6 degrees, for all four airfoils, see Figures 50 to 53. Looking at the skin friction, the general trend is that the EllipSys code predicts transition slightly aft of the prediction by the Xfoil code in regions of accelerating flow as observed in the leading edge region on the suction side. The EllipSys code predicts the transition location slightly upstream of the location predicted by the Xfoil code in the decelerating regions at the aft part of the suctions and pressure side of the airfoil. This could suggest that the empirical expressions for determining the transition location is to sensitive too the acceleration parameters or pressure gradients, at least compared to the Xfoil model.

The performance of the Xfoil code is well known, and along with previous work the present work indicates that the EllipSys CFD code produces the same level of accuracy. In contrast to the Xfoil code, a general purpose CFD solver can be used both for 2D and full 3D computations. A general CFD solver can be used in both steady and unsteady mode. Finally, a CFD code allows any type of geometry to be investigated, from cylinders, flat-back airfoils, to geometries with dynamic actuators such as micro-taps and flaps. Based on this, a CFD solver is a very general tool, for investigating different aerodynamic aspects of relevance for wind turbine applications, with an accuracy comparable to the accuracy of the 2D steady Xfoil code.

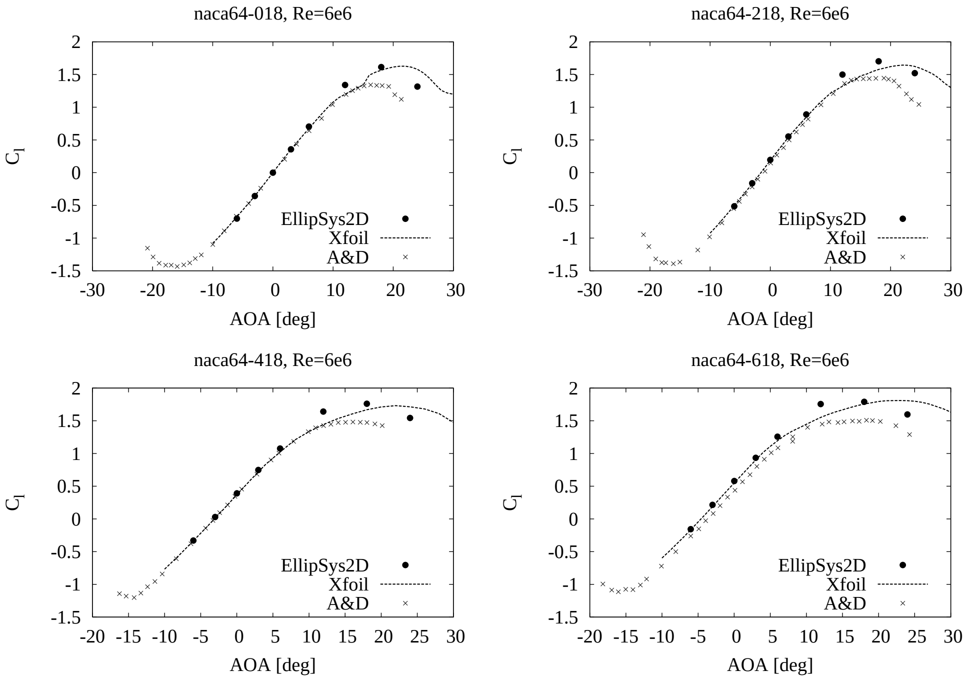

Figure 48. Computed lift for the four NACA64-x18 airfoils.

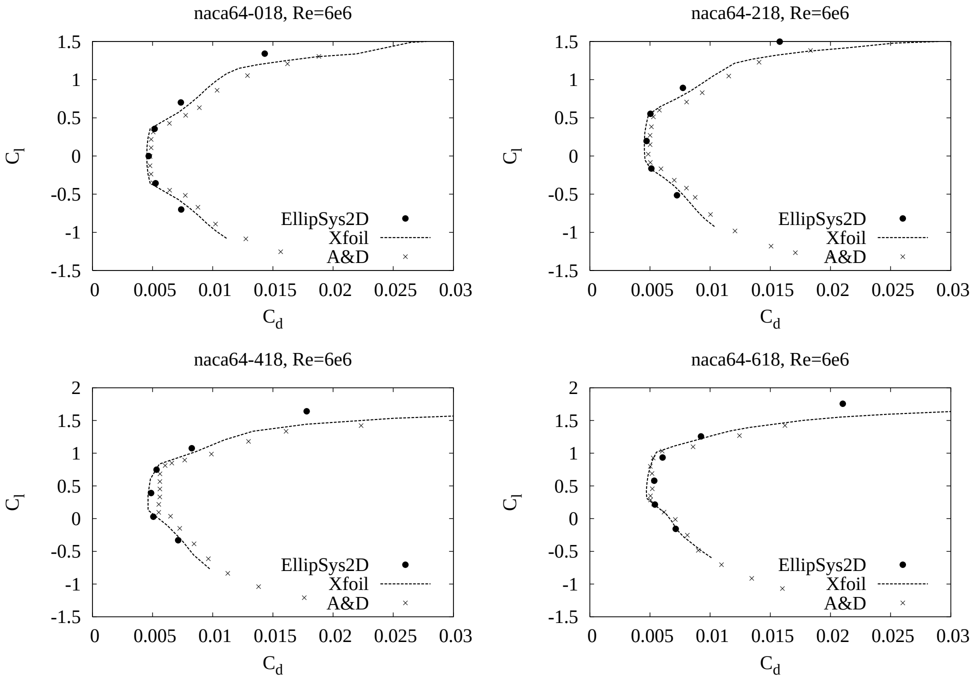

Figure 49. Computed lift/drag for the four NACA64-x18 airfoils.

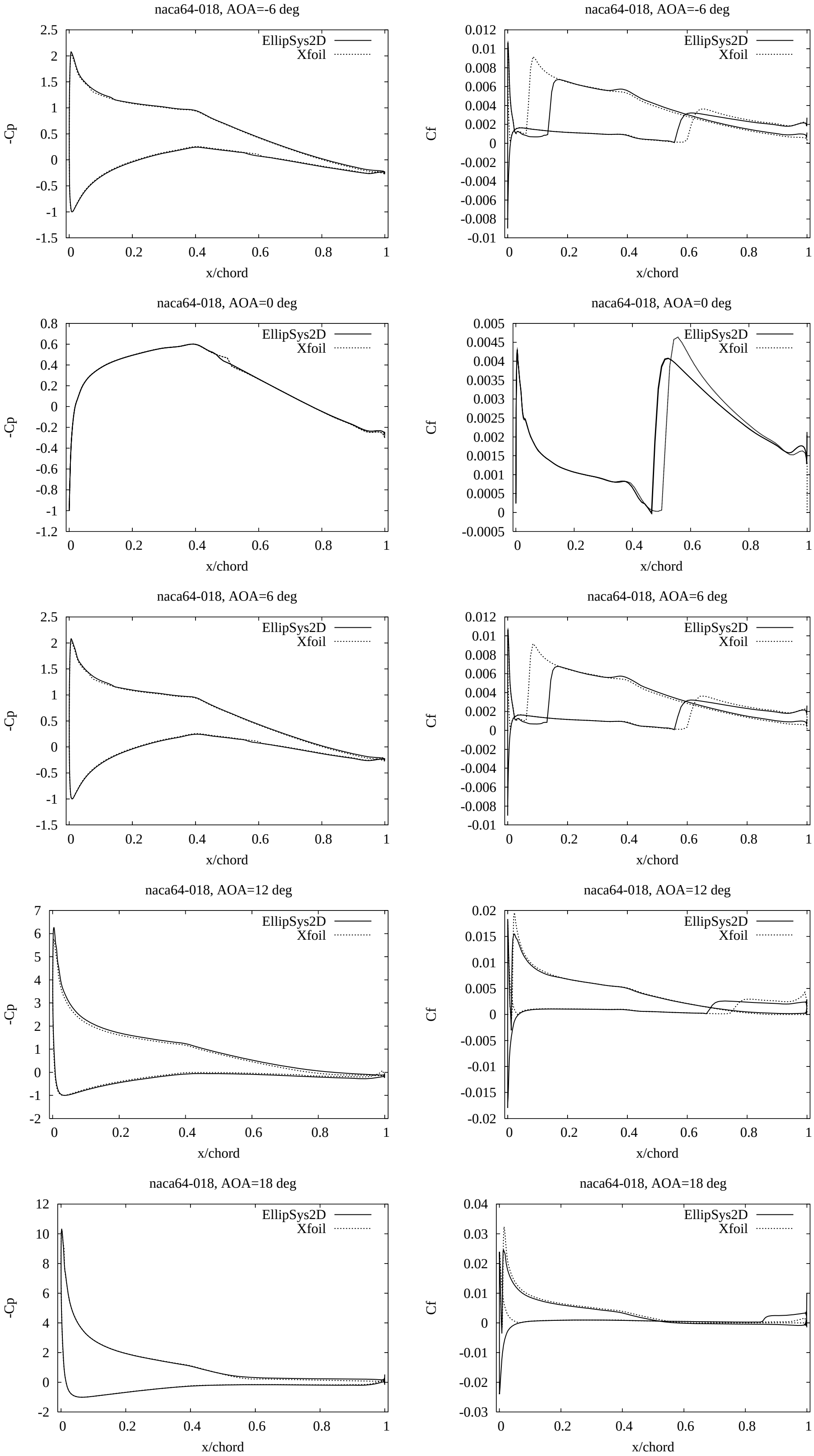

Figure 50. C_p and C_f distributions for the NACA64-018 airfoil.

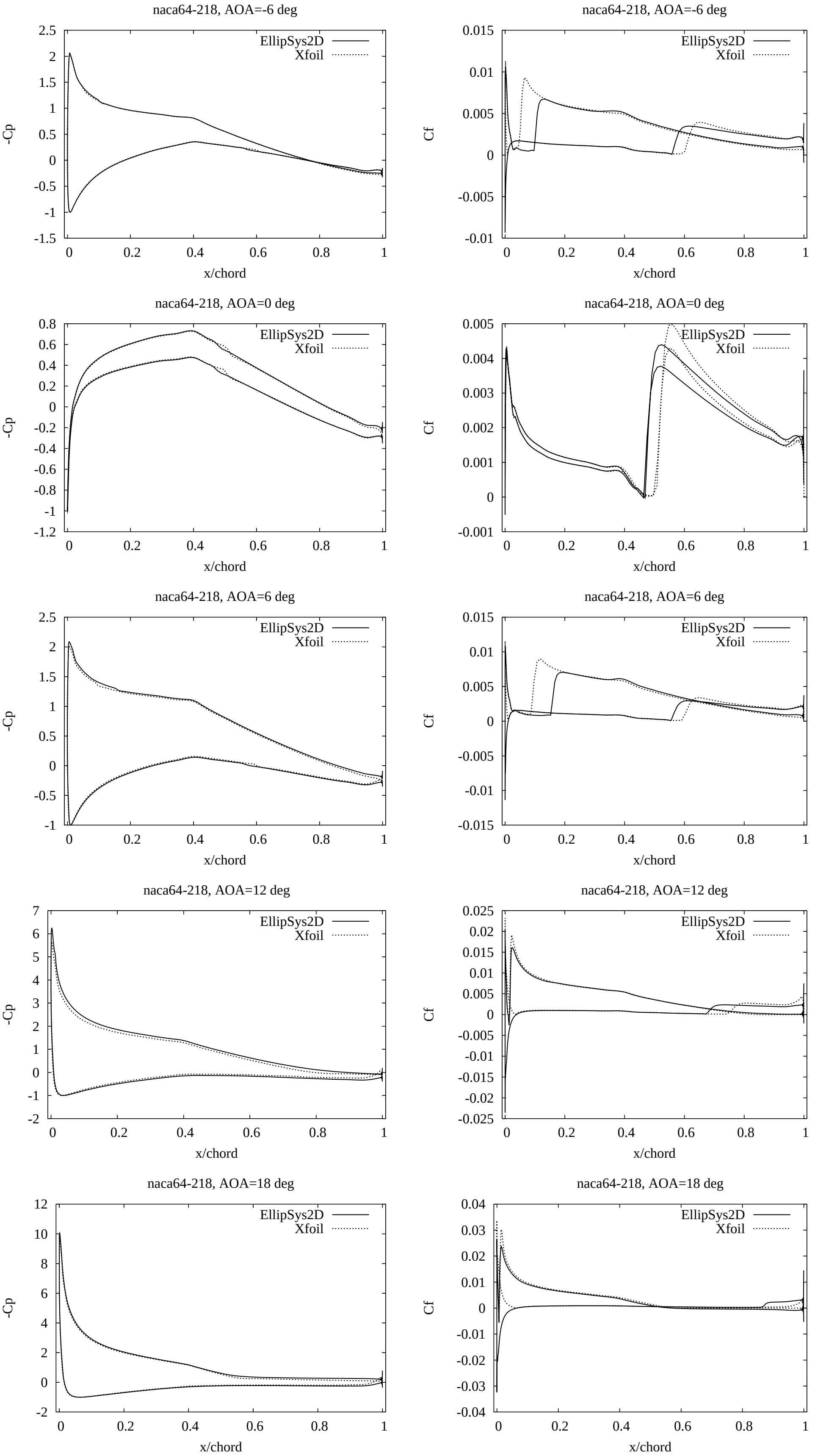

Figure 51. C_p and C_f distributions for the NACA64-218 airfoil.

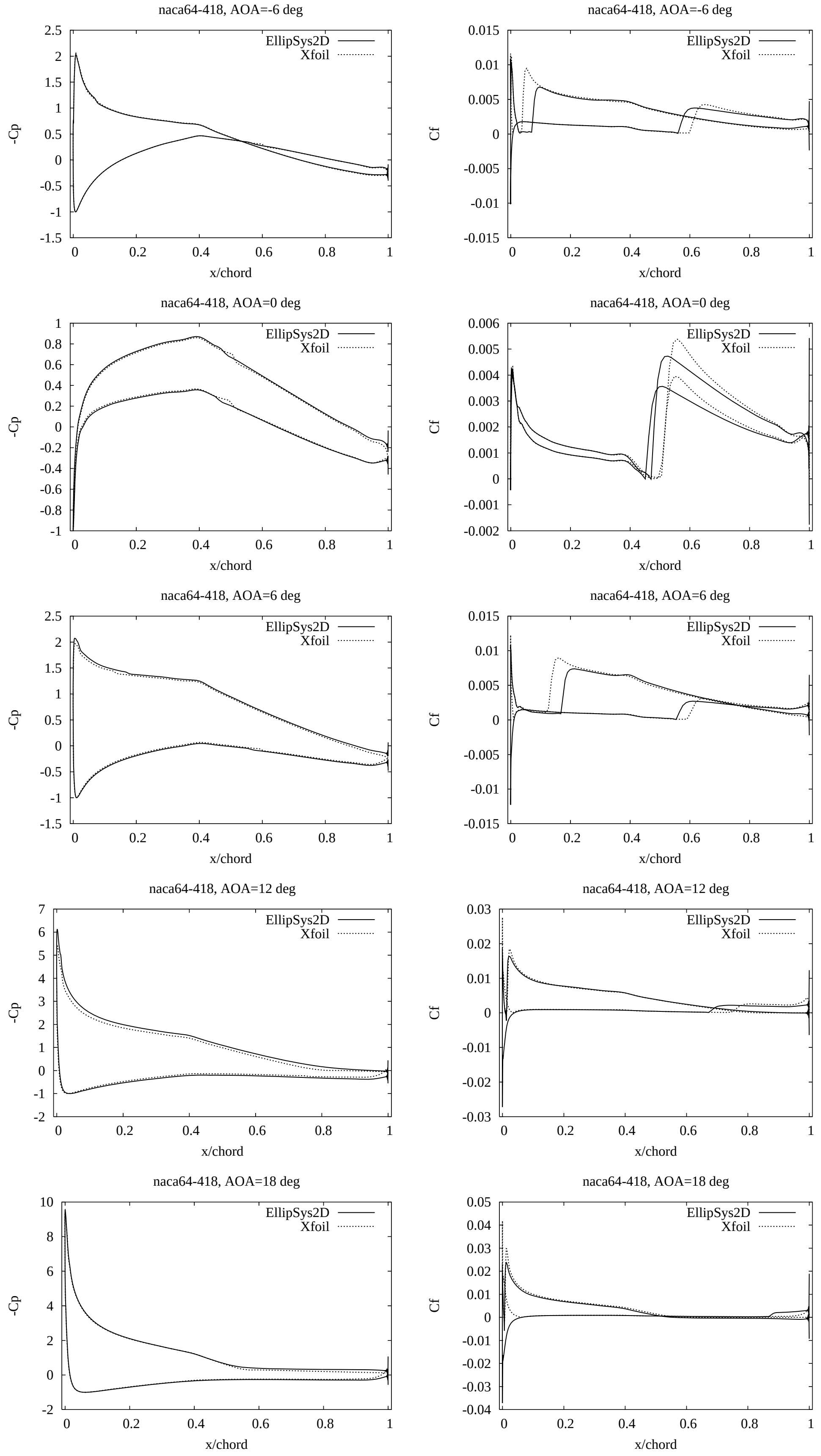

Figure 52. C_p and C_f distributions for the NACA64-418 airfoil.

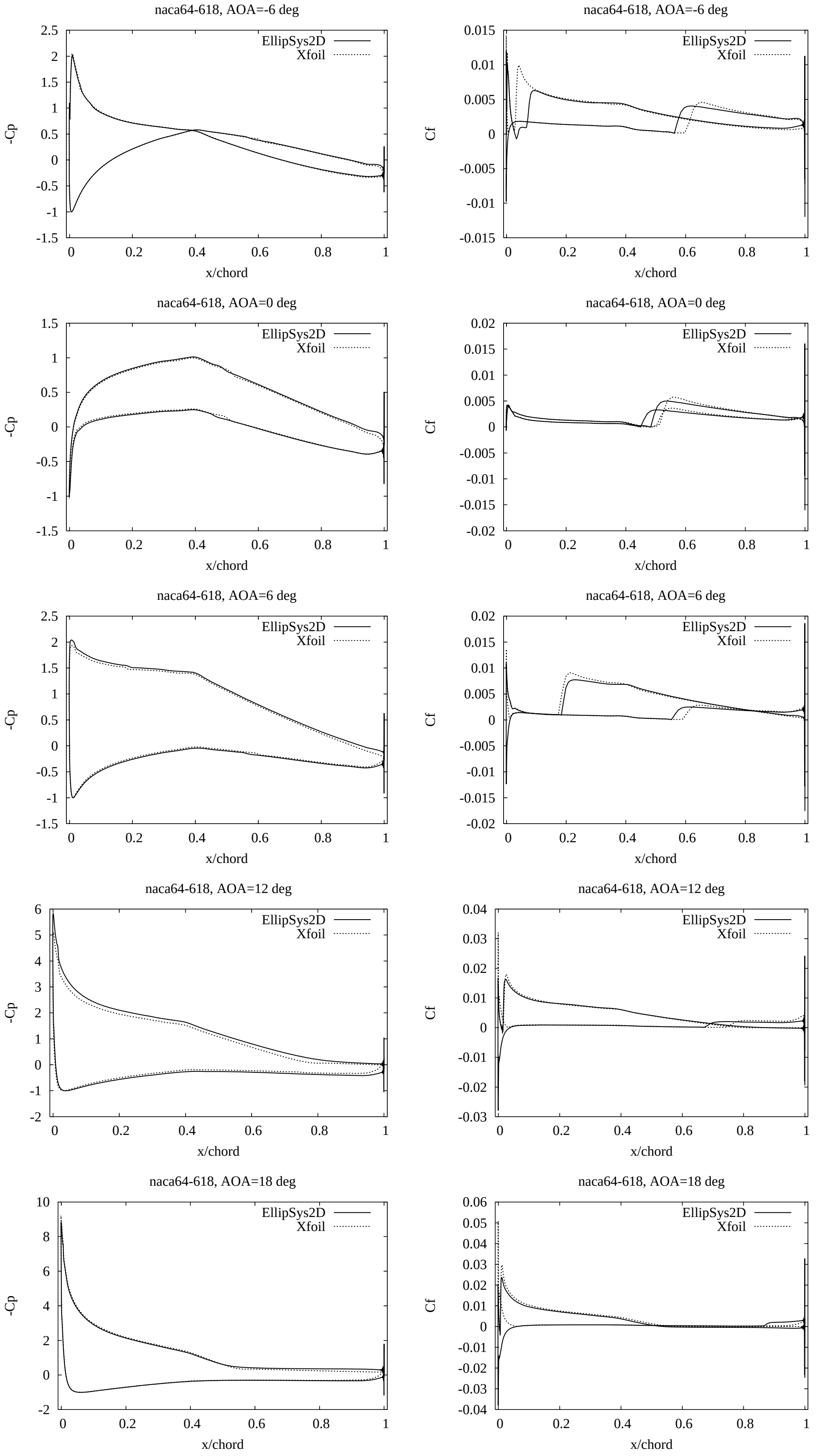

Figure 53. C_p and C_f distributions for the NACA64-618 airfoil.

5.4.1 Conclusion; Airfoil Computations

Looking at the computed lift and drag a very good agreement is observed between measurements, Xfoil computations and predictions by the EllipSys code for low angles of attack between -6 and 6 degrees for all airfoils, with the exception of the NACA64-618 airfoil. As also reported by Timmer, there seems to be an angle offset in the measurements for this case supported by the present study by the good agreement between the EllipSys and Xfoil results. Looking at the lift/drag curves similarly good agreement is observed, especially at the low lift values. For the lift/drag curves the good agreement with the measured values support the assumption that the offset observed for the lift as function of angle of attack for the NACA64-618 is caused by an angle offset in the measurements. The performance of the Xfoil code is well known, and along with previous work the present work indicates that the EllipSys CFD code produces the same level of accuracy. With the additional possibilities of a general purpose 3D steady/unsteady CFD solver, a versatile tool for investigating different aspects of wind turbine aerodynamics is available.

5.5 3D Cylinder Computations

Based on the good agreement observed in two dimensions, the challenging case of flow over the cylinder covering the full range from laminar flow at low Reynolds numbers to transitional flow at high Reynolds numbers is investigated. The case is chosen to show how the transition model can account both for the pure laminar flow at low Reynolds numbers and the complex physics taking place around the drag crisis at the critical Reynolds number of the cylinder. From a practical point of view, the circular cylinder is often used on the inboard part of many modern wind turbine blades as well as for typical turbine towers.

The computations are performed at a time step of $\Delta t \cdot U/c = 0.01$ using four sub-iterations and the PISO algorithm. Typical computing times for the 8.4 million grid points are approximately 16 seconds per time-step using 32 Dell PowerEdge 750 one processor machines, based on Intel Pentium 4 (Prescott) 3.2 GHz processors with 1 MB cache. Each machine has 2GB of memory, the interconnect is based on Gigabit Ethernet network. To obtain reliable statistics the computations were typically performed for at least 200 to 300 $\times U/D$, requiring around a week of computations on a 32 processors.

A typical time trace of the drag force is shown in Figure 54, where a strong variation of the drag at the startup of the computations is observed, and the more stochastic behavior in the 'periodic' state. To obtain reliable drag estimates, typically the first 50 dimensionless times are discarded and only the remaining part of the time series is used for analysis. This practice is used both in connection with the spectral analysis of the results as well as for determining the mean values.

Comparing the computed drag ($\frac{F_D}{0.5\rho U^2}$) as function of Reynolds Number with measured values [20], an improved agreement around the drag crisis is observed, see Figure 55, where the transitional computations predict the increase of the drag in the region of Reynolds number from 1×10^4 to 2×10^5 observed in the measurements. The fully turbulent computations, in contrast, predict a gradual decrease of drag underestimating the drag more than 30 % in this region. Additionally, using the transition model the flow around the cylinder can be predicted with the same computational settings from a Reynolds number of 10 to 1×10^6 without any changes, with excellent results.

The Strouhal number ($\frac{fD}{U}$) is determined from the power spectrum of the normal force, and an example of a power spectrum for a Reynolds number of 1×10^4 is shown in Figure 56. The power spectrum indicates that the Strouhal frequency is clearly defined and most energy is concentrated at this frequency. Looking at the variation of the Strouhal number as function of Reynolds number shown in Table 10 and Figure 57, the typically reported value of 0.2 is found for the lower range of Reynolds numbers below $Re = 1 \times 10^5$. In the range between

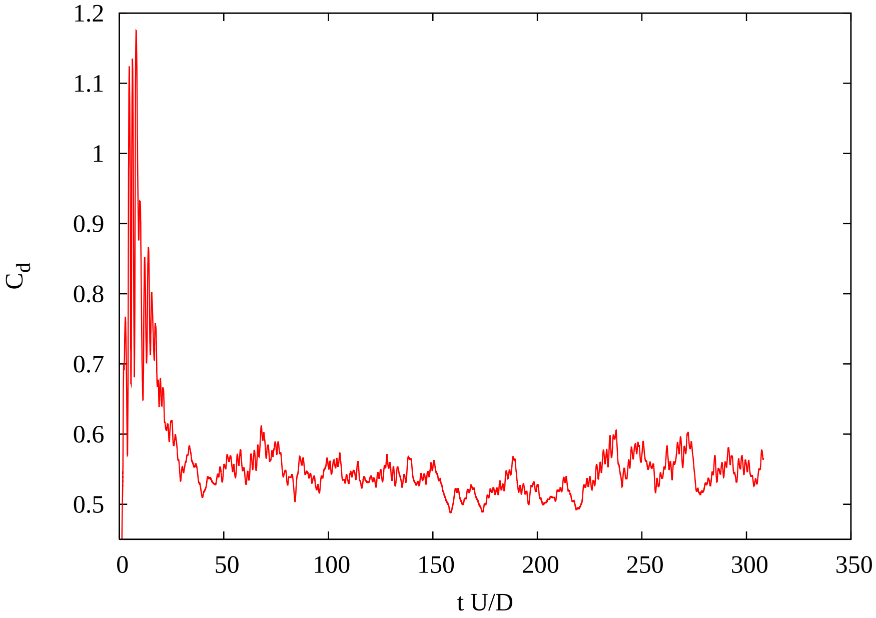

Figure 54. The time history of the drag force for the case of a Reynolds number of 5×10^5*, showing the strong transient at the impulsive startup and the stochastic behavior in the 'periodic' state.*

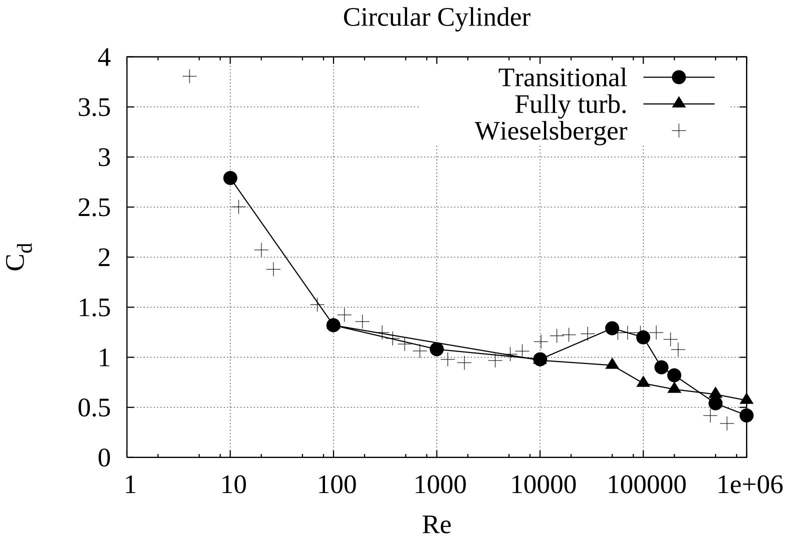

Figure 55. Comparison of computed drag force for the fully turbulent and the transitional computations with the measurements.

$Re = 1 \times 10^5$ to $Re = 1 \times 10^6$ the computations predict an increase of the Strouhal frequency, not normally discussed, but in fair agreement with several references [21–23]. In this range the Strouhal frequency increase more than 60%, which for some applications may be of importance.

Observing the development of the limiting streamlines at the surface of the cylinder and the movement of the laminar to turbulent transition, insight about the actual physical process can be obtained. For the lowest Reynolds number computed, a steady solution without spanwise variation is obtained, with a small separation bubble at the aft part of the cylinder. Increasing the Reynolds number to 100, a periodic solution with vortex shedding is obtained, still with

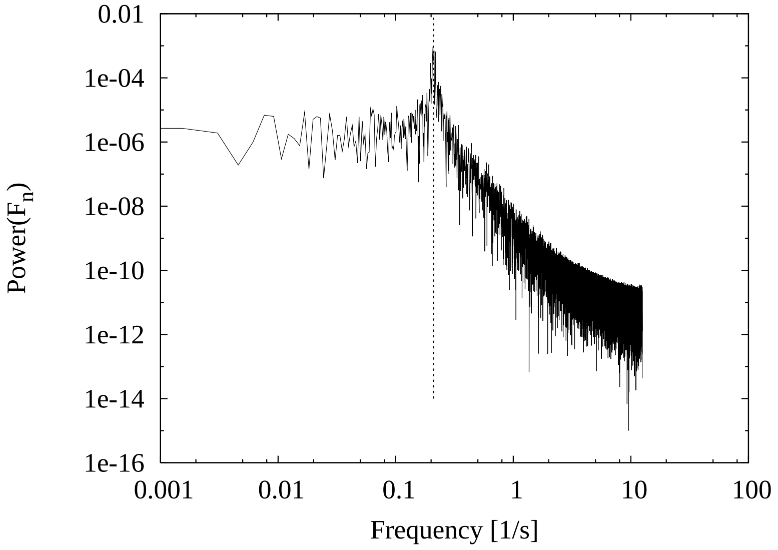

Figure 56. Identification of the Strouhal number for the Re=10000 case, using the power spectrum.

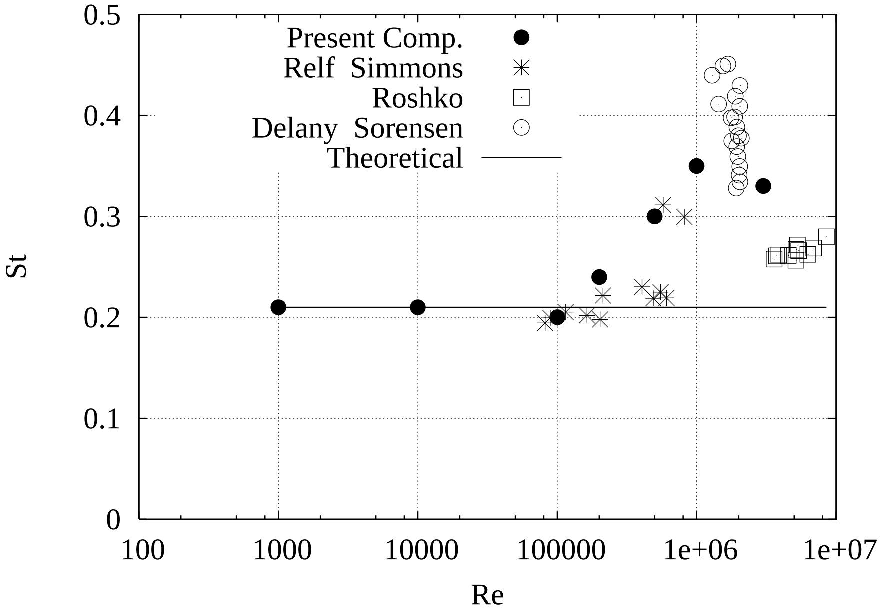

Figure 57. Variation of Strouhal number with with Reynolds number.

zero spanwise variation. For a Reynolds number of 1×10^3, the wake is starting to be turbulent, and the flow is no longer fully correlated along the span of the cylinder. For a Reynolds number around 1×10^4, Figure 58, the flow is laminar over the front part of the cylinder in good agreement with observations from experiments, and separates around 80 degrees and definitely before 90 degrees. At these high Reynolds numbers the wake becomes fully turbulent. A similar picture is observed at a Reynolds number of 2×10^5, but here the transition point is moving upstream closer to the separation line. For a Reynolds number of 5×10^5 the transition process takes place immediately after the laminar separation, forcing the flow to reattach as turbulent flow, followed by turbulent separation further downstream. For the highest Reynolds number shown in Figure 58, the laminar separation immediately reattaches as turbulent flow, followed by a substantial region of attached flow before the flow finally has turbulent separation further downstream. The mechanism controlling the development of the drag crisis is clearly connected to the laminar turbulent transition process, interacting with the separation process and narrowing of the wake by delaying the separation as seen from the visualizations in Figure 59.

Even though the overall behavior is the same for different experiments, there is a wide spread in the details of the flow, as shown by Achenbach [24] for the drag variation. These differences are caused by variation in the inflow turbulence, the surface roughness, and the aspect ratio of the cylinder among other parameters. Therefor exact agreement should not be expected between computations and measurements either.

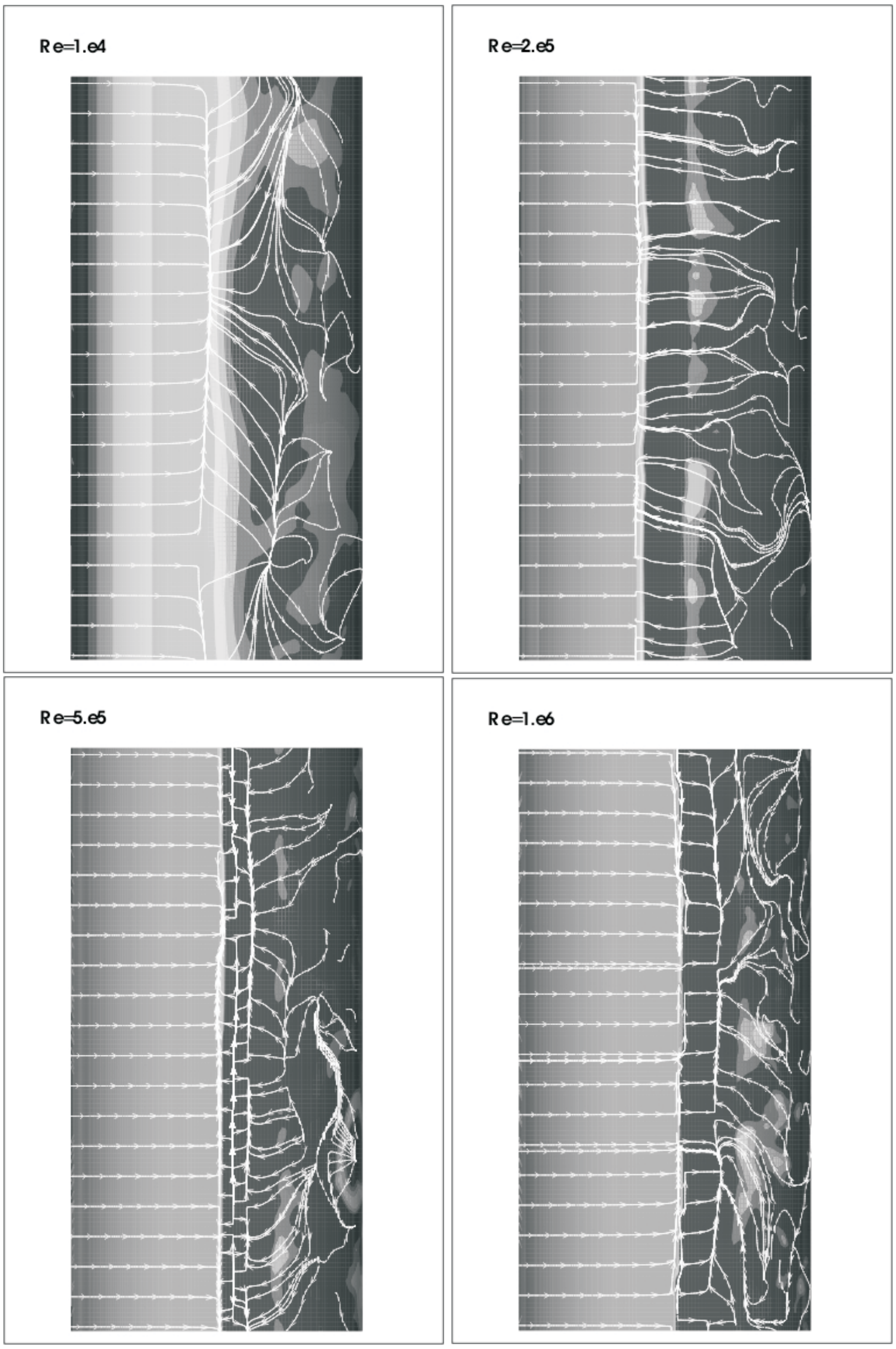

Figure 58. Instantaneous limiting streamlines on the surface of the cylinder for four cases of the simulations for transitional flow.

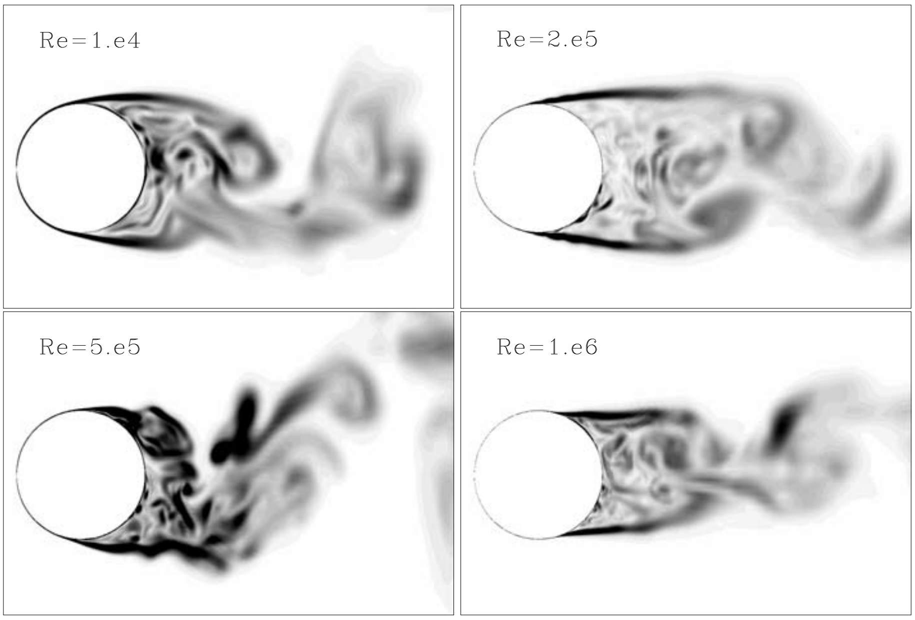

Figure 59. Representative snapshots of the absolute value of the vorticity behind the cylinder at four different Reynolds numbers, showing the narrowing of the wake with increasing Reynolds number.

Table 10. The Strouhal number ($\frac{f \cdot D}{U}$) as function of Reynolds number.

Re	1×10^3	1×10^4	1×10^5	2×10^5	5×10^5	1×10^6
St	0.21	0.21	0.20	0.24	0.30	0.35

5.5.1 Discussion of Cylinder Results

Generally, the code is capable of predicting the flow from the laminar region at a Reynolds number of 10 to fully turbulent/transitional flow at a Reynolds Number above one million. The use of the combined DES/transitional methodology improves the prediction of the drag crisis on the cylinder compared to pure DES simulation. Additionally, the DES/transitional methodology predicts the correct flow phenomena, with laminar separation, turbulent reattachment followed by turbulent separation along with backward shift of the separation point and the narrowing of the cylinder wake with increasing Reynolds number. All cylinder computations presented here are computed by the DES technique. It has afterwards been verified that recomputing these with DDES (shielding the boundary layer from LES) the results are not influenced by the MSD that was later observed for the DU-96-W-351 airfoil described next.

5.6 Flow over a thick airfoil

Next, the method is applied to predicting the flow over the DU-96-W-351 airfoil, that has a thickness of 35% chord. Similar to the cylinder case, the separation of the flow over an airfoil is controlled by the momentum in the boundary layer flow and the skin friction distribution. With the good agreement obtained for the cylinder, it is of interest to investigate whether the transition/DES methodology can perform equally well for airfoil stall. As already addressed by Roshko [23], typical wall corrections used in wind tunnel experiments do not account for possible interference effects connected to flow separation which may be problematic for cases with a high degree of separation. Limited aspect ratio of two to four are often used in wind tunnels in connection with testing of airfoil sections due to the desire to obtain a high Reynolds number. When focusing on deep stall aerodynamics, this may work against the desire to limit the effects of the tunnel wall on the separation. The present data are kindly provided by LM Glasfiber, showing the stalling behavior of a thick DU-96 airfoil in the LM Glasfiber tunnel having a span to chord ratio of 1.5.

Using the previously described computational mesh, the flow over the DU-96-W-351 airfoil was computed at a Reynolds Number of 3 million, with an aspect ratio (chord/span) of two using periodic conditions in the spanwise direction. Different values of inflow turbulence was investigated [0.05%, 0.10% and 0.15%], in order to judge the importance of this parameter. A typical time trace of the lift coefficient is shown for the 15 degree angle of attack case for a period of $\tilde{4}00$ dimensionless times, see Figure 60. For an airfoil with a chord of 0.9 meter and a velocity of 80m/s this would correspond to approximately 1.8 seconds; Eqn. 6. Considering the highly unsteady signal, this must be considered a short averaging period, which will be reflected in the averaged pressure curves which do not fully collapse to a single curve for each considered case. The first series of computations were performed with the standard DES methodology, but these results showed a high dependency on the level of inflow turbulence, even at low angles of attack. This was identified as grid induced separation or MSD, and the application of the DDES methodology seems to alleviate this problem.

$$t^* = \frac{Chord}{Velocity} \tag{6}$$

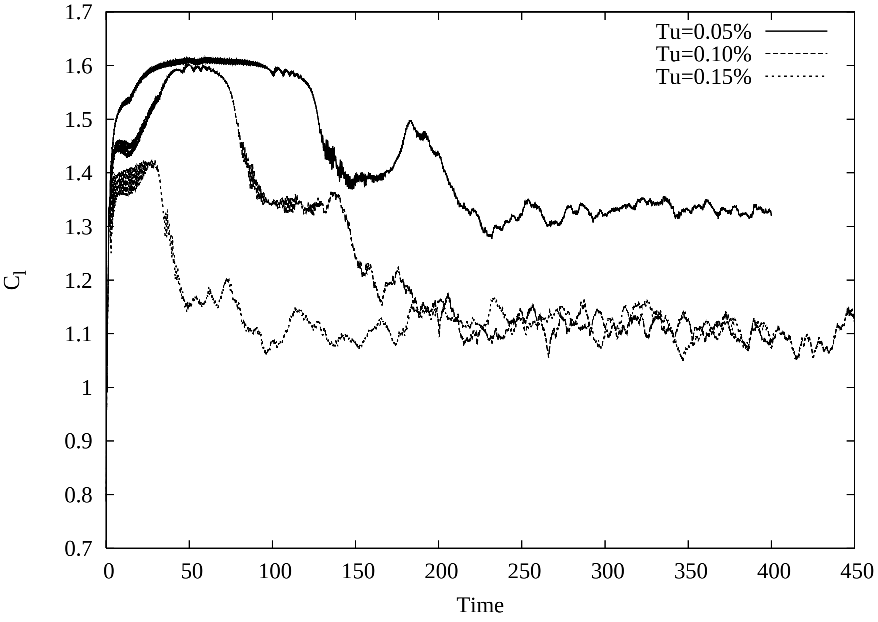

Figure 60. Time trace of computed normal force from a simulation at 15 degrees angle of attack for three different inflow turbulence intensities.

Comparing the averaged lift and drag computed using the different turbulence intensities the following can be observed: At 10 degrees and below, the influence of the turbulence intensity is very limited. Right around the abrupt stall at 15 degrees, the computed results exhibit a large dependency on the inflow turbulence, showing a variation of nearly 20%, see Figure 61 and 62. The turbulence intensity in the LM tunnel is reported to be around 0.1%, but even small variations around this value in the computations give rather high variation right at stall. Comparing the computed 3D results using the Transition/DES methodology with measurements and standard 2D RANS transitional computations, we observe an increased accuracy of the 3D simulations.

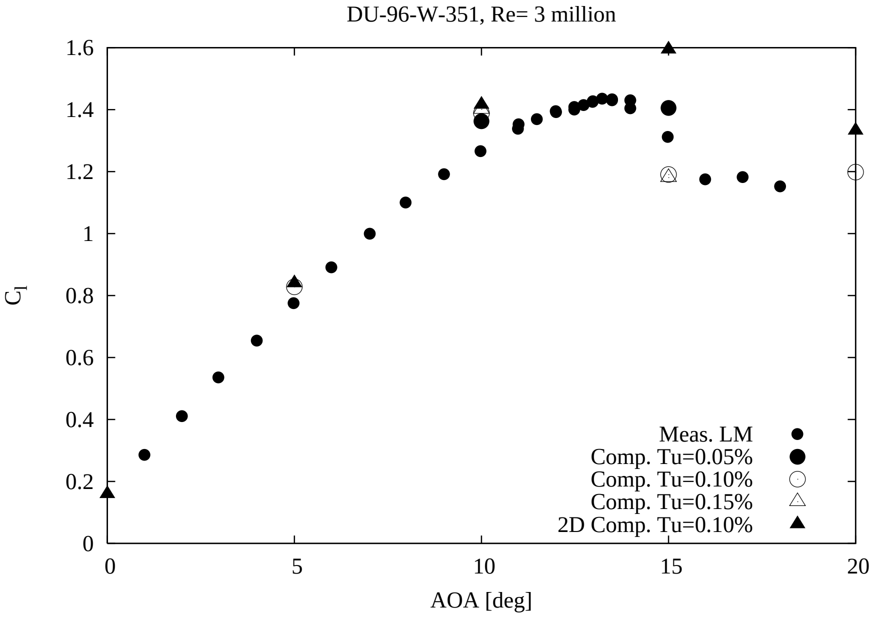

Figure 61. Comparison between computed lift at various turbulence intensities and measured values from the LM tunnel.

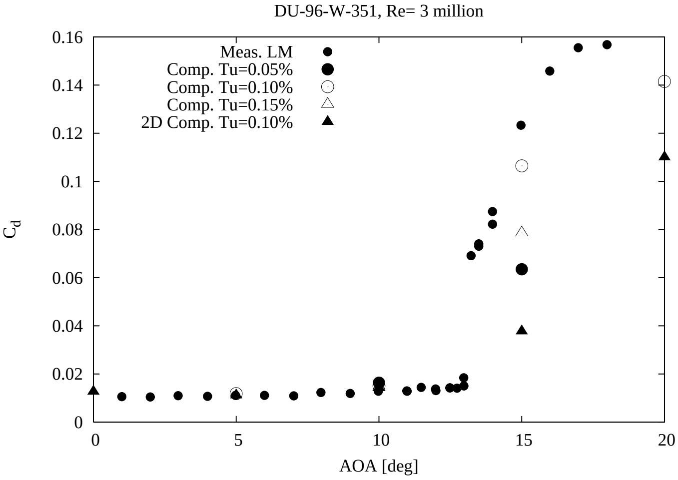

Figure 62. Comparison between computed drag at various turbulence intensities and measured values from the LM tunnel.

Similar to the case of flow over a cylinder, the stalling characteristics of the thick DU-96-W-351 airfoil is controlled by a balance between the momentum of the boundary layer flow and skin-friction at the wall. As a shift from laminar to turbulent flow will change the skin friction from a low to a high value, large changes in the separation pattern will result. The influence of the change to the inflow turbulence is clearly observed in Figure 64, where the best agreement is shown for a turbulence intensity of 0.1%.

Similar to the cylinder analysis, the power spectrum of the tangential force for the DU-96-W-351 airfoil is analyzed to determine the Strouhal frequency of most energetic variations, performed for the case of 45 degrees angle of attack. As seen from Figures 56 and 65, the airfoil spectrum deviates from the cylinder spectrum in that high energy exists on frequencies lower than the shedding frequency. The Strouhal frequency can still be clearly identified at a frequency of 0.25 based on the airfoil chord. An alternative choice may be the projection of the

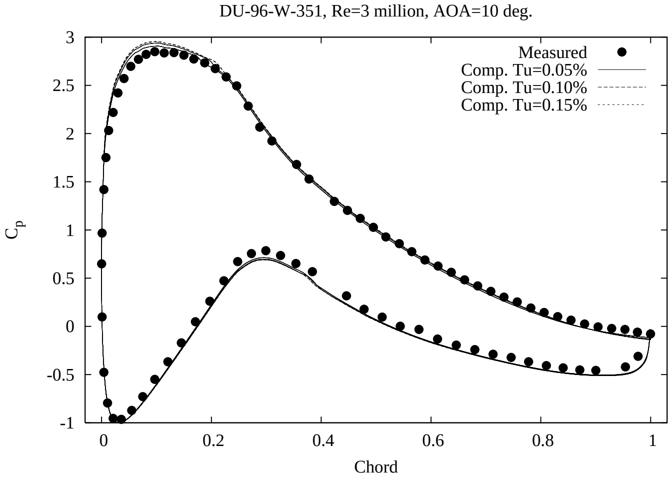

Figure 63. Pressure distribution around the DU-96-W-351 airfoil, comparison between computed values and measured distribution at 10 degrees.

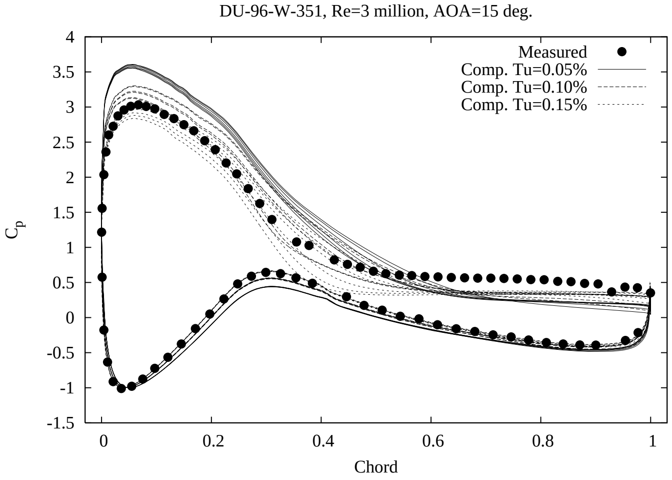

Figure 64. Comparison of pressure distributions around the DU-96-W-351 airfoil at 15 degrees for three different turbulence intensities. Averages at six spanwise positions are shown for each computation.

chord on the direction perpendicular to the flow direction which would lower the frequency to around 71 percent of the previously mentioned value.

5.7 Discussion of Airfoil Results

In the present work, computations of the flow over the DU-96-W-351, 35% thick airfoil in the region of stalled flow have been compared to measurements from the LM tunnel. In the computations the airfoil section is modeled with an extent of two chords in the spanwise direction and the use of periodic conditions. This is done to limit the number of cells needed to model the actual configuration, where the airfoil section is enclosed by walls. Alternatively, symmetry conditions could be used at the two spanwise boundaries of the domain. This would prevent flow over these boundaries limiting the size of the turbulent structures in the separated area. This could be the focus of further work, along with efforts to actually resolve the wind tunnel walls. The problem of the wind tunnel corrections, that do not account for the interaction of the separation and the wall effects would additionally require further studies. The results

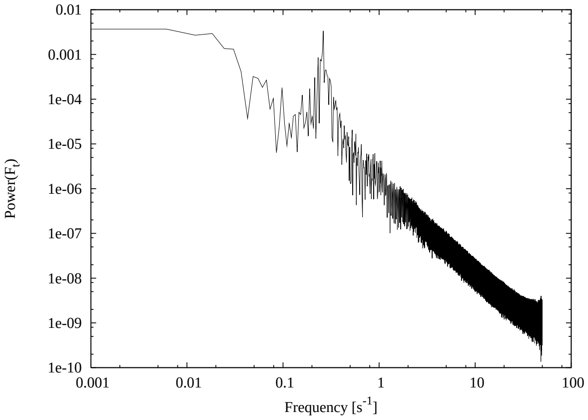

Figure 65. Power spectrum of the tangential force for the DU-96-W-351 airfoil at 45 degrees angle of attack, a clear Strouhal frequncy of 0.26 Hz is visible.

show an improved agreement with the measured data, compared to 2D computations. Whether this increased accuracy will justify the much higher increase in computational requirements will depend on the application. The computing time increases from a few minutes for a 2D computations to several days for the 3D DES computations.

5.8 Acknowledgement

The work was funded by the Danish Energy Agency under contract ENS-33033-0055, Computations were made possible by the use of the MARY and Thyra PC-cluster at Risø National Laboratory and the DCSC, PC-cluster Yggdrasil and Alfheim. Measurement for the DU-96-W-351 airfoil along with the airfoil contour was kindly provided by LM Glasfiber. Additional funding for the 2D airfoil computations was provided by the European Union under contract SES6 No 019945 The UPWIND project.

References

[1] F. R. Menter, R. B. Langtry, S. R. Likki, Y. B. Suzen, P. G. Huang, and S. Völker. A Correlation-Based Transition Model Using Local Variables, Part I - Model Formulation. In *Proceedings of ASME Turbo Expo 2004, Power for Land, Sea, and Air*, Vienna, Austria, June 14-17 2004. ASME. GT2004-53452.

[2] F. R. Menter, R. B. Langtry, S. R. Likki, Y. B. Suzen, P. G. Huang, and S. Völker. A correlation-based transition model using local variables, part ii - test cases and industrial applications. In *Proceedings of ASME Turbo Expo 2004, Power for Land, Sea, and Air*, Vienna, Austria, June 14-17 2004. ASME. GT2004-53454.

[3] J. A. Michelsen. Basis3D - a Platform for Development of Multiblock PDE Solvers. Technical Report AFM 92-05, Technical University of Denmark, 1992.

[4] J. A. Michelsen. Block structured Multigrid solution of 2D and 3D elliptic PDE's. Technical Report AFM 94-06, Technical University of Denmark, 1994.

[5] N. N. Sørensen. General Purpose Flow Solver Applied to Flow over Hills. Risø-R- 827-(EN), Risø National Laboratory, Roskilde, Denmark, June 1995.

[6] C. M. Rhie. *A numerical study of the flow past an isolated airfoil with separation*. PhD thesis, Univ. of Illinois, Urbana-Champaign, 1981.

[7] S. V. Patankar and D. B. Spalding. A Calculation Prodedure for Heat, Mass and Momentum Transfer in Three-Dimensional Parabolic Flows. *Int. J. Heat Mass Transfer*, 15:1787, 1972.

[8] S. V. Patankar. *Numerical Heat Transfer and Fluid Flow*. Hemisphere Publishing Corporation, 1980. ISBN: 0891165223.

[9] R. I. Issa. Solution of the Implicitly Discretised Fluid Flow Equations by Operator-Splitting. *J. Computational Phys.*, 62:40–65, 1985.

[10] R. I. Issa, A. D. Gosman, and A. P. Watkins. The Computation of Compressible and Incompressible Recirculating Flows by a Non-iterative Implicit Scheme. *J. Computational Phys.*, 62:66–82, 1986.

[11] P. K. Khosla and S. G. Rubin. A diagonally dominant second-order accurate implicit scheme. *Computers Fluids*, 2:207–209, 1974.

[12] F. R. Menter. Zonal Two Equation k-ω Turbulence Models for Aerodynamic Flows. AIAA-paper-932906, 1993.

[13] M. Strelets. Detached Eddy Simulation of Massively Separated Flows. AIAA Paper 2001-0879, Russian Scientific Center "Applied Chemistry" St. Petersburg, 2001.

[14] F.R. Menter and Kuntz M. *The Aerodynamics of Heavy Vehicles: Trucks, Buses, and Trains*, volume 19 of *Lecture Notes in Applied and Computational Mechanics*, chapter Adaptation of Eddy-Viscosity Turbulence Models to Unsteady Separated Flow Behind Vehicles, pages 339–352. Springer, 2004.

[15] N. N. Sørensen. HypGrid2D a 2-D Mesh Generator. Risø-R- 1035-(EN), Risø National Laboratory, Roskilde, Denmark, Feb 1998.

[16] I. H. Abbott and A. E. von Doenhoff. *Theory of Wing Sections*. Dover Publications, Inc., New York, 1959.

[17] M. Drela and M. B. Giles . Viscous-Inviscid Analysis of Transonic and Low Reynolds Number Airfoils. *AIAA Journal*, 25(10):1347–1355, October 1987.

[18] A.E. von Doenhoff and Jr. F.T. Abott. Technical report.

[19] W.A. Timmer. An overview of NACA 6-digit airfoil series characteristics with reference to airfoils for lage wind turbine blades. AIAA Paper 2009-268, 2009.

[20] C. Weiselsberger. New Data on The Laws of Fluid Resistance. AIAA Paper 84, NACA, 1922.

[21] E.F. Relf and L.F.G. Simmons. The frequency of eddies generated by the motion of circular cylinders through a fluid. Rep. and Mem. no. 917, Aero. Res. Counc., Lond., 1924.

[22] N.K. Delany and N.E. Sorensen. Low-speed drag of cylinders of various shapes. Tech. Note 3038, Nat. Adv. Comm. Aero., Wash., 1953. Note 3038.

[23] A. Roshko. On the wake and drag of bluff bodies. *J. Fluid Mech., year = 1961, month = , volume = , number = 10, pages = 345-356, note = ,*.

[24] E. Achenbach. Distribution of local pressure and skin friction around a circular cylinder in cross-flow up to $Re = 5 \times 10^6$. *J. Fluid Mech.*, 34(4):625–639, 1968.

6 Validation of and Airfoil Optimization with Trailing Edge Noise Model

Author: Franck Bertagnolio, Helge Aa. Madsen and Christian Bak - Risø DTU

6.1 Introduction

In order to increase public acceptance of wind turbines, there is a strong need to reduce their noise emission. There is a general agreement that one of the main sources of high-frequency noise from wind turbines originates from the scattering of aerodynamic noise at the trailing edge of the blades.

Various models can be used to predict the acoustic noise radiated from an airfoil trailing edge [1–3]. In the present study, the so-called TNO model [4] based on a solution of the turbulent boundary layer pressure field giving access to the airfoil surface pressure near the trailing edge is considered. Theoretical work synthetized by Blake [5] is used as a foundation to formulate this solution. From there, it is possible to express the acoustic noise scattered by the trailing edge in the far field using a theory originating from the works of Ffwocs-Williams and Hall [6]. It was subsequently improved by various authors as summarized and unified by Howe [7].

As input, the previously mentioned model requires a description of the turbulent boundary layer near the airfoil trailing edge. For example, a panel method coupled to an integral boundary layer formulation as in the software XFOIL [8] can be used. Alternatively, any Computational Fluid Dynamic (CFD) code including a turbulence model for the boundary layer can be considered. In this paper, both XFOIL and CFD calculations will be used for the model validation. However, only XFOIL will be used for airfoil optimization in Section 6.3, since it is considerably less computationally expensive. This is indeed an important issue for airfoil optimization that typically requires a large number of cost function evaluations, each of these usually requiring several flow field calculations.

The aim of this work is two-sided. Firstly, wind tunnel measurements of airfoil surface pressure are used to validate the surface pressure prediction part of the aeroacoustic model. Experiments for which far field noise has been measured are presented as well and sound pressure level spectra are compared with the model results. Secondly, this study is concerned with the optimization of wind turbine airfoils in order to reduce their trailing edge noise emission. The noise model introduced above is implemented in an in-house airfoil design code and noise-optimized airfoil designs subject to various geometric and aerodynamic constraints are proposed. The results of the design process are analyzed.

6.2 Validation of a Trailing Edge Noise Model

In this section, the formulation of the trailing edge noise model that will be used in the remainder of this paper is presented. Measurements are used to validate the two components of the model: pressure spectra on the airfoil surface and far field noise Sound Pressure Levels (SPL).

6.2.1 The TNO Model

This model originally proposed by Parchen [4] is gathering several results from previous studies. These are used to formulate a far field noise SPL expression as a function of turbulent boundary layer characteristic quantities.

In more detail, the first part of the model is based on a formula expressing the contribution of the mean-shear/turbulence interaction in the boundary layer, which relates the turbulent boundary layer characteristic quantities to the fluctuating surface pressure (see Blake [5], Vol.II, pp.513-524). Manipulating the previous formula, Parchen [4] arrived to the following result for the wavenumber-frequency surface pressure spectrum:

$$\Phi_p(k,\omega) = 4\rho_0^2 \frac{k_1^2}{k_1^2+k_3^2} \int_0^{+\infty} L_2(y_2)\,\overline{u_2^2} \left(\frac{\partial U_1}{\partial y_2}(y_2)\right)^2 \Phi_{22}(k) \times \Phi_m(\omega - U_c(y_2)k_1)\, \mathrm{e}^{-2|k|y_2}\, \mathrm{d}y_2 \quad (7)$$

where the subscripts $1,2,3$ denote directions parallel to the airfoil surface in the main flow direction, perpendicular to the surface, and along the trailing edge, respectively, $|k|$ is the norm of the 'surface' wavenumber $k = (k_1, 0, k_3)$, ω is the circular frequency, ρ_0 is the density, L_2 is the vertical integral length that characterizes the vertical extent of the turbulent eddies, $\overline{u_2^2}$ is the vertical velocity Reynolds stress component assumed proportional to the turbulent kinetic energy k_t, U_1 is the streamwise mean velocity (its derivative, the mean shear, actually appears in the integral), Φ_{22} is the spectrum of the vertical velocity fluctuations (modelled using the classical Von Karman theory), Φ_m is the so-called moving axis spectrum that describes how Φ_{22} is distorted by the generation and destruction of eddies during their convection past the trailing edge, and U_c is the convection velocity of these eddies. The various quantities involved in the previous formula can be deduced from the fluid flow solver (such as the velocity profile), or from theoretical results (usually assuming isotropy), or a combination of both. Turbulent kinetic energy is directly available from a CFD code or can be related to the mean shear [9] if using XFOIL. As for the integral length scale, the approach followed by Lutz *et al* [10] is implemented when using CFD, otherwise it is determined using Prandtl theory [9]. The remaining quantities are defined as specified in the model implementation by Moriarty [9]. Note that the surface pressure frequency spectrum is obtained from Eq.(7) by integrating over the whole surface wavenumber space and reads:

$$\Phi_{\mathrm{surf}}(\omega) = \iint_{-\infty}^{\infty} \Phi_p(k,\omega)\, \mathrm{d}k_1 \mathrm{d}k_3 \quad (8)$$

The second part of the model consists in expressing the far field noise as a function of the previous wavenumber-frequency spectrum of the surface pressure fluctuations. Using the formula of Brooks and Hodgson [11], the far field pressure spectrum density can be expressed as an integral of the wall pressure spectrum over the wavenumber component in the flow direction:

$$S(\omega) = \frac{L}{4\pi R^2} \int_{-\infty}^{+\infty} \frac{\omega}{c_0 k_1} \Phi_p(k,\omega)|_{k_3=0}\, \mathrm{d}k_1 \quad (9)$$

where R denotes the distance from the trailing edge to the observer (located 90^o with respect to the main flow direction above the trailing edge), L the span extent of the trailing edge, and c_0 is the speed of sound.

In this section, CFD calculations are performed with the in-house two-dimensional incompressible Navier-Stokes solver EllipSys2D. The $k-\omega$ SST model by Menter [12] is used as a turbulence model. The reader is referred to previous publications for more details about this code [13, 14].

6.2.2 Surface Pressure Validation in LM Wind Tunnel

The NACA0015 was equipped and measured in the LM Glasfiber wind tunnel, which is specifically designed for the aerodynamic testing of wind turbine airfoils. In the absence of turbulence grid (as it is considered herein), a previous study has shown that turbulence intensity in the incoming flow is of the order of 0.1% at all speeds [15]. The airfoil section was instrumented with an array of high-frequency microphones mounted beneath its surface. Only the microphone located the most downstream on the airfoil surface, at a non-dimensionalized distance from the trailing edge equal to $x/C = 0.567$, is considered here.

Measurement results at two inflow velocities, resulting in Reynolds numbers equal to $Re = 1.6 \times 10^6$ and 3×10^6, and at various angles of attack ($\alpha = 0, 4, 8, 12^o$) are presented. These are compared with results obtained with the TNO model using equation (8) and for which the flow

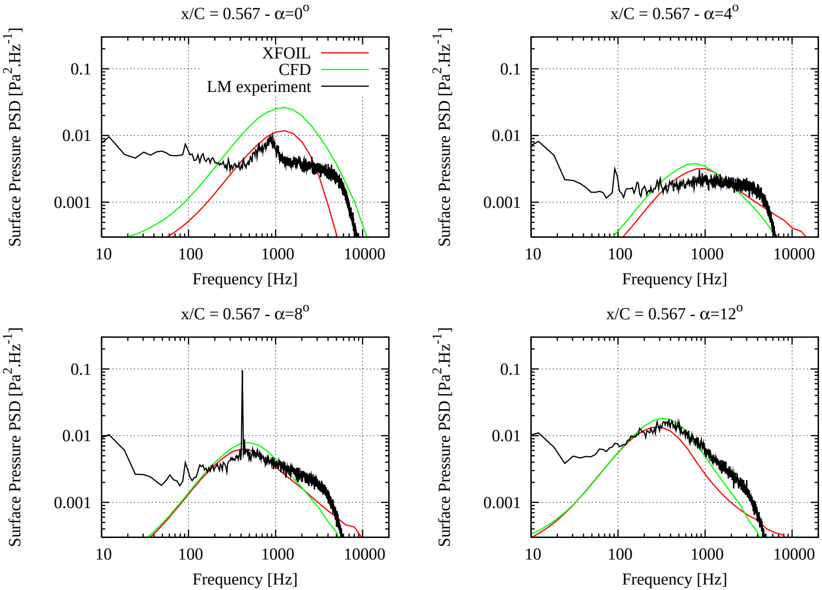

(a) $Re = 1.6 \times 10^6$

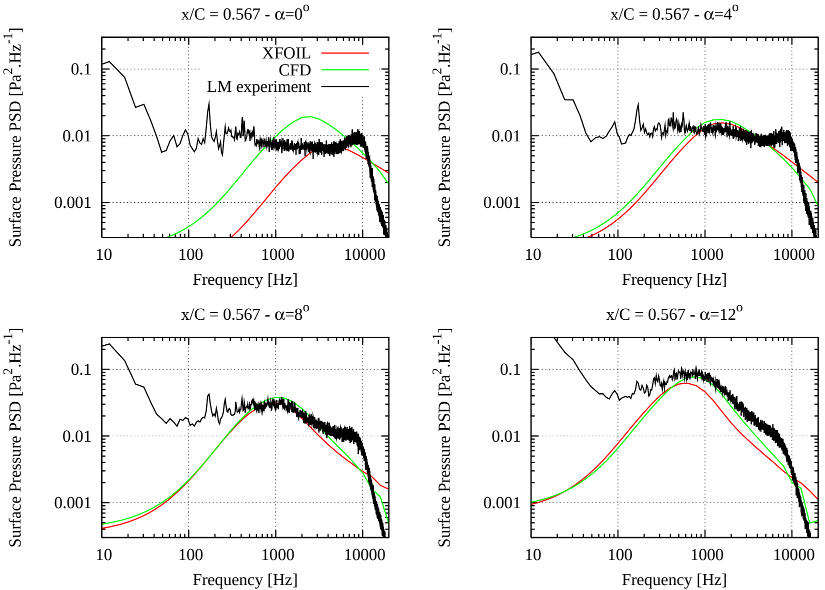

(b) $Re = 3 \times 10^6$

Figure 66. Surface pressure spectra on NACA0015 airfoil at various angles of attack

field is computed either with XFOIL or the CFD code EllipSys2D. Figures 66(a) and (b) show the surface pressure spectra for the two Reynolds numbers, respectively, for increasing angles of attack. It can be seen that for an angle of attack $\alpha = 0^o$, the model results diverge noticeably from measurements. This is due to the fact that the turbulence transition is located immediately upstream of the measurement point $x/C = 0.567$. The assumption of a fully developed turbulent boundary layer does not hold here and this results in a surge of pressure fluctuations in this region. This feature was also observed in experimental data [16]. At higher angles of attack, transition occurs closer to the leading edge and is not felt at the measurement point. Indeed, the numerical results reproduce quite well the increase in power spectral density in the frequency range $300 < f < 9000\,\text{Hz}$ as the angle of attack increases. However, the TNO model does not capture the lower frequency part of the measured spectra. It is probable that these frequencies are dominated by additional sources originating from flow conditions or various perturbating effects (acoustic reflections, etc...) in the wind tunnel, which is not designed for aeroacoustic measurements. In addition, the Von Karman spectrum used in the model is usually a poor

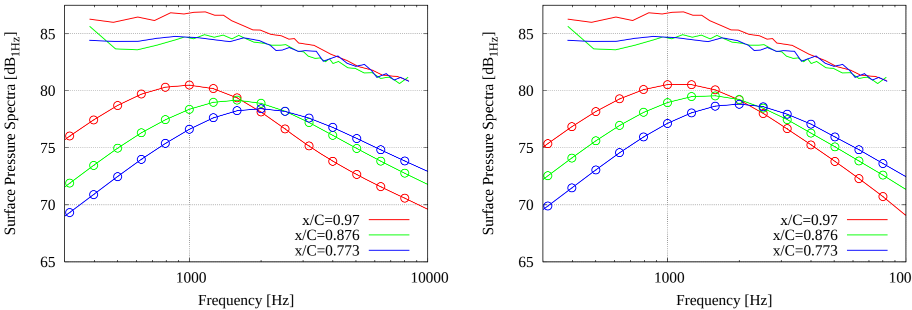

(a) XFOIL Flow Solver (b) CFD Flow Solver

Figure 67. Surface pressure on NACA0012 airfoil (Lines: Experiment [11]; Lines with points: TNO model)

estimation at low frequencies where these particular flow characteristics dominate. It should finally be noted that the CFD flow calculations perform slightly better than XFOIL for higher frequencies.

6.2.3 NACA0012 Airfoil Measurements at NASA Langley

The measurements performed by Brooks and Hodgson [11] in the anechoic quiet flow wind tunnel facility at NASA Langley Research Center are now reported. The considered airfoil is the NACA0012 airfoil section with a sharp trailing edge and a chord $C = 0.6224\,\mathrm{m}$. Inflow velocities are equal to 38.6 and 69.5 m/s resulting in Reynols numbers equal to $Re = 1.6 \times 10^{6}$ and 2.9×10^6. Two angles of attack are considered: $\alpha = 0$ and 5^o.

A series of pressure sensors were mounted on the airfoil surface at various distances from the trailing edge. In addition, microphones located in the plane perpendicular to the midspan section of the airfoil are used to measure the trailing edge far field noise.

Firstly, the measured surface pressure spectra for $Re = 2.9 \times 10^6$ and $\alpha = 0^o$ are compared with TNO model results using XFOIL and EllipSys2D calculations in Figs. 67(a) and (b), respectively. In these figures, three surface pressure sensor locations are considered: $x/C = 0.773, 0.876$ and 0.97. An offset between 5 and 10 dB is observed between the measurements and the model results. Despite checking our method for errors and dimensionalizing factors, there could exist an inconsistency between our formulation and the one used in Brooks and Hodgson [11]. Alternatively, it could be that the TNO model predicts too low pressure values. Nevertheless, an inconsistency in conventions cannot be ruled out since the model results did match quite well measurements in Section 6.2.2. In any case, it can be seen that both flow calculation methods reproduce the same tendencies as the measurement data. Indeed, the pressure spectral density increases as the trailing edge is approached and the peak frequency decreases at the same time.

Secondly, far field SPL are displayed in Figs. 68(a) and (b) for angles of attack $\alpha = 0$ and 5^o, respectively. As previously, an offset in pressure levels is observed. However, taking this offset aside, the measurement data tendencies relative to the varying inflow velocity are well reproduced by the model. The spectrum peak frequency is slightly underestimated by the model in particular for XFOIL calculations at $\alpha = 5^o$.

6.2.4 NACA0012 Airfoil in the Aeroacoustic Windtunnel Braunschweig

The NACA0012 airfoil was also measured in the Aeoroacoustic Windtunnel Braunschweig (AWB) facility at the Institute für Aerodynamik und Strömungstechnik (DLR) [17]. The acoustic measurement device consists of an elliptic mirror system. The considered measurements involve the 0.4 m chord airfoil at zero angle of attack, for wind speeds equal to 40, 50 and 60 m/s.

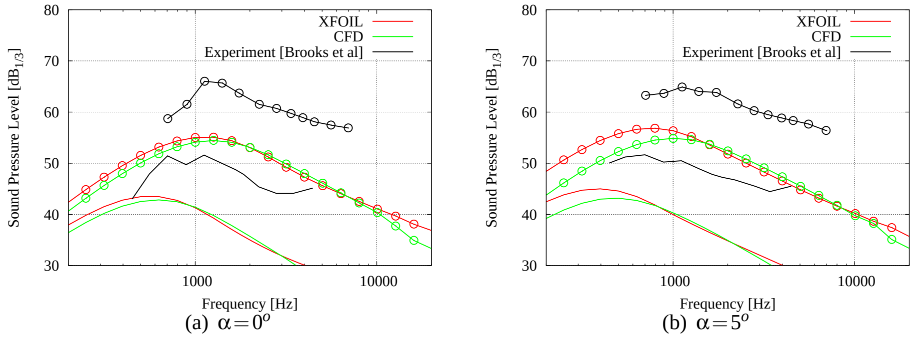

(a) $\alpha = 0^o$ (b) $\alpha = 5^o$

Figure 68. Far field SPL for NACA0012 airfoil (Lines: $U = 38.6\,m/s$; Lines with points: $U = 56.5\,m/s$)

Far field SPL at $\alpha = 0$ are displayed in Figs. 69(a) and (b) using XFOIL and EllipSys2D, respectively. As in the previous section, a similar offset in SPL is observed. Nevertheless, the model reproduces the tendencies of the measurements (increase in SPL and shifting to the right of the spectrum peak frequency) with respect to increasing velocity.

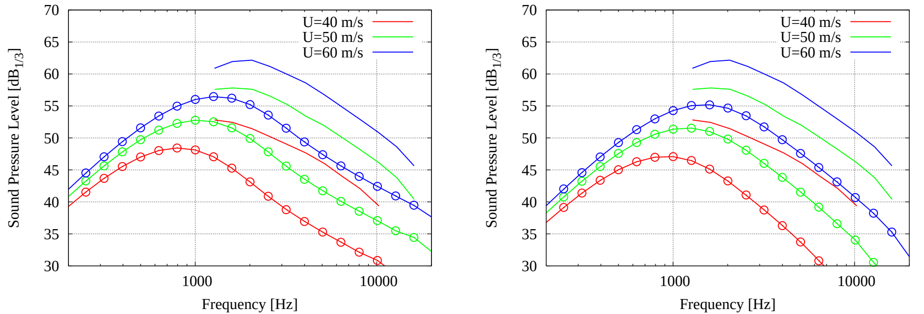

(a) XFOIL Flow Solver (b) CFD Flow Solver

Figure 69. Far field SPL for NACA0012 airfoil (Lines: AWB experiment [17]; Lines with points: TNO model)

6.2.5 Discussion

In this section, various measurements data were compared with the TNO trailing edge noise model using both XFOIL and CFD calculations. In some cases, the quantitative agreement between the experimental data and calculated results was quite poor. In particular, it seems that the TNO model (in the present implementation) in some cases predicts too low pressure levels (both surface pressure and far field SPL) compared to measurements. This was, however, also observed in other studies by various authors [18, 19]. Results obtained with the CFD flow solver proved in most cases to give results slightly closer to experimental data compared to XFOIL calculations.

Nevertheless, all these comparisons indicate that the TNO model is capable of reproducing the tendencies observed in measurements independently of the flow solver. Therefore, this model is a good candidate for implementation in an airfoil design code since optimization algorithms are based on relative improvements from one particular airfoil to the other and not on quantitatively accurate results.

6.3 Airfoils Aeroacoustic Optimization

In this section, the TNO model is implemented into an optimization program that is normally used for airfoil aerodynamic design. Our goal is now to improve the acoustic properties of given airfoils.

6.3.1 The Optimization Program *AirfoilOpt*

The optimization code *AirfoilOpt* is an airfoil/blade section profile design tool that was developed at Risø National Laboratory [20, 21]. It is based on a so-called Sequential Linear Programming technique to reduce a given cost function subject to various constraints. In short, for a given set of design parameters, at each iteration of the numerical procedure the code calculates the local gradients of the cost function associated to each parameter in order to find a new iterate improving the value of the cost function. This cost function can be a linear combination of various geometric (surface curvature, camber, thickness distribution, etc...) or aerodynamic (lift, drag, moment coefficients, lift/drag ratio, transition location, etc...) characteristics of the airfoil section. The aerodynamic data are computed with the airfoil analysis code XFOIL by Drela [8]. In addition, non-linear constraints on the geometric and aerodynamic properties of the airfoil can be enforced during the optimization process. Note that the cost function and constraints may involve aerodynamic characteristics of the airfoil calculated both using fully turbulent flow conditions and transition modelling in the flow solver.

As part of the present work, the original optimization code has been extended by introducing trailing edge noise as a possible component of the cost function or constraints. In this study, the maximum value of the non-filtered far field SPL spectrum across the whole frequency range is used as the cost function. It was found in a preliminary study that A-weighting alters the convergence of the optimization algorithm by smearing out the cost function gradients. Both the pressure and the suction side noise spectra are considered and added to each other. However, only the suction side generated noise will be of interest for the flow conditions that we are interested in.

6.3.2 RISØ-B1-18 Airfoil

The RISØ-B1 airfoil family was designed for use on MW-size wind turbines with variable speed and pitch control [22]. It was designed to have high maximum lift and high design lift and allow a slender flexible blade while maintaining high aerodynamic efficiency. Only the airfoil with 18% thickness-to-chord ratio is considered here.

In this section, the RISØ-B1-18 is considered as the reference airfoil. The airfoil is optimized with a cost function based only on the SPL which is evaluated at the single angle of attack, $\alpha = 6^o$, in the fully turbulent case. Geometric and aerodynamic characteristics of the resulting airfoil are enforced by constraints. It must be noted that for each optimization calculation, the iterative procedure is started from the original reference airfoil. All calculations are pursued until a local optimum for the cost function is reached.

• Preserving Original Constraints

As a first step, a new airfoil is acoustically optimized so that the geometric and aerodynamic design properties of the original RISØ-B1-18 are preserved by using constraints. This set of constraints, referred to as "*All constraints*", involves in particular the airfoil shape and thickness distribution in relation to fabrication constraints, transition location, aerodynamic performance in the linear region, at maximum lift and in deep stall. Those relevant for the present study read:

- Geometric constraints:
  On the suction side: $y_{,xx}(0.4 < x < 0.9) < -0.15$
  $0.28 < x(y_{\max}) < 0.35$
  On the pressure side: $y_{,xx}(0.7 < x < 0.9) > -1.1$
  $0.28 < x(y_{\min}) < 0.35$
- Aerodynamic constraints:
  Maximum lift: $1.825 < C_l(\alpha_0 = 17^o)$
  Lift beyond stall: $1.69 < C_l(\alpha_0 = 22^o)$
  $1.66 < C_l(\alpha_0 = 24^o)$
  $1.63 < C_l(\alpha_0 = 30^o)$

where x denotes the chordwise coordinate non-dimensionalized with the airfoil chord and which origin is at the trailing edge. The airfoil shape is then defined by $y(x)$, the vertical distance to the chord axis. $y_{,xx}$ denotes the curvature, i.e. the second order derivative of the airfoil shape relatively to the chordwise coordinate. $x(y_{\mathrm{min}})$ and $x(y_{\mathrm{max}})$ denote the chordwise locations of the minimum and maximum values of y on the airfoil profile. The lift coefficient C_l is defined as a function of the angle of attack relative to zero-lift α_0. All the previous aerodynamic constraints (except the one concerning transition location) are enforced for fully turbulent flow conditions.

• Relaxed Geometric and Aerodynamic Constraints

The geometric constraints that were enforced above can be relaxed in order to widen the feasible design space and further reduce trailing edge noise. Two designs are proposed. Preserving all the remaining constraints present in the "*All constraints*" design introduced above, the new designs are obtained by modifying only the following aerodynamic related constraints:

- Design "$y_{\mathrm{min,max}}$"
  On the suction side: $0.23 < x(y_{\mathrm{max}}) < 0.40$
  On the pressure side: $0.23 < x(y_{\mathrm{min}}) < 0.40$
- Design "$y_{,xx}$"
  On the suction side: $y_{,xx}(0.4 < x < 0.9) < -0.12$
  On the pressure side: $y_{,xx}(0.7 < x < 0.9) > -1.3$

The results of these design constraints after optimization, namely the airfoil shapes, lift-drag characteristics and SPL spectra, are displayed in Figs. 70(a), 71(a) and 72(a). It can be seen that the largest noise reduction is obtained with the "$y_{\mathrm{min,max}}$" design, yielding also the largest change in airfoil shape. All designs yield similar aerodynamic characteristics.

The aerodynamic constraints are now relaxed. As in the two previous designs, all remaining constraints of the "*All constraints*" design remain unchanged. Two designs are proposed with the following modified constraints:

- Design "C_l *beyond stall*"
  Lift beyond stall: $1.59 < C_l(\alpha_0 = 22^o)$
  $1.56 < C_l(\alpha_0 = 24^o)$
  $1.53 < C_l(\alpha_0 = 30^o)$
- Design "*All* C_l"
  Maximum lift: $1.725 < C_l(\alpha_0 = 17^o)$
  Lift beyond stall: $1.59 < C_l(\alpha_0 = 22^o)$
  $1.56 < C_l(\alpha_0 = 24^o)$
  $1.53 < C_l(\alpha_0 = 30^o)$

Airfoil shapes, lift-drag characteristics and SPL spectra after optimization are displayed in Figs. 70(b), 71(b) and 72(b). All designs yield similar noise reductions and aerodynamic characteristics indicating that lift constraint in deep stall is the main parameter for noise reduction. Indeed, even when relaxed, the maximum lift is not modified.

Note that the RISØ-B1 airfoil series is proprietary and therefore the shapes have been slightly altered in Fig. 70.

• Discussion

In order to get an insight into the design results, quantities relevant for trailing edge noise emission are compared before (i.e. for the RISØ-B1-18 airfoil) and after optimization. The optimized airfoil obtained with the "*All* C_l" set of constraints is considered here.

Fig. 73(a) displays the velocity profiles across the boundary layer at several locations along the airfoil chord, the last one ($x/C = 0.975$) nearest to the trailing edge is used for trailing

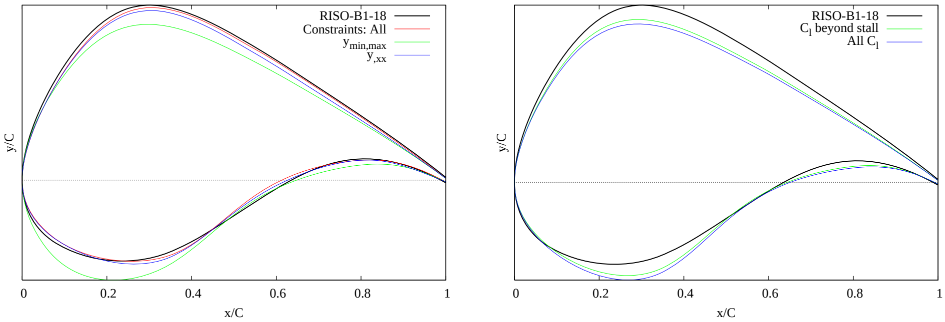

(a) Geometric Constraints (b) Aerodynamic Constraints

Figure 70. Airfoil shapes after optimization (Note: the RISØ-B1 airfoil series is proprietary and therefore the shapes have been slightly altered)

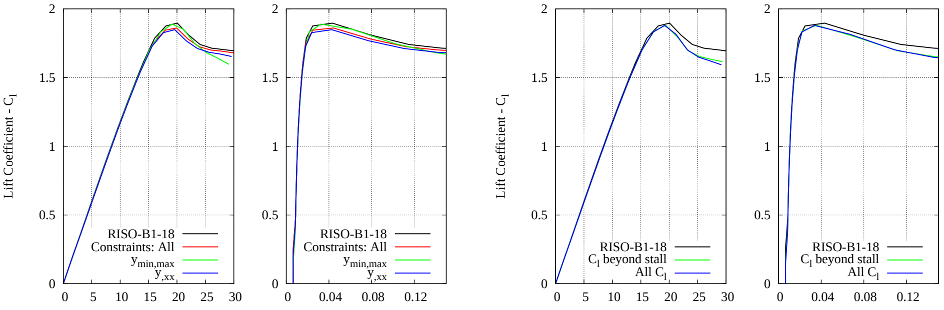

(a) Geometric Constraints (b) Aerodynamic Constraints

Figure 71. Aerodynamic characteristics after optimization (α_0)

edge noise calculation. As it can be observed, the profiles are rather similar before and after optimization. The boundary layer thickness (evaluated by the extent of each curve on the y_2-axis, i.e. the distance to the wall) is neither significantly modified by the optimization procedure. Both boundary layer and momentum thicknesses on the suction side, the latter being more physically characteristic for trailing edge noise [11], along the airfoil chord are plotted in Fig. 73(c). There are again rather small differences between the original and optimized design. As a last comparison, the Turbulent Kinetic Energy (TKE) profiles across the boundary layer are plotted at several chordwise positions in Fig. 73(b). TKE directly relates to trailing edge noise through the vertical velocity turbulent shear stress $\overline{u_2^2}$ in Equation (7). It is clearly observed that the TKE is reduced for the optimized design, in particular near the trailing edge.

In return, the price to pay for the achieved noise reduction is a reduced airfoil camber and increased surface curvature, which resulted in a more abrupt decrease of lift in deep stall.

The reduction in generated noise remains small (1 to 2 dB), but substantial enough to make a difference for wind turbine design. In addition, the A-weighted SPL show a reduction in emitted noise though to a slightly lower level due to the filtering.

Note that the previous study remains quite subjective since different constraints from the original design were relaxed but no consideration about the specific importance of each constraint was taken into account, as well as to which extent each constraint could be relaxed without compromising the structural or aerodynamic properties of the final wind turbine blade.

6.3.3 NACA63-418 Airfoil

The NACA63-418 airfoil is a 18% thick airfoil of the well-known NACA series, and it has been used for the design of various commercial wind turbines.

Similarly to Section 6.3.2, the NACA63-318 is considered as the reference airfoil. The airfoil

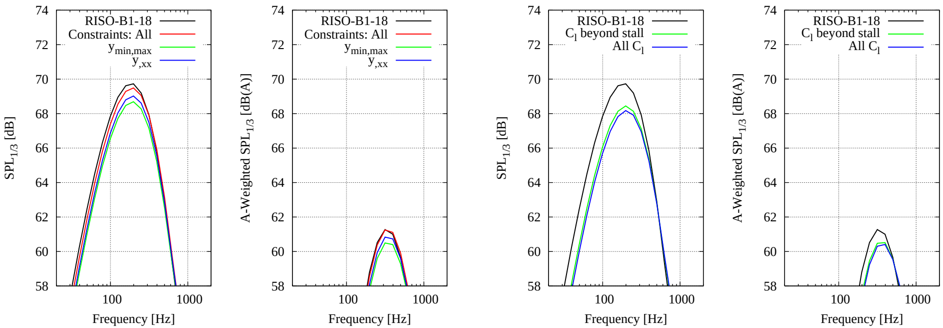

(a) Geometric Constraints (b) Aerodynamic Constraints

Figure 72. Far field noise after optimization - $\alpha = 8^o$

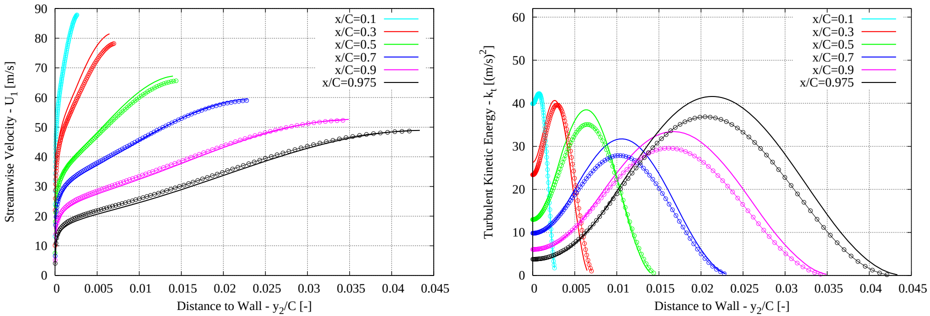

(a) Streamwise Velocity (b) Turbulent Kinetic Energy

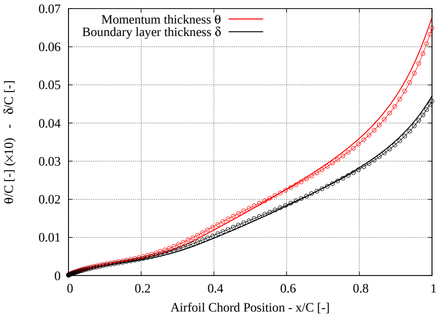

(c) Momentum and Boundary Layer Thicknesses

Figure 73. Boundary layer characteristics - $\alpha = 8^o$ *(Lines: RISØ-B1-18 airfoil; Lines with points: Optimized airfoil (“All* C_l*”)*

is optimized with a cost function based only on the SPL which is evaluated at the single angle of attack $\alpha = 8^o$ in the fully turbulent case.

- **Preserving Original Constraints**

As in the previous section, a new airfoil is acoustically optimized so that the geometric and aerodynamic properties of the original airfoil are preserved by using constraints. This set of constraints, referred to as “*All constraints*”, involves the airfoil shape and thickness distribution in relation with fabrication constraints, transition location, aerodynamic performances in the linear region, at maximum lift, and in deep stall. This set of constraints reads:

- Geometric constraints:

Maximum thickness: $17.9\% < t_{\max} < 18.1\%$
Thickness distribution: $14\% < t(0.14 < x < 0.56)$
On the suction side: $y_{,xx}(0.4 < x < 0.7) < -0.12$
$0.307 < x(y_{\max}) < 0.407$
On the pressure side: $y_{,xx}(0.7 < x < 0.9) > -1.4$
$0.257 < x(y_{\min}) < 0.357$
Trailing edge thickness: $t(x = 0.90) > 0.0125$
$t(0.94 < x < 0.97) > 0.0025$

- Aerodynamic constraints:
  On the suction side: $x_{\mathrm{tr}}(\alpha_0 = 15^o) < 0.03$
  Design lift: $1.283 < C_l(\alpha_0 = 11^o)$
  $0.876 < C_{l,\mathrm{tr}}(\alpha_0 = 7^o)$
  Lift/drag ratio at $C_{l,\max}$: $24.5 < C_l/C_d(\alpha_0 = 21^o)$
  $28.9 < C_l/C_{d,\mathrm{tr}}(\alpha_0 = 21^o)$
  Maximum C_l ($C_{l,\max}$): $1.734 < C_l(\alpha_0 = 21^o)$
  $1.813 < C_{l,\mathrm{tr}}(\alpha_0 = 21^o)$
  C_l after stall: $1.621 < C_l(\alpha_0 = 27^o)$
  $1.637 < C_{l,\mathrm{tr}}(\alpha_0 = 27^o)$

where x denotes the chordwise coordinate non-dimensionalized with the airfoil chord, with origin at the trailing edge. The airfoil shape is then defined by $y(x)$, the vertical distance to the chord axis. $y_{,xx}$ denotes the second order derivative of the airfoil shape relatively to the chordwise coordinate, also denoted as curvature. $x(y_{\min})$ and $x(y_{\max})$ denote the chordwise locations of the minimum and maximum values of y on the airfoil profile. t denotes the airfoil thickness and $t_{\max}$ its maximum value. x_{tr} denotes the transition chordwise location (for flow calculations using transition modelling). The lift coefficient C_l is defined as a function of the angle of attack relative to zero-lift α_0. The notation $C_{l,\mathrm{tr}}$ indicates that the lift has been calculated with transition modelling, otherwise fully turbulent conditions are assumed.

• Relaxed Geometric and Aerodynamic Constraints

The geometric constraints that were enforced above can be relaxed in order to widen the feasible design space and further reduce trailing edge noise. Four different designs are proposed. Preserving all the remaining constraints present in the "*All constraints*" design introduced above, the new designs are obtained by modifying only the following constraints:

- Design "Thickness"
  Thickness distribution: $14\% < t(0.14 < x < 0.56)$
- Design "$y_{\min,\max}$"
  On the suction side: $0.207 < x(y_{\max}) < 0.507$
  On the pressure side: $0.157 < x(y_{\min}) < 0.457$
- Design "$y_{,xx}$"
  On the suction side: $y_{,xx}(0.4 < x < 0.7) < -0.10$
  On the pressure side: $y_{,xx}(0.7 < x < 0.9) > -1.6$
- Design "Relax all geometric constraints"
  Combines all the above geometrically relaxed constraints

The results obtained for these design constraint sets above after optimization, namely the airfoil shapes, lift-drag characteristics and SPL spectra (at an angle of attack equal to 8^o), are displayed in Figs. 74(a), 75(a) and 76(a). The largest noise reduction is obtained with the "All geometric" relaxed constraints set, and is approximately 2.5dB lower than for the original profile.

The aerodynamic constraints are now relaxed. As in the geometrically relaxed designs, all remaining constraints of the "*All constraints*" design remain unchanged. New designs are proposed with the following modified constraints:

- Design “C_l *linear*”
  Design lift: $1.183 < C_l(\alpha_0 = 11^o)$
  $0.776 < C_{l,\mathrm{tr}}(\alpha_0 = 7^o)$
- Design “C_l *maximum*”
  Maximum C_l ($C_{l,\max}$): $1.634 < C_l(\alpha_0 = 21^o)$
  $1.713 < C_{l,\mathrm{tr}}(\alpha_0 = 21^o)$
- Design “C_l *stall*”
  C_l after stall: $1.521 < C_l(\alpha_0 = 27^o)$
  $1.537 < C_{l,\mathrm{tr}}(\alpha_0 = 27^o)$
- Design “*All* C_l”
  Combines all the above aerodynamically relaxed constraints

Airfoil shapes, lift-drag characteristics and SPL spectra after optimization are displayed in Figs. 74(b), 75(b) and 76(b). The reduction in noise is smaller than in the geometrical case and only reaches 1.5dB.

An additional constraint set, denoted as “Combined geometric and aerodynamic”, is introduced and basically sums up all the relaxations of the previous constraints introduced above, both geometrically and aerodynamically. Results are displayed in Figs. 74(c), 75(c) and 76(c), together with the “All constraints”, “All geometric” and “All C_l” designs. In the best case (turbulent calculation), the reduction obtained with this new design is slightly larger than the “All geometric” case and is about 3dB.

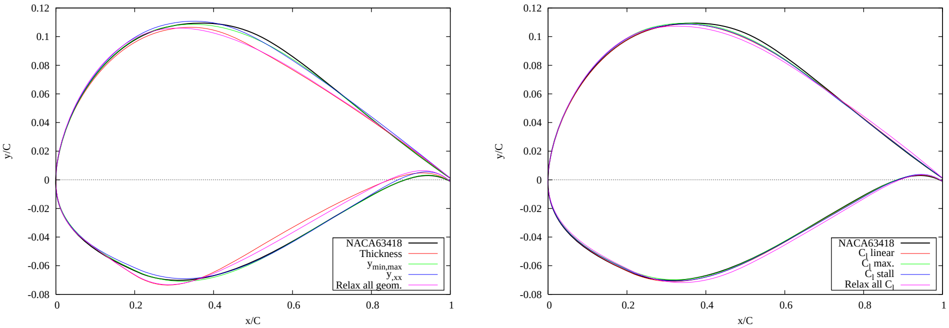

(a) Geometric Constraints (b) Aerodynamic Constraints

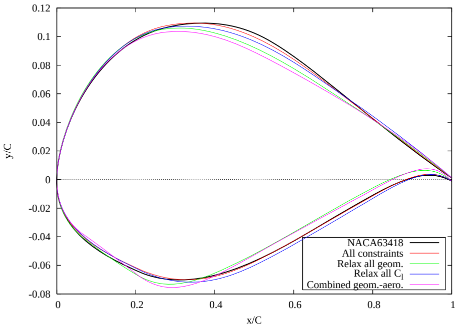

(c) Combined Constraints

Figure 74. Airfoil shapes after optimization

• Discussion

Quantities relevant for trailing edge noise emission are compared for the original NACA63-418 airfoil, the “All constraints” design, and the three designs resulting from combining several relaxed constraints.

The integral length scale L_2 and the turbulent kinetic energy k_t across the boundary layer near the trailing edge are displayed in Figs. 77(a) and (b), respectively. Momentum thickness along the airfoil chord is displayed in Fig. 77(c). From the previous figures displaying the noise

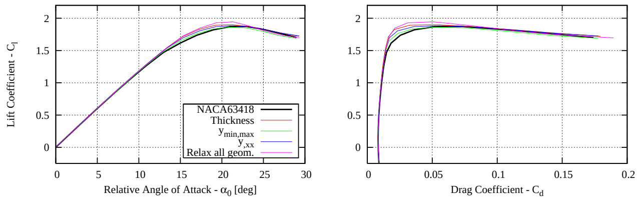

(a) Fully Turbulent

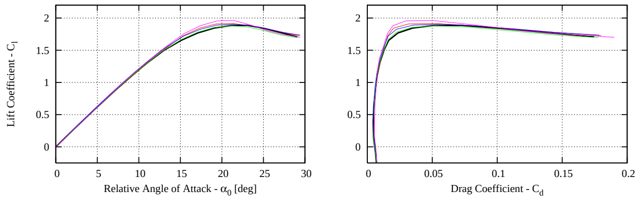

(b) Transition Model

(a) Geometric Constraints

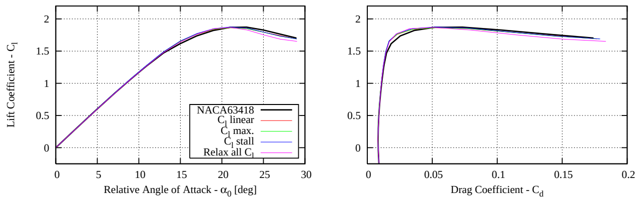

(a) Fully Turbulent

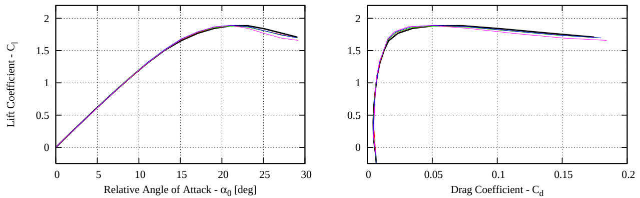

(b) Transition Model

(b) Aerodynamic Constraints

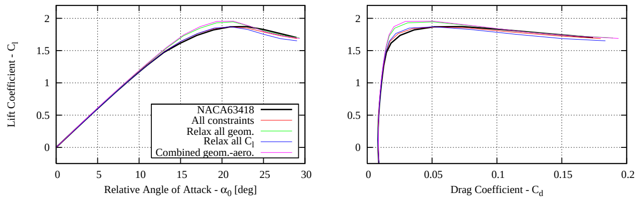

(a) Fully Turbulent

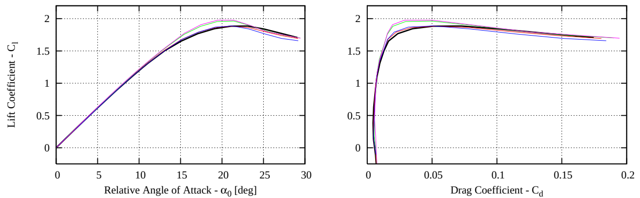

(b) Transition Model

(c) Combined Constraints

Figure 75. Aerodynamic characteristics after optimization (α_0)

spectra, it can be deduced that noise reduction is mainly achieved by reducing the turbulent kinetic energy during the design processes. The integral length scale also plays a role but to a lesser extent, and it seems that the change in momentum thickness is quite small as well.

6.4 Conclusions

In this work, results obtained with the TNO trailing edge noise model for various test cases have been compared with experimental data. It was found that in one case the measured airfoil

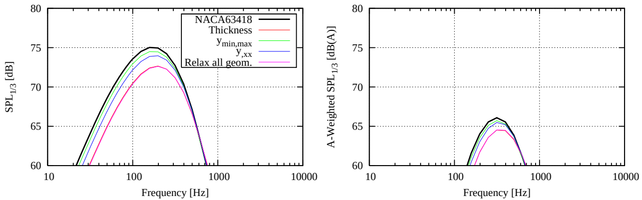

(a) Fully Turbulent

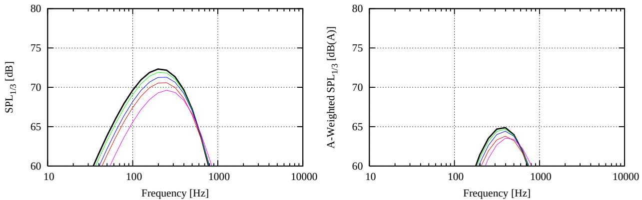

(b) Transition Model

(a) Geometric Constraints

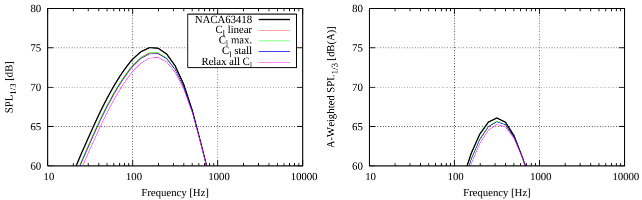

(a) Fully Turbulent

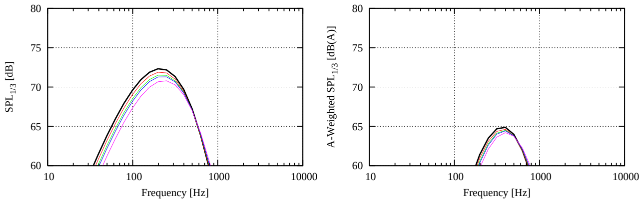

(b) Transition Model

(b) Aerodynamic Constraints

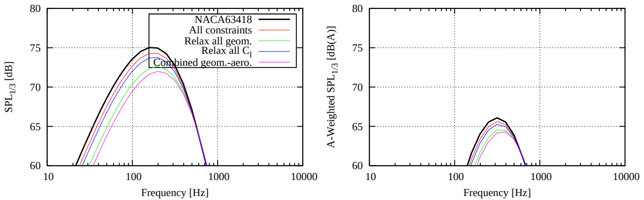

(a) Fully Turbulent

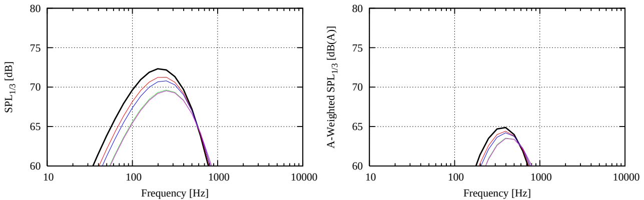

(b) Transition Model

(c) Combined Constraints

Figure 76. Far field noise after optimization - $\alpha = 8^o$

surface pressure were quite well predicted by the model. In two other cases, both the surface pressure and far field noise were largely underpredicted by the model, even though the tested airfoil and flow conditions didn't significantly differ from the previous case. However, the latter experiments were performed in wind tunnels designed for aeroacoustic measurements. The TNO model was still found reliable for relative comparisons and was used for aeroacoustically optimizing an existing airfoil. The noise emission could be reduced by up to 3 decibels. The noise reduction mechanism was found to be related to a reduction of the boundary layer turbulence intensity near the trailing edge. This was achieved by de-cambering the airfoil and the subsequent flattening of the suction side.

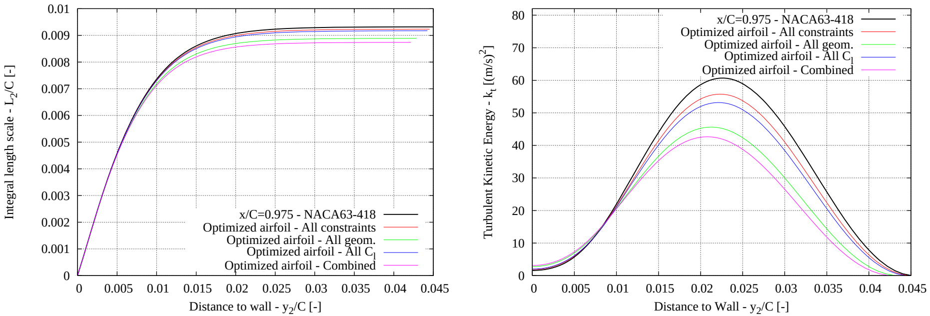

(a) Integral Length Scale (b) Turbulent Kinetic Energy

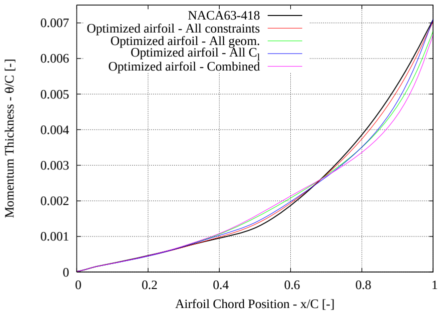

(c) Momentum Thicknesses

Figure 77. Boundary layer characteristics - $\alpha = 8^o$

Acknowledgments

Computations were made possible by the use of the PC-clusters at the Risø central computing facility and the DCSC Center for Scientific Computing at DTU.

References

[1] T. F. Brooks, S. D. Pope, and M. A. Marcolini. Airfoil self-noise and prediction. Nasa reference publication 1218, Langley Research Center, 1989.

[2] R. K. Amiet. Noise due to turbulent flow past a trailing edge. *J. Sound Vib.*, 47(3):387–393, 1976.

[3] T. Fukano, Y. Kodama, and Y. Senoo. Noise generated by low pressure axial flow fans, i: Modeling of the turbulent noise. *J. Sound Vib.*, 50(1):63–74, 1977.

[4] R. Parchen. Progress report draw: A prediction scheme for trailing-edge noise based on detailed boundary-layer characteristics. Tno rept. hag-rpt-980023, TNO Institute of Applied Physics, The Netherlands, 1998.

[5] W. K. Blake. *Mechanics of Flow-Induced Sound and Vibration, Vol.I and II*, volume in Applied Mathematics and Mechanics. Frenkiel, F.N. and Temple, G. (eds.), Academic Press, 1986.

[6] J. E. Ffowcs Williams and L. H. Hall. Aerodynamic sound generation by turbulent flow in the vicinity of a scattering half plane. *J. Fluid Mech.*, 40(4):657–670, 1970.

[7] M. S. Howe. A review of the theory of trailing edge noise. *J. Sound Vib.*, 61(3):437–465, 1978.

[8] M. Drela. *Low Reynolds Number Aerodynamics*, volume 54, chapter XFOIL: An Analysis and Design System for Low Reynolds Number Airfoils, pages 1–12. Mueller, T.J. (ed.), Lecture Notes in Engineering, Springer-Verlag, Berlin, 1989.

[9] P. Moriarty, G. Guidati, and P. Migliore. Prediction of turbulent inflow and trailing-edge noise for wind turbines. In *Proc. of the* 11^{th} *AIAA/CEAS Aeroacoustics Conf.*, AIAA Paper 2005-2881, Monterey, CA, 2005.

[10] T. Lutz, A. Herrig, W. Würz, M. Kamruzzaman, and E. Kr"amer. Design and wind-tunnel verification of low-noise airfoils for wind turbines. *AIAA Journal*, 45(4):779–785, 2007.

[11] T. F. Brooks and T. H. Hodgson. Trailing edge noise prediction from measured surface pressures. *J. Sound Vib.*, 78(1):69–117, 1981.

[12] F. R. Menter. Zonal two-equations $k-\omega$ turbulence models for aerodynamic flows. In *blabla*, AIAA Paper 93-2906, 1993.

[13] J. A. Michelsen. Block structured multigrid solution of 2d and 3d elliptic pde's. Tech. rep. afm 94-06, Technical University of Denmark, 1994.

[14] N. N. Sørensen. General purpose flow solver applied to flow over hills. Risø-r-827-(en), Risø National Laboratory, Roskilde, Denmark, June 1995.

[15] H. D. Papenfuß. Aerodynamic commissioning of the new wind tunnel at lm glasfiber a/s (lunderskov); private communication. Property of LM Glasfiber, June 2006.

[16] M. Døssing. High frequency microphone measurements for transition detection on airfoils. Tech. rep. risø-r-1645(en), Risø-DTU, Roskilde, Denmark, June 2008.

[17] M. Herr. Design criteria for low-noise trailing-edges. In *Proc. of the* 13^{th} *AIAA/CEAS Aeroacoustics Conf.*, Rome, 2007.

[18] A. Humpf. Investigation of computational aeroacoustic tools for wind turbine aerofoils. Diploma thesis, CENER, Sarriguren, Spain, 2006.

[19] M. Kamruzzaman, T. Lutz, A. Herrig, and E. Krämer. Rans based prediction of airfoil trailing edge far-field noise: Impact of isotropic & anisotropic turbulence. In *Proc. of the* 14^{th} *AIAA/CEAS Aeroacoustics Conf.*, AIAA Paper 2008-2867, Vancouver, 2008.

[20] P. Fuglsang and K. S. Dahl. Multipoint optimization of thick high lift airfoil wind turbines. In *Proc. EWEC'97*, Dublin, Ireland, 1997.

[21] P. Fuglsang and C. Bak. Development of the risø wind turbine airfoils. *Wind Energy*, 7:145–162, 2004.

[22] P. Fuglsang, C. Bak, M. Gaunaa, and I. Antoniou. Design and verification of the risø-b1 airfoil family for wind turbines. *Journal of Solar Energy Engineering*, 126(4):1002–1010, 2004.

7 Design of High Lift Airfoils With Low Noise and High Aerodynamic Performance

Author: Christian Bak, Franck Bertagnolio, Helge A. Madsen (Risø DTU)

This chapter presents the design of a high performance, low noise airfoil for incompressible flow and for Reynolds numbers at $6x10^6$ with a lift performance, which is resistant to surface contamination and turbulence intensity. The new airfoil is dedicated for MW-size wind turbines, which are exposed to varying inflow conditions and surface contamination from bugs and dust. The objectives in the design process were to have high maximum lift coefficient, while maintaining high aerodynamic efficiency and reduced noise emission. The results from the design process showed that the design tool was capable of designing airfoils with reduced noise using Risø-C2-18 as a basis. Thus, airfoils showing 1.5dB to 3dB reduction of maximum sound power level (*SPL*) were designed, with increasing relaxation of the constraints on the geometry around the trailing edge. However, evaluating the designs using A-weightening on maximum *SPL* showed another picture. It appears that the Risø-C2-18 has around 1dB higher *SPL*(A) as the Risø-B1-18 and that the new design obtained a similar maximum $SPL(A)$ as the Risø-B1-18. Thus, the conclusions when analyzing the maximum *SPL* with A-weight is that it is possible to reduce the A-weighted noise compared to the initial airfoil and that the new airfoil tended towards a thinner trailing edge, the same low noise emission as the Risø-B1-18, and higher aerodynamic performance.

7.1 Nomenclature

AOA	Angle of attack [deg]
AOA_r	Angle of attack relative to zero lift AOA [deg]
c	Chord length [m]
c_l	Lift coefficient [-]
c_d	Drag coefficient [-]
c_p	Normalized coefficient for the pressure on the airfoil surface [-]
C_P	Normalized coefficient for the wind turbine rotor power [-]
f	Frequency [Hz]
N	Force on airfoil normal to the rotor plane [N]
Re	Reynolds number [-]
SPL	Sound Power Level [dB]
$SPL(A)$	A-weighted Sound Power Level [dB]
t	Airfoil maximum thickness [m]
T	Force on airfoil parallel to the rotor plane [N]
U	Flow speed [m/s]
x	Coordinate in chordwise direction [m]

7.2 Introduction

Wind turbine airfoils should differ from traditional aviation airfoils.

Design of tailored airfoils for wind turbine rotors is essential for the continuing development of wind turbines. It has been known for decades that wind turbine airfoils should differ from traditional aviation airfoils in choice of design point, off-design characteristics and structural properties. The development of wind turbine airfoils has been ongoing since the mid 1980's, where significant efforts were made by Tangler and Somers [1], Timmer and Van Rooij[2], Björk [3], and Fuglsang and Bak [4]. For wind turbine airfoils operating in the atmospheric boundary layer there is influence from the turbulence intensity and contamination of bugs and dust and the airfoils should under these conditions show both high performance in terms of high lift-drag ratio, constant maximum lift and low noise.

In this work a new airfoil was designed for MW-size wind turbines. The blade lengths for such rotors are at the moment, year 2009, between 35m and 63m corresponding to 1MW and 5MW, respectively. Modern blades are commonly designed with thicknesses between 15% and 100% with thin airfoils ($t/c < 24\%$) on as much of the blade as possible. The airfoil was designed for rotors controlled with variable rotor speed and pitch control to maintain the optimum ratio between tip speed and wind speed (tip-speed-ratio). Many characteristics from the Risø-C2-18 airfoil [5] were inherited because this airfoil has shown to be both efficient and to have a high degree of insensitivity to leading edge roughness. However, there is a need for reducing the noise emission for airfoils to be mounted on the outer part of rotor blades. Finally, the new airfoil was as well designed to be aerodynamically very efficient both with and without a contaminated surface.

Based on the Risø-C2-18 airfoil new airfoils were designed with reduced noise.

The design was carried out with a Risø DTU in-house multi disciplinary optimization tool, AIRFOILOPT, that has been developed since 1996 [6]. The numerical optimization algorithm works directly on the airfoil shape providing a direct and interdisciplinary design procedure, where multiple design objectives for aerodynamics and structure may be handled simultaneously. This chapter describes the extension of the airfoil design tool and the development of a new noise reduced airfoil.

7.3 Method for Airfoil Design

The airfoil design tool can be divided into a 2D design tool and a 3D design tool. The 2D design tool has been used to design the former Risø airfoil families except of the Risø-C2 family [4, 5]. It uses a direct method where numerical optimization is coupled with either the flow solver XFOIL , which is a panel code with inviscid/viscous interaction, or the flow solver EllipSys2D, which is a code based on the solution of the Navier Stokes equations in 2D [7–9]. The latter solver is not used in the present work. A number of design variables form the airfoil shape, which is optimized subject to design objectives and constraints. Direct methods, such as the method used here, are basically interdisciplinary and multi-point and they allow direct use of integrated response parameters such as airfoil c_l, c_d and trailing edge noise directly as design objectives. Also, boundary layer response parameters, e.g., skin friction and transition point location can be constrained or used as objectives. Structural characteristics can be controlled by constraining the shape in terms of coordinates, gradients, curvatures or moment of resistance.

The airfoils were designed using the numerical optimization tool AIRFOILOPT.

The 3D tool models a complete blade with all its airfoil sections to form the blade surface and compute the aerodynamic rotor performance. Gradients and curvatures in the direction from the root to the tip were included to quantify the compatibility. Also, the 3D tool opens up the possibility of maximizing the rotor power performance in terms of, e.g. the power coefficient C_P. With the 3D tool follows a graphical user interface so that information about the geometry can either be extracted for use in the optimization process or existing blades can be inspected visually and quantitatively.

7.3.1 Design Algorithm

The design variables are changed in an optimization problem to minimize the objective function. This is done subject to constraints. In this case the design variables are the control points that describe the airfoil shape. The constraints are side values for the design variables and bounds on response parameters from flow and structural calculations. A traditional Simplex optimizer was used with a finite difference sensitivity analysis. This is a simple and robust solution method, which however, is computationally expensive because of the large number of necessary flow calculations. The optimization process is iterative, involving numerous calculations of flow and structural response parameters where the design gradually changes to improve the objective. The calculated flow and structural response parameters are used to estimate the value of the objective function and the constraints. Multiple angles of attack are calculated to allow off-design optimizations. The combination of flow and structural responses allows multidisciplinary optimization (MDO).

7.3.2 Geometry Description

A smooth shape is important for the optimization results. The 2D airfoil shape was represented by a single B-spline defined from the trailing edge around the airfoil contour by a set of control points. The blade shape, which, however, was not modeled in this work, is represented by cubic B-splines fixed at the top and bottom of the 2D sections and at the leading and trailing edge. In between these four fixed points at the sections the splines were distributed evenly along the surface length. The splines creating the 2D sections and the connection between the 2D sections form a mesh from where coordinates, gradients and curvatures can be extracted and used either for inspection or for use in the optimization process.

7.3.3 Flow Analysis

The XFOIL code by Drela [10] was used for the flow calculations during the optimization. For a given *AOA* and *Re*, XFOIL provides the C_p-distribution and c_l, and c_d. In addition, numerous boundary layer parameters are calculated. Transition was modeled by the e^n method with n = 9. Prescribing transition to $x/c = 0.001$ after the leading edge on the suction side and at $x/c = 0.10$ after the leading edge on the pressure side simulated leading edge roughness. XFOIL is well suited for optimization because of the fast and robust viscid/inviscid interaction scheme. However, the integral boundary layer formulation is not well suited for separated flows. XFOIL should therefore be used with caution at and above $c_{l,max}$. Others find that it may be necessary to modify or even tune XFOIL to better match measured results [2], but the computations seem to compare relatively well with EllipSys2D computations especially in the attached flow region.

7.3.4 Noise Analysis

The noise emission is, as in earlier investigations, e.g. by Brooks *et al.* [11], divided into five different sources: 1) Tip noise, 2) Blunt trailing edge noise, 3) Laminar vortex shedding noise, 4) Turbulent inflow noise and 5) Turbulent trailing edge noise. Experience shows that especially the last source is important because the trailing edge noise is broadband and a distributed source. This is the reason for focusing on this source and two models for predicting this source in detail are developed: The TNO model and the Glegg *et al.* model [12, 13]. These two models are implemented into AIRFOILOPT . A single or few entities for evaluating the noise emission is important to simplify the design process. The simplification of the noise emission could either be integration of the spectrum or simply the maximum noise. The simplification of the noise emission was investigated in this work.

Trailing edge noise is a very important source and therefore is the source of noise to minimize in this design process.

7.4 Strategy for Airfoil Design

The desirable airfoil characteristics form a complex matrix of properties of which some are in conflict with others. This has been a topic of discussion in the literature [14–16]. There seems to be consensus on most of the general desirable characteristics. However, the means of achieving them are strongly related to the design method and the philosophy of the designer. The new airfoil was designed for operation on a wind turbine rotor. The force that contributes to the rotor power is the tangential force, T, whereas the force that contributes to the rotor thrust, is the normal force, N. As it was the case with the Risø-B1 airfoil family T can be used as the objective function, but also the lift-drag ratio (c_l/c_d) can be used. The latter is a common measure of the airfoil efficiency because c_l can be considered as the production and c_d can be considered as the loss. The new airfoil was designed with maximum c_l/c_d ratio as was the case for the Risø-C2 series. Some of the characteristics that are taken into account in the design process will be described in the following.

7.4.1 Structure

A wind turbine blade may be divided into the root, mid and tip parts. The mid and tip parts are determined mainly from aerodynamic requirements whereas structural objectives are relevant mainly for the inboard part of the blade, e.g., for $t/c > 24\%$. Another issue is the geometric compatibility between airfoils of the same family to ensure smooth transition from neighboring airfoil sections. However, in this work the structure was not part of the design process, but was used to evaluate the influence of the noise requirements on the structural stiffness.

7.4.2 Insensitivity of $c_{l,max}$ to Leading Edge Roughness

Roughness on the airfoil leading edge region formed by accumulation of dust, dirt and bugs is well recognized as a main design driver for wind turbine airfoils [14]. The new airfoil was designed for minimum sensitivity of $c_{l,max}$ to leading edge roughness by two separate design objectives: (1) The suction side natural transition point was constrained to move to the very leading edge for *AOA* around 3° below $c_{l,max}$ predicted with forced transition. This determined the local shape of the leading edge region so that a small pressure rise at the leading edge caused natural transition to turbulent flow at the leading edge a few degrees before $c_{l,max}$. Premature transition caused by roughness will therefore be eliminated close to $c_{l,max}$ by a very forward position of the natural transition point. (2) The level of $c_{l,max}$ resulting from a flow analysis with simulation of leading edge roughness, i.e. forced transition from the very leading edge, was constrained to a sufficiently high value compared to results from analysis assuming free transition. This shapes the airfoil suction side so that the pressure recovery region does not separate prematurely because of an increase of the boundary layer thickness caused by roughness, which would reduce $c_{l,max}$. Even with this constraint massive roughness will inevitably reduce $c_{l,max}$. Also, the existence of even minor leading edge roughness will result in an unavoidable reduction in the c_l/c_d ratio.

The design process is multi-disciplinary involving both aerodynamics, structure and noise.

7.4.3 Design $c_{l,max}$

The airfoil sections were designed for high $c_{l,max}$. This was chosen because the airfoil sections can be used for design of slender blades and in general ensuring minimum fatigue loads and extreme loads. Also, this choice was made to compare to the Risø-B1 and Risø-C2 airfoils. However, a disadvantage from this choice is the loss of stiffness for the blade if the relative airfoil thicknesses are maintained even though the chord distribution is reduced. Thus, the choice of high maximum lift is closely related to the choice of concept in the blade design. No matter which concept is used in the blade design, the inner part of the rotor needs airfoil sections with both high relative thickness and high maximum lift.

7.4.4 Design Objective

A compound objective function was defined as a weighted sum of c_l/c_d ratio values resulting from multiple angles of attack in the design *AOA* range and trailing edge noise values at one angle of attack close to maximum c_l/c_d. Some were for a clean airfoil surface whereas others were for flow with simulated leading edge roughness to ensure good performance at both conditions. The airfoil design *AOA*-region is also determined from the requirements to the wind turbine off-design operation. Because of the stochastic nature of the wind, turbulence gusts and wind direction changes will always lead to some off-design operation due to non uniform inflow. However, the extend of off-design operation is mainly given by the power control principle. In most cases it is desirable that the design *AOA*-region is close to $c_{l,max}$ since this enables low rotor solidity and/or low rotor speed. For all the new airfoils the design point region was AOA_r = [5°;14°], where c_l/c_d are computed both assuming transition from laminar to turbulent forced at the leading edge (fully turbulent) and free transition. High aerodynamic performance is important because the power output from wind turbines is very dependent on this. For instance, an increase from c_l/c_d=140 to 150 for a rotor results in an increase of around 0.4% in power output. The chosen angles of attack for maximizing c_l/c_d will lead to an expected high $c_{l,max}$ at around AOA_r =16° corresponding to $c_{l,max}$ = 1.8 assuming a lift curve slope of $2\pi rad^{-1}$. The airfoil family was designed for $Re = 6x10^6$, because this corresponds to modern blade designs of the 3MW size. Furthermore, it will be investigated whether to include the noise prediction as constraints or in the objective function.

7.5 Airfoil Designs with Noise Reduction

The results from the design process of the new airfoil with t/c=18% can be divided into three parts:

- The entity to measure noise: Should maximum values or integrated values of the spectra be used in the design process? Should A-weighted values be used? And should noise from fully turbulent airfoil flow or free transitional airfoil flow be used as the noise entity?
- Setup of the design problem: Because the aerodynamic characteristics of airfoils for wind turbine are very important, should the noise reduction be handled as constraints to the design problem or should it be a part of the objective function?
- The final airfoil design

In the design process the Risø-C2-18 airfoil was the starting point and most of the characteristics for this airfoil were inherited. However, because this type of airfoil typically is used on the outer part of a rotor, the bending stiffness is of secondary importance and therefore it was allowed in the design process to reduce this stiffness somewhat.

7.5.1 The Entity to Measure Noise

Because noise is experienced at a wide range of frequencies and the human ear dampens some frequencies in this range, it is not straight forward to state an unambiguous measure for noise. Basically, there are four ways to evaluate the noise 1) Maximum sound power level (*SPL*) without A-weight, 2) Maximum $SPL(A)$ with A-weight, 3) Integrated *SPL* spectrum without A-weight and 4) Integrated *SPL* spectrum with A-weight.

Because aerodynamic noise from wind turbines are integrated from all airfoil sections along the rotor blades, the main contribution to the total wind turbine *SPL* at the different frequencies stems from airfoil sections at different radii. This can be seen in Figure 78, where *SPL* spectra are seen for the Nordtank 500/41 (500kW turbine with 41m diameter rotor) using an implementation of the semi-empirical noise model described by Fuglsang and Madsen [17]

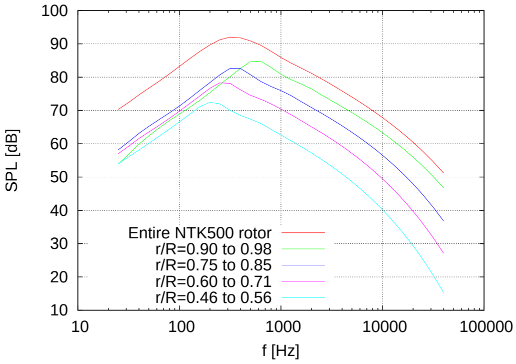

Figure 78. SPL spectrum for the NTK 500/41 for the entire rotor and for sections of the rotor at different radii using the BPM model.

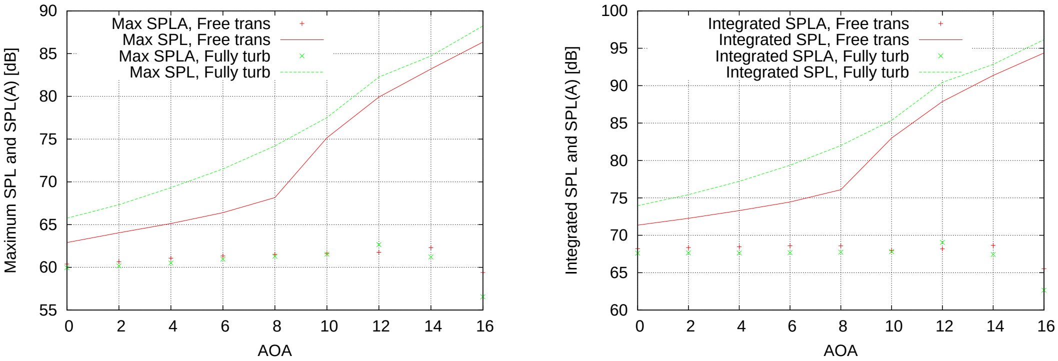

Figure 79. Left: Maximum SPL and $SPL(A)$ as function of angle of attack, Right: Integrated SPL and $SPL(A)$ as a function of angle of attack.

and based on Brooks, Pope and Marcolini [11] and Lowson and Fiddes [18], which in short is called the BPM model. The spectra show the *SPL* for the entire rotor (red curve) and for annular elements as stated in the plot. Maximum *SPL* appears at 630Hz at the outer part of the rotor continuously decreasing to 200Hz at the mid part of the blade span. For the entire rotor maximum *SPL* appears at 315Hz. Thus, *SPL* is greater at some frequencies in the spectra and the maximum value is decreasing with decreasing radius of the rotor. Also, the plot shows that the noise from the outer part of the rotor contributes more than from the mid or inner part of the rotor. This plot also makes it clear that when reducing the aerodynamic noise, focus should mainly be put on the airfoils on the outer part of the rotor.

The entity to measure noise was in this work maximum sound power level without A-weight for turbulent flow.

Figure 79 shows the computed maximum and integrated *SPL* and $SPL(A)$ for the Risø-C2-18 airfoil assuming both free transition and fully turbulent flow in the XFOIL computations. An increase in both maximum and integrated *SPL* without A-weight as a function of *AOA* is seen in contrast to maximum $SPL(A)$ that shows only a very weak increase with *AOA*. Also, integrated $SPL(A)$ shows no unambiguous increase with *AOA*. Even though maximum and integrated *SPL* for fully turbulent flow is significantly higher compared to flow with free transition, this is not the case for the A-weighted values. Therefore, designing airfoils using maximum or integrated $SPL(A)$ will potentially cause some difficulties. From this investigation either maximum or integrated *SPL* without A-weight can be used as a measure for the noise. In this work it was decided to measure the noise using maximum *SPL*. Finally, as stated before it is seen from Figure 79 that maximum *SPL* from fully turbulent flow is higher than for flow assuming free transition. That is the reason for choosing maximum *SPL* without A-weight for fully turbulent flow as the entity to reduce.

It was observed that the A-weighted noise in general was weakly dependent of angle of attack.

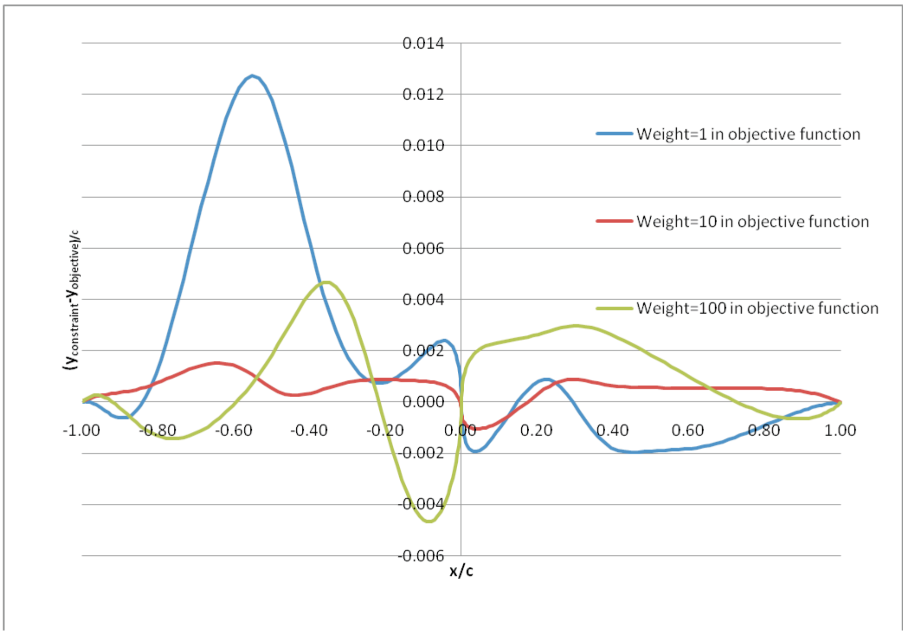

Figure 80. Difference in surface contour for the airfoils designed with noise in the objective function compared to the airfoil designed with noise as constraints denoted by the y-coordinates $(y_{constraint} - y_{objective})/c$.

7.5.2 Setup of the Design Problem

There are two ways of including the noise modeling in the design process. Either it is included as constraints or in the objective function. This is investigated in the following. One design, where the noise was included as a constraint, was carried out so that the noise emission was reduced as much as possible without reducing or changing the aerodynamic performance. Another design, where the noise was a part of the objective function, was carried out. However, the question to be answered for this type of setup was how the weight between aerodynamic and noise characteristics should be. Figure 80 shows the changes in the surface contour, when including noise in the objective function, compared to the surface contour, when including the noise in constraints. The pressure/lower side of the airfoil is plotted as negative values of x/c and the suction/upper side is plotted as positive values. It is seen that a weight of 10 for the noise in the objective function ensures the contour that best matches the contour designed using noise as constraints because the maximum changes in the contour is below 0.002. The noise for the four airfoils were maximum SPL=74.5dB for the airfoil designed with constraints and maximum $SPL = 75.4dB$, $74.6dB$ and $74.5dB$ for the three airfoils designed using noise in the objective function with weight 1, 10 and 100, respectively, compared to the aerodynamic performance. Figure 81 shows the corresponding airfoil characteristics evaluated using XFOIL, which reflects that no significant changes in the airfoil performance were introduced when the trailing edge noise was reduced except for the case with a weight of the noise in the objective function of 100. From the figures it is indicated that using an objective function with the weight of the noise 10 times higher than the c_l/c_d ratio resulted in a fairly good weight between noise and aerodynamics, because the noise was reduced sufficiently without sacrificing the aerodynamic performance and the surface contour agreed well with an airfoil designed with noise as constraints. The weight relation between noise and aerodynamic performance of 10 to 1 was kept in the objective function in the rest of the investigation.

Both aerodynamic characteristics and noise were used in the objective function.

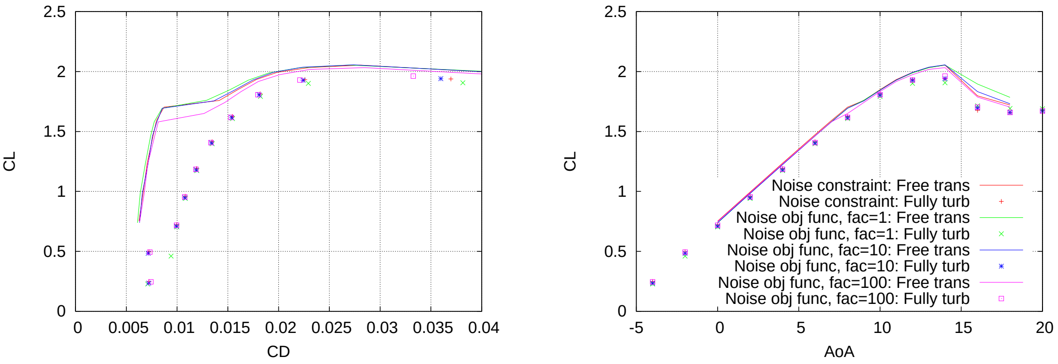

Figure 81. Airfoil characteristics of different designs to determine the weights in the compound objective function.

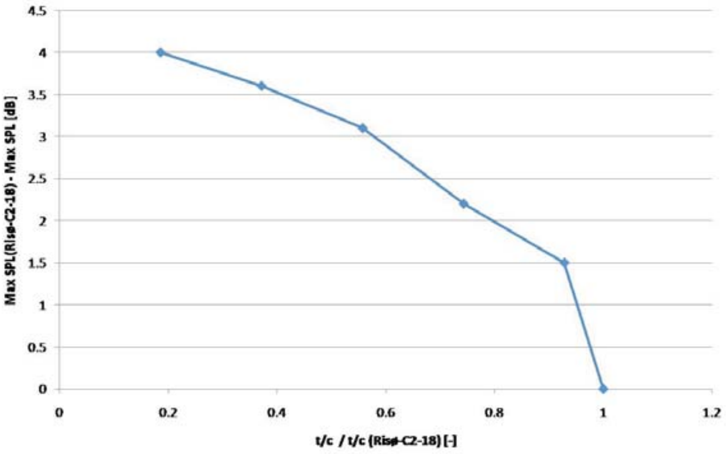

Figure 82. Reduction of maximum SPL as a function of the airfoil thickness ratio at the trailing edge.

7.5.3 Final Airfoil Design

With the Risø-C2-18 airfoil as the starting point in the design process several airfoils were designed:

Airfoil name	Description
No 1	Similar constraints as for Risø-C2-18
No 2	Up to 20% reduction in airfoil thickness close to trailing edge
No 3	Up to 40% reduction in airfoil thickness close to trailing edge
No 4	Up to 60% reduction in airfoil thickness close to trailing edge
No 5	Up to 80% reduction in airfoil thickness close to trailing edge

More airfoils were designed in the investigation, where constraints especially on the airfoil contour were relaxed. However, it turned out that the listed constraints were the most important concerning the reduction of trailing edge noise.

Figure 82 shows how the design maximum *SPL* at an angle of attack of 14° from zero-lift angle-of-attack reduces for decreasing trailing edge thickness. Thus, reducing the trailing edge thickness has a significant effect on maximum *SPL*. However, when reducing the trailing edge thickness, the total bending stiffness of the airfoil reduces as showed in Figure 83, but loosing stiffness at the outer part of wind turbine blades is acceptable compared to, e.g. the inner part of blades.

It was possible to reduce the trailing edge noise without A-weight significantly using AIRFOILOPT by decreasing the rearward thickness of the airfoil.

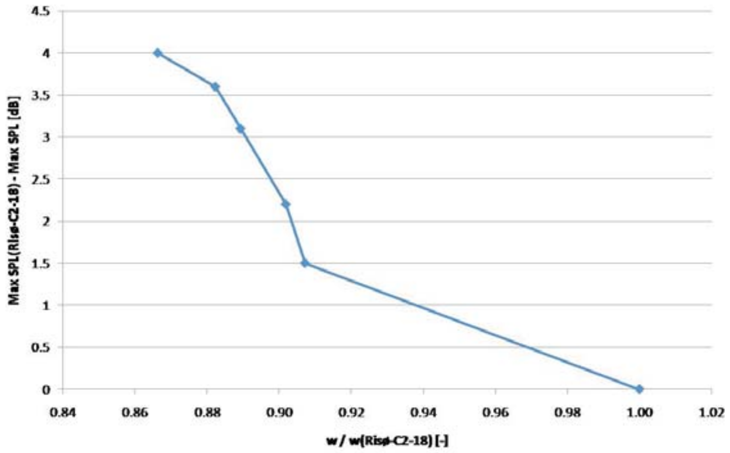

Figure 83. Reduction of maximum SPL as a function of the airfoil bending stiffness for the Risø-C2-18.

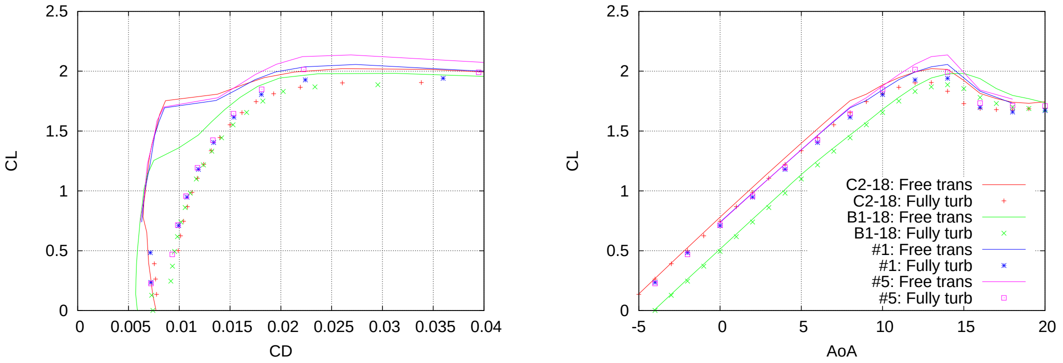

Figure 84. Aerodynamic characteristics of two of the new design, No 1 and No 5 compared to Risø-C2-18 and Risø-B1-18. To the left: c_l as function of c_d and to the right c_l as a function of AOA.

Figure 84 shows the aerodynamic performance of some of the new airfoil designs, the Risø-C2-18 airfoil and the Risø-B1-18, which is a well established airfoil design [4]. No significant changes from Risø-C2-18 airfoil are seen. However, even though the performance of c_l is similar for the Risø-B1-18 compared to Risø-C2-18, c_l/c_d is significantly higher for the Risø-C2-18 airfoil at c_l values between 1.2 and 1.7 making this airfoil aerodynamically much more efficient. Figure 85 shows to the left maximum SPL as a function of c_l and to the right SPL spectra for c_l around 1.2. Apart from the Risø-C2-18 airfoil and two of the new airfoil designs also Risø-B1-18 and NACA 63-418 are shown. Reductions of maximum SPL are seen for the two new designs of 1.5dB and 3dB respectively, confirming the ability of the design tool to design airfoils with reduced noise emission. Furthermore, Risø-B1-18 shows similar noise emission as the Risø-C2-18, but the NACA 63-418 has significantly higher maximum SPL for a given c_l value. Investigating the trends using A-weight shows, however, another picture. Figure 86 shows to the left maximum $SPL(A)$ as a function of c_l, and to the right $SPL(A)$ spectra for c_l around 1.2. It appears that the Risø-C2-18 has a somewhat higher $SPL(A)$ (around 1dB) compared to the Risø-B1-18 and that the design No 5 obtains a similar maximum SPL as the Risø-B1-18. Thus, the conclusions when analyzing the maximum SPL with A-weight is that it is possible to reduce the A-weighted noise compared to the initial airfoil and that the new airfoil showed the same low noise emission as the Risø-B1-18, but with higher aerodynamic performance.

With A-weight it was possible to design an airfoil with similar noise emission and improved aerodynamics compared to Risø-B1-18.

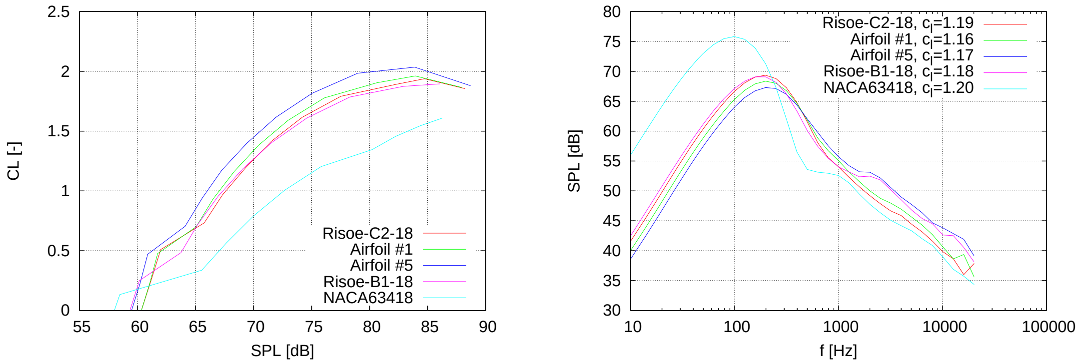

Figure 85. Left: Maximum SPL as a function of c_l for different airfoils. Right: Spectra of SPL at c_l around 1.2 for different airfoils.

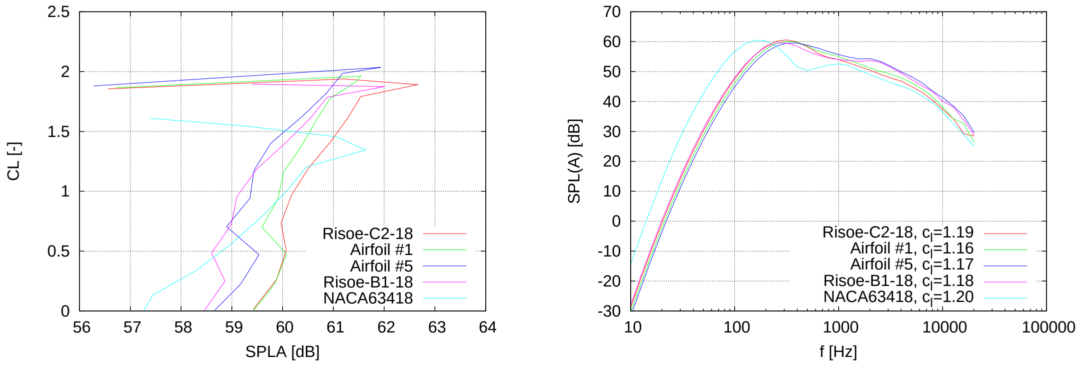

Figure 86. Left: Maximum $SPL(A)$ as a function of c_l for different airfoils. Right: Spectra of $SPL(A)$ at c_l around 1.2 for different airfoils.

The conclusions above were based on designs with maximum SPL in the objective function. However, using maximum $SPL(A)$ in the objective function did not reduce the maximum $SPL(A)$ further.

7.6 Conclusions

This chapter presented the design of a new low noise airfoil with 18% thickness. The airfoil dedicated for wind turbines was developed considering excellent aerodynamics and low noise. For this purpose the airfoil design tool AIRFOILOPT was used. The airfoil was developed for variable speed operation and pitch control of large MW sized rotors. Design objectives were used with simultaneous use of airfoil flow simulations assuming both free and forced transition. A compound objective function was used, where the c_l-c_d ratio over a range of design angles took care of the design for aerodynamic efficiency, and where the trailing edge noise predicted by the TNO model took care of the reduced noise. Also, numerous constraints on flow and structural response parameters to ensure a high maximum lift coefficient and insensitivity of this to leading edge roughness were put on desired characteristics.

The results from the design process showed that AIRFOILOPT was capable of designing airfoils with reduced noise using Risø-C2-18 as a basis. Thus, airfoils showing 1.5dB to 3dB reduction of maximum SPL were designed, with increasing relaxation of the constraints on the geometry around the trailing edge for increased reduction in SPL. However, evaluating the designs using A-weight on maximum SPL showed another picture. It appears that the Risø-C2-18 has around 1dB higher $SPL(A)$ relative to the Risø-B1-18 and that the design No 5 (see section 7.5.3) obtained a maximum $SPL(A)$ similar to the Risø-B1-18. Thus, the conclusions when analyzing the maximum *SPL* with A-weight is that it is possible to reduce the A-weighted noise compared to the initial airfoil and that the new airfoil showed a thinner trailing edge, the same low noise emission as the Risø-B1-18, and higher aerodynamic performance.

References

[1] Tangler J.L. and Somers D.M. Nrel airfoil families for hawt's.

[2] Timmer W.A. and van Rooij R.P.J.O.M. Summary of the delft university wind turbine dedicated airfoils. *Proc. AIAA-2003-0352*, 2003.

[3] Björk A. Coordinates and calculations for the ffa-w1-xxx, ffa-w2-xxx and ffa-w3-.xxx series of airfoils for horizontal axis wind turbines. Ffa tn 1990-15, FFA, Stockholm, Sweden, 1990.

[4] P. Fuglsang and C. Bak. Development of the risø wind turbine airfoils. *Wind Energy*, 7:145–162, 2004.

[5] Madsen H A Gaunaa M Bak C, Andersen P B. Design and verification of airfoils resistant to surface contamination and turbulence intensity. *AIAA 2008-7050, 26th AIAA Applied Aerodynamics Conference 18 - 21 August 2008, Honolulu, Hawaii*, 2008.

[6] P. Fuglsang and K.S. Dahl. Multipoint optimization of thick high lift airfoil wind turbines. *Proc. EWEC´97, Dublin, Ireland*, pages 468–471, 1997.

[7] N.N. Sørensen. General purpose flow solver applied to flow over hills. Risø-r-827(en), Risø National Laboratory, Denmark, June 1995.

[8] JA. Michelsen. Basis3d - a platform for development of multiblock pde solvers. Technical report afm 92-05, Technical University of Denmark, 1992.

[9] JA. Michelsen. Block structured multigrid solution of 2d and 3d elliptic pde's. Technical report afm 94-06, Technical University of Denmark, 1994.

[10] M. Drela. *XFOIL, An Analysis and Design system for Low Reynolds Number Airfoils. Low Reynolds Number Aerodynamics*, volume 54. In Springer- Verlag Lec. Notes in Eng., 1989.

[11] Marcolini M.A. Brooks T.F., Pope D.S. Airfoil self-noise and prediction. Nasa reference publication 1218, NASA, USA, 1989.

[12] Parchen R. Progress report draw: A prediction scheme for trailing-edge noise based on detailed boundary-layer characteristics. Tno rept. hag-rpt-980023, TNO Institute of Applied Physics, The Netherlands, 1998.

[13] Atassi O. Glegg S., Morin B. and Reba R. Using rans calculations of turbulent kinetic energy to provide predictions of trailing edge noise. *14th AIAA/CEAS Aeroacoustics Conference (Proc.), AIAA Paper 2008-2993, Vancouver, Canada*, 2008.

[14] J.L. Tangler and D.M. Somers. Status of the special purpose airfoil families. *Proc. WINDPOWER'87, San Fransisco*, 1987.

[15] A. Björk. Airfoil design for variable rpm horizontal axis wind turbines. *Proc. EWEC'89, Glasgow, Scotland*, 1989.

[16] P. Fuglsang. Aerodynamic design guidelines for wind turbine rotors. *Proc. 4th GRACM Congress on Computational Mechanics GRACM 2002, Patra, Greece*, 2002.

[17] Madsen H. A. Fuglsang P. Implementation and verification of an aeroacoustic noise prediction model for wind turbines. Risø-r-867(en), RisøNational Laboratory, Denmark, March 1996.

[18] Fiddes S.P. Lowson M.V. Design prediction model for wind turbine noise. Etsu w/13/00317/rep, 1994.

8 Noise prediction of NACA 64418 airfoil

Author: Wei Jun Zhu, Wen Zhong Shen and Jens Nørkær Sørensen - DTU MEK

This chapter describes an aeroacoustic simulation of the flow past a NACA 64418 airfoil. The flow/acoustics splitting method is applied for predicting flow generated noise and the acoustics governing equations are discretized with high-order finite difference schemes. The splitting method consists of dividing the acoustic problem into a viscous incompressible flow part and an inviscid acoustic part. The incompressible flow equations are solved by the second-order finite volume code EllipSys2D/3D. The incompressible pressure and velocity form the input to the acoustic equations. The acoustic equations are solved by using high-order finite-difference schemes. To achieve low dissipation and dispersion errors, either Dispersion-Relation-Preserving (DRP) schemes or optimized compact finite difference schemes are used for the spatial discretizations. For time integration the classical fourth-order Runge-Kutta scheme is applied to the acoustic equations. Results are presented for turbulent flow past a NACA 64418 airfoil and rather good agreement against experimental data was found.

8.1 Introduction

The flow/acoustic splitting method, was originally proposed by Hardin and Pope [1] in 1994. Shen and Sørensen [2] remedied the original splitting technique by changing the basic decomposition of the variables. To reduce the growth of hydrodynamic instabilities, some other modifications of the original splitting method were proposed by Ewert and Schröder [3], Seo and Moon [4]. The first part of the splitting approach is the viscous flow part which solves the incompressible NS equations. The variables obtained from the incompressible solver are used in the second part of the calculation, where the acoustic or perturbed equations are solved. Under the assumption of low Mach number, the perturbed quantities represent the difference between the compressible and the incompressible flow. Therefore, the perturbed variables are solved in the compressible equations by knowing all incompressible quantities. The modified splitting method has been applied by Shen and Sørensen for flows past a cylinder and an airfoil for both laminar and turbulent flow cases where second-order finite volume/finite difference methods were used for the flow and the acoustic computations [5–7]. Encouraging results were obtained from previous computations and demonstrated that the splitting method is an effective and convenient method for near field acoustic simulations at low Mach numbers. As an extension to the previous work, in the present work, high-order finite difference schemes are used to solve the acoustic equations. The use of high-order schemes is due to the large disparity between the length and time scales of flow and acoustics. A 4th -order wave number optimized scheme was developed by Tam and Webb [8] which is the so-called Dispersion-Relation-Preserving (DRP) scheme. Using the strategy of the DRP scheme and applying it on the original high-order compact finite difference schemes of Lele [9], Kim and Lee [10] derived wave number optimized compact schemes. Both the high-order DRP schemes and the optimized compact schemes have the characteristics of low dissipation and dispersion errors which are designed for wave propagation problems.

8.2 Governing equations

The energy of flow generated noise is very small at low Mach numbers and it has very limited influence on the flow and thus the feedback of the acoustic field to incompressible flow field can be neglected. We first obtain the flow solution from the incompressible NS equations. Consider the incompressible flow with a constant density ρ_0. The incompressible equation is written as

$$\frac{\partial U_i}{\partial t} + \frac{\partial (U_i U_j)}{\partial x_j} = -\frac{1}{\rho_0}\frac{\partial P}{\partial x_i} + \nu \frac{\partial^2 U_i}{\partial x_i \partial x_j} \tag{10}$$

$$\frac{\partial U_i}{\partial x_i} = 0 \tag{11}$$

where $P(x_i,t)$ and $U_i(x_i,t)$ are time dependent unsteady incompressible pressure and velocity components.

The formulation of the acoustic equations was originally proposed by Hardin and Pope and further developed by Shen and Sørensen. For more details the reader is referred to Hardin and Pope [1] and Shen and Sørensen [2]. By neglecting the viscous terms, the acoustic equations are written in a conservative form such as follows

$$\frac{\partial Q}{\partial t} + \frac{\partial E}{\partial x} + \frac{\partial F}{\partial y} + \frac{\partial G}{\partial z} = S \tag{12}$$

where matrices Q, E, F, G and S are

$$Q = \begin{pmatrix} \rho' \\ \rho u' + \rho' U \\ \rho v' + \rho' V \\ \rho w' + \rho' W \\ p' \end{pmatrix}, E = \begin{pmatrix} \rho u' + \rho' U \\ \rho(2Uu' + u'^2) + \rho' U^2 + p' \\ \rho(Vu' + Uv' + u'v') + \rho' UV \\ \rho(Wu' + Uw' + u'w') + \rho' UW \\ c^2(\rho u' + \rho' U) \end{pmatrix},$$

$$F = \begin{pmatrix} \rho v' + \rho' V \\ \rho(Vu' + Uv' + u'v') + \rho' UV \\ \rho(2Vv' + v'^2) + \rho' V^2 + p' \\ \rho(Vw' + Wv' + v'w') + \rho' VW \\ c^2(\rho v' + \rho' V) \end{pmatrix},$$

$$G = \begin{pmatrix} \rho w' + \rho' W \\ \rho(Wu' + Uw' + u'w') + \rho' UW \\ \rho(Wv' + Vw' + v'w') + \rho' VW \\ \rho(2Ww' + w'^2) + \rho' W^2 + p' \\ c^2(\rho w' + \rho' W) \end{pmatrix}, S = \begin{pmatrix} 0 \\ 0 \\ 0 \\ 0 \\ -\frac{\partial P}{\partial t} \end{pmatrix}, \tag{13}$$

In the matrices the quantities with a superscript (’) indicate acoustic variables and the capital letters U, V, W and P are flow variables.

8.3 High-order discretizations

The use of high-order numerical schemes is known as one of the most important issues of CAA. In CAA simulations, large number of grid points and small time steps are typically required. High-order schemes are thus commonly used for CAA simulations to reduce the number of grid points per wavelength. The numerical schemes are usually originated from traditional schemes and further developed for CAA problems. Among those schemes, DRP [8] schemes and Compact/Optimized Compact schemes [9, 10] are popularly used for CAA applications [17] .

The idea of a finite-difference representation for a derivative can be introduced by a weighted summation of the value at its neighboring points. For a sufficiently small but finite Δx, the standard central difference scheme with a $(2N+1)$-point stencil can be written as

$$\frac{\partial f}{\partial x}(x) \approx \frac{1}{\Delta x}\sum_{j=-N}^{N} a_j f(x+j\Delta x) \tag{14}$$

The standard way of determining the coefficients consists of two steps: the first step is to perform Taylor expansion at each points f_i where $i \in [-N,N]$; the second step is to eliminate high-order terms obtained from Taylor series such that the maximum accuracy of $2N^{\,th}$-order is obtained.

We require that the exact derivative f_i' is identical to the finite difference approximation as shown in Equation 14. The difference between the exact and the approximated derivative is the Truncation Error (TE) which represents the accuracy of the approximation. The equations are set up in the manner that all terms lower than fifth-orders must vanish in the TE. Since symmetric stencil is used, only two equations are needed for solving two unknowns.

Finite difference approximation such as Equation 14 can be alternatively designed to have a minimal dispersion and dissipation. Tam and Webb [8] derived a new scheme with fourth-order accuracy using 7-point stencils. The spatial derivatives are approximated in an optimized way such that the new scheme resolves a wider range of wavenumbers which is essential for solving wave equations. Following the technique of Tam and Webb, a series high-order optimized schemes can be constructed use arbitrary stencil points.

As an example, here we consider the 7-point scheme which originally has sixth-order accuracy. The optimized scheme which is the so-called DRP scheme has fourth-order accuracy while still using the 7-point stencil. Since fourth-order scheme can be derived using a 5-point stencil, therefore the use of a 7-point stencil will give us a free parameter a_j. The value a_j is the one to be optimized and the new scheme will have less dispersion error. The starting point is still the same finite difference approximation given in Equation 14. By doing Fourier transformation of $f(x)$ and its inverse one gets

$$\tilde{f}(\alpha) = \frac{1}{2\pi}\int_{-\infty}^{\infty} f(x)\mathrm{e}^{-i\alpha x}dx, \qquad f(x) = \int_{-\infty}^{\infty} \tilde{f}(\alpha)\mathrm{e}^{-i\alpha x}d\alpha. \tag{15}$$

Inserting these to the finite difference approximation we have

$$i\alpha\tilde{f} \cong \frac{1}{\Delta x}\left[\sum_{-N}^{N} a_j \mathrm{e}^{ij\alpha\Delta x}\right]\tilde{f}, \tag{16}$$

and after a little arrangement the relation becomes

$$\bar{\alpha}\Delta x \cong -i\left[\sum_{-N}^{N} a_j \mathrm{e}^{ij\alpha\Delta x}\right] \tag{17}$$

where it has to be noticed that $i=\sqrt{-1}$ and j is the index. In fact there is nothing new in Equation 17 except that the finite difference approximation in physical space is transformed into the wave space. In this way, the left hand side $\bar{\alpha}\Delta x$ is named as modified wave number which is a function of exact wave number $\alpha\Delta x$ shown on the right hand side. One of the key issues of solving wave problems is that the numerical solution in the resolvable wavenumber range should be as close as possible to the exact solution. In other words, the physical shape of a wave should be well represented by numerical simulations. Thus, $\bar{\alpha}\Delta x$ should be as close as possible towards the exact wavenumber $\alpha\Delta x$. Similarly as we define the truncation error, we define an integral error between $\bar{\alpha}\Delta x$ and $\alpha\Delta x$ which reads

$$E = \int_{-\eta}^{\eta} \mid \alpha\Delta x - \bar{\alpha}\Delta x \mid^2 d(\alpha\Delta x) \tag{18}$$

where η is the integral range with $\eta = \pi/2$ representing the full wavenumber range. Recall that we have a free parameter a_j which is used here to minimize the integral E. This is done by taking the derivative of E with respect to the only unknown a_j and force the derivative to be zero.

$$\frac{\partial E}{\partial a_j} = 0, \qquad j \in [-N, N] \tag{19}$$

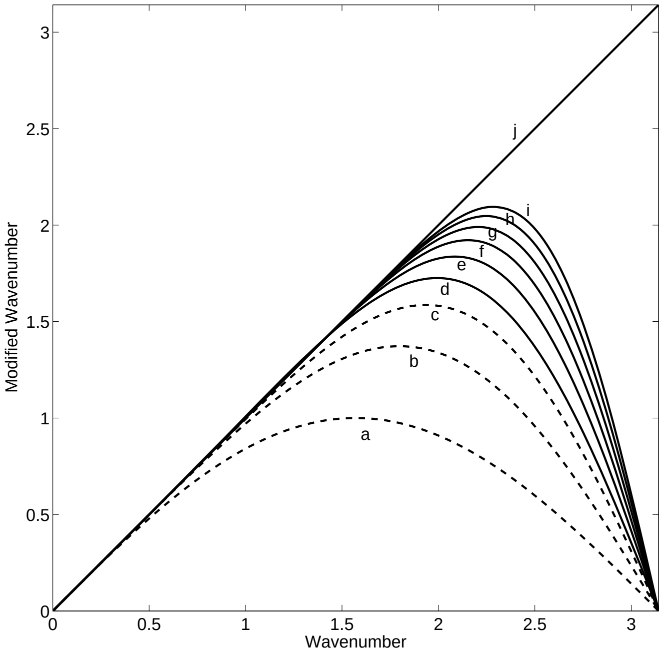

Figure 87. Wave number versus modified wave number for standard and optimized finite difference schemes. Dashed lines: original schemes; Solid lines: optimized schemes. (a) second-order finite difference; (b) fourth-order finite difference; (c) sixth-order finite difference; (d) fourth-order DRP; (e) sixth-order DRP; (f) eighth-order DRP; (g) tenth-order DRP; (h) twelfth-order DRP; (i) fourteenth-order DRP; (j) exact solution.

Figure 87 shows the plots of modified wave number versus exact wave number for schemes with different order of accuracy. For the fourth-order optimized scheme, the modified wavenumber $\bar{\alpha}\Delta x$ follows well with the straight line $\bar{\alpha}\Delta x = \alpha\Delta x$ in the range of $\bar{\alpha}\Delta x < 1.5$. At $\bar{\alpha}\Delta x$ greater than 1.5, the modified wavenumber starts to deviate from the exact line which mean that it produces dispersion errors to the original PDEs. This limited wavenumber corresponds to the smallest wavelength that is resolvable on the mesh. By noticing that the wavelength λ is calculated as $\lambda = 2\pi/\alpha$ and use the relation that $\bar{\alpha}\Delta x < 1.5$, one immediately finds that the resolvable wavelength is limited to $\lambda > 4.2\Delta x$. To resolve waves with smaller wavelength, either the mesh size needs to be reduced or higher-order schemes have to be employed. Different schemes have different limitations of resolvable short wave components. Here we compare them qualitatively by introducing a parameter: the resolving efficiency. First, it is defined that $\varepsilon \geq \frac{|\bar{\alpha}\Delta x - \alpha\Delta x|}{\alpha\Delta x}$ where ε is the error tolerance, e.g. $\varepsilon = 0.01$. Each tolerance ε corresponds to a highest modified wavenumber which directly relates to the resolving efficiency. For different schemes shown in Figure 87, their resolving efficiencies are quantified and tabulated in Table 11. It is evident that the optimized schemes stay close to the exact solution over a wider range of wavenumbers. Also, as the order of accuracy increases the scheme is able to resolve shorter waves. As seen in Table 11, in case $\varepsilon = 0.001$ the schemes with fourteenth-order (curve i) resolves maximum wavenumber around 1.68 which is about 22 times better than the second-order scheme (curve a).

Schemes	$\varepsilon = 0.1$	$\varepsilon = 0.01$	$\varepsilon = 0.001$
(a)	0.707	0.243	0.075
(b)	1.254	0.743	0.417
(c)	1.536	1.089	0.731
(d)	1.717	1.509	1.431
(e)	1.834	1.605	1.481
(f)	1.921	1.695	1.525
(g)	1.990	1.776	1.576
(h)	2.045	1.848	1.629
(i)	2.091	1.913	1.682

Table 11. Maximum resolvable wavenumber of the schemes shown in Figure 87.

8.4 Results

Noise generation from an airfoil in turbulent flow is of our interest. Some previous work have concerned noise generation from symmetric airfoils, such as NACA 0012 [16–18] and NACA 0015 [15]. In this section flow/aeroacoustics computations are carried out for flow over a two-dimensional NACA 64418 airfoil which is used for some wind turbine blades. The flow is set at the same conditions as in the experiment [11], which is at Reynolds number of 3.1×10^{6}, an angle of attack of 2.7^{0} and a Mach number of 0.178. The computational domain extends about 25 chord-lengths in the radial direction. A structured body-fitted O-mesh is generated with 48 blocks of 96×96 mesh cells in each blocks which yields a total number of grid points of 442368. The mesh configuration is shown in Figure 88 where the smallest grid height near the airfoil surface is within the order of 10^{-5}. The 2nd-order finite volume code EllipSys2D [13, 14] is used for flow simulation. Small scale turbulence structures are modeled with a Sub-Grid Scale (SGS) model for Large-eddy Simulation (LES). For acoustic computation, the 6th-order optimized compact finite difference scheme is used in space and the 4th-order Runge-Kutta scheme is used for time advancing.

The acoustic simulation is started after the flow reaches a periodic state. An example of a fully developed flow field is given in Figure 89 where the hydrodynamic pressure contour is presented. After that, flow and acoustic computations run together at each time iterations. For each iteration, the solution from flow field form the input to the acoustic simulation. However, the acoustic field does not give any feed back to the flow field with the assumption of low Mach flow. The snapshot of the acoustic pressure field is shown in Figure 90 at a dimensionless time of t=5. The time step used for the acoustic simulation is 10^{-5}, therefore t=5 is equal to a iteration number of 500000. It is found in this case that the main sound source is located at the trailing edge and propagates radially with the speed of sound.

At each time step, the acoustic pressure signals are saved in a data file. About 2000000 time iterations are performed for acoustic simulation. For post-processing, FFT is carried out for the acoustic pressure signal that contains 2000000 sampling data. The resulting sound spectrum is shown in Figure 91 as 'DTU CAA Model'. The sound spectrum, referred to 'DTU Empirical model' is based on results from the semi-empirical airfoil noise prediction code [12] developed in DTU.

It is noticed from Figure 91 that low frequency noise is omitted from the experiment data due to the influence of the background noise from the tunnel itself. The comparison shows good

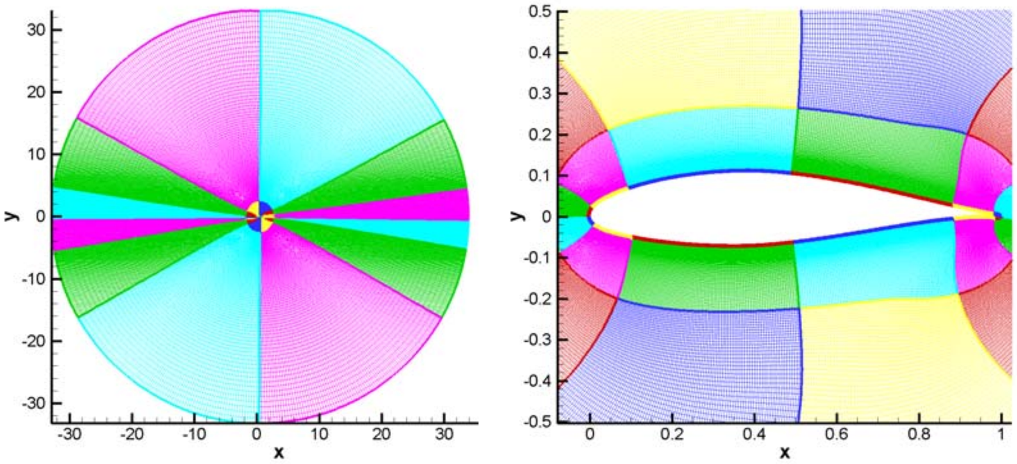

Figure 88. Mesh configuration.

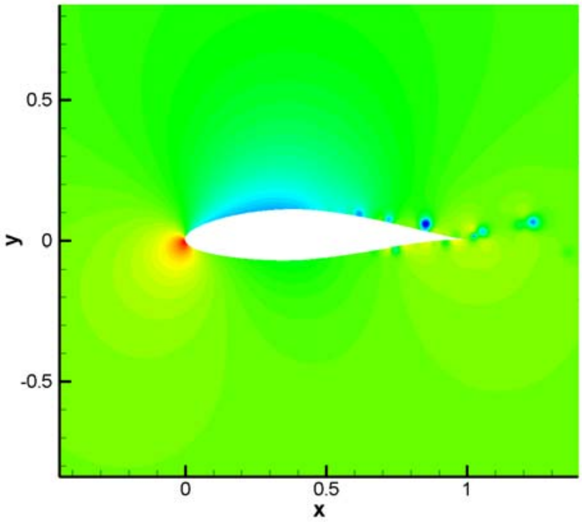

Figure 89. Incompressible pressure.

agreement for frequencies below 3000 Hz. The predicted sound level is dissipated at very high frequencies due to limited number of mesh points per wave length, therefore noise at higher frequencies are not predictable with the present mesh size.

8.5 Conclusions

This chapter presented an flow/acoustic splitting method for airfoil noise prediction. The flow and acoustic field are solved with the inhouse code EllipSys where a 6th-order optimized compact scheme is used for the acoustic simulation. The NACA 64418 airfoil has been chosen for aeroacoustic study since it is one of the most popular airfoil profiles used for wind turbine blades. Also, wind tunnel measurements exist for NACA 64418 airfoil and can be used for com-

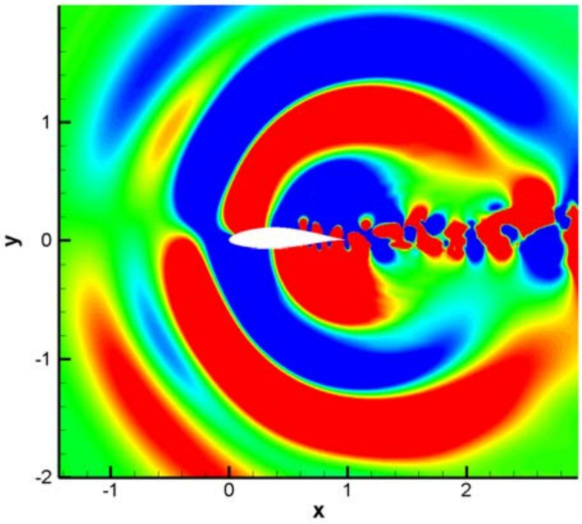

Figure 90. Acoustic pressure

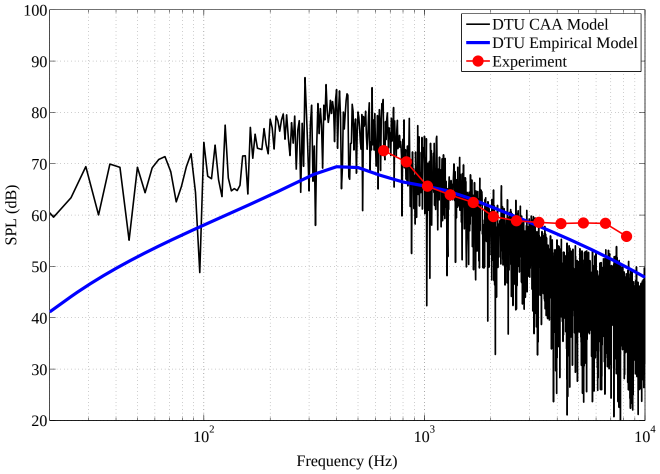

Figure 91. Sound spectrum comparison with measurement [11].

parison. The numerical predictions showed good agreement with measurements. The highest frequency appears at 600 Hz and the spectrum is generally broadband without significant tonal behavior.

References

[1] J.C. Hardin, D.S. Pope, An acoustic/viscous splitting technique for computational aeroacoustics, *Theoret. Comput. Fluid Dynamics* 6 (1994) 321.

[2] W.Z. Shen, J.N. Sørensen, Comment on the aeroacoustic formulation of Hardin and Pope, *AIAA J.* 1 (1999) 141.

[3] R. Ewert, W. Schröder, Acoustic perturbation equations based on flow decomposition via source filtering, *J. Comput. Phy.* 188 (2003) 365.

[4] J.H. Seo, Y.J. Moon, Perburbed compressible equations for aeroacoustic noise prediction at low Mach numbers, *AIAA J.* 43 (2005) 1716.

[5] W.Z. Shen, J.N. Sørensen, Acoustic modeling of low-speed flows, *Theoret. Comput. Fluid Dyn.* 13 (1999) 271.

[6] W.Z. Shen, J.N. Sørensen, Aero-acoustic modelling of turbulent airfoil flows, *AIAA J.* 39 (2001) 1057.

[7] W.Z. Shen, J.N. Sørensen, A collocated grid finite volume method for aeroacoustic computations of low-speed flow, *J. Comput. Phy.* 196 (2004) 348.

[8] C.K.W. Tam, J.C. Webb, Dispersion-Relation-Preserving finite difference schemes for computational acoustics, *J. Comput. Phy.* 107 (1993) 262.

[9] S.K. Lele, Compact finite difference schemes with spectral-like resolution, *J. Comput. Phy.* 103 (1992) 16.

[10] J.W. Kim, D.J. Lee, Optimized compact finite difference schemes with maximum resolution, *AIAA J.* 34 (1996) 887.

[11] A. Herrig, W. Würz, S. Wagner, Silent Rotors by Acoustical Optimization,Report,University of Stuttgart

[12] W. J. Zhu, N. Heilskov, W.Z. Shen, and J.N. Sørensen, Modeling of Aerodynamically Generated Noise from Wind Turbines, *Journal of Solar Energy Engineering*, Vol. 127, 2005, pp. 517-528.

[13] J.A. Michelsen, Basis3D - A platform for development of multiblock PDE solvers, (1992) Technical Report AFM 92-05. Technical University of Denmark.

[14] N.N. Sørensen, General purpose flow solver applied over hills, (1995) RISø-R-827-(EN) Risø National Laboratory, Roskilde Denmark.

[15] W. Z. Shen, W. J. Zhu and J. N. Sørensen, Aero-acoustic computations for turbulent airfoil flows, *AIAA Journal* DOI: 10.2514/1.40399, March 2009.

[16] W. J. Zhu, J. N. Sørensen and W. Z. Shen, Computational Aero-acoustic using high-order finite-difference schemes, *TWIND Conference*, Copenhagen, Denmark, August 2007.

[17] W. J. Zhu, Aero-acoustic computations of wind turbines, Doctorial thesis, MEK-PHD 2007-09/ISBN 978-87-7475-348-3 (2007).

[18] W. J. Zhu, J. N. Sørensen and W. Z. Shen, Numerical study on turbulent airfoil noise with high-order schemes. *European Wind Energy Conference (EWEC)*, Marseille, France, March 2009.

9 Prediction of Multi Element Airfoils With the EllipSys Code

Author: Niels N Sørensen

9.1 Introduction

The present work aims at verifying the capability of the EllipSys2D code to predict the performance of multi-element airfoils. The verification consists of two parts: firstly to construct a good quality computational mesh around a three element airfoil, and secondly comparing the results from Reynolds Averaged Navier-Stokes predictions including both free and fixed transition using the EllipSys2D code with measurements from wind tunnels. The airfoil used in the present computations are the AGARD A2 configuration, see [1].

9.2 Code description

The in-house flow solver EllipSys3D is used in all computations presented in this paper. For a more thorough description of this code, see Page 42.

9.3 Computational grids

The grid around a multi-element airfoil is slightly more complex than the grids normally used for single element airfoils, that is routinely computed in connection with wind energy applications. Therefore, the study of multi element airfoils pose additional challenges to the grid generation process. As the basic EllipSys code, used in the present study, is a structured multi-block patched grid solver, the grid needs to conform to these requirements. For the single element airfoils, O-grid configurations have been shown to be well suited for predicting lift-drag polars. And as the in-house HypGrid2D code is efficient at producing these type of grids, the obvious choice is to investigate whether the O-mesh topology can be applied to the multi-element configuration as well. The idea, is simply to imagine that we draw a line around the total geometry, forming an unbroken line from the trailing edge of the flap airfoil, along its pressure side over the gap between the flap and the main airfoil, along the pressure side of the main airfoil, over the gap to the trailing edge of the slat, around the slat, and returning along the suction side of the main and flap airfoil. In this process, it is necessary to assure that the grid cells coincide along the top and bottom side of the two gaps between the three airfoil sections. Based on this unbroken o-line, the mesh can be generated in the standard way using the HypGrid2D code. Alternatively, a more advanced blocking of the geometry could be used, similar to the one used by Fritz [2]. In order to allow generation of grids based on the O-mesh topology, the existing HypGrid2D grid generator was enhanced with two additional possibilities: A scaling factor that increases the dissipation in the off-wall region away from the geometry, and a feature that allows the grid generator to coarsen the grid in the normal direction removing e.g. every second vertex. Both features help the grid generator to avoid crossing of grid lines in the strongly concave regions that exist between two closely spaced airfoil sections. Based on the described O-mesh technique a 135 block mesh, with 32×32 cells in each block was generated for the AGARD A2 multi-element airfoil section, see Moir [1]. The mesh has 27 blocks in the chordwise direction, 8 blocks on the flap airfoil, 9 blocks on the main airfoil, 6 blocks on the slat airfoil, and the last 4 blocks used to span each side of the two gaps between the flap and main airfoil and main airfoil and slat, respectively. In the normal direction 5 blocks are used. The total number of cells is 138240 cells, with 864 cells in the chordwise direction and 160 cells in the normal direction, see Figure 92.

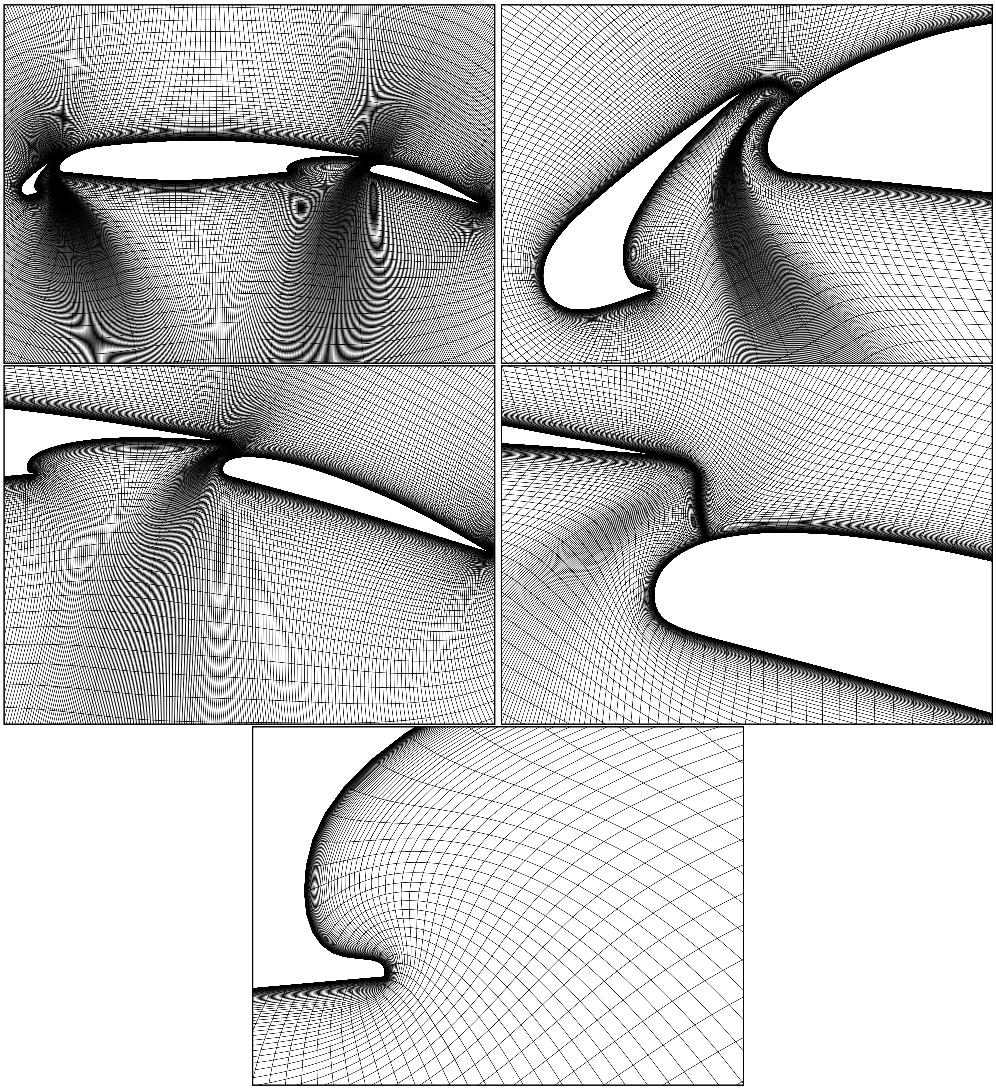

Figure 92. Mesh around the full multi-element airfoil, showing the full geometry (top left), detail near the slat (top right), zoom on the flap (center left), and the details of the mesh between the main and the flap airfoil (center right), and finally a detail at the cavity of the main airfoil where the flap airfoil is located when not deployed (bottom).

9.4 Results

The computed case corresponds to the AGARD A2 multi-element airfoil case of Moir [1], and the coordinates of the slat, main and flap airfoils are given in Tables 12, 14 and 13. The Reynolds number used in the computations is 3.52×10^6 based on the chord of the main airfoil. In the test the free stream Mach Number was 0.197 which should be well approximated by the incompressible assumption of the EllipSys code. One exception may be the highly accelerated flow in the gap between the slat and the main airfoil. The transition location on the configuration was fixed on the main element at 0.125 on both upper and lower side, while both the flap and slat have free transition. All results are presented normalized with a chord of one. In the EllipSys2D computations a low inflow turbulence level of 0.01% was used, to emulate a natural transition environment.

Comparison of the computed lift values with two different series of wind tunnel tests is shown in Figure 94. Good agreement is found in the region between zero and twenty degrees AOA, where the EllipSys computations closely follow the measured lift behavior. Similar to the behavior observed for single element airfoils, the airfoil stall around 21-22 degrees is not well

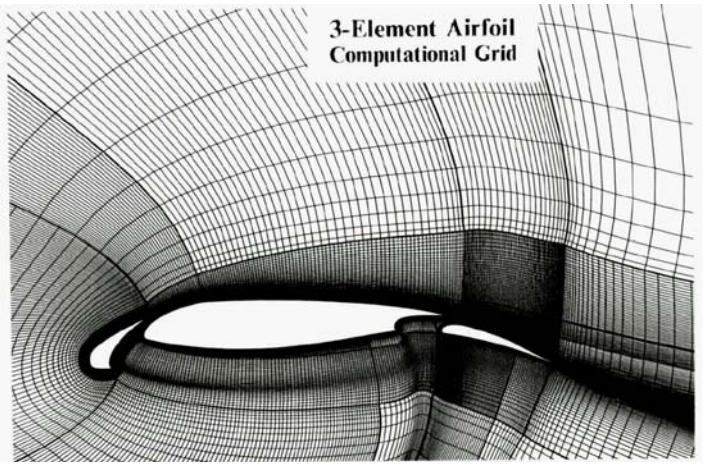

Figure 93. A general multi-block mesh, taken from Fritz [2].

captured. With the use of multi-element airfoils it is possible to retain attached flow all the way to 20 degrees angle of attack. Additionally, extremely high lift values can be obtained without a prohibitive drag penalty.

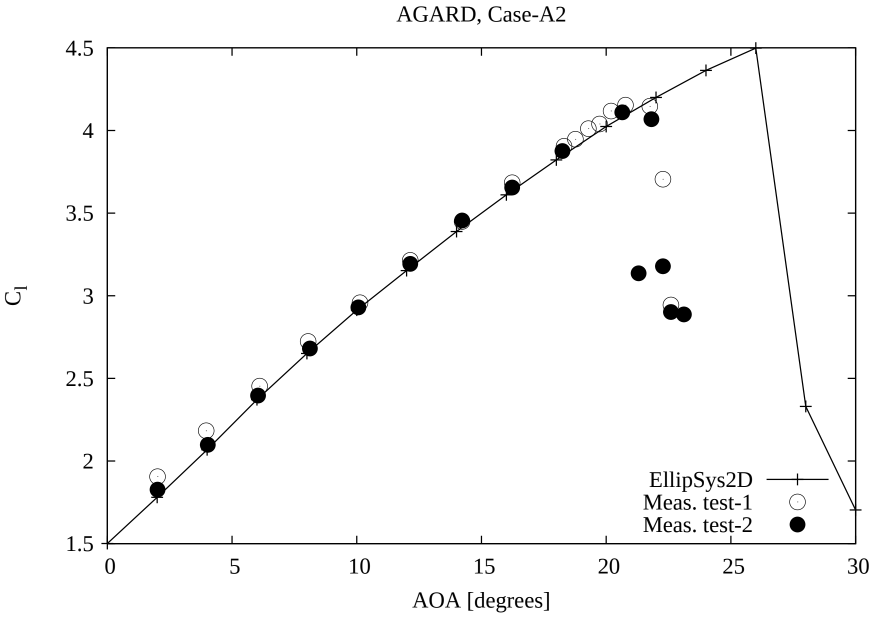

Figure 94. Comparison of computed and measured lift values for the AGARD A2 test case.

The drag predictions are also reasonable good in the attached region between 0 and 20 degrees, whereas the increase in drag due to flow separation in the computations is delayed to around 26 degrees instead of the measured 21-22 degrees. see Figure 95.

Looking at limiting stream lines around the AGARD A2 configuration for 20 degrees angle of attack, see Figure 96 and 97, it can be observed that even at this extremely high angle of attack and high lift value, the flow stays attached due to the advanced airfoil configuration.

Unfortunately, the full data set from the AGARD test has not been available, but comparison with the pressure distribution at 4.01 degrees is shown in Figure 98. Generally, the agreement

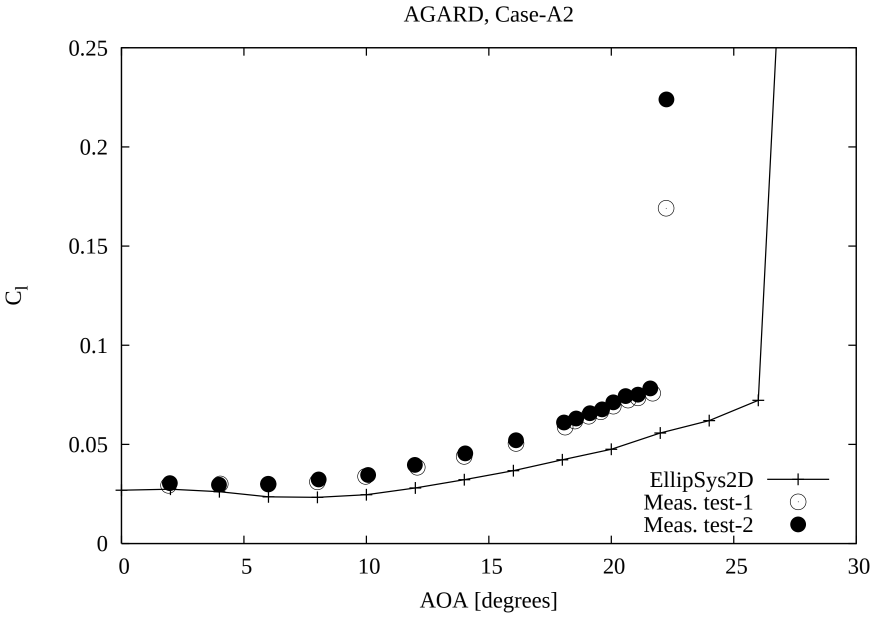

Figure 95. Comparison of computed and measured drag values for the AGARD A2 test case.

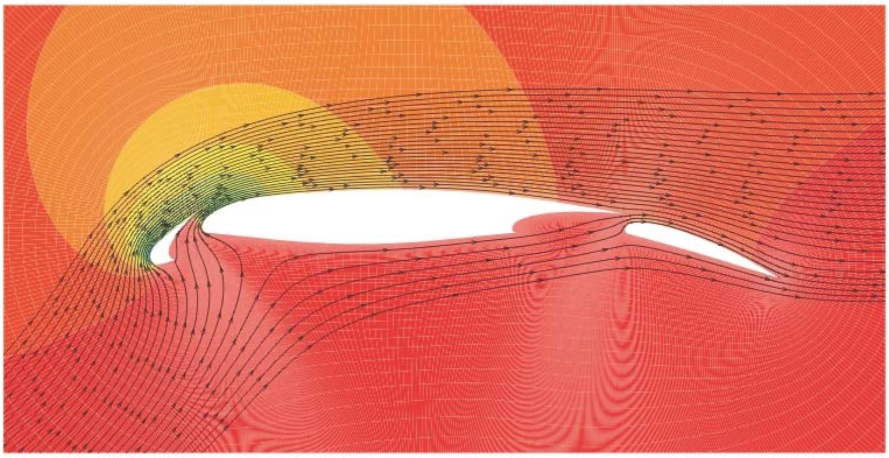

Figure 96. Flow around the AGARD A2 configuration at 20 degrees angle of attack, visualized by pressure contours and limiting streamlines. The red colors indicate high pressure while the green and blue colors indicate low pressure regions.

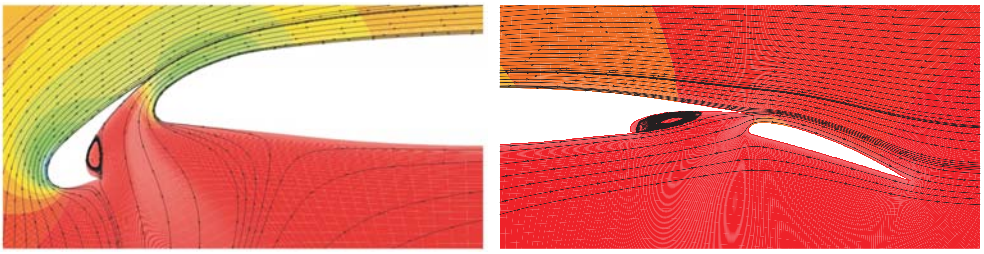

Figure 97. Details of the flow around the AGARD A2 configuration at 20 degrees angle of attack, showing the recirculation at the slat left and at the flap cavity of the main airfoil. The red colors indicate high pressure while the green and blue colors indicate low pressure regions.

is excellent. Only near the gap between the slat and the leading edge of the main airfoil, some discrepancies exist. In this area, the flow may be slightly compressible due to the high local flow velocity. The details of the pressure distribution on both the slat and the flap are well reproduced by the flow solver.

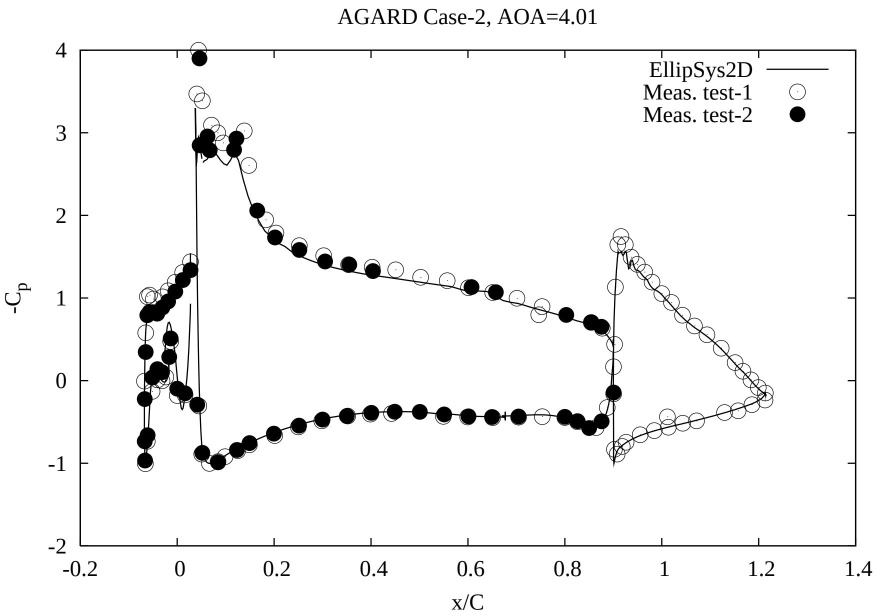

Figure 98. Comparison of computed pressure distribution and measured for the case

9.5 Conclusion

Based on the comparison between the computed results and the available measured data, it has been verified that the EllipSys2D code is capable of predicting the flow around a multi element airfoil. Secondly, it has been shown the correlation based transition method implemented in the code is robust and stable also under these conditions. The mesh used in the present computations has a very high resolution and ongoing test have shown that the mesh is more than fine enough in the normal direction. Additional test with coarser resolutions should be performed in the future. Based on these findings, the EllipSys2D code seems to be a valid tool for verifying high lift configurations based on the multi element concept.

9.6 Acknowledgement

The work was funded by the Danish Energy Agency under contract ENS-33033-0055, Computations were made possible by the use of the MARY and Thyra PC-cluster at Risø National Laboratory and the DCSC, PC-cluster Yggdrasil and Alfheim.

References

[1] I.R.M. Moir. Measurements on a Two-Dimensonal Aerofoil with High-Lift Devices. In *A Selection of Experimental Test Cases for the Validation of CFD Codes*, volume II. AGARD ADVISORY REPORT NO 303, August 1993.

[2] Fritz W. Calculation of Maximum and High Lift Characteristics of Multi Element Airfoils.

In *High-Lift System AerodynamicsTurbulence and Transition Modelling*, pages 96–107. AGARD-CP-515, September 1993.

9.7 Appendix: Geometry description

Table 12. The 37 coordinates describing the slat airfoil and its position

x_{slat}^{1-13}	y_{slat}^{1-13}	x_{slat}^{14-26}	y_{slat}^{14-26}	x_{slat}^{27-37}	y_{slat}^{27-37}
0.027490	0.017991	-0.017118	-0.075335	-0.063478	-0.055113
0.021231	0.013241	-0.016780	-0.076060	-0.059726	-0.049766
0.011552	0.004325	-0.025493	-0.079097	-0.053690	-0.043024
-0.004135	-0.011795	-0.035315	-0.082430	-0.046491	-0.036434
-0.012160	-0.021418	-0.042170	-0.084269	-0.034454	-0.026043
-0.018975	-0.031128	-0.049084	-0.085176	-0.019737	-0.014303
-0.022844	-0.037478	-0.055933	-0.084663	-0.006940	-0.004739
-0.027273	-0.046152	-0.059101	-0.083382	0.008486	0.006239
-0.029451	-0.052343	-0.062122	-0.081635	0.013998	0.010012
-0.030201	-0.061288	-0.066395	-0.076400	0.019714	0.013891
-0.028411	-0.069148	-0.067831	-0.070173	0.027025	0.018988
-0.024596	-0.073614	-0.067150	-0.063754		
-0.018756	-0.075514	-0.066302	-0.060865		

Table 13. The 39 coordinates describing the flap airfoil and its position.

x_{flap}^{1-13}	y_{flap}^{1-13}	x_{flap}^{14-26}	y_{flap}^{14-26}	x_{flap}^{27-39}	y_{flap}^{27-39}
1.214624	-0.113530	0.909167	-0.023871	0.971630	-0.005932
1.193291	-0.106968	0.905108	-0.022393	0.977522	-0.007257
1.150970	-0.093895	0.901391	-0.019944	0.989221	-0.010143
1.123617	-0.085397	0.900339	-0.012133	0.995344	-0.011797
1.097197	-0.077260	0.907722	-0.004509	1.001430	-0.013554
1.058932	-0.065674	0.915378	-0.001953	1.020150	-0.019516
1.034620	-0.058528	0.920255	-0.001185	1.034272	-0.024486
0.996129	-0.047562	0.926453	-0.000706	1.063809	-0.035726
0.967841	-0.039703	0.930333	-0.000745	1.097886	-0.050076
0.953663	-0.035852	0.937713	-0.000877	1.125638	-0.063296
0.940446	-0.032286	0.941848	-0.001212	1.155608	-0.079195
0.926244	-0.028500	0.950351	-0.002146	1.183517	-0.094908
0.917211	-0.026096	0.960400	-0.003718	1.214740	-0.113210

Table 14. The 84 coordinates describing the main airfoil and its position.

x_{main}^{1-28}	y_{main}^{1-28}	x_{main}^{29-56}	y_{main}^{29-56}	x_{main}^{57-84}	y_{main}^{57-84}
0.899870	0.017200	0.368260	-0.043910	0.134530	0.047900
0.871260	0.019430	0.333670	-0.043750	0.153460	0.050670
0.835990	0.021190	0.300070	-0.042880	0.168330	0.052460
0.802400	0.021820	0.267800	-0.041420	0.172890	0.052960
0.766470	0.020920	0.232870	-0.039160	0.182440	0.054030
0.753490	0.019960	0.202590	-0.036530	0.200270	0.055850
0.735200	0.017900	0.167000	-0.032930	0.203160	0.056150
0.729540	0.017030	0.136730	-0.029770	0.234300	0.058920
0.718900	0.015170	0.101460	-0.026280	0.266130	0.061280
0.709580	0.013210	0.084170	-0.024550	0.301060	0.063370
0.701600	0.011010	0.071120	-0.023250	0.335000	0.064970
0.690290	0.007120	0.067860	-0.022820	0.366270	0.066030
0.682300	0.003430	0.061240	-0.022290	0.401530	0.066770
0.676980	-0.000170	0.054720	-0.021660	0.434460	0.067000
0.672990	-0.004160	0.052890	-0.021420	0.468400	0.066730
0.669990	-0.011380	0.048640	-0.021060	0.499000	0.066030
0.673320	-0.019060	0.043550	-0.019330	0.533270	0.064740
0.677310	-0.020330	0.039060	-0.015140	0.567860	0.062840
0.677310	-0.020960	0.037490	-0.009480	0.599800	0.060480
0.668660	-0.021720	0.039190	-0.001600	0.635400	0.057520
0.634730	-0.024850	0.043650	0.006190	0.668660	0.053560
0.602130	-0.028010	0.048240	0.010880	0.701260	0.049500
0.567860	-0.031570	0.055920	0.016870	0.734530	0.044940
0.534930	-0.034700	0.062110	0.020990	0.765140	0.040450
0.500670	-0.037820	0.072390	0.026910	0.799070	0.035100
0.466730	-0.040350	0.083730	0.032240	0.833330	0.029440
0.432470	-0.042250	0.104760	0.040220	0.867930	0.023520
0.400200	-0.043450	0.117300	0.044210	0.899870	0.017900

10 Thick airfoils & High lift

Author: Mac Gaunaa, Niels Sørensen & Christian Bak, Risø-DTU

The work presented in this section shows that is possible to increase the lift and performance characteristics of thick airfoils significantly by use of a multiple airfoil approach. Specifically, investigations of using a single airfoil as a slat in front of a thick airfoil is investigated. The possible increase in lift for the thick airfoils opens up possibilities for significant increase in maximum power production of conventionally designed MW-size wind turbines at the cost of an increased thrust force.

10.1 Introduction

10.1.1 Why is high lift and thick airfoils an interesting combination?

Recent aerodynamic investigations [1] have shown that the terms neglected standard Blade Element Momentum (BEM) theory as outlined by Glauert [2] causes a less than optimal power production due to a too low loading on the inner part of the rotor. The additional loading needed should counterbalance the increased pressure jump over the rotor disc due to the rotation of the wake after the rotor[1]. Since most tools for rotor design are based on the standard BEM formulation, a rotor designed for maximum energy yield will be too lightly loaded toward the rotor centre. Apart from this, the combination of material cost, stand still loads and maximum chordlength due to transportation requirements have resulted in the inner part of conventionally designed MW-size wind turbine rotors being loaded significantly less than what is required for optimal power production. A quantification of the obtainable additional maximum power production can be seen in the work by Johansen et.al. [3], where CFD computations on a rotor designed for maximum power production is compared to the IEA 5MW Reference Wind Turbine (RWT), which is believed to be representative of modern commercial blade designs. Figure 99 below show the spanwise distribution of local power and thrust coefficients of the rotor designed for maximum energy production compared to the IEA 5MW RWT. It is seen from the left hand side figure that the possible increase in power is quite large on the inner part of the rotor. The cost of this in terms of loads is the added thrust, which is shown in the right hand side of the figure. In terms of integral power and thrust coefficients, listed in Table 15, it is seen that the possible increase in maximum power is 8%, which comes at the cost of 12% increase in thrust.

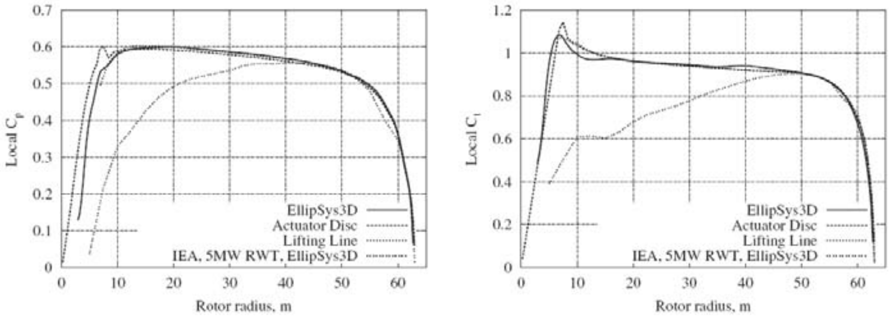

Figure 99. Spanwise distribution of local $C_p = (dP/dr)/(\rho V_\infty^3 \pi r)$ (left) and $C_t = (dT/dr)/(\rho V_\infty^2 \pi r)$ (right) for the optimal power production case and the IEA 5MW RWT, from [3].

The maximum power output of conventionally designed commercial MW size wind turbines can be significantly increased by increasing loading on the inner part of the rotor

In order to obtain a rough estimate of the the increase in lift force needed for the RWT case to harvest the extra available production near the root, we note that, to a good approximation,

---

[1] This is the term that is neglected in the standard BEM formulation

Table 15. Integral power and thrust coefficients for the IEA 5MW RWT and the optimal power production case from [3].

	C_P	C_T
IEA 5MW RWT	0.477	0.78
Optimal	0.515 (+8%)	0.87 (+12%)

thrust is proportional to lift. Therefore we get the approximate relation

$$\frac{L_{needed}}{L_{RWT}} \simeq \frac{C_{t,opt}}{C_{t,RWT}} \tag{20}$$

In fact, if we use the original blade chord as reference when nondimensionalizing the forces, the same relation hold for the nondimensional quantities:

$$\frac{C_{L,needed}}{C_{L,RWT}} \simeq \frac{C_{t,opt}}{C_{t,RWT}} \tag{21}$$

Table 16 below show the approximate ratio $C_{t,opt}/C_{t,RWT}$ taken from the results in Figure 99.

Table 16. Local thrust coefficient ratios for the optimal power output turbine and the IEA 5MW RWT, results from [3] shown in Figure 99.

r/R	0.2	0.3	0.4	0.5
$C_{t,opt}/C_{t,RWT}$	1.7	1.5	1.3	1.2

That is, the lift needed for optimal power production in for instance the 20% radius position is 1.7 times the magnitude of the lift in the conventional design.

Since the inner part of the blades carry the big flapwise loads from the thrust forces, a certain building height is needed from the structural requirements[2]. The transport requirements, on the other hand, require that the maximum chordwise dimension of the blades do not exceed a maximum value.This results in airfoil sections on the inner part that have a high relative thickness, which is not advantageous seen from the aerodynamic point of view. When combining this with the increased lift force needed to tap into the "unused power potential" from the root section, we see that modifications of thick airfoils, or some sort of add-on's to thick airfoil sections, that produce significantly higher lift than what can be accomplished with standard thick airfoil sections alone are needed. Since, furthermore, the drag component is counterproductive with regards to power power production, we aim for a method for which the added drag component associated with the increase in lift is as small as possible.

10.1.2 Selection of high lift method for thick airfoils

As can be seen in standard aerodynamic literature (Abbott and Von Doenhoff [4] is an excellent source with regards to this), a multitude of methods and devices exist for obtaining high lift on the relatively thin airfoils typically used for aviation purposes. Since we are looking for methods and devices that will increase lift significantly whilst keeping a low drag, both vortex generators and Gurney flaps are discarded. Due to the load carrying requirements of the thick inner sections, it may be problematic with slotted main airfoils. Active boundary layer control methods such as suction or blowing can produce very high lift on thick airfoils with a relatively low drag, but due to the requirements wind turbines operate under[3], the authors of this work lean towards opting for passive methods due to their robustness. One method/concept that has shown to be able to provide very high lift with a relatively small drag penalty for the aviation-type airfoils is multi element airfoils. This approach has the added benefit that the additional

Thin multi element airfoils have the properties we are looking for for the thick airfoils

---

[2] bending resistance for a given material thickness is proportional to building height squared

[3] Very long maintenance intervals, inconvenient having too much machinery in the blades, suction/blowing holes being filled with dirt, etc.

airfoils can be mounted on the load carrying thick main airfoil at the erection site, and that manufacturing as well as mounting can be quite straightforward. Since we are looking for a change in the mean/steady characteristics of the rotor, the additional airfoil elements should be stationary with respect to the main airfoil.

Since multiple element airfoils is well documented for aviation purposes, the interesting question in our case is how well the multiple element airfoil approach will work for thick main airfoils, and how to design multiple element airfoils and configurations for thick main airfoils.

How well will the multiple element airfoil approach work for thick main airfoils?

10.1.3 Overview of the contents of this work

The remainder of this work is grouped into four sections.

The first section contains a short explanation on how and why multiple element airfoils work. This was explained in great depth by Smith [5], so that section is basically a recap of the conclusions from his comprehensive work.

In order to answer how well a multiple airfoil with a thick main airfoil can perform, a new fast aerodynamic model for evaluation of of the performance of a given setup of a multiple element airfoil was implemented. The basis of that model is explained in the second section. The method is based on a panel method and has a boundary layer solver for determination of whether the flow around the airfoil will stay attached to the airfoil. In order for the airfoil configuration to have high lift and low drag we search for cases that remain relatively attached. A partial validation of the evaluation code is performed using Risø's in-house CFD code EllipSys, which is developed in co-operation between the Department of Mechanical Engineering at the Technical University of Denmark and The Department of Wind Energy at Risø National Laboratory, see [6, 7],[8].

In the third section the reasoning behind investigating a combination of a standard thick main airfoil and a smaller airfoil in front of it acting as a slat is first given. After this the main results of the parametric study is given.

The fourth and last section contains the conclusions of this work as well as suggestions for further work.

10.2 How And Why Do Multiple Element Airfoils Work

An excellent explanation of why and how multiple element airfoils work is given by Smith [5]. However, for the sake of explaining the mechanics at play, the main conclusions from his comprehensive work is given here. Interested readers are referred to the original work.

For attached flow, the region where the viscous effects are not negligible is in the thin boundary layer near the airfoil surface. This is the boundary layer concept formulated by Prandtl. Outside this layer the flow is governed by inviscid theory, which for the incompressible flow we usually have in wind energy applications is the well known standard potential flow theory. The Kutta condition, which is applicable for attached flows, states that the flow should leave the trailing edge in a 'nice' way, that is: the gradients at the trailing edge should be finite. Having infinite gradients at the relatively sharp trailing edge would imply infinite viscous forces, which is not physically meaningful. Therefore, the Kutta condition can be thought of as an enforcement of the effect of viscosity that needs to be taken into account even for flows where the effects of viscosity are confined to an extremely thin layer at the solid surfaces. Upon neglecting the displacement effect of the boundary layer, one obtains after the solution of the inviscid, incompressible airfoil flow around a single airfoil that the lift is almost linearly increasing with the angle of attack, up to very high lift coefficients $C_l = 4\pi$ with zero lift in 2D inviscid flow. The physical mechanism responsible for this high lift not being achievable in real life is due to well known effects of viscosity: The adverse pressure gradients (or equivalently

For unseparated flows the inviscid solution using the Kutta condition should represent the flow physics well.

from Bernoulli's equation: the deceleration of the flow) makes the flow separate from the airfoil surface. When the flow is separated from the airfoil, the boundary layers are no longer thin and the simple potential flow methods using the airfoil shape cannot be used to determine the forces on the airfoil. For most practical single airfoil flows the 2D lift coefficient will very seldom exceed $C_l = 2.5$. Roughness introduced by for instance soiling of the airfoil surface significantly reduces maximum obtainable lift coefficient. Potential flow solutions of multiple airfoil configurations correspond well to the single airfoil cases. The lift increases almost linearly to extremely high (and in real life non-obtainable) values, and the mechanism responsible for this not happening is the same as for the single airfoil case. Therefore: in order to develop high lift, one must find the scenarios that put the least amount of stress on the boundary layer, i.e. preventing stall. As pointed out by Smith [5] these scenarios can be analyzed with inviscid solutions such as panel methods as long as the flow is not stalling. Therefore, boundary layer solutions in one form or another are needed when developing high lift configurations and/or airfoil shapes.

Smith's five primary effects of gaps between airfoil elements.

According the Smith [5], the five primary effects of gaps between airfoil elements is:

1. **Slat Effect** Due to the circulation on the forward element, the pressure peak on the downstream element is reduced. The main effect of a forward element (a slat) is to delay the angle of stall.
2. **Circulation Effect** The disturbance of the flow at the trailing edge of the forward element (from an intelligently located element) causes increased circulation (loading) of the forward element.
3. **Dumping Effect** The trailing edge of a forward element "dumps" the trailing edge flow at a higher velocity than what it would have done if it was alone. That is, the deceleration of the flow over that element from its suction peak is not as big as it would have been if it was a single airfoil with the same suction peak. This considerably alleviates separation compared to a single airfoil.
4. **Off-the-surface Pressure Recovery** The deceleration of the "dumped" wake is done more efficiently than can be done in contact with a solid surface.
5. **Fresh Boundary Layer Effect** Each airfoil element starts out with a fresh boundary layer. Fresh (thin) boundary layers can withstand stronger adverse pressure gradients than thick boundary layers.

As comments to items 1 and 2 is that it is evident from potential flow solutions that airfoils in the vicinity of other airfoils greatly influences each other. As is well known from e.g. thin airfoil theory, the loading on a single airfoil is highly dependent on what the conditions is at the trailing edge. Therefore, if anything is disturbing the flow near the trailing edge of an airfoil, the loading on that airfoil will be greatly influenced. A comment that should be added to clarify item 3 above is that analysis of the boundary layer flows show that what determines if the boundary layer will separate is to a good approximation how big a part of the maximum kinetic energy is left in the flow just outside the viscous boundary layer. That is: a slat airfoil having an extremely high maximum suction peak of $C_P = -20$ and "dumping" the boundary layer at it's trailing edge at $C_P = -10$ is not more likely to separate than a flow decelerating from a pressure coefficient of $C_P = -1.5$ to $C_P = -0.75$.

10.3 Multi Element Aerodynamic Computational Tool

As outlined previously, inviscid flow solutions agrees fairly well with real life cases when the flow is not separation for the surface. Therefore, a fast computational tool based on an inviscid 2D panel code by Gaunaa [9] was implemented. The basic panel code splits each airfoil up in N linear elements in which piecewise constant strength sources and vorticity is distributed. Neumann boundary conditions provide N conditions, and the Kutta condition, enforced as the tangential velocity components at the trailing edge panels on the upper and lower sides having the same size. This is sums up to $N+1$ conditions for the linear system and $2N$ variables. To reduce the number of variables, the vorticity distribution along the surface of the airfoil go from zero at the trailing edge parabolically to maximum at the surface length midpoint (close to the leading edge) to zero again at the trailing edge. This way the total circulation of each airfoil is adjusted with one variable, this reducing the number of variables to $N+1$ such that the total linear system including all airfoil elements can be solved for all the strengths. Once this is done, the (tangential) velocities on the surfaces of the airfoils can be evaluated, and with these also the inviscid forces on the airfoil elements through integration of the surface forces, from the Bernoulli equation. A more thorough description of the elements in the panel code can be found in [9].

As mentioned in the previous section, the physics of the flow is fairly well represented by the panel code solution as long as the flow is not separating. Therefore a boundary layer algorithm was coupled with the panel code solution in order to determine whether separation occurred. In order to facilitate stable aerodynamic calculations, there was not introduced a coupling from the viscous BL solution back into the panel code. This can be done using the transpiration concept as for instance in the well known XFoil code by Drela [10], but was not done in the present work. The viscous BL computations consisted in prediction of laminar BL quantities (Momentum thickness) using Thwaites method, see White [11], and estimation of laminar separation point for Thwaites parameter $\gamma = -0.09$. The transition point where onset of turbulence is located may be determined using the Cebeci-Smith transition criterium (Michel-type) [11], or simply by prescribing a transition point. For all results shown in the present work, transition to turbulence was prescribed 4% of the chordlength on each side of the stagnation point to run with what corresponds to a tripped boundary layer. Due to this, laminar separation does not occur for the simulations in this work. For estimation of the turbulent boundary layer parameters two different turbulent BL models was implemented. The first uses the Karman-type closure of the Karman integral relation with a $\Pi - \beta$ corelation as described in White [11]. The second turbulent BL model uses the more stable method given by Kroo [12], which is also based on the Karman integral relation, but this time the closure of the problem involves an expression describing the entrainment of flow into the boundary layer. The interested reader is referred to Kroo [12] for further details. Separation of the turbulent boundary is estimated using a limit of the shape factor H of 2.3. The two different ways of solving the turbulent BL gives quite similar results, but the second one is used for all parameter investigations because it is by far more stable than the first one.

The fast computational code is based on a 2D panel code for multiple airfoil elements combined with a boundary layer solver to estimate whether separation occurs.

The way in which the model is used is then to compute the inviscid solution and from that to determine whether the BL solution indicates that the flow is stalling. If the flow stalls more than 10% of the airfoil chordlengths from the trailing edge, the solution cannot be trusted. Otherwise the solution is assumed to be fairly close to what happens in reality. This way it is a simple task to quickly run through a lot of parameter studies to determine which setup has the highest lift without separating. In mean one configuration takes a half second to compute. The level of the estimated lift is somewhat dependent on how far from the trailing edge the flow is allowed to separate, but the configurations that turn out to be the optimal is fairly insensitive to this limit.

10.3.1 Validation of computational tool with CFD

In order to validate the results from the present code, a two-element thick airfoil case predicted to have a good performance was simulated in the 2D version of EllipSys. The code is developed in co-operation between the Department of Mechanical Engineering at the Technical University of Denmark and The Department of Wind Energy at Risø National Laboratory, see [6, 7],[8]. Please refer to the references for the general description of the code and Chapter 9 for validation of the code in a multiple element airfoils environment. The validational case uses the FFA3301 (30% thick) as the main thick airfoil and a FFA3360 (36% thick) of the 50% main chordlength as a "slat airfoil". The trailing edge of the slat airfoil is located at 15% of the surface length from the leading edge toward the trailing edge and 5% main chordlenghts out from the main airfoil in the direction normal to the surface. The angle of the slat airfoil is -15^{o} (positive nose up) compared to the main airfoil. Details of the computational grid for this case is shown in Figure 100.

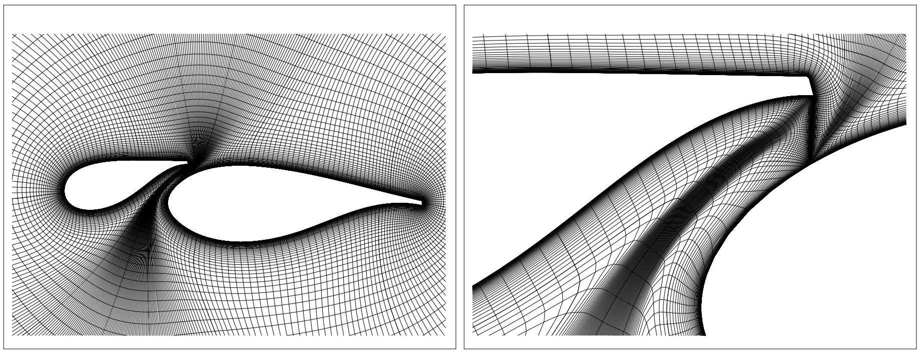

Figure 100. Details of the computational grid.

Figure 101 show the streamlines and pressures for the main airfoil alone and for the main+slat airfoil case, both for the case of a free stream flow angle of $\alpha = 16^{0}$ relative to the main airfoil. It is seen that the flow does not separate for the multiple element case, whereas the

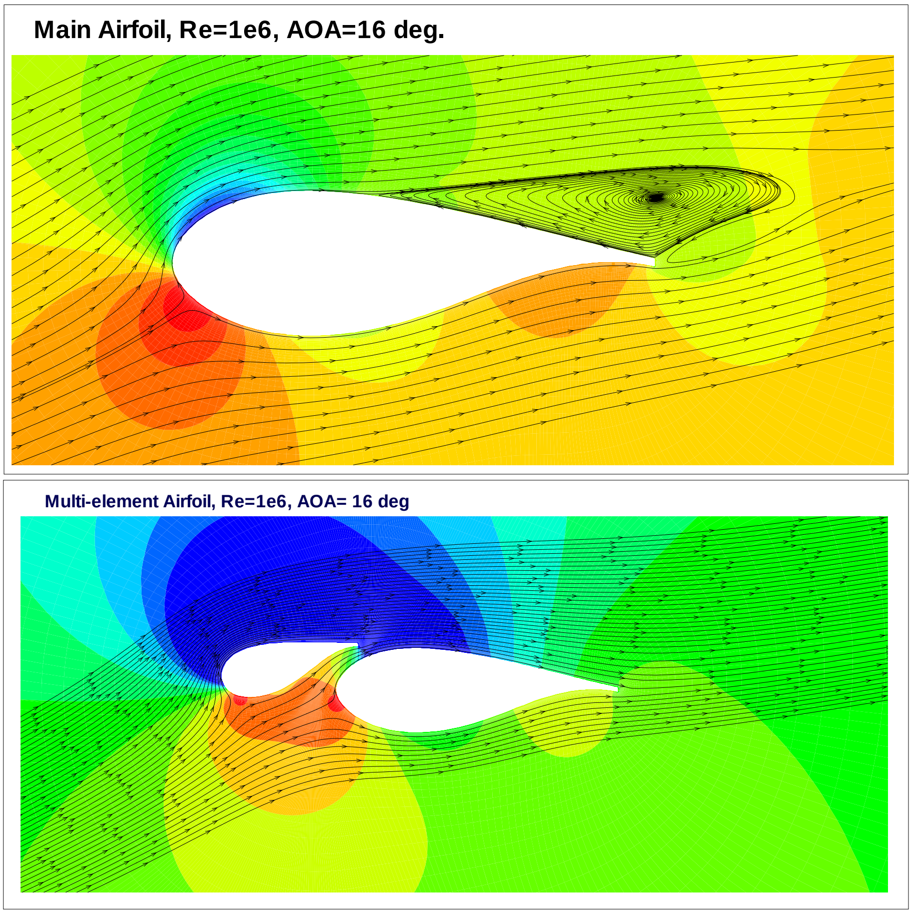

Figure 101. Details of the EllipSys computations at angle of attack $\alpha = 16^{o}$. Streamlines and pressures (Red=high, blue=low) for Re=$1 \cdot 10^{6}$. Free transition used in the computations.

single element case alone has a big region where the flow is separated. In order to evaluate the performance of the multiple element airfoil case, Figure 102 shows lift versus angle of attack (left graphs) and lift versus drag (right graphs). The length used for nondimensionalization of the forces from the multiple element airfoil is the chordlength of the main airfoil for the upper graphs and the total length of the combined two element airfoil for the lower graphs. Nondimenzionalization using the main airfoil chordlength is convenient if one is interested in comparing directly how the forces change when applying a slat airfoil. In each plot curves for

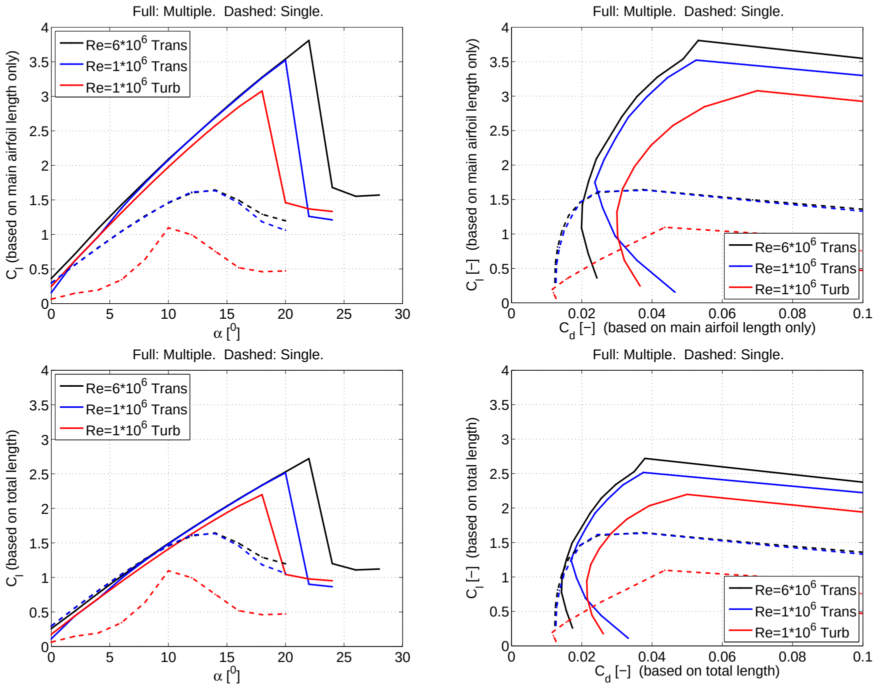

Figure 102. Lift versus angle of attack (left graphs) and lift versus drag (right graphs) for the multi element airfoil and for the main airfoil alone. The length used for nondimensionalization of the forces from the multiple element airfoil is the chordlength of the main airfoil for the upper graphs and the total length of the combined two element airfoil for the lower graphs. Full lines: Multiple airfoil. Dashed lines: Single main airfoil. Black: $Re = 6 \cdot 10^6$ *Free transition. Blue:* $Re = 1 \cdot 10^6$ *Free transition. Red:* $Re = 1 \cdot 10^6$ *Fully turbulent.*

Reynolds numbers $1 \cdot 10^6$ and $6 \cdot 10^6$ are shown. For the high Reynolds number free transition was used in the computations, whereas both free transition and fully turbulent conditions was used for the low Reynolds number. From the upper plots it is seen that the maximum lift is increased drastically for all cases, with a factor of between approx. 2.2 to 3.0. It is seen that the roughness sensitivity indicated by the poor performance of the single airfoil for the fully turbulent case is significantly lower for the multiple element case. Furthermore it is seen that the lift-to-drag ratio is actually increased for the multiple element case compared to the single element airfoil. This is shown clearly also in Figure 103, where the lift-to-drag ratios are shown as function angle of attack.

Overall, the prediction from the fast code that this multiple element airfoil combination should have good characteristics is validated using the CFD results. Returning now to the lower graphs in Figure 102, where the total length of the multiple airfoil is used for nondimensionalization. Here we see that the slope of the multi element lift curves approximately is the same as for the single airfoil, indicating that the combined airfoil acts much like a single airfoil, but with a significantly higher lift coefficient. Furthermore, it is seen that the addition of the slat airfoil does not offset the lift curve significantly. From the plots of lift versus drag it is observed that even though the minimum lift coefficient of the multiple element case is slightly higher than the single airfoil case, the drag penalty for having a more complex flow is relatively low. One thing that could be pointed out is that the simulations predict a relatively violent stall, so care

The CFD results confirms the good characteristics of the multiple element airfoil setup predicted by the fast panel code.

The CFD analysis show that the two element airfoil is superior to the single element airfoil: Lift more than doubles, lift-to-drag ratios increase, and the multiple element airfoil is less sensitive to roughness.

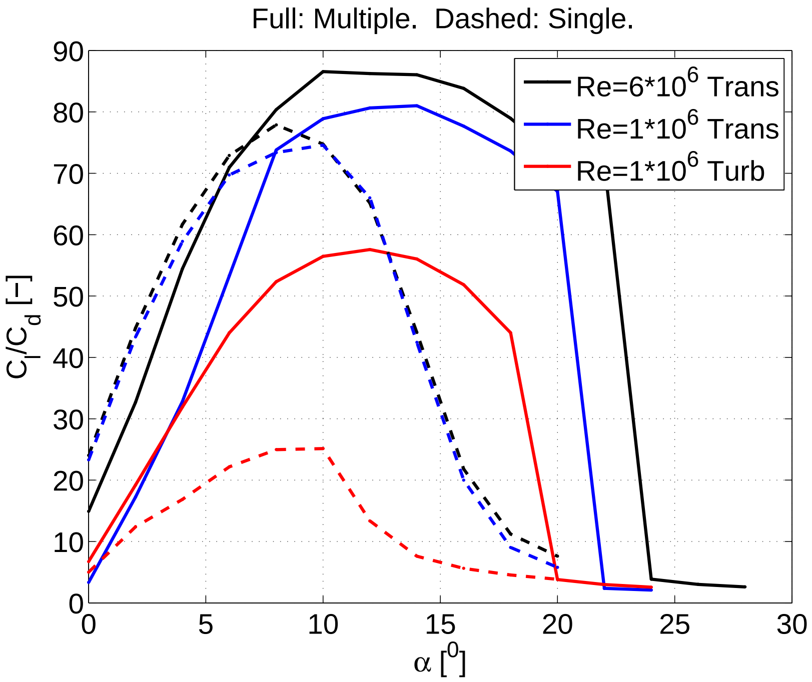

Figure 103. Lift over drag versus angle of attack. See caption of 102 for further description.

should be taken to avoid getting into this region for wind turbines to avoid unstable aeroelastic behavior. Since these thick airfoils are intended for use on the inner part of the rotor where the blade is relatively stiff this might not be that critical.

10.4 Parametric Study of Two-Element Airfoils

In order to get a fist insight into what results can be obtained with the multiple element airfoil approach for thick airfoils it was chosen to do parametric studies of two-element airfoils. Since the angles of attack at the inner part of the blades may be rather high it was chosen to investigate the case where the thick main airfoil is supplemented with a smaller airfoil in front of it to act as a slat. This configuration generally results in a delayed stall, whereas adding an extra airfoil element after the main airfoil usually lifts the zero (main airfoil) angle of attack lift considerably. In order to limit the number of parameters, it was chosen to use two well known and widely used thick airfoils as the main airfoils: The FFA3301 (30% relative thickness) and the FFA3360 (36% relative thickness). For both of these airfoils two slat airfoils was used: The thick FFA3360 (36% relative thickness) and the thin NACA63615 (15% relative thickness). Two sizes of the leading edge airfoils was tested, $c_{slat}/c_{main} = 0.3$ and $c_{slat}/c_{main} = 0.5$. The position of the slat airfoils relative to the main airfoil was defined using three parameters, two of which determines the position of the trailing edge of the slat airfoil: $s_{TE,slat}$ and $n_{TE,slat}$ and one angle offset β, positive nose-up. The surface length parameter $s_{TE,slat}$ is normalized to -1 at the (lower) trailing edge of the main airfoil, 0 at the leading edge and 1 at the (upper) trailing edge, while the parameter for the normal distance away from the main airfoil $n_{TE,slat}$ is normalized with the main airfoil length. The last parameter used in the parametric study adds parabolic camber to the slat airfoil. $k_{camber} = 0.05$ corresponds to a parabolic camber such that the surface coordinates normal to the chordline of the slat is moved 5% of the slat cordlength towards the suction side at the mid-chord. The angle of the free stream flow with respect to the main airfoil is given by α. Table 17 outlines the parameter space investigated. For all the cases investigated the Reynolds number based on the main airfoil length was $2 \cdot 10^6$.

Computations of each of the 303264 cases in the parametric study was performed using the

Table 17. Parameter space for the parametric investigations.

Main Airfoils	Slat Airfoils	Slat Size	Surface parameter slat TE pos.
FFA3301(30%) FFA3360(36%)	NACA63615(15%) FFA3360(36%)	$c_{slat}/c_{main} =$ $[0.3, 0.5]$	$s_{TE,slat} =$ $[0.0 : 0.05 : 0.25]$

Norm. param. slat TE pos.	Slat angle	Slat parabolic camber	free str. flow angle
$n_{TE,slat} =$ $[0.05, 0.10]$	$\beta =$ $[-30^o : 2.5^o : 0^o]$	$k_{camber} =$ $[0.0, 0.05, 0.10]$	$\alpha =$ $[0^o : 0.5^o : 40^o]$

described algorithms implemented in Matlab during 30 hours on a standard laptop computer.

As mentioned earlier the goal when working with high lift aerodynamics is essentially to find the conditions where stall is postponed as much as possible. The main findings from the analysis of the cases in the parameter study are listed below.

Results from the parameter study indicate that the lifting performance of a thick airfoil may be significantly increased by use of a relatively small slat airfoil. The main findings of the parametric study is listed in the items here.

- The lift force on the standard thick main airfoils can be drastically increased by use of a slat airfoil. Increases in total maximum lift of more than three times using a slat airfoil of half the main chordlength was found (see specific results later below)
- The maximum obtainable lift was found to be highly dependent on the size of the slat airfoil
- When using standard airfoils as the slat airfoil the thick airfoil gives better results than the thin one
- The maximum total lift was lower for the cases with thicker main airfoil than for the cases with a thinner main airfoil.
- An additional positive camber of the slat airfoil was found to be beneficial
- Maximum lift for a specific combination of main and slat airfoils occur for the slat angle that causes the main airfoil and slat airfoils to stall at the same flow angle. Both airfoils has to be at the edge of stalling at the same time
- The maximum lift of the multiple airfoil configurations increase with Reynolds number
- A relatively big part of the total loading is on the slat airfoil (see specific results later below)
- The computations indicated that locating the TE of the slat airfoil at surface coordinate $s_{TE,slat} = 0.15$ was an overall good position for all combinations of airfoils tested. Also independently of normal distance between the airfoils.
- The effect of the normal distance between main and slat airfoil was weaker. However, simulations indicated that the smaller normal distance (5% of the main chordlength) between main airfoil and slat airfoil TE was better than the larger normal distance (10 % of the main chordlength).

Table 18 lists the key parameters and results for the four best cambered and uncambered slat airfoil combinations ($c_{slat}/c_{main} = [0.3, 0.5]$ and $k_{camber} = [0.0, 0.1]$) using main airfoil FFA3301 and slat airfoil FFA3360

It is seen that drastic increases in the maximum lift can be achieved by mounting slat airfoils in front of the thick main airfoils. When comparing the obtained increases in maximum lift with the increases needed to achieve maximum power output as stated in the introduction it is seen that the needed lift increases can be obtained with slat airfoils smaller than 30% of the main chordlength. As mentioned earlier, the slat airfoil is very highly loaded. The simulations

Table 18. Main results from the part of the parameter study where the 30% thick FFA3301 is used as the main airfoil.

L_{main}/L_{tot}	β	c_{slat}/c_{main}	$s_{TE,slat}$	$n_{TE,slat}$	k_{camber}	$L_{max,tot}/L_{max,single}$
53%	-20.0^o	0.3	0.15	0.05	0.0	2.02
46%	-27.5^o	0.3	0.15	0.05	0.1	2.27
37%	-20.0^o	0.5	0.15	0.05	0.0	2.82
28%	-27.5^o	0.5	0.15	0.05	0.1	3.17

indicate that a 30% slat airfoil may account for more than half of the total lift. This must be taken into account if designing blades using slats, since the aerodynamic moment around some specified point on the main airfoil is changed a lot by addition of an extra airfoil.

Since the thick multiple airfoils are rather effective, it may be possible to use multiple element airfoils when designing blades. Possibilities for savings in material cost could be investigated. This could be another way of producing high lift airfoils also for the regions where the airfoils need not be thick.

10.5 Conclusions & Further work

The following main conclusion shave been drawn form the present work

- A new fast aerodynamic prediction tool based on a coupling of a 2D panel code and solution of the viscous boundary layer equations has been developed.
- The good aerodynamic performance of a multi element setup with a thick main airfoil predicted by the fast panel code was verified using the CFD code EllipSys.
- The lift force on the standard thick main airfoils can be drastically increased by use of a slat airfoil. Increases in total maximum lift of more than three times using a slat airfoil of half the main chordlength was found.
- The maximum obtainable lift was found to be highly dependent on the size of the slat airfoil.
- When using standard airfoils as the slat airfoil the thick airfoil gives better results than the thin one.
- The loading on the slat airfoil is generally very high. A 30% slat airfoil may carry as much as 50% of the total lift.
- CFD results indicate that a two element airfoil is superior to the thick main airfoil alone when considering maximum lift, lift to drag ratio and roughness sensitivity.
- The results in this work concluded that a significant increase in maximum power production (8% in case of the IEA 5MW RWT) can be achieved by using relatively small slat airfoils (smaller than 30% of the main chordlength). The increase in thrust due to this is significant (12% for the IEA 5MW RWT).
- The fast prediction tool can be used as the first part of a "design suite". This tool points out where the interesting areas are. After this detailed analysis and design can be done using the CFD code EllipSys.

10.5.1 Further work

- Better validation of the fast prediction tool
- Investigations of the implications of the aerodynamic pitching moment

- Investigate slotted airfoil configurations
- Investigate flap airfoil configurations
- Investigate 3 element airfoil setups
- Using the fast prediction tool to optimize the shape of the multiple element airfoils
- The structural requirements for the highly loaded slat airfoil could be investigated
- The possibility of producing more slender blades using multiple element airfoils could be investigated

References

[1] H.Aa. Madsen. Two modifications of the bem method based on validation with results of actuator disc results, in research in aeroelasticity efp-2006. Technical Report 1611, Risø National Laboratory, Roskilde (DK), 2006.

[2] H. Glauert. *Airplane propellers. Volume IV in Aerodynamic Theory*. The Dover Edition 1963.

[3] Madsen H Aa. Gaunaa M. Johansen, J. and Bak C. Design of a wind turbine rotor for maximum aerodynamic efficiency. *Wind Energy*, 12:261–273, 2009.

[4] I.H. Abbott and A.E. von Doenhoff. *Theory of Wing Sections, including a summary of airfoil data*. Dover, 1949.

[5] A.M.O. Smith. High-lift aerodynamics. *Journal of Aircraft*, 12(6):501–530, 1975.

[6] J. A. Michelsen. Basis3D - a Platform for Development of Multiblock PDE Solvers. Technical Report AFM 92-05, Technical University of Denmark, 1992.

[7] J. A. Michelsen. Block structured Multigrid solution of 2D and 3D elliptic PDE's. Technical Report AFM 94-06, Technical University of Denmark, 1994.

[8] N. N. Sørensen. General Purpose Flow Solver Applied to Flow over Hills. Risø-R- 827-(EN), Risø National Laboratory, Roskilde, Denmark, June 1995.

[9] M Gaunaa. *Unsteady Aerodynamic Forces on NACA 0015 Airfoil in Harmonic Translatory Motion*. PhD thesis, Technical University of Denmark, 2002.

[10] M. Drela. Xfoil: An analysis and design system for low reynolds number airfoils. In *Proc. Low Reynolds Number Aerodynamics*, 1989.

[11] F. White. *Viscous Fluid Flow*. McGraw-Hill, 1991.

[12] I. Kroo. *Desktop Aerodynamics (internet/CD-rom book)*. www.desktopaero.com/products/AACatalogPage.html or www.desktopaero.com/appliedaero/preface/welcome.html.

11 Stall-induced vibrations of a blade section in deep-stall

Author: Morten H. Hansen - Risø DTU

Stall-induced vibrations of wind turbines at standstill have been observed more frequently for simulated than real turbines; maybe because of inadequate modeling of the unsteady aerodynamic forces on the blades when they are in deep-stall. A new stochastic model of these forces [1] inspired this search for a bias effect of self-induced turbulence on the stability limits of an airfoil section. The work has been performed under the milestone “Kortlægning af den reelle risiko for stall-inducerede svingninger under stilstand” of the EFP-2007 project.

Stall-induced vibrations, also known as stall-flutter, have previously only been a concern for stall-regulated turbines, where the blades operate in a partly separated flow (below deep-stall) at angles of attack (AOA) in the range of 10° to 25°. The negative slope of the lift versus AOA curve at these AOAs may cause the aerodynamic damping to become negative for a turbine mode, where the blades are vibrating in a particular critical *direction of vibration* [2]. The blades of pitch-regulated turbines are operating in attached flow without the risk of stall-flutter, except at standstill. Here, wind direction and rotor position are arbitrary, and the inflow to the blades can have any angles relative to the chord of the blade airfoil sections (determining the mean AOA denoted α_m), and relative to the directions of vibration of the blade modes (denoted θ), as shown in Figure 104.

Buhl [3] has studied the risk of stall-induced edgewise (i.e. chordwise $\theta \approx \alpha_m$) blade vibrations for a turbine at standstill by estimating the aerodynamic damping of the first edgewise bending mode for various mean AOAs from simulations using a state-of-the-art aeroelastic model for wind turbines. He shows that the most critical AOAs are around $\pm 90^\circ$. Politis *et al.* [4] come to the same conclusion from aeroelastic eigenvalue analysis of another wind turbine blade at standstill. Both Buhl and Politis *et al.* point out that the state-of-the-art models of unsteady aerodynamic forces are inadequate in deep-stall at these high AOAs. Their results show only small differences in the predicted aerodynamic damping based on quasi-steady or unsteady aerodynamics. The state-of-the-art models of the dynamic stall phenomenon in unsteady aerodynamics reduce to quasi-steady models describing the aerodynamic forces by the static lift and drag coefficients at the local quasi-steady AOAs [5].

When the flow around a stationary airfoil is fully separated, the aerodynamic forces will not be constant as deterministic models predict. Sørensen *et al.* [6] have computed the forces on a stationary wind turbine blade at very high AOAs using 3D CFD with Detached Eddy Simulation (DES), and compared their results to measurements on the same blade. Measurements and simulations show that the aerodynamic forces fluctuate stochastically due to complex vortex structures shed from the blade.

Figure 105 shows mean values of lift and drag coefficients as function of AOA in the (x,y)-plane. These means are obtained from measurements (only low AOAs) and recent DES computations performed by Bertagnolio *et al.* [1] for a stationary S809 airfoil. On the third axis are shown the histograms of the computed lift and drag coefficients, which can be considered as scaled Probability Density Functions (PDFs) of these stochastic processes. Based on their observations, Bertagnolio *et al.* propose a stochastic model for the lift and drag in deep-stall, where Gaussian stochastic components are added to the static mean lift and drag coefficients at the quasi-steady AOA.

These new insights lead to the question: how is the risk of stall-induced vibrations affected by the stochastic fluctuations of lift and drag in deep-stall? The mechanism of stall-flutter is based on specific relations between AOA and aerodynamic forces [5]; can the stochastic fluctuations become sufficient large to affect this mechanism? To answer these questions, this chapter focuses on possible bias effects of the stochastic forces on the stall-flutter limit of an

Figure 104. Stall-induced blade vibrations of wind turbine at standstill may occur when the wind direction relative to the airfoil chord and the direction of vibration for a blade mode is critical.

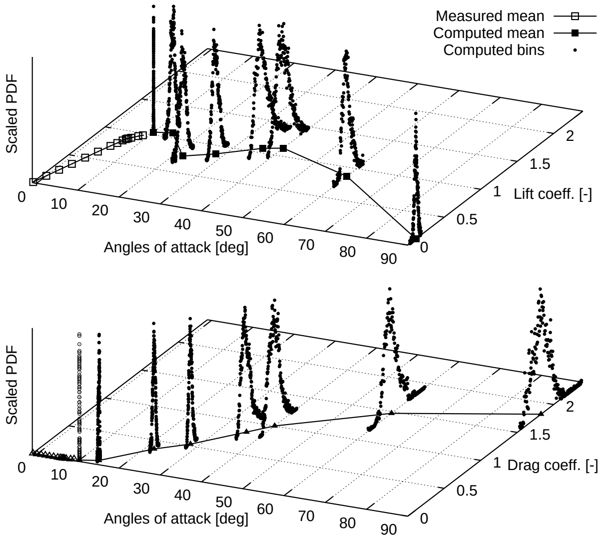

Figure 105. Measured and computed lift and drag coefficients of stationary S809 airfoil showing histograms of the computed coefficients on the third axis. Computations performed by Bertagnolio et al. *[1] using 3D CFD with Detached Eddy Simulation (DES) on a finite length wing section with periodic boundary conditions.*

airfoil with one degree of freedom subject to quasi-steady aerodynamic forces. The stochastic fluctuations of lift and drag on the airfoil in deep-stall is modeled by stochastic fluctuations of the inflow velocities induced by the complex vortex structures shed from the airfoil. Numerical simulations and local bifurcation analysis using averaging of the nonlinear equations of motion show that there is a small stabilizing bias effect on the linear damping of the airfoil motion. The added damping is proportional to the variance of the lateral self-induced turbulence, and it is too small to significantly affect the risk of stall-induced vibrations.

11.1 Models

Figure 106 illustrates the simplest model that can describe the stall-induced vibrations of a critical blade mode observed in advanced aeroelastic simulations of wind turbines at standstill with the blade in deep-stall: A typical section with one degree of freedom $X(t)$ in the direction of vibration θ relative to the mean inflow velocity, which is subjected to quasi-steady aerodynamic lift and drag. Neglecting apparent fluid mass terms, the equations of motion can be written as:

$$m\ddot{X}+2\zeta m\omega_0\dot{X}+m\omega_0^2X=\frac{1}{2}\rho cU^2\left(\bar{C}_L(\alpha)\sin(\theta-\varphi)-\bar{C}_D(\alpha)\cos(\theta-\varphi)\right) \qquad (22)$$

where $\dot{()}=d/dt$ denotes the time derivative, m is the mass per unit-length of the section, ω_0 and ζ are the natural frequency and damping ratio of the critical blade mode, ρ is the air density, c is the chord, U is the relative speed, and $\bar{C}_L$ and $\bar{C}_D$ are the static lift and drag coefficients evaluated at the quasi-steady AOA α. The relative speed, inflow angle, and quasi-steady AOA are (cf. Figure 106):

$$U^2=(U_m+U_T+\dot{X}\cos\theta)^2+(V_T+\dot{X}\sin\theta)^2$$

$$\varphi=\arctan\left((V_T+\dot{X}\sin\theta)/(U_m+U_T+\dot{X}\cos\theta)\right), \text{ and } \quad \alpha=\alpha_m-\varphi \qquad (23)$$

where U_m is the mean relative speed of the inflow, α_m is the mean AOA, and U_T and V_T are the small longitudinal and lateral self-induced turbulence components, respectively.

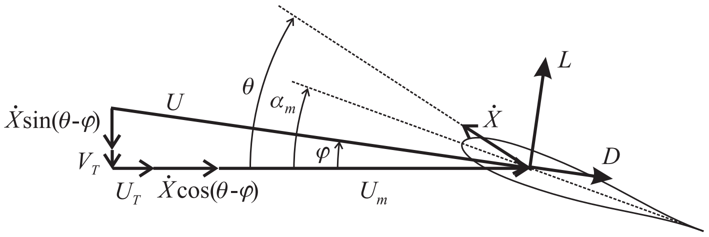

Figure 106. A typical blade section at a mean AOA of α_m can vibrate X in a direction θ relative to the mean inflow direction. Turbulent inflow velocities U_T and V_T, and the section velocity $\dot{X}$ gives the inflow velocity U and angle φ, and the quasi-steady forces $L = \frac{1}{2}\rho c U^2 \bar{C}_L(\alpha)$ and $D = \frac{1}{2}\rho c U^2 \bar{C}_D(\alpha)$.

Introducing the non-dimensional time τ, translation of the section x from its equilibrium, turbulence velocities u and v, reduced natural frequency k_0, and air-to-section mass ratio Λ

$$\tau = tU/c\ ,\ \ x = \left(X - \tfrac{1}{2}\rho c U_m^2(\bar{C}_L(\alpha_m)\sin\theta - \bar{C}_D(\alpha_m)\cos\theta)/(m\omega_0^2)\right)/c\ ,$$

$$u = U_T/U_m\ ,\ \ v = V_T/U_m\ ,\ \ k_0 = \omega_0 c/U\ ,\ \text{and}\ \ \Lambda = \tfrac{1}{2}\rho c^2/m \tag{24}$$

the equations of motion (22) can be written as

$$\ddot{x} + 2\zeta k_0 \dot{x} + k_0^2 x = \Lambda\left(C_L \sin(\theta-\varphi) - C_D\cos(\theta-\varphi) - \bar{C}_L(\alpha_m)\sin\theta + \bar{C}_D(\alpha_m)\cos\theta\right) \tag{25}$$

where $(\dot{\ }) = d/d\tau$ denotes the non-dimensional time derivative, and

$$\begin{aligned}\varphi &= \arctan\left((v + \dot{x}\sin\theta)/(1 + u + \dot{x}\cos\theta)\right)\\ C_L &= ((1 + u + \dot{x}\cos\theta)^2 + (v + \dot{x}\sin\theta)^2)\bar{C}_L(\alpha_m - \varphi)\\ C_D &= ((1 + u + \dot{x}\cos\theta)^2 + (v + \dot{x}\sin\theta)^2)\bar{C}_D(\alpha_m - \varphi)\end{aligned} \tag{26}$$

The turbulent velocities u and v are now modeled independently from the airfoil motion assuming that their stochastic processes are independent of inflow velocity and small variations of AOA.

The turbulence velocities u and v can also be used to model the atmospheric turbulence, however, the length-scales of these ambient components are too long (up to hundreds of meters), and thereby the frequencies are too low, to have a non-trivial bias effect on the aerodynamic damping of a critical blade mode [3]. The length-scales of the self-induced turbulence of an airfoil in deep-stall are up to the order of the chord length (0.5–2 m). Power Spectral Densities (PSDs) of the lift and drag coefficients obtained by Bertagnolio *et al.* [1] show about 25 dB reduction of the energy in stochastic fluctuations at a reduced frequency of one ($fc/U_m = 1$). The PSDs also show energy decrease with the power law $k^{5/3}$ known from energy dissipation in turbulent flows.

Based on these observations, the frequency contents of the self-induced turbulence velocities u and v are assumed to be described by the theoretical PSDs

$$S_u(k) = 2\sigma_u^2 l_u/(1 + l_u^2 k^2)\ \ \text{and}\ \ S_v(k) = 2\sigma_v^2 l_v/(1 + l_v^2 k^2) \tag{27}$$

where $k = \omega c/U_m$ is the reduced angular frequency, σ_u and σ_v are the turbulence intensities (or standard deviations of u and v), and l_u and l_v can be considered as non-dimensional length scales of the self-induced velocities. The turbulence intensities are later tuned to obtain similar levels of lift and drag fluctuations as computed by Bertagnolio *et al.*, and the length scales are set to two ($l_u = l_v = 2$) corresponding to approximately 22 dB reduction at a reduced frequency of one ($k = 2\pi$).

Assuming that the stochastic processes behind the self-induced turbulence are stationary (not dependent on the airfoil motion), time series related to the PSDs (27) can be considered as the response of systems with the transfer functions $H_u(k) = \sigma_u\sqrt{2l_u}/(1 + il_u k)$ and $H_v(k) = \sigma_v\sqrt{2l_v}/(1 + il_v k)$ driven by a Gaussian White Noise excitation with unit variance. Assuming that the self-induced velocities are furthermore uncorrelated, they can be determined in the time-domain from the equations

$$\dot{u} + l_u^{-1} u = \sigma_u \sqrt{2/l_u} e_u(\tau) \quad \text{and} \quad \dot{v} + l_v^{-1} v = \sigma_v \sqrt{2/l_v} e_v(\tau) \tag{28}$$

where $e_u(\tau)$ and $e_v(\tau)$ are two Gaussian White Noise signals normalized to have unit variances.

11.2 Stall-induced vibrations

To study the stall-induced vibrations of the airfoil section, steady limit-cycle oscillations are sought beyond the stability limits of the equilibrium solution $x = 0$ in the (α_m, θ)-plane. This study is based on a third order Taylor expansion of the equation of motion (25) with (26) assuming that the state variables are small $(\dot{x}, u, v << 1)$:

$$\ddot{x} + k_0^2 x + \varepsilon\Lambda \left((2\zeta k_0/\Lambda + \beta_1)\dot{x} + \beta_2 \dot{x}^2 + \beta_3 \dot{x}^3 + p_1(\tau)\dot{x} + p_2(\tau)\dot{x}^2 \right) = \varepsilon\Lambda f(\tau) \tag{29}$$

where the functions of the external and two parametric excitations are given by

$$f = c_1 u + c_2 v + c_3 u^2 + c_4 v^2 + c_5 uv + c_6 v^3 \ , \quad p_1 = \beta_1 u + c_7 v + c_8 v^2 \ \text{, and} \quad p_2 = c_9 v \tag{30}$$

The important (seen later) coefficients of the Taylor expansion are

$$\begin{aligned}
\beta_1 = & \Big((3 + \cos 2\theta)\, \bar{C}_D + (1 - \cos 2\theta)\, \bar{C}'_L - \big(\bar{C}_L + \bar{C}'_D\big) \sin 2\theta \Big)/2 \\
\beta_3 = & \Big((3 + \cos 4\theta - 4\cos 2\theta)\, \bar{C}_D + (2 \sin 2\theta - \sin 4\theta)\, \bar{C}_L \\
& + \big(\tfrac{1}{3} \sin 4\theta - \tfrac{2}{3} \sin 2\theta\big)\, \bar{C}'_D + \big(1 + \tfrac{1}{3}\cos 4\theta - \tfrac{4}{3}\cos 2\theta\big)\, \bar{C}'_L \\
& + (3 + \cos 4\theta - 4\cos 2\theta)\, \bar{C}''_D + (2 \sin 2\theta - \sin 4\theta)\, \bar{C}''_L \\
& + \big(\tfrac{1}{3} \sin 4\theta - \tfrac{2}{3} \sin 2\theta\big)\, \bar{C}'''_D + \big(1 + \tfrac{1}{3}\cos 4\theta - \tfrac{4}{3}\cos 2\theta\big)\, \bar{C}'''_L \Big)/16 \qquad (31) \\
c_8 = & \Big((3 - 3\cos 2\theta)\, \bar{C}_D + (1 - \cos 2\theta)\, \bar{C}'_L + (3\bar{C}_L - \bar{C}'_D) \sin 2\theta \\
& + (3 - 3\cos 2\theta)\, \bar{C}''_D + (1 - \cos 2\theta)\, \bar{C}'''_L + (3\bar{C}''_L - \bar{C}'''_D) \sin 2\theta \Big)/4
\end{aligned}$$

where $()' = d/d\alpha$ denotes the derivative of the static lift and drag curves evaluated at the mean AOA α_m. The remaining coefficients of (29) and (30) are not included for brevity; note that they are also only functions of α_m and the relative direction of vibration θ.

A small booking parameter $\varepsilon << 1$ in (29) denotes that the damping and aerodynamic forces are small compared to the inertia and elastic forces. Applying the van der Pol transformation

$$x = a(\tau) \cos(k_0 \tau + \phi(\tau)) \quad \text{and} \quad \dot{x} = -a(\tau) k_0 \sin(k_0 \tau + \phi(\tau)) \tag{32}$$

under the condition that $\dot{a} \cos\psi - a\dot{\phi} \sin\psi = 0$ with $\psi = k_0\tau + \phi$, Equation (29) can be rewritten as

$$\begin{aligned}
\dot{a} = & \, \varepsilon\Lambda \Big(k_0 \beta_2 a^2 \sin^3 \psi - (2\zeta k_0/\Lambda + \beta_1) a \sin^2 \psi - k_0^2 \beta_3 a^3 \sin^4 \psi \\
& - \tfrac{1}{2} p_1 a \,(1 - \cos 2\psi) + \tfrac{k_0}{4} p_2 a^2 \,(3 \sin\psi - \sin 3\psi) - \tfrac{f \sin\psi}{k_0} \Big) \\
\dot{\phi} = & \, \varepsilon\Lambda \Big(\beta_2 k_0 a \sin^2 \psi \cos\psi - (2\zeta k_0/\Lambda + \beta_1) \sin\psi \cos\psi - k_0^2 \beta_3 a^2 \sin^3 \psi \cos\psi \qquad (33) \\
& - \tfrac{1}{2} p_1 \sin 2\psi + \tfrac{k_0}{4} p_2 a \,(\cos\psi - \cos 3\psi) - \tfrac{f \cos\psi}{a k_0} \Big)
\end{aligned}$$

which shows that the amplitude a and phase ϕ of (32) are varying slowly because their time derivatives are of the order $O(\varepsilon)$. Variations of these variables over the period of oscillation $T = 2\pi/k_0$ are therefore assumed to be of the order $O(\varepsilon)$, the T-averaged equations for a and ϕ

can be derived as

$$\begin{aligned}\dot{a} =& -\varepsilon(\zeta k_0 + \tfrac{1}{2}\Lambda\beta_1)a - \varepsilon\tfrac{3}{8}\Lambda k_0^2\beta_3 a^3 \\ & -\varepsilon\Lambda\tfrac{k_0}{2\pi}\int_0^{\frac{2\pi}{k_0}}\left(\tfrac{1}{2}p_1 a\,(1-\cos 2\psi) - \tfrac{k_0}{4}p_2 a^2\,(3\sin\psi - \sin 3\psi) + \tfrac{f\sin\psi}{k_0}\right)d\tau + O(\varepsilon^2) \\ \dot{\phi} =& -\varepsilon\Lambda\tfrac{k_0}{2\pi}\int_0^{\frac{2\pi}{k_0}}\left(\tfrac{1}{2}p_1\sin 2\psi - \tfrac{k_0}{4}p_2 a\,(\cos\psi - \cos 3\psi) + \tfrac{f\cos\psi}{ak_0}\right)d\tau + O(\varepsilon^2)\end{aligned} \tag{34}$$

where the error is of the order $O(\varepsilon^2)$. To evaluate the remaining integral terms, it is first noted that the functions f and p_1 do not have zero means. They can be represented by

$$f = c_3\sigma_u^2 + c_4\sigma_v^2 + \xi_f(\tau) \quad \text{and} \quad p_1 = c_8\sigma_v^2 + \xi_1(\tau) \tag{35}$$

where $\xi_f(\tau)$ and $\xi_1(\tau)$ are stochastic processes with zero means. The first term $\frac{1}{2}p_1 a$ in the first integral of (34) will therefore lead to an added damping term $\frac{1}{2}c_8\sigma_v^2 a$ in the T-averaged forces, whereas the remaining terms involving the excitations ξ_f, ξ_1, and p_2 must be evaluated according to stochastic averaging techniques due to possible correlations with a and ϕ (i.e. ψ).

When the excitations are broad-banded compared to k_0, the time interval $\Delta\tau_c$ where for example ξ_f and ϕ are correlated, will be small. Assuming that $\Delta\tau_c < T$, the variations of a and ϕ correlated with the excitations over the period T must be of the order $O(\varepsilon)$ according to Equation (33). The remaining terms of the integrals in (34) will therefore be of the order $O(\varepsilon^2)$, and the averaged equations become

$$\dot{a} = -\varepsilon(\zeta k_0 + \tfrac{1}{2}\Lambda(\beta_1 + c_8\sigma_v^2))a - \varepsilon\tfrac{3}{8}\Lambda k_0^2\beta_3 a^3 + O(\varepsilon^2) \quad \text{and} \quad \dot{\phi} = O(\varepsilon^2) \tag{36}$$

They show that the averaged damping ratio is $\zeta + \frac{1}{2}\Lambda(\beta_1 + c_8\sigma_v^2)/k_0$ and that the amplitude and phase of the k_0-harmonic response varies in the order of ε^2, where ε is the size of the damping and aerodynamic forces. Equation (36) shows that there exists a steady solution if the self-induced turbulence is neglected ($\sigma_u = \sigma_v = 0$) with the amplitude:

$$a = \sqrt{-\tfrac{4}{3k_0^2\beta_3}\left(\tfrac{2\zeta k_0}{\Lambda} + \beta_1\right)} \tag{37}$$

which appears when the averaged damping comes negative. A steady solution does not exist when the self-induced turbulence is included; however, the averaged level of vibration is predicted to be lower than (37) due to the added averaged damping.

11.3 Numerical example

Stall-induced vibrations are investigated for a typical blade section with the reduced natural frequency of $k_0 = 2\pi/20$ corresponding to a critical blade mode with a natural frequency of 1 Hz, a section with 1 m chord, and a wind speed of 20 m/s. The structural damping is set to $\zeta = 0.03/(2\pi)$ corresponding to a high-end value of 3 % logarithmic decrement. The air-to-section mass ratio is set to $\Lambda = 0.01$ corresponding to 1 m chord and a typical mass-per-unitlength of about 50 kg/m.

To ensure an easy (but unrealistic) access to higher order derivatives of the airfoil characteristics, an artificial thin symmetric airfoil is defined with the static lift and drag coefficients given by

$$\bar{C}_L = 2\pi\alpha h + C_N\,(1-h)\cos\alpha \quad \text{and} \quad \bar{C}_D = C_D^{\text{fric}}h + \tfrac{3}{4}C_N\,(1-h)\sin\alpha \tag{38}$$

where $h = \frac{1}{2} + \frac{1}{2}\tanh((\alpha_s - |\alpha|)/\Delta\alpha_s)$ is an interpolation function defining the stall characteristics, C_D^{fric} is the drag in attached flow due to viscosity, and $C_N = 2.25\,(2\pi\sin\alpha)\,/\,(4+\pi|\sin\alpha|)$ is the normal force coefficient for a flat plate in a fully separated flow [7].

The top plot in Figure 107 shows the aerodynamic coefficients for the chosen parameters. The maximum lift and drag coefficients are about 1.5 with maximum lift around 15 ° AOA. The bottom plot in Figure 107 shows areas in the (α_m,θ)-plane with stall-induced vibrations

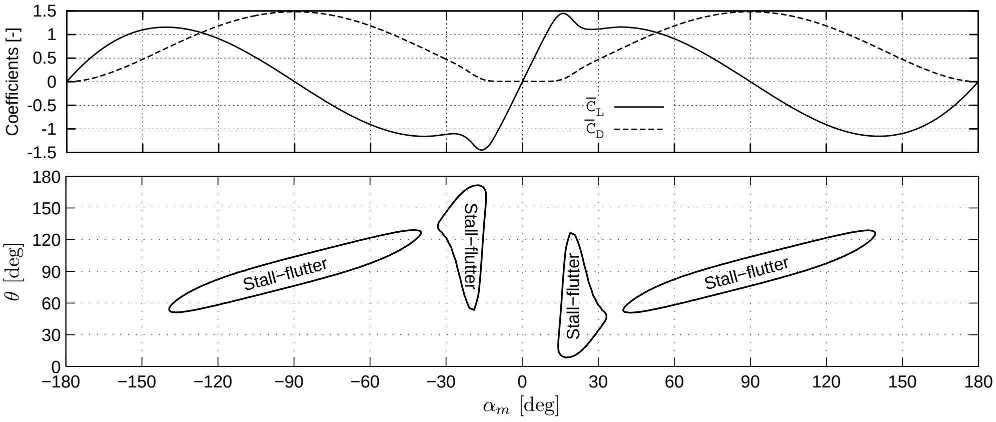

Figure 107. Top: Static lift and drag coefficients (38) *for* $C_D^{fric} = 0.005$, α_s*=18°* *and* $\Delta\alpha_s$*=5°. Bottom: Stability diagram in the (*α_m*,*θ*)-plane for the zero solution without self-induced turbulence given by the sign of the combined structural and aerodynamic damping coefficient* $2\zeta k_0/\Lambda + \beta_1$.

(without the effect of self-induced turbulence) given by the sign of the combined structural and aerodynamic damping coefficient $2\zeta k_0/\Lambda + \beta_1$, where the aerodynamic damping coefficient β_1 is given by (31). The area in the partly stalled region of 15° – 40° AOA are well-known from stall-flutter problems on stall-regulated turbines, and this area (and its point-symmetric counter part) is reduced by the addition of dynamic stall effects [2, 5]. The areas in the deep-stall regions are known from the previous studies of stall-induced vibrations at standstill [3, 4], where the critical edgewise blade bending modes ($\theta \approx \alpha_m$) have been shown to have lowest damping around $\alpha_m = 90°$ as also seen in Figure 107.

To investigate the effect of self-induced turbulence on these stability limits, the fully nonlinear equation of motion (25) are integrated over $2^{15} + 2^{16}$ steps (the first 2^{15} are discarded as transients) of size $\sqrt{2}T/2^6$ (the factor $\sqrt{2}$ ensures smoother histograms) without and with the stochastic inflow velocities obtained from simultaneous integrations of (28). The mean AOA is chosen as $\alpha_m = 90°$ and the relative direction of vibration is varied around the deterministic stability limit of $\theta \approx 76.28°$. The intensities of the longitudinal and lateral self-induced turbulence are $\sigma_u = 0.03$ and $\sigma_v = 0.06$, which through (26) yield similar standard deviations of lift and drag obtained by Bertagnolio *et al.* [1].

The top plot of Figure 108 shows scaled histograms of the integrated responses (bin size of 0.02) for the various θ. The most frequent bins of x are used in the bottom plot to represent averaged amplitudes of vibration in a bifurcation diagram with θ as parameter. The numerical amplitudes of the steady limit-cycle oscillations without self-induced turbulence lie on the analytically predicted curve given by (37). Self-induced turbulence increases the averaged amplitudes of vibration below the stability limit, whereas these most frequent amplitudes of vibration are reduced beyond the stall-flutter point. The arrow in the bottom plot indicates the delayed stall-flutter point when the damping term $c_8\sigma_v^2$ from the self-induced turbulence is added. The decrease of the most frequent amplitudes of vibration around the stall-flutter point before the amplitudes increase again is still unexplained.

Figure 109 shows a part of the simulated responses without and with self-induced turbulence from Figure 108 for $\theta = 76.35°$. It shows that the amplitude of the k_0-harmonic response with self-induced turbulence varies. The zoom onto a time frame of 10 periods shows that this amplitude variation and the variation of the phase are very slow compared to the variations of the turbulence velocities, which supports the assumptions made for obtaining the averaged equation (36).

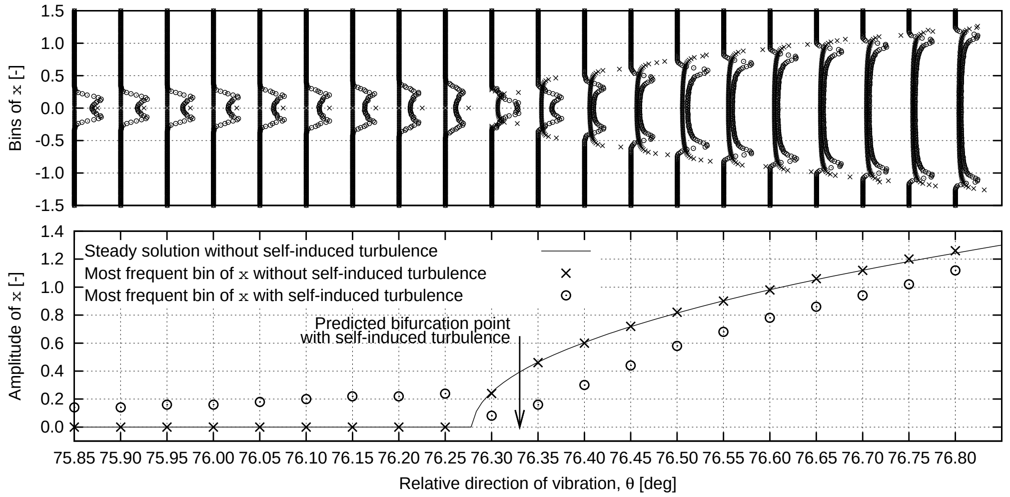

Figure 108. Top: Scaled histograms of the response x obtained from integrations of (25) *for* $\alpha_m = 90^\circ$ *and various* θ *without and with self-induced turbulence based on* (28)*. Bottom: Bifurcation diagram showing most frequent bins of the histograms and the steady state amplitude* (37) *as function of* θ.

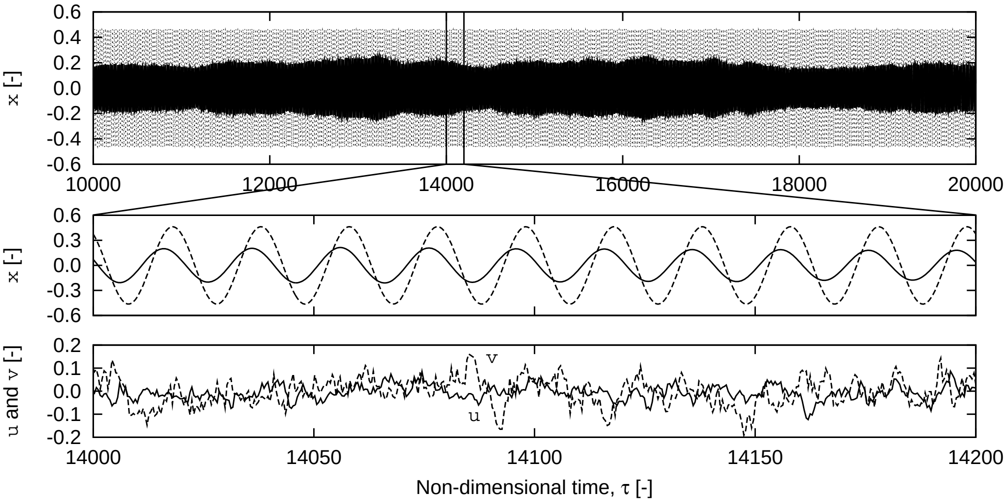

Figure 109. Responses of the airfoil section without (dashed curve) and with (solid curve) self-induced turbulence obtained by integrations of (25) *and* (28) *for* $\theta = 76.35^\circ$ *and* $\alpha_m = 90^\circ$*. Zooms show the harmonic properties of these responses and the stochastic behavior of the inflow velocities.*

11.4 Conclusion

A bias effect of self-induced turbulence on the stall-flutter limit for an airfoil section in deep-stall, e.g. a wind turbine blade section at standstill, is sought and found in the simplest model that can generically represent real stall-induced vibrations: A typical section with a single degree of freedom subjected to quasi-steady aerodynamic forces. This model also represents (on a blade section level) the state-of-the-art in advanced aeroelastic codes used to predict stall-flutter of wind turbines in deep-stall, because their implemented models of the unsteady aerodynamic forces reduces to quasi-steady aerodynamic models when the flow is fully separated. Measurements and CFD show however that the lift and drag on blades in deep-stall vary stochastically due to the complex vortex structures shed of the blade. The present results show that this stochastic behavior of the forces may add very small damping to a critical blade mode, if the phenomenon is modeled as a stochastic inflow of the quasi-steady aerodynamic model. The next step is to consider more advanced models of the lift and drag forces in deep-stall; time lags between the angle of attack and aerodynamic forces (similar to traditional dynamic stall models) may have a larger effect on the stall-flutter limits.

References

[1] F. Bertagnolio, F. Rasmussen, H. Aagaard Madsen, N.N. Sørensen, and J. Johansen. A stochastic static stall model applied to wind turbine blade. In *Proceedings of the 42nd AIAA Aerospace Sciences Meeting and Exhibit, 26th AIAA Applied Aerodynamics Conference*, pages 18–21, Honolulu, USA, August 2008. American Institute of Aeronautics and Astronautics. AIAA-2008-6723.

[2] F. Rasmussen, J. T. Petersen, and H. Aa. Madsen. Dynamic stall and aerodynamic damping. *ASME Journal of Solar Energy Engineering*, 121:150–155, 1999.

[3] T. Buhl. Edgewise vibrations in stand still. In C. Bak, editor, *Research in Aeroelasticity EFP-2006*, number Risø-R-1611(EN), pages 63–72, Roskilde, June 2007. Risø National Laboratory for Sustainable Energy, Technical University of Denmark. (Available from www.risoe.dtu.dk).

[4] E. S. Politis, P. K. Chaviaropoulos, V. A. Riziotis, S. G. Voutsinas, and I. Romero-Sanz. Stability analysis of parked wind turbine blades. In *Scientific Proceedings of the European Wind Energy Conference 2009*, pages 59–63, Marseille, March 2009. EWEA.

[5] M. H. Hansen. Aeroelastic instability problems for wind turbines. *Wind Energy*, 10:551–577, 2007.

[6] N. N. Sørensen, J. Johansen, and S. Conway. CFD computations of wind turbine blade loads during standstill operation. Technical Report Risø-R-1465(EN), Risø National Laboratory for Sustainable Energy, Technical University of Denmark, Roskilde, June 2007. (Available from www.risoe.dtu.dk).

[7] S. F. Hoerner and H. V. Borst. *Fluid-Dynamic Lift*. Hoerner Fluid Dynamics, New York, 1975.

12 Global Blade Deflections Effect on Local Airfoil Deformation and Performance

Author: Bjarne S. Kallesøe and Peter Bjerring - Risø DTU

Wind turbine blades can have a considerable tip deflection even at normal operation. This chapter examines the local effects on the airfoil deformation and aerodynamic performance caused by such global blade deflections. The analysis is based on numerical aeroelastic modeling of a 34 m blade from SSP Technology A/S. First, an aerodynamic force distribution is extracted from an aeroelastic simulations with HAWC2[1]. Next, these aerodynamic loads are imposed on a detailed finite element model of the blade together with gravity. Third, the airfoil deformation and blade twist are illustrated and discussed, and finally, the airfoil lift, drag and moment coefficients are compared for the deformed and undeformed airfoils.

12.1 The Wind Turbine Blade

The blade used in this analysis is the 34 m blade from SSP Technology A/S, the blade is designed for a 1.5 MW turbine with a rotor diameter of 70 m. This blade has been used for comprehensive analysis of ultimate strength, both numerical and in experiments. Therefore a detailed finite element model of this blade exists, which can be used for this study.

12.2 Aerodynamic Forces

The aerodynamic forces are extracted from the aeroelastic simulations of a turbine with the SSP blade. The blade model uses SSP aerodynamic data, but the structural blade data is a scaled version of the NREL 5 MW RWT, since this data is not available in the beam formulation needed. The rest of the turbine is disregarded by making it rigid. The turbine is operated with a constant speed and fixed pitch. The inflow conditions are uniform, without turbulence or wind shear. A wind speed of 12 m/s is used in the simulations, since this is around rated wind speed, where the thrust on a pitch regulated turbine is largest, hence the blades have the largest deflections. Figure 110 shows the aerodynamic forces projected onto and normal to the rotor plane, and the aerodynamic moment, all referred to the pitch axis. Two load cases are used, one at normal operation conditions and one where the air density is increased ($\rho = 2.2$ kg/m ^{3}) to increase the aerodynamic forces and herby the global deflections and local deformations. The objective of this study is to analyze the local effects of the global deformation, the local distributed pressure forces on the airfoil section can also effect the deformation. The effect of global blade deflection is isolated by applying a force distribution on the load carrying beam instead of the pressures on the airfoil surface.

12.3 Finite Element Model

A detailed finite element model of a 34 meter wind turbine blade from SSP technology A/S, is analyzed using the pre-processor MSC-Patran and geometric nonlinear solver MSC-Marc. The cross section of the blade analyzed can be divided into four main groups:

- Aerodynamic shell
- Caps (flanges)
- Adhesive bond between the cap and the aerodynamic shell
- Shear webs

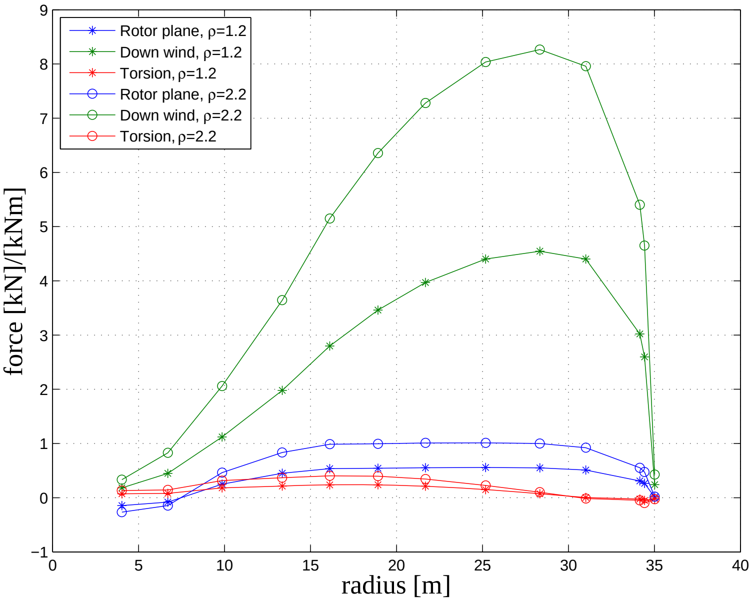

Figure 110. Aerodynamic forces on the blade computed by HAWC2 for fixed speed and pitch, and uniform inflow at 12 m/s.

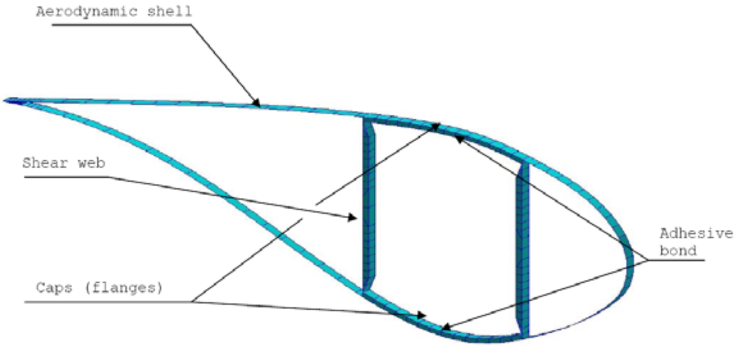

Figure 111. 2D-Cross Section of the outer shell and the box girder, 10m.

The Aerodynamic shell is a sandwich structure consisting of two thin skins of mainly biax and triax layers and a low density core material. This shell is modelled with 4-noded layered shell elements (Quad4) located in the mid-thickness of the material and an offset configuration is therefore not applied, as this normally results in an incorrect torsion response. The shell elements have a thick shell formulation and takes therefore shear deformation into account.

The caps/flanges are thick laminates, with most of the fibres in the longitudinal direction to limit tip deflection. These caps are modelled with 4-noded layered shell elements (Quad4), using a thick shell formulation. The elements are located at the mid-thickness of the caps and shell offsets are therefore not needed.

The Adhesive bonds between the caps and the aerodynamic shell are modelled with 8-noded 3d orthotropic brick elements. The caps and the aerodynamic shell are modelled applying a mid-thickness configuration. This approach gives an additional thickness of the adhesive bond, which slightly affects both the global and local response of the blade. To compensate for this additional global stiffness a reduced Youngs modulus in the longitudinal direction is used. Also reduced material properties in the transverse direction are applied so the out-of-plan stiffness of the adhesive bonds in the numerical model corresponds to the real bond.

The shear webs are sandwich structures, with the main purpose is to transfer the flapwise shear forces. The webs are modelled with a combination of shell and solid elements. The thin skins on each side of the webs consisted mainly of biax layers and are modelled with 4-noded layered shell elements placed in the mid-thickness of the material. The core material in the shear webs are modelled with one 8-noded orthotropic solid brick elements (Hex8) through the thickness. The corner stiffness of the box girder is adjusted by a shell element so the deformation measured during the experimental testing fits the numerical results. For a more detailed description of this adjustment see [2].

The model has a high mesh density and the entire model has approximately 143200 nodes. The analyses is done through a computer cluster with up to 240 nodes (one processor machine). In this particular case, 24 nodes are used. The deformed result of one of the analyses is illustrated in figure 112.

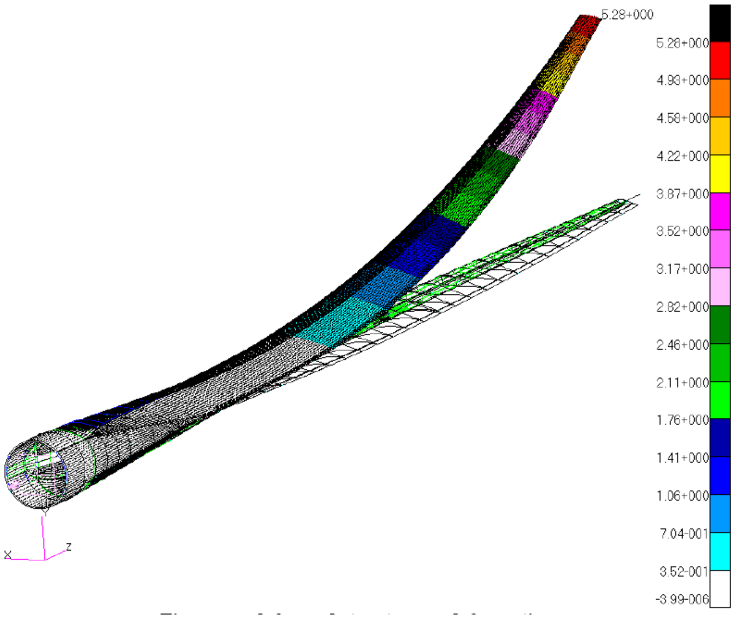

Figure 112. deformed structure, y-deformation.

12.3.1 The Loads Applied in the Numerical Model

The aerodynamic forces from HAWC2 are given as line loads in a number of points along the z-axis (the longitudinal axis). These loads are the flapwise load Fy [kN/m], the edgewise load Fx [kN/m] and the torsional moment Mz [kN], all given according to the global coordinate system located in the center of the hub. The loads are summed up and applied in 10 cross sections along the blade axis as point loads. This is done by creating a master node in each of the sections with an x- and y-location equal to zero. This master node is then coupled to the nodes in the load carrying box girder using a Multi Point Constrain (MPC) element of the type RBE3. This is a linear interpolation element, which does not constrain the sections. The point loads and torsional moments for the different sections are applied in these master nodes, as illustrated in figure 113. Additionally the gravity loads are also imposed on the FE-model and is in the analysed cases acting towards the leading edge of the blade (positive in the x-direction). In the geometric nonlinear analysis, the loads follow the deformation of structure and are therefore always perpendicular to the deformed blade axis.

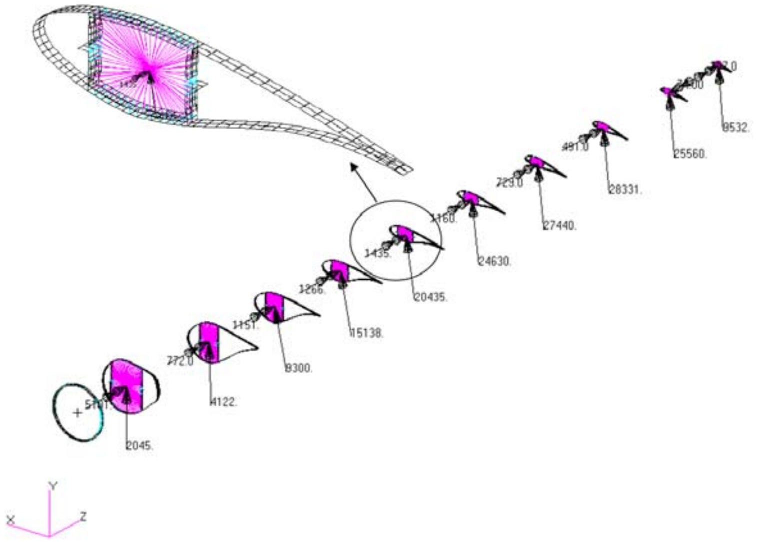

Figure 113. The Applied aerodynamic loads (load case 2)

12.3.2 Comment

Large tip deflection causes large longitudinal curvature, which produces brazier loads also known as crushing forces [3]. These forces are generated from the rotated (due to curvature) compressive/tensile forces arising due to bending. In the numerical studies it is observed that the soft sandwich panels in the trailing edge are deformed towards each other, which could indicate that this soft part of structure is affected by the Brazier effect.

The trailing edge in the cross sections is deformed positive in the y-direction. This response is also observed in both experimental and numerical studies (conducted at the moment at Risø-dtu) of the response of the blade in an edgewise bending test towards the leading edge. A mirrored response is observed when the blade bends towards the trailing edge. This response is most likely caused by the asymmetric geometry and the asymmetric layup of the sandwich panels.

Also the load carrying box girder is deformed, which is illustrated in figure 114, where the local deformation is scaled up by a factor of five (the rigid body movement is subtracted). This deformation is known as shear distortion and can cause fatal stability problems of the structure.

12.4 Deformed Airfoil Section

The finite element analysis gives the global blade deflection and twist. These are shown on figure 115 for the two load cases ($\rho = 1.2$ kg/m^3 and $\rho = 2.2$ kg/m^3). The elastic blade twist is seen to contribute with 0.6 deg to the pitch at the blade tip at normal conditions ($\rho = 1.2$ kg/m^3) which will affect the aerodynamic performance.

The cross section deformations are evaluated at seven different stations along the blade. The airfoil data for the undeformed and two deformation cases ($\rho = 1.2$ kg/m^3 and $\rho = 2.2$ kg/m^3) are computed on basis of the finite element results using Xfoil. The main Xfoil computations parameters are: a Reynolds number of 4 million, free transition using e^n with $n = 9$ and a mach number of 0.2. Figure 116 to 122 shows the seven different cross sections. The undeformed cross section is shown together with the two deformation cases and a cross section with up-scaled deformations to visualize the deformation pattern. The aerodynamic lift, drag and moment coefficients are also shown for the undeformed cross section and the two deformation

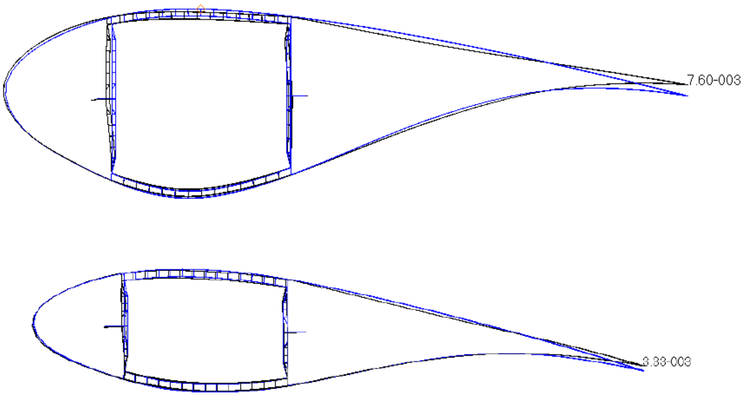

Figure 114. Cross section 15m and 19m for the load case with $\rho = 2.2$ kg/m^3, with a scaled up local deformation of a factor 5 (blue is the undeformed section and black is the deformed sction).

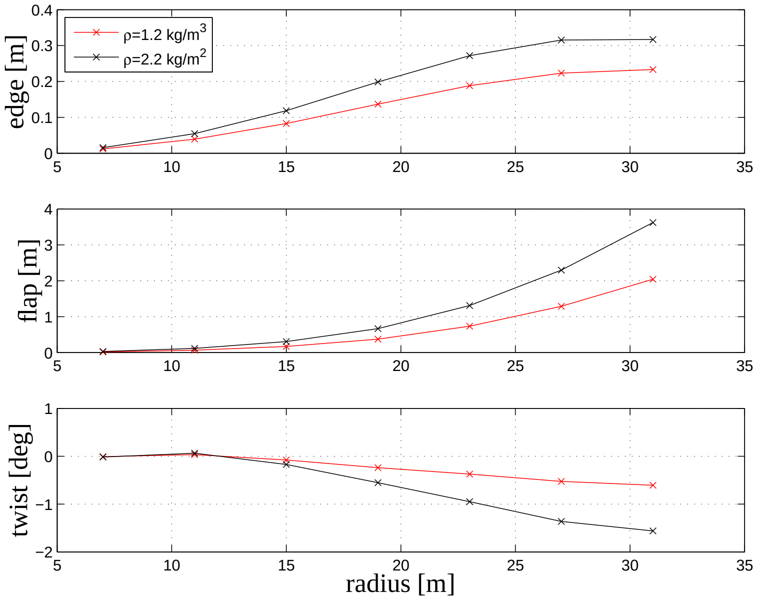

Figure 115. Elastic deflection and twist of blade. Positive in rotation direction, down wind and nose up, respectively.

cases. For the innermost section (Figure 116) the airfoil data seems to be erroneous, and it is a known issue that Xfoil has problems with thick airfoils, so these results are disregarded. For the rest of the cross sections no significant changes in the airfoil shape or aerodynamic properties are seen.

12.4.1 Aerodynamic Blade Performance

To evaluate the performance changes caused by the airfoil deformation the airfoil data for the undeformed cases, and the two deformation cases are reimplemented in the aeroelastic model and used in aerodynamic simulations on a rigid turbine. Table 19 shows the changes in power, thrust and blade root bending moments for the two deformed cases relative to the undeformed airfoil data. It is seen that the deformations does not affect the turbine performance.

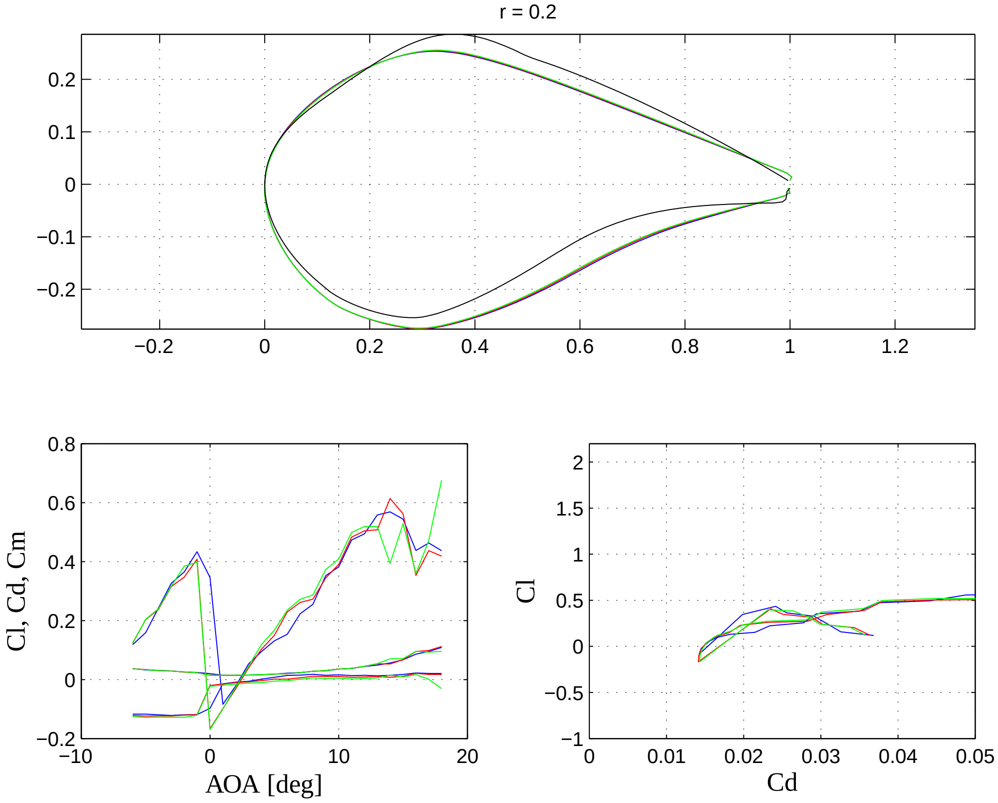

Figure 116. Top graph shows the undeformed (blue) and deformed (red for $\rho = 1.2$ *and green for* $\rho = 2.2$*) airfoil sections together with one where the deformation at normal operation is scaled by a factor of 20 (black). Bottom left graph shows the aerodynamic lift, drag and moment coefficients for the three deformation cases. Bottom right graph shows the lift versus drag.*

Table 19. Power, trust and blade root moments for a rigid turbine with the airfoils from the two deformation cases relative to the undeformed airfoils.

	airfoils from $\rho = 1.2$ kg/m^3 v.s. undeformed airfoils	airfoils from $\rho = 2.2$ kg/m^3 v.s. undeformed airfoils
Power	0.0 %	0.1 %
Trust	-0.1 %	-0.5 %
Blade root flap	-0.2 %	-0.7 %
Blade root edge	0.0 %	0.1 %
Blade root pitch	0.0 %	-6.6 %

12.5 Conclusion

This chapter deals with the local effects on airfoil deformation and performance, caused by global blade deflections. Is is found that the local airfoils only have a very small deformation and the aerodynamic lift, drag and moment coefficients are almost identical. Simulations with the new airfoil data support the conclusion that the airfoil deformations do not affect the aerodynamic performance.

However, the results may be blade design dependent, so a more flexible blade or a blade with another load carrying design can have another and more severe response.

The finite element analysis also shows an elastic blade twist of 0.6 deg at normal operation conditions. This will effect the aerodynamic performance of the blade, but this is already accounted for in e.g. the aeroelastic code HAWC2, which has a torsional degree of freedom in the blades.

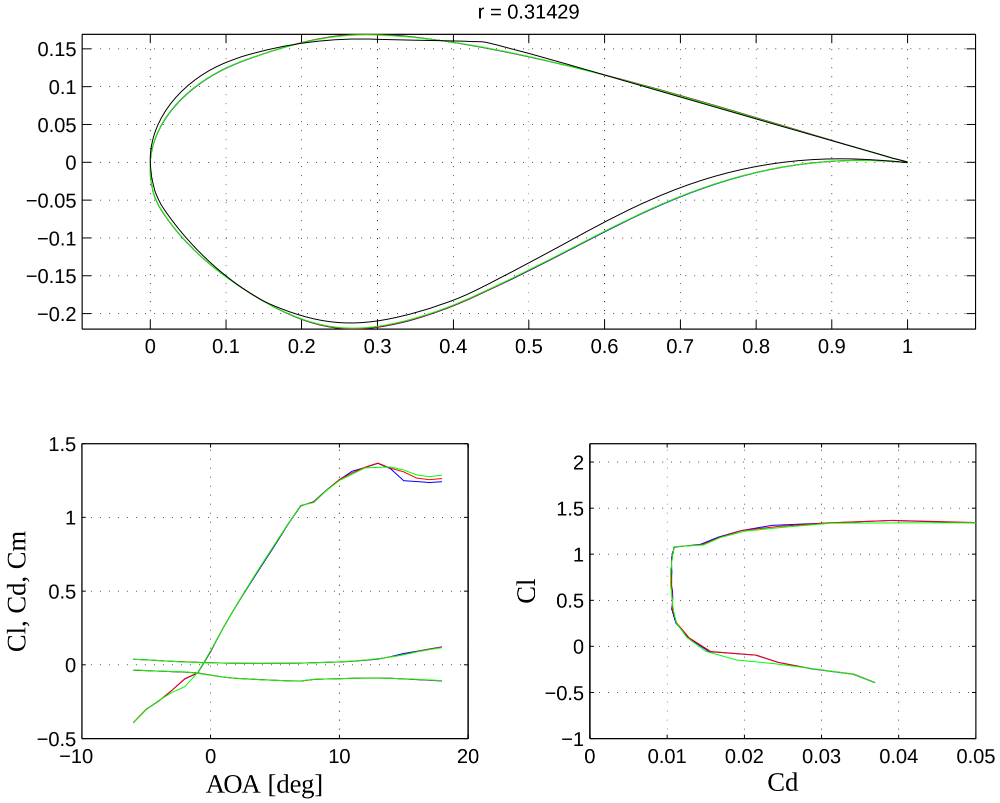

Figure 117. Top graph shows the undeformed (blue) and deformed (red for $\rho = 1.2$ *and green for* $\rho = 2.2$*) airfoil sections together with one where the deformation at normal operation is scaled by a factor of 20 (black). Bottom left graph shows the aerodynamic lift, drag and moment coefficients for the three deformation cases. Bottom right graph shows the lift versus drag.*

References

[1] T. J. Larsen (Editor). How 2 HAWC2, the user's manual. Risø-r-1597(ver. 3-7)(en), Risø-National Laboratory, 2009.

[2] F.M. Jensen, B.G. Falzon, J. Ankersen, and H. Stang. Structural testing and numerical simulation of a 34m composite wind turbine blade. *Composite Structures*, 76:52–61, 2006.

[3] L.S. Cecchini and P.M. Weaver. The brazier effect in multi-bay aerofoil sections. Technical report, University of Bristol - UK.

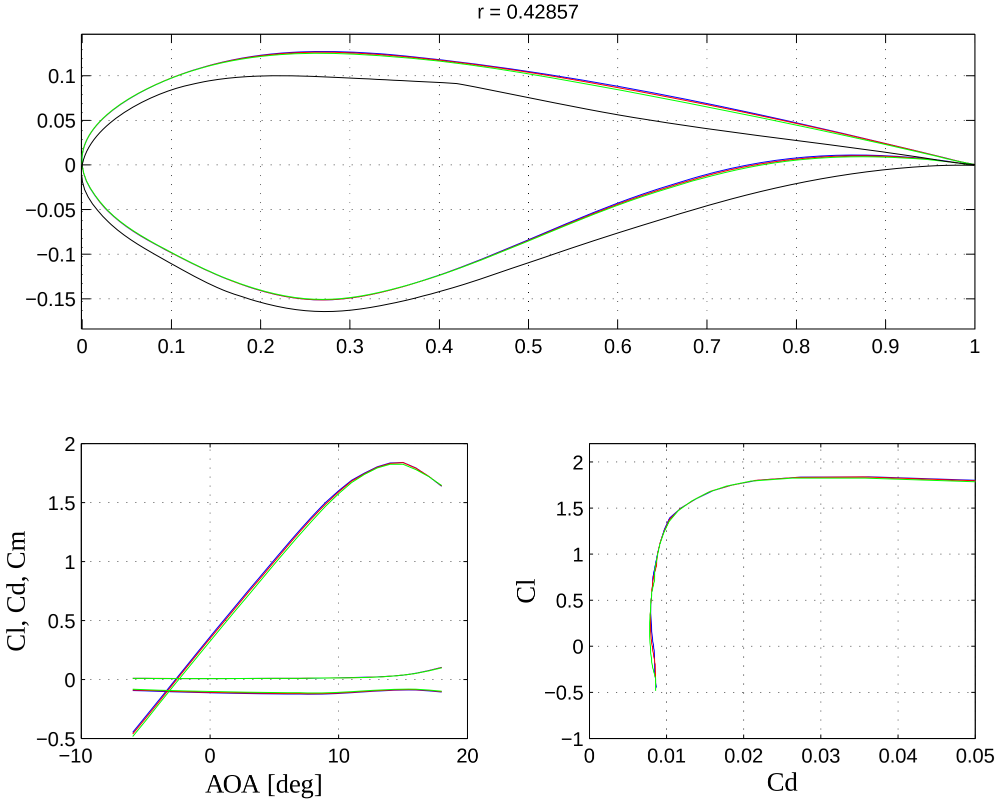

Figure 118. Top graph shows the undeformed (blue) and deformed (red for $\rho = 1.2$ *and green for* $\rho = 2.2$*) airfoil sections together with one where the deformation at normal operation is scaled by a factor of 20 (black). Bottom left graph shows the aerodynamic lift, drag and moment coefficients for the three deformation cases. Bottom right graph shows the lift versus drag.*

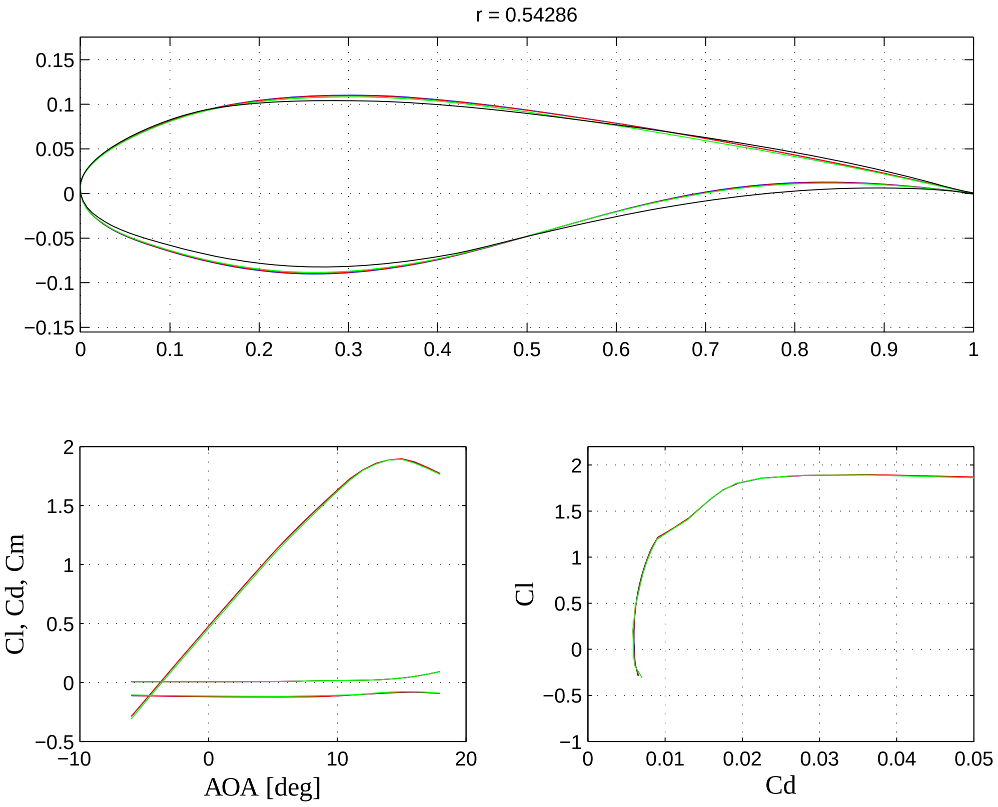

Figure 119. Top graph shows the undeformed (blue) and deformed (red for $\rho = 1.2$ *and green for* $\rho = 2.2$*) airfoil sections together with one where the deformation at normal operation is scaled by a factor of 20 (black). Bottom left graph shows the aerodynamic lift, drag and moment coefficients for the three deformation cases. Bottom right graph shows the lift versus drag.*

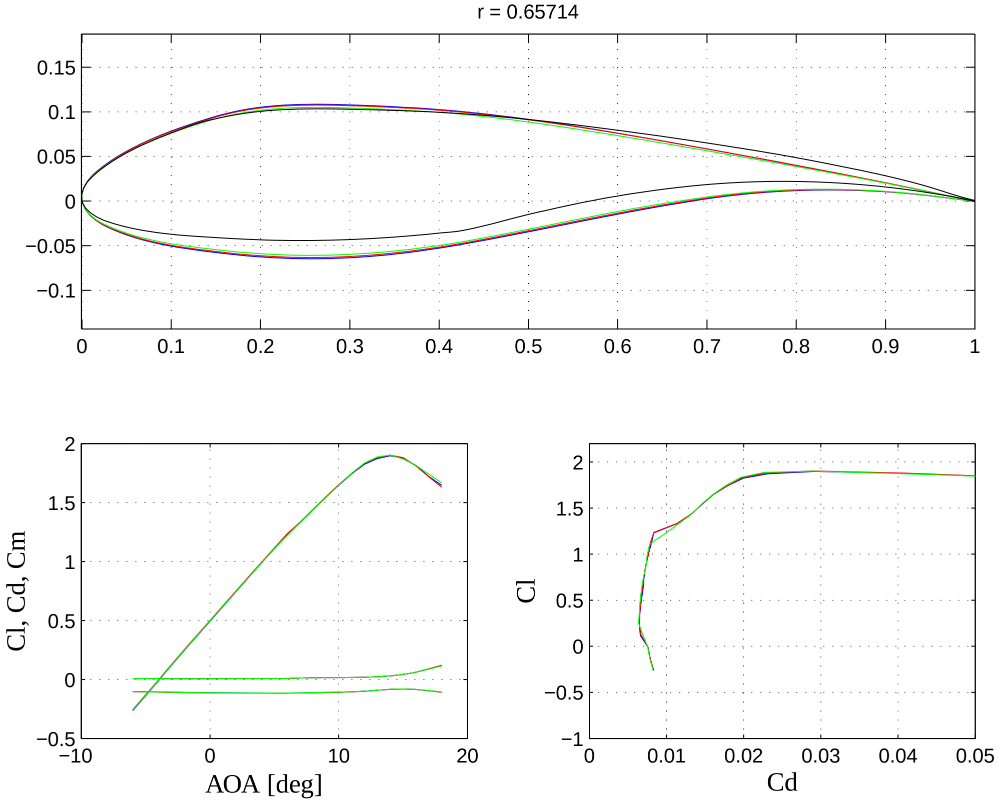

Figure 120. Top graph shows the undeformed (blue) and deformed (red for $\rho = 1.2$ and green for $\rho = 2.2$) airfoil sections together with one where the deformation at normal operation is scaled by a factor of 20 (black). Bottom left graph shows the aerodynamic lift, drag and moment coefficients for the three deformation cases. Bottom right graph shows the lift versus drag.

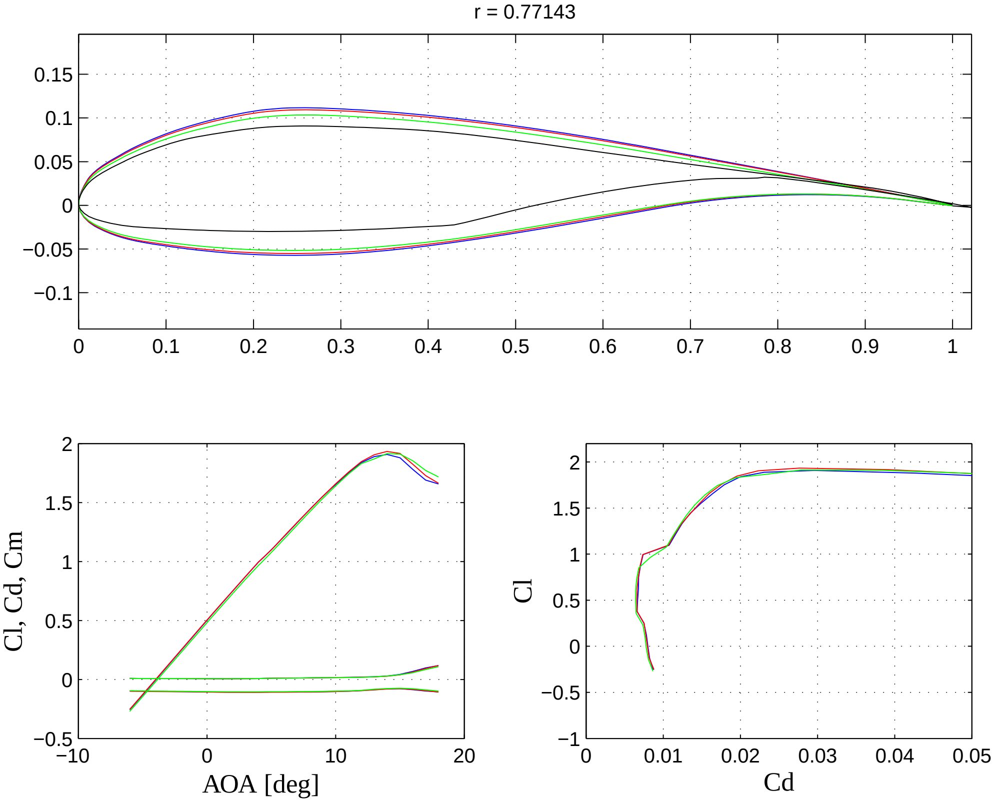

Figure 121. Top graph shows the undeformed (blue) and deformed (red for $\rho = 1.2$ *and green for* $\rho = 2.2$*) airfoil sections together with one where the deformation at normal operation is scaled by a factor of 20 (black). Bottom left graph shows the aerodynamic lift, drag and moment coefficients for the three deformation cases. Bottom right graph shows the lift versus drag.*

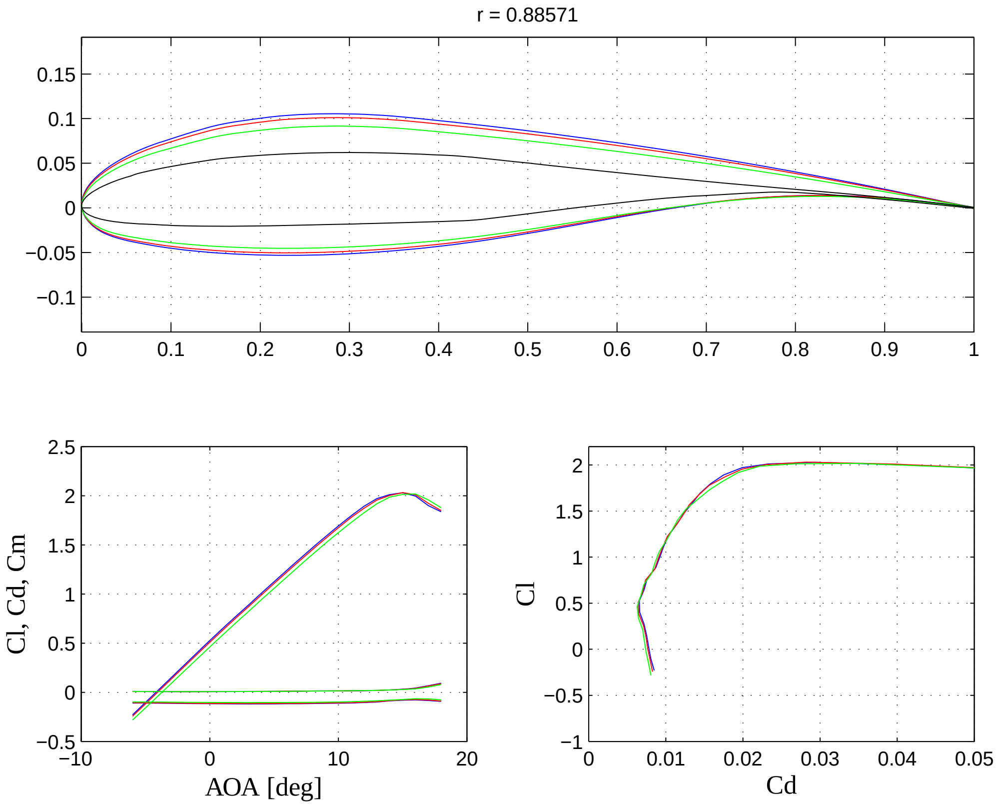

Figure 122. Top graph shows the undeformed (blue) and deformed (red for $\rho = 1.2$ *and green for* $\rho = 2.2$*) airfoil sections together with one where the deformation at normal operation is scaled by a factor of 20 (black). Bottom left graph shows the aerodynamic lift, drag and moment coefficients for the three deformation cases. Bottom right graph shows the lift versus drag.*

13 Gear Dynamics

Author: Anders M. Hansen and Torben J. Larsen - Risø DTU

Within the present EFP project a facility to couple external systems to the aeroelastic code HAWC2 through a DLL interface has been developed. The aim of that was to follow up on the gear box dynamics with particular focus on the double contact situation.

This chapter is compiled in two parts. First the double contact phenomenon and the expected consequence of such is explained. Then the DLL interface which makes it possible to make coupled simulations of a gearbox model and a wind turbine model is explained and exemplified.

13.1 Double contact theory

Even though gear boxes using planetary stages has been used for centuries, the drive train layout normally used in wind turbines, see Figure 123, has special design features, which might cause problems not seen in other planetary stage applications. Apart from the torque transfer from low speed side to high speed side, the gear box also works as a second main bearing of the main shaft. Hereby all force reactions from the rotor as well as the gravity and inertial loads from the gear box itself will be transferred through the main bearings between carrier and housing down to the gear box suspension normally consisting of two rubber bushing arrangements. A special and important feature of the planetary gear is the load alleviating effect of the floating sun-wheel suspension. This floating sun-wheel suspension allows for small movements of the sun-wheel which ensures an excellent load distribution between the three planets. The theory of this chapter is that the load transfer through the main bearings can cause a double contact situation inside the planetary stage if an unfortunate ratio between bearing clearance and teeth clearance occurs. A double contact is a situation where the tooth is in normal contact on the driving side and at the same time in contact on the back side as illustrated in Figure 126. Such a double contact situation is not considered a problem if it only occurs between one set of planet-sun and planet-ring teeth connections, but in the case where double contact on two sets of planet-sun and planet-ring connections occurs simultaneously a completely changed load sharing between the planet wheels occurs. The reason for the changed load sharing during a double double-contact is that the two planet wheels involved with the double-contact makes a small rotation which forces the sun-wheel to be in contact with only these two planets. The third planet is then completely unloaded which causes the input torque to be taken by two instead of three planets causing a load increase of 1.5 at the teeth and bearings during this moment of contact.

In the quest for the explanation of the many gear box failures especially seen in the period from 1995 to 2005, the dynamics of the traditional drive train layout, was investigated. In a research project funded by the Danish Energy Agency under ENS j.nr. 1363/00-0025, a dynamical model of the drive train arrangement was modeled by Larsen et. al [1],[2]. In this model the main components in the drive train was modeled using a lumped spring/mass approach coupled to a 2D spring mass model of the planetary stage which was originally formulated by Lin and Parker [3]. The drive train model is illustrated in Figure 125. The tooth contact in the planetary stage illustrated in Figure 124 is modeled using linear springs for the tooth flexibility and lumped inertia for the wheel bodies. The main results from that investigation was that the load alleviating effect of the floating sun-wheel suspension together with the limited inertia of the sun-wheel caused a very fine load distribution in all investigated load cases. Another result of the investigation was that the inertia of the gear box mounted on the main shaft and gear stay suspension through a carrier that was surprisingly flexible caused vibration modes mainly dominated by the gear box translation with frequencies down to 10Hz which is in the frequency range of the aerodynamic input loads. However, the analysis did not give a reason for the gear box failures. One limitation of the analysis was that the drive train model was not coupled to the rest of the turbine.

The behaviour of the planetary gear stage was further investigated by Parker et al.[4]. The focus of this analysis was directly on the double contact situation. The model used for the analysis was again the original model by Lin and Parker, [3], but now also equipped with extra non-linear springs representing the clearance between the teeth and inside the bearings and an extra set of springs for the double contact, see Figure 127. In this analysis performed with constant input torque it was clearly seen that a change in loads occurred. However instead of a load increase by a factor of 1.5 the load increased to 1.75 as seen in Figure 128.

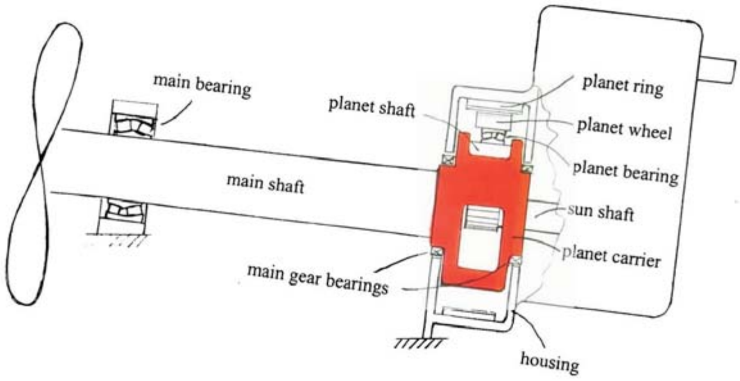

Figure 123. Traditional layout of wind turbine drive train. The gear box which consists of a planetary stage and two parallel stages also works as the second main bearing on the main shaft.

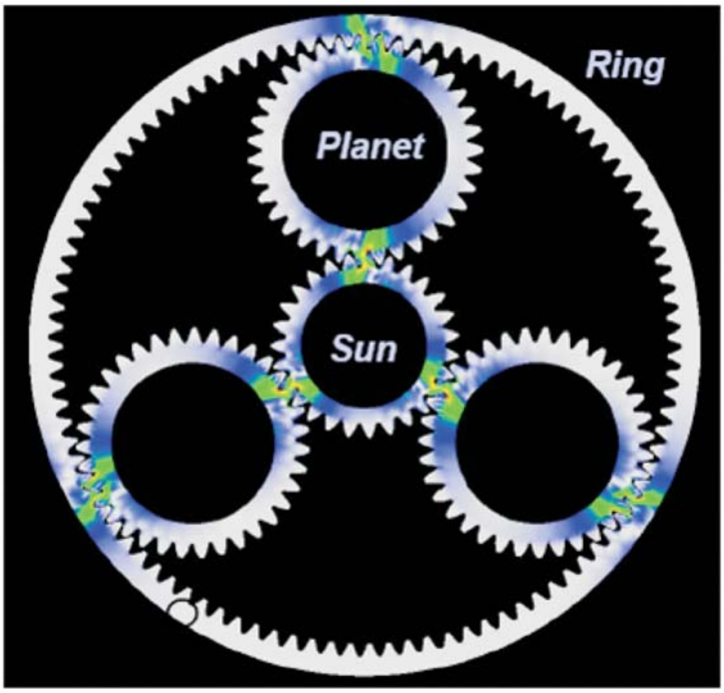

Figure 124. Compression forces in a normal tooth contact situation of a planetary gear stage.

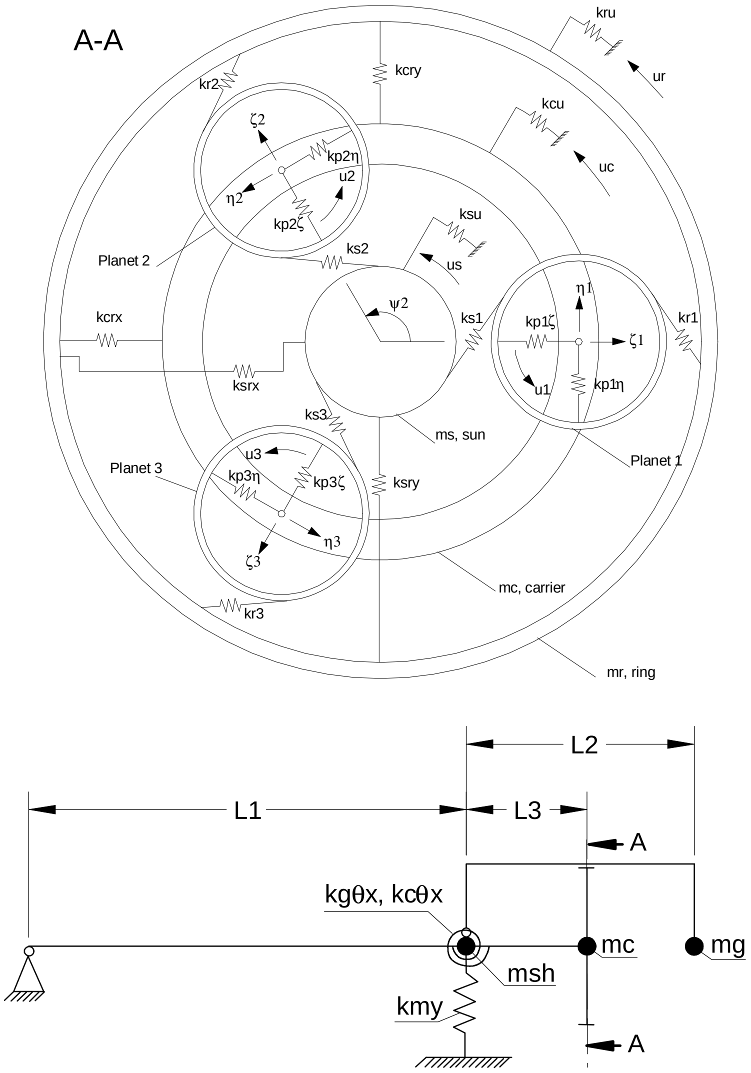

Figure 125. Dynamical model used to investigate the drive train dynamics with particular focus on gear teeth and bearing forces.

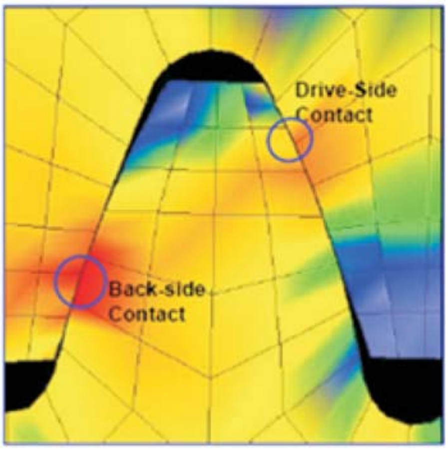

Figure 126. Example of a double contact situation where the backside of the teeth are also in contact.

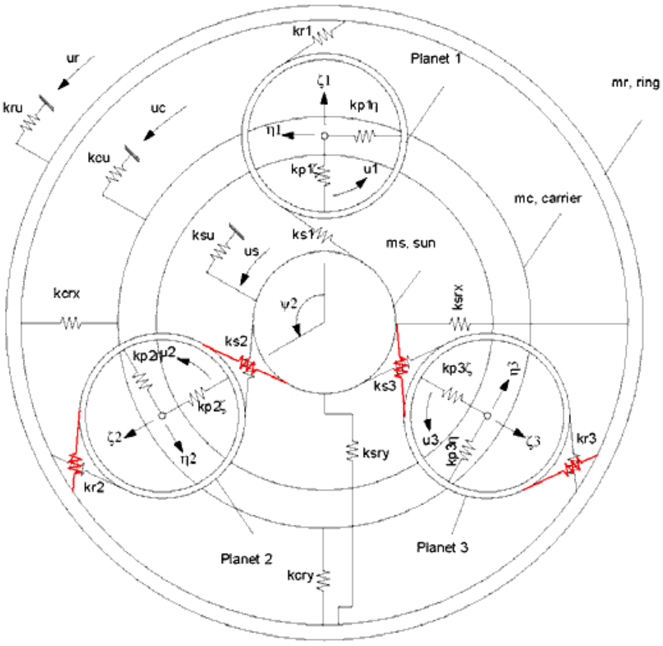

Figure 127. Double contact springs inserted (with red). Springs are non-linear and only active during compression. Only double contact spring is illustrated for the two lower planets even though they are also present for the upper planet.

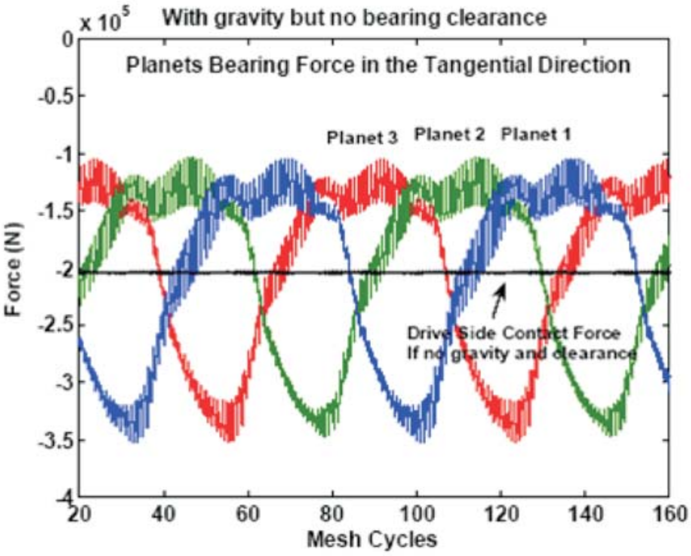

Figure 128. Preliminary analysis of the double-contact situation. It can be seen that planet forces are highly un-equall depending on the azimuth position during a double-contact situation even though the input torque is constant.

13.2 Interface

This work starts where the EFP-2006 project reported in [5] ended. In [5], a simple gear box model focussing on the torsional behavior of the gearbox mounted in the nacelle of a wind turbine was implemented in HAWC2. That specific gearbox model was hard-coded into HAWC2 which first of all is inconvenient seen from the code developers point of view who has to maintain the HAWC2 code. It was therefore decided to generalise the ability of HAWC2 to interface to other external systems in order to keep the HAWC2 kernel clean from 2nd party interference, and also to give access to the HAWC2 simulation capabilities from other expert areas - e.g. gearbox manufactures, giving them the possibility to simulate their own gearbox models together with a wind turbine model. The result of this work is that a set of user specified equations of motion for a dynamic system can be solved together with the equations of motion (EOMs) for the HAWC2 wind turbine model. The external system interact with the HAWC2 model through a set of constraint equations which describes how the external system degrees of freedom (DOFs) and the HAWC2 DOFs are related. Both the EOMs for the external system and the constraint equations are specified in an external DLL which is then called by the HAWC2 solver during the simulation.

In order for HAWC2 to be able to solve the combined EOMs, the external system DLL must return some specific information to HAWC2. To understand what is required by the DLL, it is useful to explain how the EOMs are formulated in HAWC2. The basic assumption is that the EOMs for the external system can be formulated by use of some kind of variational principle, such as e.g. the Virtual Work Principle or Hamiltons Principle - if so, the sum of virtual work, δW, for the internal (i.e. the HAWC2 system, subscript i) and external system (subscript e) is:

$$\delta W = \delta W_i + \delta W_e = \delta \mathbf{q_i} \cdot \mathbf{B_i} + \delta \mathbf{q_e} \cdot \mathbf{B_e} = 0$$

In the 2nd last part of the equation above, the virtual work is expressed as a function of the virtual DOFs, $\delta \mathbf{q_i}$ and $\delta \mathbf{q_e}$ for the internal and external DOFs, respectively. The virtual work must be zero for the systems to be in equilibrium for all the virtual variations of the DOFs which requires the vectors $\mathbf{B_i}$ and $\mathbf{B_e}$ to be equal to $\mathbf{0}$. (Note that if the external system is a simple mass/damper/spring system with external forces acting on it, then $\mathbf{B_e} = \mathbf{M} \cdot \ddot{\mathbf{q}}_\mathbf{e} + \mathbf{C} \cdot \dot{\mathbf{q}}_\mathbf{e} + \mathbf{K} \cdot \mathbf{q_e} - \mathbf{F}$

The vectors $\mathbf{B_i}$ and $\mathbf{B_e}$ express the un-constrained EOMs for the systems. The systems are not interacting with each other since they do not share any DOFs. If somehow the systems were constrained to move in a certain manner relative to each other, we would have to introduce external forces acting on both systems in order to obtain the constrained movement of the systems. This is done by introducing the Lagrange Multiplier Method, cf. [6], which adds some extra virtual energy to the system virtual energy necessary to satisfy the constraints. The constrained movement between the systems are formulated in a set of constraint equations gathered in the constraint vector $\mathbf{g}(\mathbf{q_i}, \mathbf{q_e}) = \mathbf{0}$. For each constraint equation, a new DOF (called a Lagrange multiplier) is introduced and collected in the vector λ. Now the virtual constraint energy is added to the system virtual energy, like this

$$\begin{aligned}
0 &= \delta W + \delta(\lambda \cdot \mathbf{g}) \\
&= \delta W + \delta\lambda \cdot \mathbf{g} + \delta\mathbf{g} \cdot \lambda \\
&= \delta \mathbf{q_i} \cdot \left(\mathbf{B_i} + (\nabla_{q_i}\mathbf{g})^T \cdot \lambda\right) + \delta \mathbf{q_e} \cdot \left(\mathbf{B_e} + (\nabla_{q_e}\mathbf{g})^T \cdot \lambda\right) + \delta\lambda \cdot \mathbf{g} \\
&= \delta \mathbf{q_i} \cdot (\mathbf{B_i} + \mathbf{G_i} \cdot \lambda) + \delta \mathbf{q_e} \cdot (\mathbf{B_e} + \mathbf{G_e} \cdot \lambda) + \delta\lambda \cdot \mathbf{g}, \quad \forall \delta\mathbf{q_e}, \forall \delta\mathbf{q_i}, \forall \delta\lambda
\end{aligned}$$

The last line in the equation above introduces the gradient matrices $\mathbf{G_e}$ and $\mathbf{G_i}$ (or rather the transpose of that), which contain the derivatives of the constraint vector wrt. $\mathbf{q_e}$ and $\mathbf{q_i}$, respectively. Since the total virtual energy must be zero for all virtual variations of the DOFs, we finally get these EOMs:

$$\mathbf{B_i} + \mathbf{G_i} \cdot \lambda = \mathbf{0}$$

$$\mathbf{B_e} + \mathbf{G_e} \cdot \lambda = \mathbf{0}$$

$$\mathbf{g} = \mathbf{0}$$

It is now clear which tasks the external DLL needs to do in order to couple an external system with the HAWC2 model:

- The un-constrained EOMs for the external system, $\mathbf{B_e}$, need to be formulated, along with
- the constraint vector, $\mathbf{g}$, and the gradient matrices, $\mathbf{G_e}$ and $\mathbf{G_i}$.

The two bulleted tasks above are really not dependent and they can be specified separately in external DLLs, providing the possibility to do simulations of external systems without constraining them to any internal systems. Also, constraints between internal systems can be defined without having to introduce an external systems. Further, which is not really clear from the description above, it is also possible to specify constraints between individual external systems, so that it is possible to couple two (or more) external systems together.

13.2.1 DLL subroutines and their purpose

The programming tasks needed to define an external system DLL is described below. As indicated above, the programming tasks consist of two independent tasks, one related to the un-constrained EOMs, and one related to the constraints.

The tasks related to the EOMs are tabulated below. The left column specifies the subroutine and the left column the purpose of that subroutine.

Initialise	The dimensions of the external system are defined herein, such as number of state variables, how many output parameters is written to log file, what is needed to visualise the system, etc. (Called once)
InitCond	Initial conditions for the state variables is specified here.(Called once)
Update	This routine is called during the iterations in order to update time dependent parts of the external system, e.g. rotation matrices, external forces, etc. The routine must return the mass, damping, and stiffness matrices, NOT necessarily the exact matrices, but somthing sufficiently accurate to be used in the equilibrium iterations for the system.(Called once per iteration)
Residual	This routine must return the $\mathbf{B_e}$ vector. The name *Residual* is a bit misleading because we often expect the *residual* to be zero when "things" have converged, however, in case this external system is constrained, the $\mathbf{B_e}$ vector will be equal to the constraint force on convergence. (Called once per iteration)
Output	Parameters which are to be put in the output file together with output parameters from the HAWC2 model are returned here. (Called once per time step on convergence)
Visual	Parameters which enables the external system to be visualised are handled by this routine. This routine is called both from HAWC2 and from our in-house visualisation tool. When called from HAWC2, the routine must return the necessary parameters needed to draw the external system. When called from the visualisation tool, the routine receives the same data that were previously returned to HAWC2 during the simulation, and draws the external system based on those data. The drawing must be done using the OPENGL library functions.(Called once per time step on convergence)

The next table describes the subroutine tasks related to constraints.

Initialise	References to the internal and/or external systems are given herein and stored for future use. The dimension of the constraint vector is given as well.(Called once to return dimension + once per internal/external system involved.)
Update	Here the constraint vector **g** if calculated based on the present states of the involved systems. Further, all the gradient matrices $\mathbf{G_i}$ and $\mathbf{G_e}$ must be returned too. Note that a constraint can involve any number of internal and external systems, and for each of the systems involved, a gradient matrix must be specified. (Called once per iteration)

Common for both the EOMs and the constraint routines is that the subroutine names are decided by the programmer, and the information about those subroutine names is then specified in the HAWC2 input file.

13.3 Validation Example

The DLL interface has been validated by a number of test cases. The example used in the hard-coded version in [5] was the first test case. The EOMs for the simple gearbox model in [5] was implemented using the DLL interface, and the special constraints that were developed to couple the gear box to the HAWC2 model were moved to the DLL as well. A simulation of the hard-coded model and the DLL model showed exact agreement between the two models. This validates that the interface works correctly. This validation example in not shown herein.

The next validation example demonstrates the flexibility of the DLL interface, but first a small recap of the simple gearbox model is given: The model describes the torsional behavior of a planetary gear stage. It has a total of 9 DOFs, 6 DOFs describing rigid body translation and rotation and 3 DOFs for the rotation of the planet holder, the ring wheel, and the sun wheel. The planet holder is assumed to hold 3 planet wheels, and each planet interacts with the sun wheel and the ring wheel via springs. When such a planetary gear stage is mounted in a wind turbine, the ring wheel is (somehow) coupled to the nacelle, the planet holder to the shaft/rotor, and the "geared output" is taken from the sun wheel on which other gear stages can be coupled. Normally 3 gear stages are needed in order to obtain the decided gear ratio between the shaft/rotor rotation and the output of the whole gearbox on which the generator is coupled.

This (generic) example takes another step towards modelling the whole gearbox. It uses two instances (stage 1 and stage 2) of the simple gearbox model and couples them, both individually and to the HAWC2 model. The following constraints are defined for this coupling:

1. The ring wheels of the two instances are coupled to each other and to the tower top node of the HAWC2 model (at a certain distance).
2. The shaft end of the HAWC2 model is coupled to the planet holder of stage 1.
3. The sun wheel of stage 1 is coupled to the planet holder of stage 2, and finally,
4. The sun wheel of stage 2 is coupled generator of the HAWC2 model.

Simulation of the coupled system is made, and screen shots of the animated rotation of the individual gear wheels are shown in Figure 129. In the figure, the turbine is shown in white, stage 1 is shown in blue, and stage 2 is shown in red. The viewpoint is directly in front of the turbine, looking in the wind direction. The tower and the 3 blades can be seen for the HAWC2 model, and for the two gear stages, the 3 planet wheels, the ring wheel and the sun wheel are drawn. The snapshots start at the 1st time step, and each shot is then taken when the sun wheel of stage 2 has taken half a revolution. The gear ratio of each stage is 1:10.

It is seen that the constraints defined for the systems are fulfilled:

1. The two ring wheels coincide at all times.

2. The blades intersect the center of the blue planet wheels at all times.
3. The blue sun wheel follows the red planet holder, and finally,

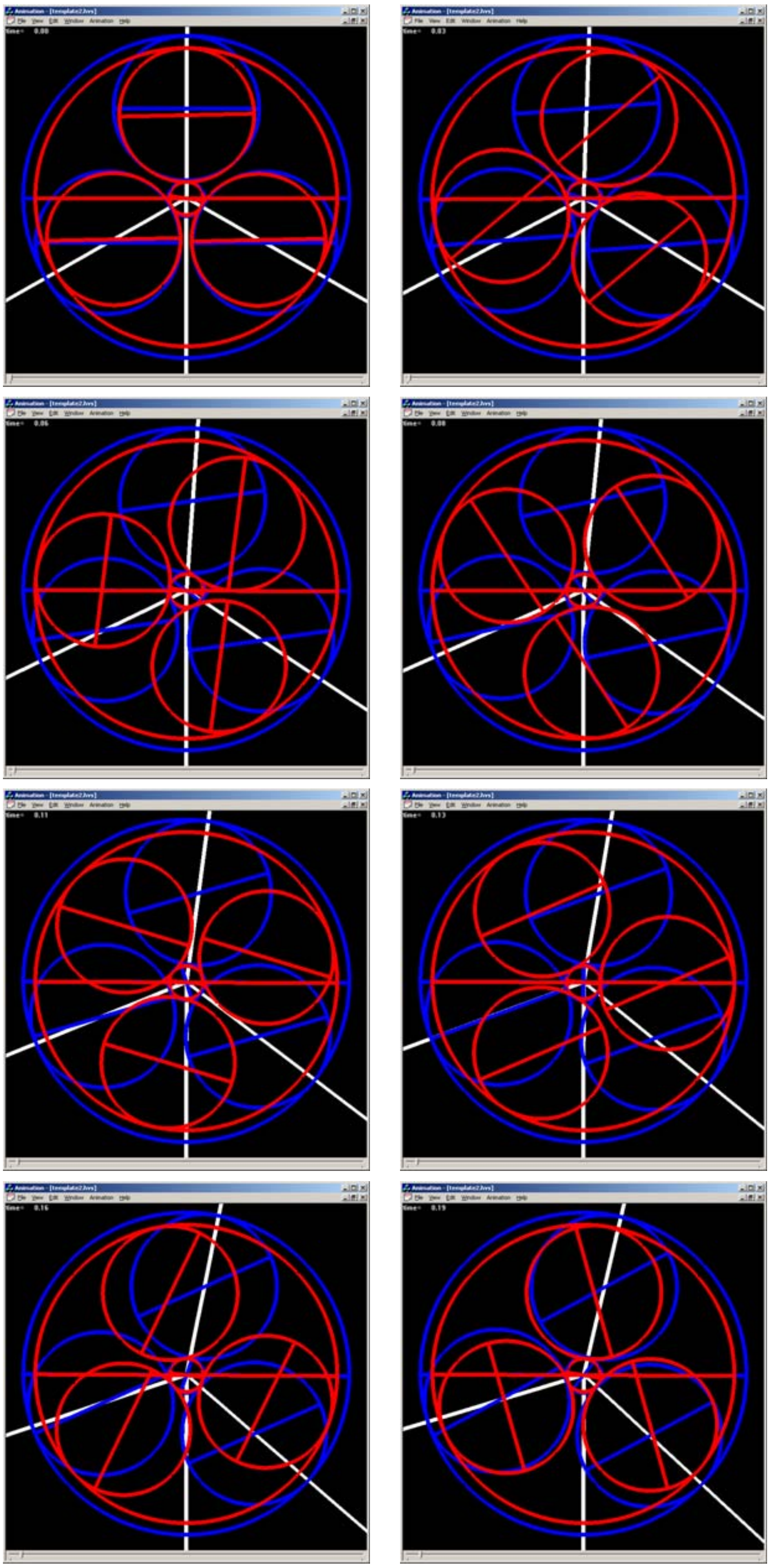

Figure 129. Snapshots of simulation of two gear stages coupled to a wind turbine model. The chronology is left -> right, up->down.

4. the red sun wheel follow the generator (cannot be seen, but it does.)

Further, at snapshot #6 in Figure 129 (picture in row 3, column 2 in Figure 129), the sun wheel of stage 2 has rotated $2\frac{1}{2}$ revolutions. With the gear ratio of 1:10, the sun wheel of stage 1 should then have rotated $\frac{1}{4}$ of a revolution. This can be validated by looking at snapshot #6.

13.4 Conclusion, Perspective, and Future Work

The project has resulted in validated interface between HAWC2 and external dynamic systems intended to simulate the dynamic response of the combined HAWC2 wind turbine model and the external system. The interface was validated by implementing a model of a gear box with two connected planetary gear stages and connecting that to a wind turbine model in HAWC2.

The DLL interface provides the possibility of other expert areas to interface their own kernel knowledge with a state of the art model of a wind turbine without having to reveal any of their key competence because no source code swapping is needed for the interface to work. Potential users could be experts on floating structures and hydrodynamics who want to develop floating foundations for wind turbines, or gearbox manufacturers who want to explore the interaction between gearbox and wind turbine dynamics, and all kinds of special use of HAWC2 which is not general enough to be included inside the HAWC2 kernel.

It should finally be mentioned that during the present project we formulated a very flexible gear model which can be used to model more advanced gear models like the one shown in Figure 127. All the necessary building blocks, *except* from a gear tooth interaction model, was formulated and programmed using the DLL interface, but at the time of reporting the work was not completed. This is left for future work.

References

[1] T. J. Larsen, K. Thomsen, and F. Rasmussen. Dynamics of a wind turbine planetary gear stage. In *Proceedings CD-ROM. CD 2. European wind energy conference and exhibition 2003 (EWEC 2003)*. EWEA, 2003.

[2] T. J. Larsen, K. Thomsen, and F. Rasmussen. Dynamics of a wind turbine planetary gear stage. Technical Report Risø-I-2112(EN), Risoe, National Laboratory, 2003.

[3] J. Lin and Parker R. G. Analytical Characterization of the Unique Properties of Planetary Gear Free Vibration. *Journal of Vibration and Acoustics*, vol. 121:pp. 316–321, 1999.

[4] R. Parker, F. Rasmussen, and T. J. Larsen. Dynamic Modelling and Analysis of a Wind Turbine Planetary Gear with Tooth Backlash and Bearing Clearance. In *Scientific Proceedings (EWEC 2006)*. EWEA, 2006.

[5] Christian Bak, editor. *Research in Aeroelasticity EFP-2006*, chapter 9: Detalied Nacelle Dynamics. Risø-R-1611(EN). Risø National Laboratory, July 2007.

[6] Ted Belytschko, Wing Kam Liu, and Brian Moran. *Nonlinear Finite Elements for Continua and Structures*. John Wiley & Sons Ltd., 2000.

14 Complete list of publications from the project

14.1 Journal papers

- Okulov, Valery; Sørensen, Jens Nørkær An ideal wind turbine with a finite number of blades Doklady Physics, vol: 53(6), p. 337-342 (2008)
- Okulov, Valery; Sørensen, Jens Nørkær Refined Betz limit for rotors with a finite number of blades Wind Energy, vol: 11(4), p. 415-426 (2008).
- Velte, Clara Marika; Hansen, Martin Otto Laver; Cavar, Dalibor Flow analysis of vortex generators on wing sections by stereoscopic particle image velocimetry measurements Environmental Research Letters, vol: 3(1), p. 1-11 (2008).
- Velte, Clara Marika; Hansen, Martin Otto Laver; Okulov, Valery Helical structure of longitudinal vortices embedded in turbulent wall-bounded flow Journal of Fluid Mechanics, vol: 619, p. 167-177 (2009).
- Pedersen, Knud Ole Helgesen; Hansen, Kurt Schaldemose; Schmidt Paulsen, Uwe; Sørensen, Poul Ejnar Wind Turbine Measurement Technique-an Open Laboratory for Educational Purposes Wind Energy, vol: 11, p. 281-295 (2008).
- Larsen, Gunner Chr.; Hansen, Kurt Schaldemose Rational Calibration of Four IEC 61400-1 Extreme External Conditions Wind Energy, vol: 11, p. 685-702 (2008).
- Ivanell, S.; Sørensen, Jens Nørkær; Mikkelsen, R.; Henningson, D. Analysis of Numerically Generated Wake Structures Wind Energy, vol: 12(1), p. 63-80 (2009).
- Shen, Wen Zhong; Hansen, Martin Otto Laver; Sørensen, Jens Nørkær Determination of the angle of attack on rotor blades Wind Energy, vol: 12(1), p. 91-98 (2009).
- Shen, Wen Zhong; Zhang, Jian Hui; Sørensen, Jens Nørkær The Actuator Surface Model: A New Navier-Stokes Based Model for Rotor Computations Journal of Solar Energy Engineering, vol: 131(1) (2009).
- Niels N. Sørensen CFD modelling of laminar-turbulent transition for airfoils and rotors using the $\gamma - Re_\theta$ model, Wind Energy, 2009, To be published, Available Online

14.2 Conference papers

- Bertagnolio F., Madsen H.Aa. and Bak C., "Comparison and Validation of Trailing Edge Noise Models", Conference Proceedings, Wind Turbine Noise 2009, Aalborg, June 2009.
- Bertagnolio F., Madsen H.Aa. and Bak C., "Experimental Validation of TNO Trailing Edge Noise Model and Application to Airfoil Optimization", Conference Proceedings, European Wind Energy Conference and Exhibition, EWEC'09, Marseille, March 2009.
- Aagaard Madsen, H., Low frequency noise from wind turbines - mechanisms of generation and its modelling. In: Low frequency 2008. Proceedings. 13. International conference on low frequency noise and vibration and its control, Tokyo (JP), 21-23 Oct 2008. (Institute of Noise Control Engineering of Japan, 2008) 34-3P1
- Hansen, M. H., "Bias effect of self-induced turbulence on the stall-flutter limit of an airfoil section", In the Proceedings of the 16th International Congress on Sound and Vibration, Krakow, 5-9 July, 2009.
- Shen, Wen Zhong; Sørensen, Jens Nørkær Aero-Acoustic Moldeling using Large Eddy Simulation Presented at 37th International Congress and Exhibition on Noise Control Engineering. Shanghai, China, 2008

- Zhao, Rongyong; Su, Yongqing; Knudsen, Torben; Bak, Thomas; Shen, Wen Zhong Multi-Agent Model for Fatigue Control in Large Offshore Wind Farm Presented at 2008 International Conference on Computational Intelligence and Security. In: Proceedings of International Conference on Computational Intelligence and Security, p. 71-75-Suzhou, China
- Velte, Clara Marika; Hansen, Martin Otto Laver; Meyer, Knud Erik; Fuglsang, Peter Evaluation of the Performance of Vortex Generators on the DU 91-W2-250 Profile using Stereoscopic PIV Presented at International Symposium on Energy, Informatics and Cybernetics. Orlando, Florida, 2008.
- Frandsen, Sten Tronæs; Sørensen, Jens Nørkær; Mikkelsen, Robert Flemming; Friis Pedersen, Troels; Antoniou, Ioannis; Hansen, Kurt Schaldemose The generics of wind turbine nacelle anemometry Presented at 2009 European Wind Energy Conference and Exhibition. Marseille (FR), 16-19 March, 2009
- Gaunaa, Mac; Øye, Stig; Mikkelsen, Robert Flemming Theory and design of flow driven vehicles using rotors for energy conversion Presented at 2009 European Wind Energy Conference and Exhibition. Marseille (FR), 16-19 March, 2009.
- Behrens, Tim; Zhu, Wei Jun; Shen, Wen Zhong; Sørensen, Jens Nørkær; Sørensen, Niels N.; Wedel-Heinen, Jens Jakob Calculations of Flow around an Airfoil with a Trailing Edge Flap by Use of an Immersed Boundary Method Presented at 2009 European Wind Energy Conference and Exhibition. Marseille (FR), 16-19 March 2009.
- F. Zahle and N. N. Sørensen. Characteriszation of the unsteady flow in the nacelle region of a modern turbine. In *Proceedings of the 2009 EWEC Conference*, Marseille, France, 16-19 March 2009.
- Bak, Christian; Andersen, Peter Bjørn; Madsen Aagaard, Helge; Gaunaa, Mac; Fuglsang, P.; Bove, S. Design and verification of airfoils resistant to surface contamination and turbulence intensity Presented at: 26. AIAA applied aerodynamics conference. Honolulu, HI (US), 18-21 Aug, 2008 In: *[Technical papers] presented at the 42. AIAA aerospace sciences meeting and exhibit, p. AIAA 2008-7050-Reston, VA (US) : American Institute of Aeronautics and Astronautics, 2008*

14.3 Oral presentations

- Bertagnolio F., "Validation of TNO Trailing Edge Noise Model and Application to Airfoil Optimization", Vindkraftkonferencen, Invited Speaker, Fredericia, Mai 2009.
- Sørensen, Jens N. The aerodynamics of wind turbines Invited lecture at ICTAM 2008, Adelaide, Australia
- Sørensen, Jens N. Vortex Theory of the Ideal Wind Turbine EWEC 2009, Marseille
- Troldborg, Niels Numerical Simulations of Wakes of Wind Turbines Operating in Sheared and Turbulent Inflow EWEC 2009, Marseille
- Hansen, Kurt S. Lidar Measurements on Full Scale Wind Characteristics EWEC 2009, Marseille

14.4 Books

- Hansen, Martin Otto Laver Aerodynamics of Wind Turbines Second edition. - 2. ed. - - Earthscan, 2008 (p. 181)

14.5 PhD Theses

- Troldborg, Niels Actuator Line Modeling of Wind Turbine Wakes, Department of Mechanical Engineering, DTU, June 2008 (p. 142)

14.6 MSc Theses

- Li Na "Utilization of tip vortex energy" MEK-FM-EP 2009-04
- Babak Diznabi "Investigation of the flow relation to nacelle anemometry" MEK-FM-EP 2009-03
- Konstantinos Komninos "Modeling considerations of the optimum rotor using vortex method" MEK-FM-EP 2008-13
- Peter Bæk "Experimental Detection of Laminar to Turbulent Boundary layer Transition on Airfoils in an Industrial Wind Tunnel Facility" MEK-FM-EP 2008-12
- Kasper Mortensen "CFD Simulations of an Airfoil With Leading Edge Ice Accretion" MEK-FM-EP 2008-11
- Casper Skovby "Solution of Boundary Layer Flows about Rotating Wings" MEK-FM-EP 2008-10
- Ulrik Vølcker Andersen "Load Reduction of Support Structures of Offshore Wind Turbines" MEK-FM-EP 2008-09

Risø DTU is the National Laboratory for Sustainable Energy. Our research focuses on development of energy technologies and systems with minimal effect on climate, and contributes to innovation, education and policy. Risø has large experimental facilities and interdisciplinary research environments, and includes the national centre for nuclear technologies.

Risø DTU
National Laboratory for Sustainable Energy
Technical University of Denmark

Frederiksborgvej 399
PO Box 49
DK-4000 Roskilde
Denmark
Phone +45 4677 4677
Fax +45 4677 5688

www.risoe.dtu.dk